


# Development of Innovative Additives Targeting Glazed Ceramics

By

Aneesa Nasar Nabi

A thesis submitted to
the University of Birmingham
for the degree of
DOCTOR OF PHILOSOPHY

Soft Matter Engineering Group
School of Chemical Engineering
College of Engineering and Physical Sciences
University of Birmingham
August 2024

UNIVERSITY OF
BIRMINGHAM

## University of Birmingham Research Archive

### e-theses repository

This unpublished thesis/dissertation is copyright of the author and/or third parties. The intellectual property rights of the author or third parties in respect of this work are as defined by The Copyright Designs and Patents Act 1988 or as modified by any successor legislation.

Any use made of information contained in this thesis/dissertation must be in accordance with that legislation and must be properly acknowledged. Further distribution or reproduction in any format is prohibited without the permission of the copyright holder.

*This declaration affirms that all work presented in this thesis is solely the work of the author. All experiments and analyses were conducted by the author.*

© Copyright by ANEESA NASAR NABI, 2024

All Rights Reserved

## ABSTRACT

This thesis investigates the development and application of innovative polymer additives aimed at enhancing anti-fouling properties and overall functionality of glazed ceramic tiles. The research focuses on understanding the behaviour of polyelectrolytes and their interactions at various interfaces, addressing industrial challenges related to improving ceramic surface properties and creating effective anti-fouling coatings.

The study begins with a comprehensive review of polymers and polyelectrolytes, both in solution and at interfaces, exploring key phenomena such as adsorption, desorption, surface modification, and the anti-fouling characteristics of these polymers.

A multi-faceted methodological approach is employed, utilising advanced characterisation techniques such as Quartz Crystal Microbalance with Dissipation Monitoring (QCM-D) for real-time analysis of mass adsorption and rate constants, Atomic Force Microscopy (AFM) to examine the thickness and adhesion of polymer coatings at the nanoscale, Dynamic Light Scattering (DLS) to assess the size and charge of polymer particles in solution, and Surface Tension Measurements to elucidate interactions between polymers and ceramic surfaces, with a particular focus on wettability and coating uniformity.

The findings reveal that the architecture of polymers significantly influences their performance. For example, block copolymers form stable, hydrated layers on ceramic surfaces, which are critical for anti-fouling applications. In contrast, random copolymers exhibit varied adsorption behaviours depending on polymer concentration and environmental pH. The research also examines the impact of foulants on polymer performance, showing that certain polymer architectures provide superior resistance to fouling—a feature particularly important in applications such as household toilets, where maintaining clean surfaces is essential.

In conclusion, this work provides a detailed understanding of how innovative polymer additives can enhance the properties of glazed ceramics. The results indicate that by tailoring polymer structures, substantial improvements in the functionality of ceramic coatings can be achieved, with significant implications for industrial applications. Future research directions include optimising polymer architectures for specific applications and exploring further characterisation methods to advance the field.

## DEDICATION

To the people who think they are not enough, you are more than enough.

**Acknowledgements**

In the name of Allah, the Most Gracious, the Most Merciful. May blessings and peace be upon our Prophet Muhammad (peace be upon him). Glory be to Allah, praise be to Allah, Allah is the Greatest!

First and foremost, I extend my deepest thanks to my Lord, who taught me and guided me throughout this humble endeavour. A profound teaching from the Quran, 'Allah does not burden a soul beyond that it can bear' (Quran 2:286), gave me the strength to persevere through the challenges I faced, reminding me that Allah would not place me in a situation I could not endure. I express my highest gratitude to Allah (SWT) for granting me Sabr (patience), countless blessings, and ultimately the opportunity to make my dream a reality. Alhamdulillah (praise be to the Lord) for it all!

I would like to express my sincere gratitude to Innospec for their partial sponsorship of this doctoral project. A special thank you goes to Dr. Jack Saunders for his unwavering support in synthesising the random copolymers essential to my research. I am deeply grateful for your openness to my questions and for creating an environment where I never felt hesitant to seek clarification. Your willingness to accommodate impromptu Teams calls and your patience in explaining complex concepts were invaluable to my understanding of the project. Your guidance has been truly inspirational, reinforcing my passion for inquiry and encouraging me to continue exploring the 'why' in the world of science.

To Professor Peter Fryer, no words can fully capture the depth of my gratitude for the privilege of having you as my supervisor. Your mentorship has been an incredible honour, and I am deeply thankful for your support from the very beginning. Dr. Richard Greenwood, it has been a true pleasure getting to know you and our shared coffee breaks have been a delightful and cherished part of this journey. I owe much of where I stand today to your influence and guidance. I hope that one day you both will recognise the profound impact

you've made, not just on me, but on the countless girls and women in my culture. Because of your belief in me, I am empowered to break the mould that was set for me at birth, and I am determined to help others in my culture do the same.

I would like to thank my family. To my mum, you taught me to stand on my own two feet, to be independent, and never to let anyone stand in the way of my education. I hope I have made you proud. To my Dad and Nomaan bhai, you showed me the importance of perseverance and pushed me forward even when I wanted to give up—you are the true definition of tough love. And to Ibrahim, as your big sister, I hope that by completing this PhD, I am setting an example and showing you that the sky is the limit; if you put your mind to it, you can achieve anything inshallah. And to Nabeel bhai and Umima baji, your support during our late-night calls has been invaluable. Thank you for listening to my worries, for letting me cry, and for always reminding me that this journey would soon come to an end and that I could do it. Your words of encouragement meant the world to me, and I am deeply grateful to you both.

To the CDT management team—Sian, Estefania, and Eleanor—you embody the true meaning of empowering women. I feel incredibly fortunate to have had your support during the final stages of my PhD. Whenever I doubted myself and felt like I couldn't go on, you always found a way to make me laugh and remind me that I was capable of achieving this. I couldn't have done it without you, and for that, I am deeply grateful to each of you. And to my fellow students in the CDT and the academic staff, thank you for your words of encouragement during the writing stage. Your support motivated me to push myself and do my very best.

To Nicole, Hannah and Zoe, I can't thank you enough for always being there for me during my PhD journey and beyond. Even when I wanted to be alone, you both reminded me that I didn't have to face things alone. I treasure our shared laughter, even when hushed by others, as it only strengthened our bond.

To Dr. Tugce Caykara, my amazing PhD mentor, I feel fortunate to have had you by my side in the last two years of my doctoral journey. You came into my life just when I needed someone like you the most. I'll miss our doughnut breaks and our heartfelt talks. Seeing how much you've grown has been truly inspiring.

To Dr. Heather Mercer, you entered my life at a time when I needed someone like you the most, and I had no idea just how profound your impact would be. Words can't fully capture the difference you've made in both my personal and academic life. I feel like I won the lottery, not only gaining a secondary PhD mentor but also a life mentor. You inspire me to be a better person and to show kindness to everyone I meet. Thank you, sissy, for always believing in me, even when I struggled to believe in myself.

To everyone at SCFIT, your words of encouragement will forever be remembered. Starting CrossFit towards the end of my PhD truly saved and transformed my life. I feel incredibly fortunate to have had a place where I could release my stress. To the coaches, thank you for pushing me to become stronger, not just physically but emotionally as well.

To my love, you entered my life just as I was nearing the end of my PhD journey. A PhD can be incredibly lonely and isolating, but with you by my side, I know I won't have to feel that way again inshallah. Here's to closing this chapter and beginning all the next ones with you alhamdulillah.

Lastly, I want to thank myself. It's true that sometimes all you need is one person in your corner, and even if that person is you, it's more than enough. You are enough!

*"Everything has beauty, but not everyone sees it."*

Confucius

# Contents


**Page**

**1 Introduction** **1**

1.1 Research Motivation . . . . . 1

1.2 Industrial Relevance . . . . . 4

1.3 Research Focus and Methodology . . . . . 4

**2 Polymer Structure in Solution and at Surfaces and Interfaces** **8**

2.1 Polymer Science . . . . . 9

2.1.1 Polymer Solubility . . . . . 10

2.1.2 Polyelectrolytes . . . . . 11

2.1.3 Polyelectrolytes in Solution . . . . . 18

2.1.4 Polyelectrolytes at the interface . . . . . 21

2.1.5 pH and Temperature . . . . . 24

2.2 Surface Science . . . . . 25

2.2.1 Surface Adsorption Kinetics . . . . . 25

2.2.2 Surface Adhesion . . . . . 27

2.3 Anti-fouling properties of polymers . . . . . 29

2.3.1 Hydrophobicity and Charge Separation in Zwitterionic Peptides for Antifouling . . . . . 31

2.3.2 Polyzwitterions as Anti-fouling Interface . . . . . 33

2.4 Conclusions . . . . . 35

**3 Methodology** **37**

3.1 Quartz Crystal Microbalance - Dissipation (QCM-D) . . . . . 38

3.1.1 Principle . . . . . 38

3.1.2 Data Interpretation . . . . . 40

3.1.3 Limitations of the QCM Method . . . . . 41

3.1.4 Experimental Setup . . . . . 42

3.1.5 Cleaning Methodology: preparation of equipment . . . . . 44

3.1.6 Data Analysis . . . . . 45

3.2 Atomic Force Microscopy . . . . . 48

3.2.1 Principle . . . . . 48

3.2.2 Data Interpretation of force-distance curves . . . . . 52

3.2.3 Limitations . . . . . 55

3.2.4 Cleaning of Cantilevers . . . . . 55

3.2.5 Experimental Setup . . . . . 56

3.2.6 Data Analysis . . . . . 57

3.3 Dynamic Light Scattering (DLS) - Measurement of Particle Size . . . . . 57

3.3.1 Principle . . . . . 58

3.3.2 Data Interpretation . . . . . 60

3.3.3 Limitations . . . . . 62

3.3.4 Cleaning Method . . . . . 63

3.3.5 Experimental Setup . . . . . 64

3.3.6 Data Analysis . . . . . 66

3.4 Zeta Potential . . . . . 66

3.4.1 Principle . . . . . 66

3.4.2 Data Interpretation . . . . . 69

3.4.3 Limitations . . . . . 71

3.4.4 Cleaning Method . . . . . 72

3.4.5 Experimental Setup . . . . . 72

3.4.6 Data Analysis . . . 74
3.5 Surface Tension Measurement . . . 74
3.5.1 Principle . . . 74
3.5.2 Data Interpretation . . . 78
3.5.3 Limitations . . . 79
3.5.4 Cleaning Method . . . 80
3.5.5 Experimental Setup . . . 81
3.5.6 Data Analysis . . . 82
3.6 Flow Lubricating Solution for Household Toilets (FLuSHT) . . . 83
3.6.1 Principle . . . 83
3.6.2 Data Interpretation . . . 84
3.6.3 Limitations . . . 84
3.6.4 Cleaning Method . . . 85
3.6.5 Experimental Setup . . . 86
3.6.6 Data Analysis . . . 89
3.7 Force Board . . . 89
3.7.1 Principle . . . 89
3.7.2 Experimental Setup & Data Interpretation . . . 89
3.7.3 Limitations . . . 92
3.7.4 Cleaning Method . . . 93
3.7.5 Data Analysis . . . 93
3.8 Conclusions . . . 93

**4 The Effect of Block Co-polymer Architecture on its Surface Deposition 95**
4.1 Introduction . . . 95
4.1.1 Materials . . . 97
4.2 Results & Discussion . . . 101

4.2.1 Effect of varying concentration on surface adsorption . . . . . 101
4.2.2 Effect of varying concentration on adsorption kinetics . . . . . 107
4.2.3 Binding Energy . . . . . 115
4.2.4 Effect of foulant on block co-polymer . . . . . 117
4.2.5 Hydration Layer - QCM . . . . . 120
4.2.6 Hydration Layer - AFM . . . . . 124
4.2.7 Thickness of block copolymer samples in deionised water . . . . . 127
4.3 Conclusions . . . . . 129

**5 The Effect of Random Co-polymer Architecture on its Surface Deposition 135**
5.1 Introduction . . . . . 135
5.2 Results and Discussion . . . . . 138
5.2.1 Study of random copolymers provided by Innospec . . . . . 138
5.2.2 The Effect of pH Change on the Random Copolymers' Size in Bulk Solution . . . . . 146
5.2.3 The Effect of pH on the Random Copolymers' Zeta potential in Bulk Solution . . . . . 155
5.2.4 Effect of varying pH on the Random Copolymers' Adsorption . . . . 158
5.2.5 Effect of Varying pH on the Random Copolymers' Rate Constant for Adsorption . . . . . 161
5.2.6 Relationships Between Measured Data . . . . . 164
5.3 Conclusions . . . . . 179

**6 The Effect of Deposited Polymer on the Attachment of Viscoelastic Material 182**
6.1 Introduction . . . . . 182
6.2 Results & Discussion . . . . . 184
6.2.1 Static Contact Angle . . . . . 184
6.2.2 Dynamic Contact Angle . . . . . 188

6.2.3 Contact Angle Kinetics . . . . . 192
6.2.4 Adhesion of viscoelastic material on different random copolymer samples - Forceboard experiments . . . . . 197
6.2.5 Effect of random copolymer structure on adhesion force . . . . . 199
6.2.6 Effect of random copolymers on the work of adhesion . . . . . 202
6.2.7 Preliminary experiments with FLuSHT . . . . . 205
6.3 Conclusions . . . . . 207

**7 Final Conclusions and Future Work** **210**
7.1 Future Work . . . . . 214

**A Section A** **218**

**B Section 2** **222**

**References** **225**

# List of Figures

1.1 Projected Global Water Stress by Country in 2040. The map, created by the World Resources Institute, illustrates the anticipated water stress levels worldwide by 2040. The colours represent the ratio of water withdrawals to supply: yellow (<10%), light orange (10-20%), orange (20-40%), red (40-80%), and dark red (>80%). Regions expected to experience the highest levels of water stress include Northern Africa, the Middle East, and parts of Asia.[4] . . 2

2.1 Illustration of a few of many the basic copolymer structures, (a) random (b) alternating (c) block and (d) graft copolymers. A in pink and B in blue represent different monomers. . . . . 10

2.2 Schematic illustration of polyelectrolyte complexation. (i)Solution and (ii) Deposition behaviour of the polyelectrolyte onto the surface.[19] . . . . . 15

2.3 Illustration of a polyelectrolyte coil exhibiting an expanded conformation under low salt concentration, demonstrating the "polyelectrolyte effect," followed by a transition to a more compact conformation under high salt concentration. 20

2.4 The structure of: A) poly(styrene 4-sulfonate) (PSS) which is a polyanion; B) poly(acrylic acid) (PAA) which is a weak polyanion; C) poly(allylamine hydrochloride) (PAH) which is a polycation; and D) poly(diallyldimethylammonium chloride) (PDADMAC) which is a polycation. . . . . 21

2.5 Molecular structure of Chitosan (CHI) (left) and Poly (diallyldimethylammoniumchloride) (PDADMAC) (right). . . . . 23

2.6 Polymer chain adsorbed at the surface consisting of tail, loop and train model. 24

2.7 Zwitterionic polymers used for protein reduction applications included: A. Sulfobetaine (SB): Poly(3-[N-(2-methylacryloylethyl)-N,N-dimethylammonio] propanesulfonate) (PMAPS), poly(sulfobetaine methacrylate) (PSBMA), and poly(3-[2-(acrylamido)-ethyl dimethylammonio]propanesulfonate) (PAEDAPS); B. Carboxybetaine (CB): Poly(carboxybetaine methacrylate) (PCBMA); C. Phosphobetaine (PB): Poly(2-methacryloyloxylethyl phosphorylcholine) (PMPC). 35

3.1 Schematic representation of a basic QCM output curve, Stage A is deposition, Stage B is adsorption and Stage C is desorption. Figure 3.1 (a) shows the molecular process occurring, whilst Figure 3.1 (b) shows the changes in factors measured by the QCM. . . . . 40

3.2 QCM instrument setup. . . . . 43

3.3 QCM 5 MHz 14 mm Cr/Au/SiO2 sensor setup and chamber. . . . . 43

3.4 Frequency vs time plot with mass adsorbed (obtained from the Saurbrey equation) on the secondary y-axis. . . . . 46

3.5 Illustrates a) Change in mass adsorbed in ng per $cm^2$ vs time in seconds which can then be converted to plot b)log vs time plot using the first-order Langmuir isotherm equation. . . . . 47

3.6 Schematic diagram of an atomic force microscopy unit.[110] . . . . . 49

3.7 AFM components outside the cell.[107] . . . . . 50

3.8 (a)Force distance curve data representation. Approach and retraction curves are shown in red and blue, respectively.[113] (b) The figure illustrates the tip atoms interacting with atoms of the sample surface, where the force is measured between the tip and the surface. . . . . 53

3.9 Influence of Particle Size on Intensity in DLS Measurements. Figure shows the impact of smaller and larger particles on the intensity distribution obtained from Dynamic Light Scattering (DLS) measurements. The data highlights how particle size variations affect the overall intensity profile. . . . . 59

3.10 Schematic diagram of DLS autocorrelation function. Larger particles diffuse more slowly than small ones, resulting in a longer time to lose correlation with the original signal, while smaller particles diffuse rapidly, causing a quicker decay in signal correlation. . . . . 61

3.11 Principle of DLS Operation: A laser light is directed at suspended particles, and a high-time-resolution detector measures the intensity of the light scattered at a specific angle, $\theta$. These fluctuations in scattered light intensity over time are caused by the Brownian motion of the particles.[127] . . . . . 65

3.12 Schematic representation of zeta potential. . . . . 67

3.13 Measuring Electrophoretic Mobility of a sample placed in a DTS1070 cuvette, indicating the movement with the effect of the positive and negative electrodes. 70

3.14 Schematic of Zeta Potential Measurement Process. Illustration of how light scattered at a 17° angle merges with a reference beam to produce a varying intensity signal. The frequency of these fluctuations corresponds to the particles' speed, which is analysed by a digital signal processor to identify characteristic frequencies in the scattered light. . . . . 71

3.15 Operation of the Zetasizer Nano - Zeta potential measurements. (A) Incident, (B) Reference beam and (C) Scattering beam. 1 - Laser, 2 - Sample cell, 3 - Detector, 4 - Digital signal processor, 5 - Computer, 6 - Attenuator and 7 - Compensation optics.[129] . . . . . 73

3.16 Water droplet interaction between solid, liquid and gas, showing surface energies. Red arrow indicates the phase boundary between solid and vapour interface, Green arrow indicates the phase boundary between the liquid and vapour interface and yellow arrow indicates the phase boundary between the solid and liquid interface.[132] . . . . . 75

3.17 Illustration of lotus leaf vs cotton fabric, showing a lotus leaf having a hydrophobic surface and the cotton fabric having a hydrophilic surface. . . . . 76

3.18 Surface behaviour of high surface tension liquid vs. low surface tension liquid, giving high and low contact angles respectively. . . . . 77

3.19 Illustration of a force balance can be written as $\gamma_{SV} = \gamma_{SL} + \gamma_{LV} \cos\theta$ known as the Youngs Equation.[132,133] . . . . . 78

3.20 Illustration of different contact angle measurement scenarios for non-wetting and complete wetting along with their respective angles. . . . . 79

3.21 Image of surface tension setup. . . . . 81

3.22 Side View of FLuSHT setup. . . . . 84

3.23 FLuSHt Setup, showing the FLuSHT device, peristaltic pump and the deionised water. . . . . 87

3.24aThe plot depicts the Vertical Force (N) against time (seconds) obtained from force board measurements. Step (a) shows the tile approaching synthetic faeces, step (b) indicates the tile in contact with synthetic faeces, step (c) illustrates the tile being pulled away from synthetic faeces, and step (d) marks the tile no longer in contact with the synthetic faeces. . . . . 91

3.24bPlot showing vertical force (N) against time (s) for the bare control tile and random copolymers. . . . . 92

4.1 The chemical structures of the three-block co-polymers - PEO-*b*-PDMAEAMA (a) 5.0-*b*-2.5 (b) 5.0-*b*-5.6 and (c) 5.0-*b*-12.0. Numbers in colour show the repeat units of DMAEMA in the DMAEMA block. . . . . 98

4.2 (a)Molecular structure of 5.0-*b*-2.5 (PEO-*b*-PDMAEAMA), (b) Schematic illustration of the block copolymer and (c) Schematic illustration of block copolymer adsorption onto the QCM sensor. . . . . 99

4.3 Illustration of the theoretical deposition of three-block co-polymers - PEO-*b*-PDMAEAMA onto the substrate surface: (a) 5.0-*b*-2.5, (b) 5.0-*b*-5.6, and (c) 5.0-*b*-12.0. Red spheres illustrate the anchoring molecule - PDMAEMA, and blue spheres illustrate the functional molecule - PEO. The white slab illustrates the substrate surface. The illustration is not an accurate depiction of the system but is intended to provide a conceptual layout of molecular adsorption. . . . . 101

4.4 A typical QCM experimental plot of mass adsorbed versus time illustrated the different stages of the QCM measurement. Stage A involved deionised water, Stage B involved the block copolymer, and Stage C involved deionised water again. . . . . 102

4.5a Example representation of QCM plot, indicating polymer injection, pre-wash (Region 2) and post-wash (Region 3). . . . . 103

4.5b Plot of mass adsorbed vs. concentration of the three-block co-polymers pre and post-deionised water wash. Error bars show the standard error over five repeats and the line is added to clarify trends. . . . . 104

4.6 Plot of moles adsorbed vs. concentration of the three-block co-polymers pre and post-deionised water wash. Error bars show the standard error over five repeats and the line is added to clarify trends. . . . . 106

4.7 a) A typical QCM experimental plot of mass adsorbed versus time, illustrating the stage of polymer adsorption. b) Applying $\log(q_e - q_t)$ to the 'climb' section of the plot (a) to obtain the gradient of a straight line. . . . . 109

4.8 Plot of first-order rate constant ($s^{-1}$) against concentration (ppm) of 5.0-*b*-2.5 (light green), 5.0-*b*-5.6 (green) and 5.0-*b*-12.0 (dark blue) with their respective trend lines. Binding energy was obtained by utilising the trendlines and equation 4.1. . . . . 112

4.9 Correlation between the first-order kinetic rate constant ($s^{-1}$) and mass adsorbed (ng/cm$^2$) for PEO-*b*-PDMAEMA samples. The plot shows pre-wash (circle symbols) and post-wash (square symbols) data for three block copolymer compositions: 5.0-*b*-2.5 (green), 5.0-*b*-5.6 (red), and 5.0-*b*-12.0 (blue). This highlights the effect of washing and polymer composition on adsorption behaviour and kinetic properties. Note that a colour change has been implemented to emphasise the spread of data for clarity. . . . . 113

4.10 Determination of binding energy for 5.0-*b*-2.5 (light green), 5.0-*b*-5.6 (green) and 5.0-*b*-12.0 (dark blue) also the relationship of a straight line for 5.0-*b*-5.6 and 5.0-*b*-12.0 is illustrated. . . . . 116

4.11 Plot overlaying the change in mass adsorbed in ng cm$^{-2}$ against time in seconds for the block copolymers at a concentration of 200 ppm. Region 1 represents the polymer adsorption, region 2 is the deionised water rinse, region 3 is the BSA adsorption, and Region 4 is the final deionised water rinse. . . . . 118

4.12 Experimental procedure for densely packing PEG-OH and PEG-SH onto a gold QCM sensor in order to maximise surface coverage of PEG. . . . . 122

4.13 QCM measurement of densely packed PEG-OH/SH onto a gold QCM sensor at a constant flow rate of 56.54 $\mu$L min$^{-1}$. Region 1 is deionised water flow, Region 2 is BSA solution added and Region 3 is deionised water flow again. . 123

4.14 (a) Effect of hydration layer on protein adsorption. (b) AFM Adhesion Force curve (retract curve) of Thiol PEG in deionised water (red) and Thiol PEG in hexadecane (blue) on a gold QCM sensor coming into contact with a functionalised borosilicate cantilever tip. (c) A quantified approach of (b) showing the measured adhesion of the borosilicate cantilever tip being pulled away from the coated surface. The adhesion of an average of 300 force curves was plotted for part (c). . . . . 126

4.15 (a) Interfacial interactions are measured by the AFM when approaching a polystyrene particle of 9.5 - 11.5 $\mu$m towards the block copolymer samples at 200 ppm. (b) Schematic illustration of the configuration of the block copolymer deposited onto the surface as the cantilver tip is approaching the block copolymer chains. . . . . 129

5.1 Chemical structures of the monomers in the study. 2-(dimethylamino) ethyl methacrylate known as DMAEMA (blue), Acrylic acid known as AA (red), 2-(methacryloyloxy)ethyl[trimethylammonium chloride] known as MAETAC (black), Iso-octyl acrylate (green) known as i-OA, Ethylene glycol dimethacrylate (purple) known as EGDMA, and Dodecanethiol known as DDT (pink). . 138

5.2 Plot overlaying the change in mass adsorbed in ng $cm^{-2}$ against time in seconds for the initial random copolymers supplied (composition given in Table 5.1) by Innospec at a concentration of 200 ppm. Region 1 represents the polymer adsorption, region 2 is the deionised water rinse, region 3 is the BSA adsorption, and region 4 is the final deionised water rinse. . . . . 139

5.3 Mass adsorption of the random copolymer samples obtained *via* QCM measurements at the different stages of adsorption (see Figure 5.2). One hundred data points were collected for the mass adsorbed when the system was equilibrated. (i) Pink represented polymer adsorption in Region 1, 1800 to 1900 seconds; (ii) orange represented post-wash in Region 2, 4560 to 4660 seconds; (iii) green represented BSA adsorption in Region 3, 9660 to 9760 seconds; (iv) and blue represented the final rinse in Region 4, 13000 to 14000 seconds. The error bars represent the standard error of the mean (SEM). . . . . 140

5.4 Chemical structures of the random copolymers: Acrylic Acid (AA), [2-(methacryloyloxy)ethyl]trimethylammonium chloride (MAETAC), and [2-(dimethylamino)ethylmethacrylate] (DMAEMA). . . . . 145

5.5 (a) Schematic illustration of the random copolymer and (b) Schematic illustration of the random copolymer adsorption onto the QCM sensor. . . . . 146
5.6 Aggregation of random copolymer 10:90:0 both at pH2 (left) and pH 10 (right).149
5.7 A basic titration curve, showing the pH change whilst adding 1M NaOH drop by drop to the homopolymer and random copolymer solution. All solutions under investigation were set to approximately pH 2. This data was subsequently used to generate a pH-versus-NaOH-added graph using Python. . . . 150
5.8 Z-Average in nm (measured by DLS) against AA:MAETAC:DMAEMA (random copolymer samples) at pH 2 (pink), ambient (orange) and 10 (green) along with their respective errors. Thus, 100:0:0 is 100% acrylic acid. . . . . 152
5.9 Zeta potential in millivolts (mV) (measured by DLS, see section 3.4) for the AA:MAETAC:DMAEMA random copolymer samples at pH 2 (pink), ambient (orange) and 10 (green) along with their respective errors. . . . . 155
5.10 Mass Adsorbed of random co-polymers at pH 2, ambient pH and pH 10 at 200ppm. . . . . 158
5.11 Rate constant of random co-polymers at pH 2, ambient pH and pH 10 at 200ppm. . . . . 161
5.12 Correlation plot of mass adsorbed vs. rate constant of the random co-polymers at pH 2, ambient pH and pH 10 at 200ppm. . . . . 164
5.13 Correlation plot of mass adsorbed vs. z-average of the random co-polymers at pH 2, ambient pH and pH 10 at 200ppm. . . . . 166
5.14 Correlation plot of mass adsorbed vs. zeta potential of the random co-polymers at pH 2, ambient pH and pH 10 at 200ppm. . . . . 168
5.15 Correlation plot of z-average vs. zeta potential of the random co-polymers at pH 2, ambient pH and pH 10 at 200ppm. . . . . 170
5.16 Correlation plot of rate constant vs. z-average of the random co-polymers at pH 2, ambient pH and pH 10 at 200ppm. . . . . 172

5.17 Correlation plot of rate constant vs. zeta potential of the random co-polymers at pH 2, ambient pH and pH 10 at 200ppm. . . . . 174
5.18aCorrelation plot of bulk molecular weight vs average mass adsorbed at 200ppm.176
5.18bCorrelation plot of bulk molecular weight vs average rate constant at 200ppm. 177

6.1 Schematic of the experimental protocol to measure contact angle on 200 ppm Random Co-polymer samples of AA:MAETAC:DMAEMA. Step 1 represents the pre-rinse stage, while step 2 signifies the post-rinse stage. . . . . 186
6.2 Static Contact Angle of 200 ppm Random Co-polymer samples before and after deionised water rinse. Sample 0:0:0 is the bare ceramic surface contact angle. An average of five measurements were taken for each sample. The error bars represent the standard error of the mean (SEM), calculated for the five repeats of each polymer. . . . . 186
6.3 Schematic diagram of dynamic contact angle, illustrating how the angle of the deionised water droplet decreases over time. . . . . 189
6.4 Evolution of the water contact angle during the 45-second analysis period: dynamic contact angles of 0:0:0 (blue line), 10:90:0 (orange line), 10:60:30 (green line), 10:30:60 (red line), and 10:0:90 (purple line) are shown in (a) before rinsing and (b) after rinsing with deionised water. All random copolymer samples were deposited on a glazed ceramic tile at a concentration of 200 ppm. The plots represent individual measurements. . . . . 190
6.5 Example of water contact angle evolution over time of analysis for 10:90:0 which is 10% AA and 90% MAETAC. Blue dots are the experimental data for 10:90:0 before rinse. The red solid line was obtained by fitting equation 6.1 to the experimental data. . . . . 193
6.6 Plot showing kinetic constant *'k'* against AA:MAETAC:DMAEMA (random copolymer components), before and after rinse. . . . . 194

6.7 Plot correlating static contact angle against Kinetic constant 'k' before and after rinse. Arrows indicate the difference between before rinse and after rinse samples of the random copolymers. . . . . 196

6.8 Vertical force (N) against time (s) for the bare cleaned glazed ceramic tile. The grey rectangle represents the bare-cleaned glazed ceramic tile, while the orange sphere represents the synthetic faecal matter, and the thick black arrows indicate the direction in which the tile was headed and the applied force. In Step (a), the tile approached the synthetic faecal matter. In Step (b), the tile touched the synthetic faecal matter at a vertical force of 1N. Step (c) involved the tile being pulled away from the synthetic faecal matter to determine the vertical adhesion force (N), and Step (d) represented the complete detachment of the tile from the synthetic faecal matter. . . . . 198

6.9 Plot showing vertical force (N) against time (s) for the bare control tile (0:0:0) and random copolymers. The plot shows a single experiment, however, three of each measurement were carried out to assess reproducibility. . . . . 200

6.10 Illustrates average maximum adhesion force (N) for different copolymer compositions with standard error bars. The copolymer compositions are represented as ratios of AA:MAETAC:DMAEMA. Each bar represents the mean value from three measurements for each copolymer, with the error bars indicating the standard error of the mean. . . . . 202

6.11 Work of removal (J) calculated from equation (6.2) for different copolymer compositions with standard error bars. The copolymer compositions are represented as ratios of AA:MAETAC:DMAEMA. Each bar represents the mean value from three measurements for each copolymer, with the error bars indicating the standard error of the mean. . . . . 204

6.12 A comparison of preliminary data on sliding velocity (in millimetres per second, mm/s) before and after rinsing for various AA:MAETAC:DMAEMA polymer ratios. Pink bars represent the sliding velocity before rinsing, while orange bars depict the sliding velocity after rinsing. . . . . 206

# List of Tables


2.1 Schematic structure of various polyelectrolytes. . . . . 13

2.2 Examples of cationic polyelectrolyte (repeat units) and specific names and structures for each example. . . . . 16

3.1 Types of Tip-sample separation and measurement in AFM.[112] . . . . . 51

3.2 Composition of synthetic faeces.[5] . . . . . 88

4.1 Molecular weight and repeat units calculated for all three block copolymers. 100

5.1 Initial compositions of the random co-polymer samples provided by Innospec illustrating their weight (Wt) ratios, Mol ratios, and chemical structures for the study. . . . . 139

5.2 The compositions of the random copolymer matrix samples provided by Innospec were determined based on the QCM results of the blind study. These compositions are illustrated by their weight (Wt) ratios and molar (Mol) ratios. The rows highlighted in blue are the polymers used in Chapter 6, Section 6.2.1, to facilitate cross-referencing when discussing the results in Chapter 6. 144

5.3 Composition of the random copolymer mixtures of acrylic acid (AA), (methacryloyloxy)ethyl[trimethylammonium chloride] (MAETAC), and 2-(dimethylamino)ethyl methacrylate (DMAEMA), along with their respective pH values at $2 \pm 0.08$, ambient and $10 \pm 0.08$ . . . . . 147

# Chapter One

# Introduction

## 1.1 Research Motivation

In 2016, four billion people worldwide grappled with one of today's most pressing global issues: severe water scarcity.[1] Figure 1.1 shows a map of expected water stress by country in 2040. As the global population expands, the water demand intensifies, from domestic household usage to industrial applications. In response to this challenge, researchers have explored various approaches, including harvesting water from the atmosphere[2] and implementing water desalination and treatment technologies.[3] However, one method that has received comparatively less attention is the reduction of water consumption associated with toilet flushing, both in households and industries.

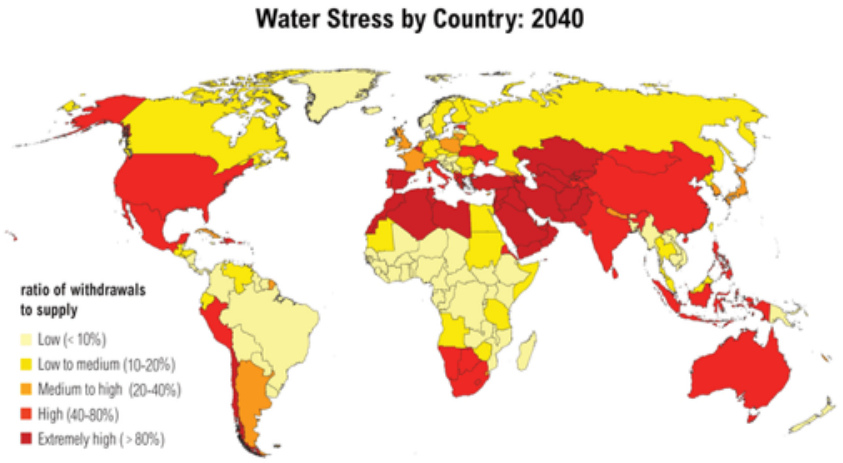



Figure 1.1: Projected Global Water Stress by Country in 2040. The map, created by the World Resources Institute, illustrates the anticipated water stress levels worldwide by 2040. The colours represent the ratio of water withdrawals to supply: yellow (<10%), light orange (10-20%), orange (20-40%), red (40-80%), and dark red (>80%). Regions expected to experience the highest levels of water stress include Northern Africa, the Middle East, and parts of Asia.[4]

It is estimated that over 141 billion litres of water are consumed daily for toilet flushing, which equates to approximately six times the daily water usage of the entire population of Africa.[5] Water and formulated polymer are necessary for the removal of faecal matter and urine, as well as containing chemical species that kill bacteria and ensure hygiene by eliminating odours and stains left behind by faecal matter. Reducing the amount of water used for flushing would offer several advantages:

- Improved water efficiency would facilitate the development of more efficient toilets, particularly crucial in regions facing water scarcity, such as sub-Saharan Africa.
- This reduction would enable the extension of hygiene access to areas with significant water scarcity.

- Even in regions where water is abundant, such reductions would lessen the environmental burden of the system.

An avenue that remains underexplored is the reduction of interfacial adhesion between toilet surfaces and human faeces, aiming to minimise the amount of water needed both for material removal and hygiene maintenance. Such an approach has the potential to reduce the volume of water required for waste removal on a global scale. The concept behind implementing the coating is to apply it within the toilet tank and have the polymer coating applied with every flush. This method ensures that each flush not only maintains a clean surface but also aids in the rapid and thorough removal of waste materials, preventing residues from adhering to toilet surfaces. Consequently, this approach could enhance waste removal efficiency and significantly reduce overall water consumption for sanitation purposes.

Suitable chemicals for adhesion reduction may exist, however, any compound used must be sustainable. Today, there exists a global imperative to conceive and refine sustainable materials. In recent decades, scientists have engineered numerous high-performing materials for various applications, albeit often at the expense of sustainability. The contemporary challenge lies in enhancing the sustainability of these materials while preserving or even enhancing their performance. Addressing this challenge necessitates a comprehensive understanding of the mechanisms underlying sustainable materials. As infectious and chronic diseases proliferate in our society, there has been an amplified emphasis on health and hygiene. One contributing factor to this trend is poor toilet hygiene, which can lead to the spread of multiple diseases, thereby exacerbating the prevalence of infectious diseases.[6] The leading global manufacturers of toilet cleaning products include P&G, Henkel AG & Co. KGaA, S. C. Johnson & Son, Inc., Unilever, Kao Corporation, The Clorox Company, Reckitt Benckiser Group Plc, and Church & Dwight, Inc., among others.[7] According to the Toilet Care Products Market Growth Analysis Report for 2023-2033, the compound annual growth rate for toilet care products is forecasted to increase by 3.4% over the next ten years. Presently

valued at US$5.8 billion, it is projected to reach US$8.1 billion.[6]

## 1.2 Industrial Relevance

Innospec is a global chemical company with twenty production and research sites. While its headquarters are in Denver, its primary manufacturing facilities are located in Europe and the U.S., with all fundamental scientific research and product discovery programs conducted at the R&D centre in Ellesmere Port. The company is involved in the development, manufacturing, blending, marketing, and supply of speciality chemicals for various applications, including fuel additives, personal care ingredients, home care products, agrochemicals, mining applications, and oilfield chemicals. Innospec operates through four main business segments: Fuel Specialties, Performance Chemicals, Oilfield Services, and Octane Additives. The primary focus of this research project associated with Innospec is to innovate a range of anti-fouling additives aimed at minimising soil attachment and repelling dirt to maintain a clean glazed ceramic surface.[8]

## 1.3 Research Focus and Methodology

The overarching objective of this research program is to create a thin polymer film capable of repelling foulants while maintaining transparency, stability, and activity, and forming a controlled layer on a glazed ceramic surface. This endeavour involves exploring a diverse range of chemical moieties to assess their deposition amounts and rate constants. Throughout this research project, the primary focus has been on the quartz crystal microbalance-dissipation (QCM-D) technique.

The QCM-D was employed to measure real-time changes in mass and viscoelastic properties at the sensor surface with nanoscale precision. This method allowed for monitoring molecu-

lar adsorption and desorption, providing insights into structural changes. The experimental setup included an advanced multichannel system with precise flow rates and thorough cleaning protocols to ensure accuracy.

Atomic Force Microscopy (AFM) was used to measure film thickness and adhesion by scanning a sharp tip over the sample surface. This technique was essential for assessing the physical properties of block copolymers, particularly focusing on film thickness and adhesion.

Dynamic Light Scattering (DLS) was employed to analyse both particle size and surface charge. DLS measured particle size by observing light scattering due to Brownian motion, while electrophoretic mobility assessments determined surface charge. This method was crucial for understanding polymer interactions in solution.

To measure the surface energy of liquids, which influences wetting and spreading behaviour on surfaces, Surface Tension Measurement was conducted. This technique helped determine the surface energy of polymers on various substrates.

The Flow Lubricating Solution for Household Toilets (FLuSHT) technique assessed polymer response to synthetic faeces, effectively bridging the gap between microscopic and macroscopic testing and evaluating polymer performance in real-world scenarios.

The Force Board Test measured the force required to detach a coated glazed ceramic tile from synthetic faeces, providing quantitative data on polymer adhesion properties under simulated real-world conditions.

Each method was selected for its specific strengths in providing detailed and accurate data essential for this study. The meticulous experimental setups, rigorous cleaning protocols, and thorough data analysis ensured the reliability and repeatability of the results.

The thesis is structured in a series of chapters:

- **Polymer Structure, in Solution, Surfaces and Interfaces:** Chapter 2 explores the fundamental aspects of polymer science, emphasising the structure and behaviour of polymers in solutions, on surfaces, and at interfaces. It begins by defining polymers and copolymers, detailing various architectures such as random, alternating, block, and graft copolymers. The chapter also investigates polyelectrolytes, their types (e.g., polycations, polyanions, polyampholytes, and polyzwitterions), and their applications in modifying surface properties for antifouling purposes. Special attention is given to understanding the adsorption, desorption, and orientation of polymers on surfaces, which is essential for developing effective antifouling polymers.

- **Experimental Methods and Instruments:** Chapter 3 outlines the experimental methods and instruments employed in this research. Key techniques include Quartz Crystal Microbalance (QCM) for monitoring adsorption and desorption, Atomic Force Microscopy (AFM) for measuring film thickness and adhesion, and Dynamic Light Scattering (DLS) for assessing particle size and polymer solution charge. Additional methods, such as contact angle measurements and the FLuSHT test, evaluate surface energy and the polymer's response to synthetic faeces. The chapter offers comprehensive insights into the principles, data interpretation, limitations, and setups of these methods.

- **Understanding the Surface Chemistry of Glazed Ceramic Tiles:** The surface properties of glazed ceramic tiles are analogous to those of silicon dioxide sensors, both characterised by the presence of silica ($SiO_2$). In this research, silicon dioxide

sensors were utilised due to their similar surface properties, making them suitable for the intended application.

- **Establishing a Model System:** A model system was established to examine the adsorption kinetics and mass adsorption of a block-copolymer system derived from literature. This involved evaluating the interaction between polymers and silicon dioxide QCM sensors to optimise polymer deposition. Additionally, binding energy and deposition thickness on the QCM sensor were measured using AFM, as detailed in Chapter 4.

- **Introduction of Innovative Additives:** The findings were shared with Innospec, who then designed a matrix of random copolymer samples and incorporated their additives. These were tested on the QCM to understand how more realistic systems, compared to the block copolymer, behave in practical applications such as toilet bowl systems, as detailed in Chapter 5.

- **Testing on Glazed Ceramic Tiles:** Finally, the random copolymers provided by Innospec were tested on glazed ceramic tiles for toilet bowl applications. Utilising a top-down approach, the study assessed surface adhesion and hydrophobicity through contact angle measurements, force board tests, and the FLuSHt test, as detailed in Chapter 6.

- **Summary of Findings and Future Work** Chapter 7 summarises the key research findings and outlines future research directions. It highlights the successful identification of polymer structures with the desired surface and solution behaviours for antifouling applications, discusses the limitations of the study, and proposes further investigations to optimise polymer designs and testing methods. Future work includes exploring new polymer combinations, improving experimental techniques, and conducting long-term performance evaluations in real-world scenarios.

# Chapter Two

# Polymer Structure in Solution and at Surfaces and Interfaces

The aim of this thesis, as discussed in Chapter 1, is to identify chemicals that might resist the adhesion of faeces to toilets. This chapter aims to review the relevant literature. To understand how polymers behave and orient themselves at the surface, it is imperative to examine both their structure and behaviour at interfaces. First, it is essential to define what a polymer is and explore the different types of polymers that can be synthesised for various applications. This chapter primarily focuses on polyelectrolytes and their behaviour both in solution and at interfaces. Additionally, it is important to consider the surface aspect of the mechanism, examining the adsorption and desorption of polymers on surfaces and how these surfaces can be modified to achieve desired outcomes.

Understanding the rate at which molecules adsorb onto surfaces and the conformations they adopt upon adsorption is crucial. Another key aspect is identifying the driving forces behind polymer adsorption, particularly electrostatic interactions. Since the project aims to identify an effective antifoulant polymer, this chapter also reviews the literature on various antifouling candidates and their applications in preventing fouling on specific substrates

## 2.1 Polymer Science

Polymers are large molecules formed by covalently linking monomers, which are small organic molecules typically around 5 Å in size. These macromolecules often have a molecular weight greater than 10,000 Da and a length typically exceeding 300 Å. Polymers composed of two or more different types of monomers are called copolymers. Polymers are integral to our daily lives. For instance, Poly(ethylene terephthalate) (PET) is widely used in the polyester film industry for applications such as food packaging, bank and ID cards, electronics, and photovoltaics. Polypropylene is found in packaging, aircraft, ropes, toys, and construction materials. Polystyrene is used in items like bottles, TV cabinets, and lids, making it one of the most common polymers in the packaging industry. Polyvinyl chloride (PVC) is employed in furniture, doors, windows, and even clothing.

Polymers can be structured in several ways, the four basic structures are random, alternating, block and graft.[9] However, the structures can be modified to achieve the desirable interfacial properties. A random structure consists of two or more different monomer units sequenced in a random orientation of repeating units illustrated in Figure 2.1(a). An alternating copolymer consists of two different monomer units distributed in an alternating regular sequence, as shown in Figure 2.1(b). Block copolymers are formed when two or more monomers group together and essentially form "blocks" of repeating units (diblock, triblock etc) illustrated in Figure 2.1(c). Finally, graft copolymers are in which blocks of one monomer are grafted onto a backbone of the other branches illustrated in Figure 2.1(d).

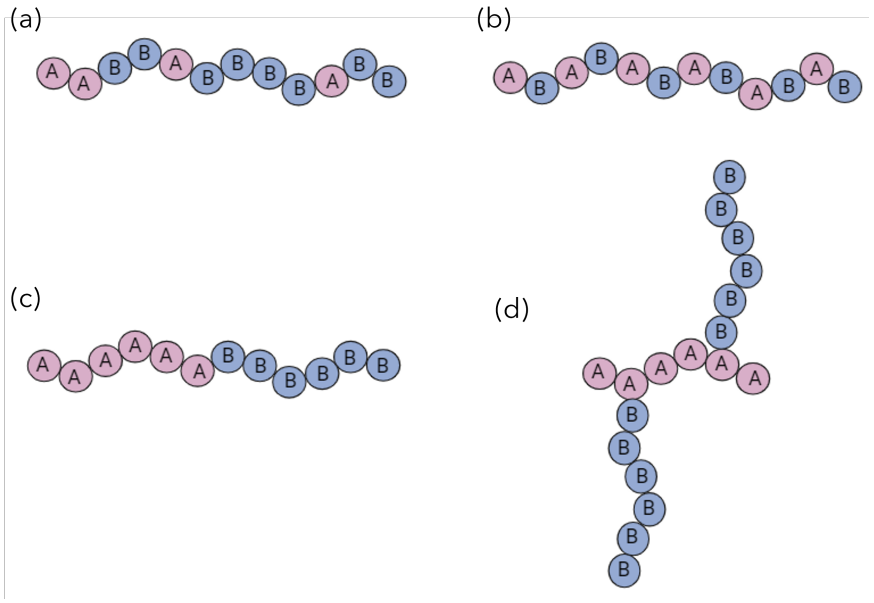



Figure 2.1: Illustration of a few of many the basic copolymer structures, (a) random (b) alternating (c) block and (d) graft copolymers. A in pink and B in blue represent different monomers.

### 2.1.1 Polymer Solubility

In solution, the conformation of polymer chains is influenced by three key factors: their volume fraction (i.e., the concentration of the solution)[10], the energetic interactions between solvent molecules and polymer monomers, and the temperature.[11] For simplicity, the energetic interactions of polymers can be categorised into two main groups: "polar" and "non-polar." Polar molecules had an uneven distribution of electron charge, creating a dipole, which made it energetically favourable for them to associate with each other. Non-polar molecules, lacking a charge dipole, preferred to associate with similar molecules. For instance, non-polar polymers like polystyrene dissolve in non-polar solvents such as toluene but precipitate in polar solvents like water.[12] An exception to this rule is polyethylene oxide, which is soluble in both polar and non-polar solvents due to its unique molecular structure and the interplay of its chemical properties. The energetic favorability of these solvent-monomer interactions

can be quantified by the Flory interaction parameter $\chi$.[13]

$$\chi = \frac{z\Delta u}{kT} \tag{2.1}$$

In this equation:

- $z$ is the coordination number, representing the number of nearest neighbours around a polymer segment or monomer.
- $\Delta u$ is the difference in interaction energy between the solvent-polymer and the average of solvent-solvent and polymer-polymer interactions.
- $k$ is Boltzmann's constant, which relates energy to temperature at the molecular level.
- $T$ is the absolute temperature, measured in Kelvin.

As $\triangle u$ represents the difference in the pairwise interaction energies between the solvent and the polymer monomers.[11] For certain solvents and polymers, solubility also depended on the volume fraction.[10] For example, there is a limit to how much polymer could be dissolved in a given volume of solvent; exceeding this limit results in the formation of two phases: "solute" and "solid".[12] It is evident that a distinct transition from a solid phase to a dissolved phase occurs in these systems, depending on three key parameters: volume fraction ($\phi$), solvent interaction parameters ($\chi$), and temperature (t).[13]

### 2.1.2 Polyelectrolytes

Polyelectrolytes (PE), unlike neutral polymers, consist of ionisable repeat units and are also known as ionic polymers.[14] They are utilised in various technological applications, including antifouling coatings, and play a significant role in the formulation of shampoos and

conditioners.[15] Polyelectrolytes are also integral to the wettability of separation membranes and the stabilisation of colloidal dispersions.[16] Due to their charged nature, polyelectrolytes can modify a substrate's surface properties by adsorbing onto it. These modifications can affect the surface's biological resistance, lubrication, adhesion, or wettability.[16,17]

Both synthetic and natural polyelectrolytes (PEs) have gained significant research interest due to their potential commercial applications. Natural PEs include charged polysaccharides and poly(nucleic acids). Polyelectrolytes with both positive and negative charges in the same monomeric unit are called polyzwitterions. Polyampholytes are copolymers that have positive and negative charges on separate monomeric units (A or B), which can be arranged randomly (e.g., BAAB) or alternately (e.g., ABAB) within the polymer chain. As shown in Table 2.1, polycations consist of an overall net positive charge, while polyanions consist of an overall net negative charge.

Common examples of polyelectrolytes include polystyrene sulfonate (PSS), polyacrylic acid (PAA), polymethacrylic acid (PMAA), their respective salts, as well as DNA and other poly acids and polybases.[18] Polyelectrolytes become charged when dissolved in water because they contain ionisable groups that dissociate, resulting in charged polymer chains.[18] The behaviour of polyelectrolytes in solution involves a balance between the electrostatic interactions of the charged side groups and the hydrophobic interactions of the polymer backbone. This interplay between hydrophilic and hydrophobic properties has been a significant focus of research interest for many years.

Table 2.1: Schematic structure of various polyelectrolytes.

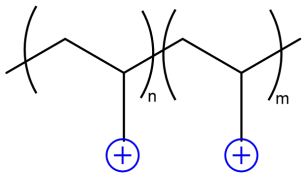
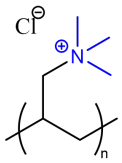
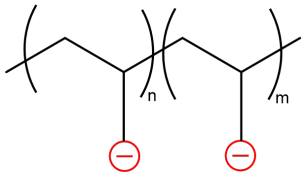
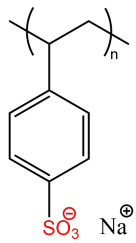
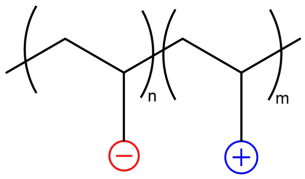
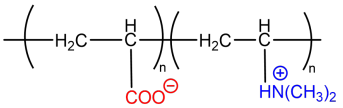
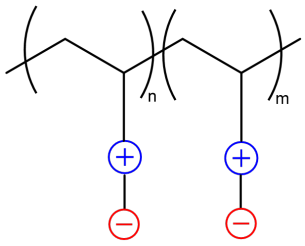
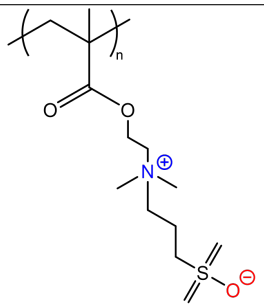
| **Polyelectrolytes** | | |
|---|---|---|
| **Name** | **Structure** | **Example** |
| Polycation |  |  Poly(allyltrimethylammonium chloride) |
| Polyanion |  |  Poly(sodium styrene sulfonate) |
| Polyampholyte |  |  Poly(acrylamidopropyltrimethylammonium chloride-co-acrylic acid) |
| Polyzwitterion |  |  Poly(sulfobetaine methacrylate) |

Figure 2.2 illustrates the behaviour of cationic and anionic polyelectrolytes in solution. Polyelectrolytes are charged under certain conditions, though not always. The figure is divided into two parts: (i) and (ii). In part (i), complex formation occurs due to the interaction between the positively charged repeating units of a cationic polyelectrolyte (polycation) and the negatively charged repeating units of an anionic polyelectrolyte. This complex formation is a result of the electrostatic interactions between the positive and negative charges.[19]

Studies have shown that such polyelectrolyte complexes provide an effective means of adsorbing substantial quantities of hydrophilic agents, enhancing bonding on different materials, and potentially leading to significant strength improvements.[20] Although synthesising polyelectrolytes may involve significant energy and procedural requirements, these processes generally occur before the agents interact with the material surface being treated. The terms 'ladder' and 'scrambled egg' were first used by Michaels in 1965 to describe how polyelectrolytes might arrange themselves to maximise electrostatic interaction.[19]

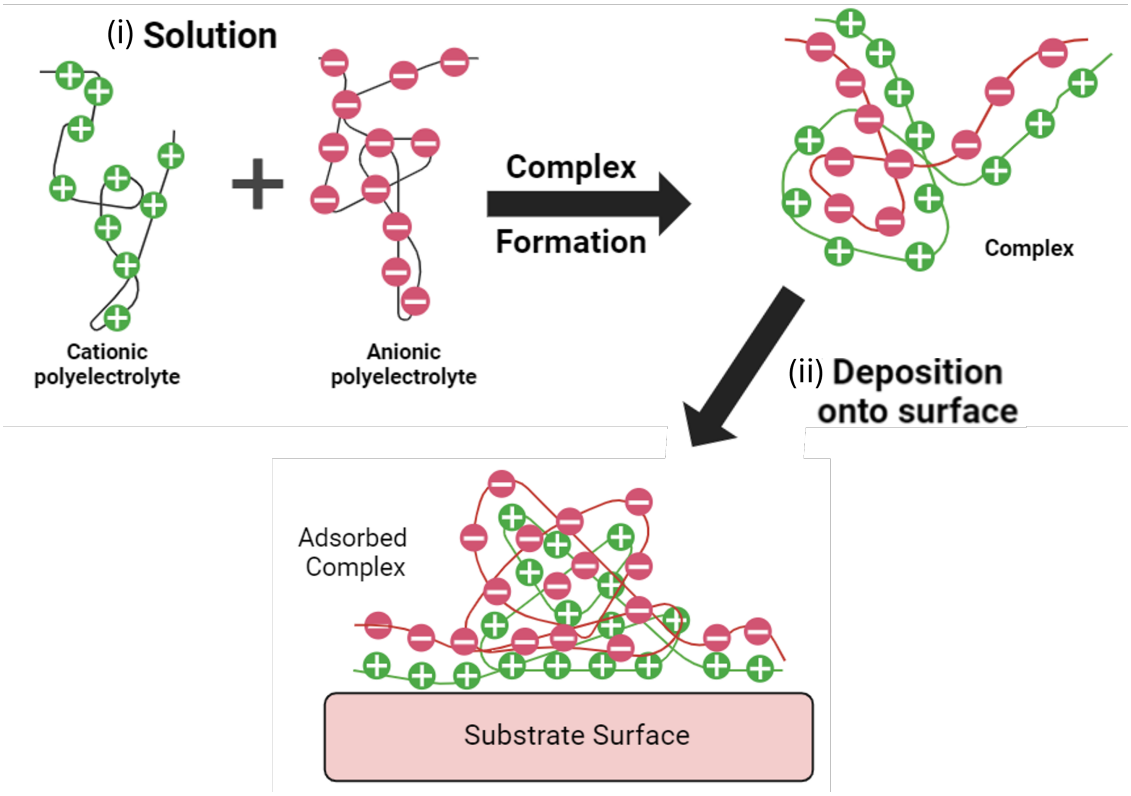
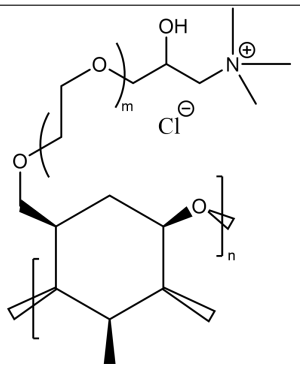
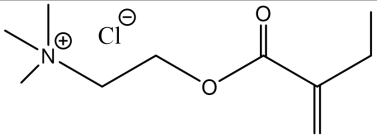
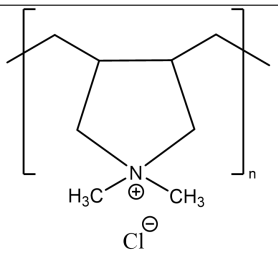
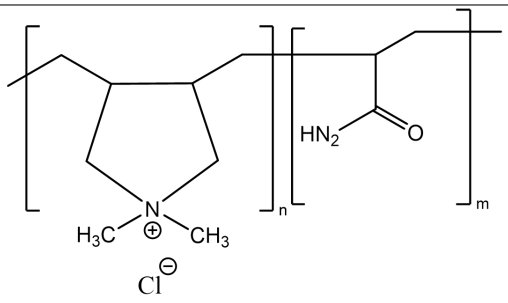



Figure 2.2: Schematic illustration of polyelectrolyte complexation. (i)Solution and (ii) Deposition behaviour of the polyelectrolyte onto the surface.[19]

Cationic polyelectrolytes, such as those employed in various industries as conditioners, thickeners, flocculants, or emulsifiers, serve critical roles in the formulation process as shown in Table 2.2.[21–24] Recently, significant interest has focused on their applications in controlling particle nucleation and growth, and as essential components in constructing polyelectrolyte multilayers for coating planar substrates or encapsulating colloidal particles.[25,26]

In these applications, the primary processes involve the adsorption of these cationic polyelectrolytes onto negatively charged substrates, resulting in charge reversal and significant modification of electrostatic and other surface forces.[27,28]

Table 2.2: Examples of cationic polyelectrolyte (repeat units) and specific names and structures for each example.

| **Example** | **Name/Structure** |
|---|---|
| Conditioner |  Polyquaternium - 10 |
| Thickener |  Polyquaternium - 37 |
| Flocculant |  Polydiallyldimethylammonium chloride |
| Emulsifier |  Polyquaternium - 7 |

Coacervation is traditionally associated with interactions between oppositely charged polyelectrolytes, driven primarily by electrostatic attractions, which are essential for the formation of various biological materials and synthetic adhesives. However, recent studies, inspired by the adhesive mechanisms of mussels, have shown that coacervation can also occur between like-charged polyelectrolytes. This discovery opens new possibilities for material design, particularly in applications requiring strong adhesion in aqueous environments.

Kim et al.[29] investigated this unconventional mechanism using recombinant mussel foot protein-1 (Rmfp-1) and poly(2-(trimethylamino)ethyl methacrylate) (MADQUAT), both of which are like-charged polyelectrolytes. To replicate the adhesive properties found in mussels, the researchers prepared mixtures of Rmfp-1 and MADQUAT, varying polymer concentrations, mixing ratios, and ionic strengths. Coacervate formation was monitored using optical microscopy, turbidity measurements, and UV-resonance Raman spectroscopy, with a focus on molecular interactions and the role of cation–$\pi$ interactions.[29]

The study confirmed that coacervates could indeed be formed between like-charged polyelectrolytes. These coacervates were found to be less dense and less sensitive to environmental changes compared to traditional coacervates formed by oppositely charged polyelectrolytes. Raman spectroscopy revealed alterations in the vibrational bands of tyrosine residues, suggesting that cation–$\pi$ interactions play a crucial role in overcoming the repulsive forces between like-charged molecules. These findings challenge the conventional view that coacervation requires oppositely charged polyelectrolytes, demonstrating that strong short-range cation–$\pi$ interactions can facilitate complexation. This insight expands the theoretical understanding of polyelectrolyte interactions, emphasising the importance of non-covalent interactions in the stability and formation of coacervates. Furthermore, the observed low interfacial tension in these coacervates underscores their potential use in biomolecule encapsulation and the development of novel materials with adaptive properties.[29]

### 2.1.3 Polyelectrolytes in Solution

In polyelectrolytes, electrostatic interactions play a fundamental role in defining their unique characteristics and must be incorporated into any theoretical model. The electrostatic interaction (potential energy) between two point charges can be expressed as $z_1 z_2 v(r)$, where $z_1$ and $z_2$ are the valences of the interacting charges (i.e., the charges expressed as multiples of the elementary charge $e$), and $v(r)$ represents the electrostatic potential. The electrostatic potential $v(r)$ is defined by Coulomb's law:[30,31]

$$v(r) = \frac{e^2}{k_B T \epsilon r} \tag{2.2}$$

In this equation:

- $e$ is the elementary charge (approximately $1.6 \times 10^{-19}$ Coulombs).
- $k_B$ is the Boltzmann constant ($1.38 \times 10^{-23}$ J/K).
- $T$ is the absolute temperature in Kelvin.
- $\epsilon$ is the dielectric constant of the medium, which indicates its ability to attenuate the electric field.
- $r$ is the distance between the two charges.

Energies are expressed in terms of thermal energy $k_B T$. This formulation indicates that the electrostatic potential diminishes with increasing distance between charges and is inversely related to the medium's dielectric constant.[30]

The total electrostatic energy of a charge distribution can be determined by summing all pairwise interactions between charges, as represented by this Coulombic interaction model.

Compared to neutral polymers, the behaviour of polyelectrolytes in solution is predominantly influenced by Coulombic attraction or repulsion among their charged monomer units. In pure water or solutions with low ionic strength, Coulombic repulsion is pronounced, often causing the polymer chains to expand due to like-charge repulsion along the chain. In contrast, in environments with high ionic strength, such as concentrated salt solutions, mobile ions effectively screen electrostatic interactions, resulting in the contraction of polymer coils and a decrease in their hydrodynamic radius, $R_h$.

This screening effect is quantitatively described by the Debye length ($\kappa^{-1}$), which measures the effective range over which electrostatic interactions are screened in a solution. The Debye length is given by:[32]

$$\kappa^{-1} = \sqrt{\frac{\epsilon k_B T}{2 N_A e^2 I}} \tag{2.3}$$

where:

- $N_A$ is Avogadro's number ($6.022 \times 10^{23}$ mol$^{-1}$).
- $I$ is the ionic strength of the solution, calculated as $I = \frac{1}{2}\sum_i c_i z_i^2$, with $c_i$ being the concentration of the $i$-th ion (in mol/L), and $z_i$ its valence.

The Debye length decreases as ionic strength increases, indicating that more ions are available to "screen" the electrostatic interactions among the charged groups of the polyelectrolyte. This enhanced screening effect leads to the contraction of the polymer chains, reducing their effective size in solution. The Debye length is thus a crucial parameter for understanding the behaviour of polyelectrolyte chains under different ionic conditions. This phenomenon, commonly referred to as the "polyelectrolyte effect," is depicted in Figure 2.3.

In summary, the Debye length provides a quantitative understanding of the extent to which electrostatic interactions are screened in a solution, directly affecting the physical properties and behaviour of polyelectrolytes in various applications.

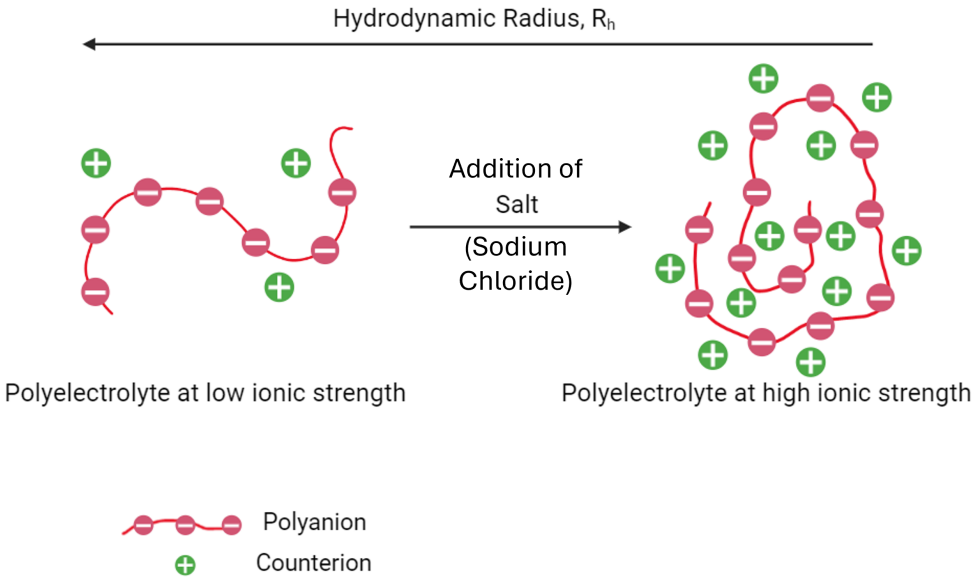



Figure 2.3: Illustration of a polyelectrolyte coil exhibiting an expanded conformation under low salt concentration, demonstrating the "polyelectrolyte effect," followed by a transition to a more compact conformation under high salt concentration.

Polyelectrolytes with linear and flexible backbones are typically classified into two main groups based on their degree of dissociation: "weak PE" such as PAA and "strong PE" such as PSS. Weak PEs undergo partial ionisation depending on the solution's pH, while strong PEs contain side units such as the sulfonate groups in PSS that fully dissociate in water due to their strong acid or base nature. The Poisson-Boltzmann equation, originally formulated by Gouy and Chapman[33], is a fundamental model for describing polyelectrolyte behaviour. Research has extensively explored rod-like polyelectrolytes[34,35] and counterion condensation[36,37] phenomena to validate experimental results. Review articles also discuss various characteristics of polyelectrolytes in solution.[38,39] Figure 2.4 provides examples illus-

trating the diversity of polyelectrolyte structures.'

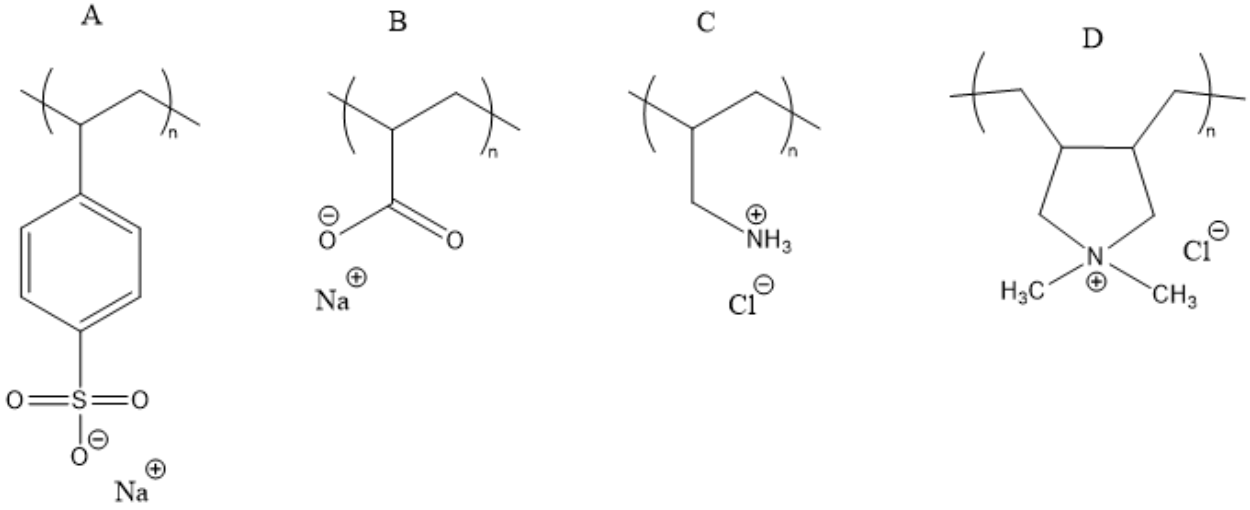



Figure 2.4: The structure of: A) poly(styrene 4-sulfonate) (PSS) which is a polyanion; B) poly(acrylic acid) (PAA) which is a weak polyanion; C) poly(allylamine hydrochloride) (PAH) which is a polycation; and D) poly(diallyldimethylammonium chloride) (PDADMAC) which is a polycation.

### 2.1.4 Polyelectrolytes at the interface

When a polyelectrolyte solution comes into contact with an oppositely charged surface, various factors influence their interaction. Physicochemical parameters, including ionic strength, pH, and temperature, can all impact the solubility of the polyelectrolyte.[40,41] Changes in these parameters can modify the interactions between the polyelectrolyte solution and the solid surface, thereby affecting the balance of electrostatic and other intermolecular interactions within the solution.[42] Other factors which affect the control of the adsorption of polyelectrolytes onto opposing charge surfaces are the concentration of the polymer solution, the flexibility of the polymer chain and the weight of the polyelectrolyte; these parameters are controlled by the chemical nature of the polyelectrolyte.[43] Thus, it is essential to understand the factors which affect the performance of the polyelectrolyte as they need to be taken into

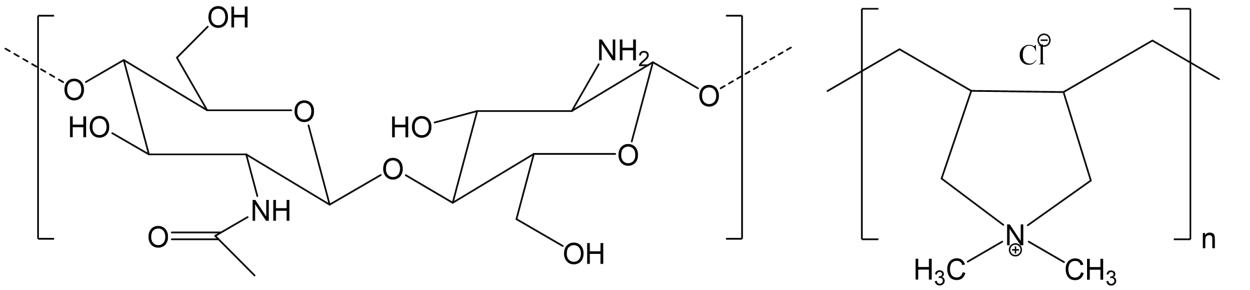
account when designing polyelectrolyte solutions with controlled structures. These can affect the deposition process of the polyelectrolyte solution onto the solid surface which in turn affects the ionic equilibrium of the polyelectrolyte solution.[16,44]

Hernández-Rivas et al.[16] provided an in-depth examination of the complex behaviour of polycation deposition on negatively charged surfaces, with a focus on the influence of factors such as polymer cationicity, ionic strength, and the presence of an anionic surfactant. Key findings indicate that the cationicity, or charge density, of the polycation, is a critical determinant of the thickness and structure of the adsorbed layers. For instance, polycations with higher charge density, such as poly(diallyldimethylammonium chloride) (PDADMAC) (shown on the right of Figure 2.5), tend to adopt a more extended conformation upon adsorption, leading to the formation of thinner, denser layers. In contrast, polycations with lower charge density, such as the pH-sensitive chitosan (CHI) (shown on the left of Figure 2.5), form thicker, more hydrated layers due to their coiled conformation, which permits greater water incorporation. The study underscores the significant effect of solution pH on the charge density of CHI, resulting in thinner layers at lower pH levels due to increased protonation—a sensitivity less pronounced in strong polyelectrolytes like PDADMAC.[16]

Ionic strength also plays a pivotal role in determining the conformation of polyelectrolyte chains. At higher ionic strengths, reduced electrostatic repulsion between polymer chains causes them to assume a more coiled conformation, resulting in thicker, more diffuse layers with increased water content. Conversely, at lower ionic strengths, polycations tend to adsorb more extended due to stronger electrostatic interactions with the surface, forming thinner, denser layers. This relationship enables controlled manipulation of polymer adsorption and layer structure by adjusting the ionic strength, thereby allowing for the tailoring of surface properties as needed.[16]

The study also explored the impact of Sodium Laureth Sulfate (SLES), an anionic surfactant, on polycation deposition. The presence of SLES introduces a competitive dynamic between

the surfactant and the polycation for surface adsorption, leading to the formation of mixed layers. Depending on the surfactant concentration and the specific polymer used, SLES can either enhance or inhibit polycation deposition. At certain concentrations, SLES can promote polycation adsorption by neutralising part of the surface charge, leading to a more compact layer. However, at higher concentrations, SLES can induce desorption or prevent further polycation adsorption, resulting in thinner layers. These results highlight the intricate interplay between polycations and surfactants in surface modification.[16]




CHITOSAN (CHI)

Poly (diallyldimethylammonium chloride)
PDADMAC

Figure 2.5: Molecular structure of Chitosan (CHI) (left) and Poly (diallyldimethylammoniumchloride) (PDADMAC) (right).

Polymer adsorption inherently involves a change in conformation, typically described by the loop-train-tail model, as illustrated in Figure 2.6. In this model, trains are segments in direct contact with the surface, loops are segments near the surface but not in direct contact, and tails are the non-adsorbed ends of the polymer chains. While the tail segments may represent a small fraction of the total polymer segments, they play a crucial role in determining the hydrodynamic layer thickness of the adsorbed polymer.[45]

The adsorption of polyelectrolytes onto surfaces is a fundamental method for surface modification. Typically, polyelectrolytes adsorb onto surfaces with an opposite charge, often adopting a flat conformation. The amount of polyelectrolyte adsorbed can be influenced by the ionic strength of the solution, though this relationship is complex. At lower ionic

strengths, increased ionic strength can enhance adsorption by reducing repulsive interactions. However, at higher ionic strengths, the screening of electrostatic forces may reduce the amount of polymer that adsorbs. The conformation of adsorbed polyelectrolytes and polymers in general can be described by the loop-train-tail model.[45] Figure 2.6 presents a schematic representation of an adsorbed polyelectrolyte molecule, illustrating the segments that form loops, trains, and tails.

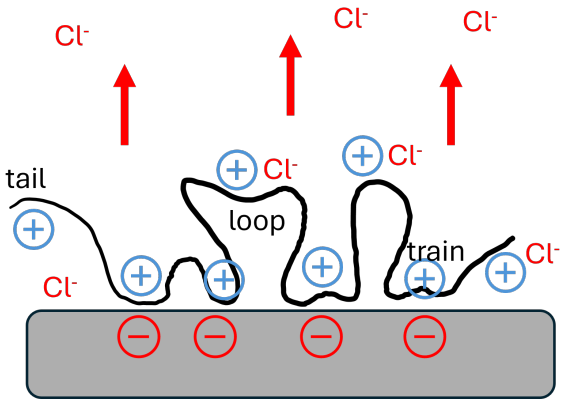



Figure 2.6: Polymer chain adsorbed at the surface consisting of tail, loop and train model.

### 2.1.5 pH and Temperature

Weak polyelectrolytes are employed in polyelectrolyte multilayers (PEMUs) due to their ability to alter properties by changing the ionisation of functional groups through pH adjustments. The mechanical properties, thickness, and molecular organisation of the film were influenced by this interaction.[46] For example, Rubner et al.[47] demonstrated that the wettability of weak PEMUs composed of poly(acrylic acid) (PAA) and PAH could be significantly modified by tuning the pH of the polyelectrolyte solutions. This stimuli-responsive behaviour could also trigger film dissolution, particularly in PEMUs containing -COOH functional groups that participated in hydrogen bonding during multilayer formation. At high pH, carboxylic acids were fully deprotonated, disrupting hydrogen bonds and leading to film disassembly.[48]

Typically, when the polyelectrolyte pair was fully ionised, intrinsic sites dominated, resulting in thinner films. However, when both polyelectrolytes were partially ionised, thicker, gel-like films were produced. These properties of ionisable polyelectrolytes were utilised in applications such as microcapsules for drug delivery systems.[49–51] For instance, Mendelsohn et al.[52] created a series of PEMUs with varying chemical architectures by adjusting the pH to study cell behaviour on cytophobic and cytophilic coatings.

While ionic strength and ionisation of the films played significant roles in multilayer formation, temperature also had a noticeable impact. PEMUs assembled at high temperatures were rougher and thicker than those built at room temperature.[42,53] In a diffusion study, Salomäki et al.[54] proposed that the increased overall film thickness at higher temperatures was due to enhanced polymer diffusion throughout the film during the buildup process.

## 2.2 Surface Science

### 2.2.1 Surface Adsorption Kinetics

Aneta et al. investigated the adsorption kinetics of poly(diallyldimethylammonium chloride) (PDADMAC) on solid surfaces using advanced techniques, including Quartz Crystal Microbalance with Dissipation (QCM-D) and streaming potential measurements. These methodologies facilitated a detailed analysis of the interactions between PDADMAC molecules and surfaces such as mica and silica, with a particular focus on the adsorption and desorption processes. The results suggested that the adsorption behaviour of PDADMAC is well-described by the Langmuir isotherm model, providing valuable insights into the mechanisms through which this polymer adheres to various substrates.[55]

The Langmuir isotherm model assumes adsorption occurs on a uniform surface with a finite number of identical binding sites, leading to monolayer formation without interactions be-

tween adsorbed molecules. The study found that PDADMAC's adsorption kinetics closely align with this model, especially under controlled conditions where surface saturation is achieved. Initially, there is a rapid adsorption phase driven by the bulk transport of PDADMAC molecules to the surface, which quickly occupies available adsorption sites. As the surface becomes increasingly occupied, the adsorption rate slows, eventually reaching a plateau indicative of monolayer coverage. This behaviour is characteristic of the Langmuir isotherm, where equilibrium is achieved due to the limited number of adsorption sites.[55]

Mechanistically, PDADMAC adsorption begins rapidly due to the high availability of unoccupied surface sites and PDADMAC molecules in the solution. This phase is primarily governed by electrostatic interactions between the positively charged PDADMAC and the negatively charged substrate surface. As adsorption proceeds and fewer sites remain available, the process slows down, largely due to surface-blocking effects. Desorption was analysed by monitoring changes in the zeta potential over time, demonstrating that desorption is quantifiable and suggesting that PDADMAC-substrate interactions are reversible under specific conditions.[55]

The study highlighted the kinetic behaviour of PDADMAC adsorption, which follows a two-stage process: an initial rapid adsorption phase followed by a slower phase influenced by surface blocking. The rapid phase is characterised by the swift occupation of available sites, while the slower phase emerges as the surface approaches saturation. The Random Sequential Adsorption (RSA) model was identified as a useful framework for understanding this slower phase. As more adsorption sites are occupied, further adsorption is impeded, leading to a reduced rate of adsorption and eventually a plateau, consistent with Langmuir isotherm predictions and further validating the model's applicability to PDADMAC adsorption.[55]

The study demonstrated that PDADMAC adsorption on solid substrates is a complex process influenced by electrostatic interactions, the availability of surface sites, and surface-blocking effects. The findings confirm that the Langmuir isotherm model provides a suitable frame-

work for describing PDADMAC adsorption under conditions favouring monolayer formation. This understanding offers valuable insights into the potential applications of PDADMAC in surface modification and coating technologies. Future research could focus on refining these models to incorporate more complex interactions, such as hydration effects and the role of multivalent ions, to better predict PDADMAC behaviour in practical applications.[55]

### 2.2.2 Surface Adhesion

A viscoelastic material is a material that has both viscous and elastic properties; these types of materials are common, for example, dough or paint.[56,57] When a material comes into contact with a substrate surface adhesion can be reduced according to the Girifalco and Good equation, shown in equation 2.4.

$$W_a = 2R\sqrt{\gamma_{13} \times \gamma_{23}} \tag{2.4}$$

Here *Wa* is the work of adhesion ($J/m^2$), R is the surface roughness specified as the ratio between the projected and apparent surface areas of the solid substrate, phases 1,2 & 3 define the solid substrate, viscoelastic solid and air, respectively, and the i-j interface is known as the interfacial energy which is represented as $\gamma$ij. Reducing the value of *Wa* can be achieved in two ways, either by physically decreasing the surface roughness (R) of the substrate or by chemically decreasing the interfacial energies of the viscoelastic solid-air interface and the solid-air interface.[5] The latter is the method studied throughout this research project.

Wang *et al.*[5] developed a non-fouling coating known as liquid-entrenched smooth surface (LESS), aimed at reducing fouling. They achieved this by using a nanoscopically smooth solid substrate (R $\approx$ 1). Roughness on surfaces typically increases the contact area, leading to higher adhesion between materials.[5] For viscoelastic materials, a critical storage modulus value of 0.3 MPa is observed, below which the material conforms closely to surface roughness,

regardless of applied pressure.[58]

Wang et al. found that increasing surface roughness also increased the adhesion of viscoelastic solids such as faecal matter, with measured roughness ranging from 0.87 ± 0.06 nm to 4.12 ± 0.26 µm.[5] Therefore, smoother substrate surfaces can effectively reduce the adhesion of viscoelastic solids.

Wang *et al.*[5] designed a liquid-entrenched smooth surface (LESS) non-fouling coating, to reduce *Wa* via the physical process of a nanoscopically smooth solid substrate was utilised of approximately 1 (R = 1). The presence of roughness increases the contact area of the two surfaces resulting in an increase in adhesion between the two.[5] 0.3 MPa is known as the critical value for a storage modulus of an adherent material, when a material has a value lower than this the adherent material runs and forms a conformal contact along the surface roughness of the adherent, irrespective of the applied pressure.[58] Wang et al stated that their adhesion measurements confirmed that as the surface roughness increases the adhesion of the viscoelastic solids also increased, their average roughness results were from 0.87 ± 0.06 nm to 4.12 ± 0.26 µm.[5] Thus, it can be said that a smooth substrate surface aids with decreasing the adhesion of the viscoelastic solids to the surface.

Decreasing water contact angle can also be achieved by applying a low surface energy coating on a smooth solid surface. This coating reduces the interfacial adhesion between the solid substrate and air. Alternatively, adding a lubricant that can be absorbed by the viscoelastic material and forms a lubricant layer on the surface reduces the interfacial adhesion between the viscoelastic solid and air. Wang et al. suggested that both types of interfacial adhesion can be simultaneously reduced by applying a stable lubricant layer between the viscoelastic material and the substrate of choice.[5]

## 2.3 Anti-fouling properties of polymers

Biomedical devices made of polymeric materials have a long history and include heart valves, catheters, ophthalmic devices, and other implanted devices. For all these devices, however, the operation is limited due to the buildup of biological deposits on the surfaces of these devices, including platelet deposition, bacterial adhesion, and protein and lipid adsorption. These results of deposition range from inconveniences such as contact lens fouling to potentially fatal hazards like thrombosis in patients.[59–62] Despite abundant research on creating materials that resist protein adsorption, thrombosis remains a major issue with artificial implants.[63,64] Thus, understanding how proteins adsorbed onto surfaces has been crucial for developing new biomaterials compatible with human tissue.

Surface modification has been the most common method to reduce protein adsorption.[65,66] The primary objective is to increase or alter the hydrophilicity of surfaces. Hydrophilic surfaces made from water-soluble polymers have been preferred in biomaterial applications due both to their similarity to living matter and their ability to reduce interfacial tension, which might decrease protein adsorption and subsequent cell adhesion. The aim has been to tailor the chemical composition of the material interface such that the adhesion is reduced.[67,68]

Surface chemistries that resist protein adsorption are thus valuable in various fields, for example in minimising nonspecific protein adsorption in biosensors and enhancing the biocompatibility of materials.[69]

The nonspecific adsorption of proteins to surfaces is influenced by both enthalpic and entropic factors. Enthalpic factors include electrostatic, hydrophobic, and Van der Waals interactions which create bonding between polymer and surface. Electrostatic interactions involve the attraction of oppositely charged species and the repulsion of similarly charged ones; this is a primary focus of this project in trying to develop species that resist adhesion. Hydrophobic interactions occur when hydrophobic regions, such as those in the protein core, attract other

hydrophobic species in a hydrophilic solvent. This reduces the number of ordered solvent molecules and minimises entropy loss.[70] On hydrophobic surfaces, proteins tend to adsorb by exposing their hydrophobic core. Van der Waals interactions result from induced dipole moments between otherwise uncharged species.

Processes driven by entropy that favour protein adsorption work by decreasing the system's overall order. Water molecules or ions surrounding proteins and surfaces have lower entropy than those in the bulk solution. When a protein adsorbs onto a surface, the disruption of these ordered layers results in an entropy gain.[70] Rearrangements in the polymer film and changes in protein conformation, leading to a more flexible structure, also promote protein adsorption due to increased entropy. For example Polyethylene glycol (PEG) resists protein adsorption largely because of its highly flexible conformation in solution, making it less entropically unfavourable for the protein to associate with protein surfaces creating local order.[71]

Another consideration on how proteins adsorb onto surfaces involves the characteristics of the protein under study. Proteins exhibit various structural properties, including size and chain flexibility. Small, rigid proteins primarily interact via electrostatic interactions, whereas larger, flexible proteins necessitate consideration of conformational changes and hydrophobic interactions.[72]

To prevent protein buildup on surfaces, PEG-based coatings are commonly used. For example, Prime and Whitesides developed self-assembled monolayers (SAMs) consisting of oligo(ethylene oxide) groups that effectively repel proteins. These SAMs were generated from thiols, such as $HS(CH_3)_{10}CH_3$ and $HS(CH_3)_{11}(OCH_2CH_2)_nOH$. The researchers analysed the extent of protein adsorption on these SAMs. Prime et al.[73] discovered that SAMs of alkanethiolates with two ethylene oxide groups exhibited significant protein-resistant properties.[73]

PEG can be applied to surfaces to repel proteins, Jeon et al.[74] found that when a protein comes into contact with the substrate, the PEG chains move closer together, generating a repulsive elastic force. They also concluded that increasing the density of grafted PEG chains on the surface enhances its protein-repellent properties. Jeon and Andrade further modelled proteins as finite spherical particles and discovered that longer PEG chains at a given surface density result in higher protein resistance.[74] Additionally, Prime and Whitesides created mixed SAMs to develop surfaces with high protein resistance, as mentioned earlier.[73]

Prime et al. discovered that the advantage of utilising longer polymer chains is their ability to cover the surface more efficiently. However, one disadvantage of the grafting technique, compared to self-assembled monolayers (SAMs), is its inability to incorporate a larger number of chains per unit surface area. By using the SAMs technique, more effective surface coverage is achieved, even with shorter chain lengths.[73]

### 2.3.1 Hydrophobicity and Charge Separation in Zwitterionic Peptides for Antifouling

Li et al.[61] examined the role of hydrophobicity and charge separation in modulating the antifouling properties of zwitterionic peptides through the incorporation of neutral amino acid spacers. Specifically, the research focused on peptides composed of repeating lysine (K) and glutamic acid (E) units, where spacers such as serine (Ser), glycine (Gly), and leucine (Leu) were strategically introduced between K and E residues. The primary objective of the study was to assess how these spacers influence the structural organisation of peptide monolayers and their effectiveness in resisting protein fouling.[61]

The research methodology employed a combination of Surface Plasma Resonance (SPR), Atomic Force Microscopy (AFM), Surface Force Apparatus (SFA), and all-atom molecular dynamics (MD) simulations to characterise the peptide-modified surfaces. SPR was partic-

ularly instrumental in monitoring the real-time assembly of the peptides on gold surfaces. The findings revealed that peptides containing glycine spacers (KGEG) achieved the highest grafting density, likely due to the flexibility of glycine, which facilitated denser surface packing. Conversely, peptides with leucine spacers (KLEL) exhibited the lowest grafting density, a result attributed to leucine's hydrophobic nature, which may have restricted peptide mobility during surface assembly. Contact angle measurements further demonstrated a decrease in the hydrophilicity of peptide monolayers in the order of Ser > Gly > Leu, with corresponding contact angles increasing from 13.2° for Ser-containing peptides to 47.7° for Leu-containing peptides. This trend is consistent with the intrinsic hydrophobicity of the spacers, where Ser, being polar, contributes to a more hydrophilic surface, while Leu, with its non-polar side chain, enhances surface hydrophobicity.[61]

The antifouling performance of these surfaces was assessed using lysozyme and bovine serum albumin (BSA) as model proteins. SPR data indicated that Ser-containing peptides exhibited superior antifouling performance, with significantly reduced protein adsorption compared to the control peptide ($KE_{10}$) that lacked spacers. In contrast, the more hydrophobic Leu-containing peptides displayed a higher propensity for protein adsorption, likely due to a diminished hydration layer resulting from hydrophobic interactions. AFM analysis supported these observations, indicating that the peptides were uniformly tethered to the gold surface, with surface roughness values ranging from 0.5 nm to 0.8 nm. This uniformity suggests that the differences in antifouling performance were predominantly influenced by the chemical properties of the spacers rather than by variations in surface structure.[61]

SFA measurements further demonstrated that hydrophobic spacers, such as Leu, enhanced the adhesion between the peptide monolayer and lysozyme, especially in peptides with Leu spacers. MD simulations corroborated these findings, showing that Ser-containing peptides maintained a well-hydrated, antifouling surface, while Leu-containing peptides led to dehydration and increased protein adhesion. The study concluded that the antifouling efficacy of zwitterionic peptides is closely linked to the hydration layer formed by zwitterionic groups.

Hydrophilic spacers like Ser enhance this hydration layer, thereby improving antifouling properties, whereas hydrophobic spacers like Leu reduce the hydration layer, thereby diminishing antifouling performance.[61]

### 2.3.2 Polyzwitterions as Anti-fouling Interface

Another alternative to PEG for surface modification is the use of zwitterionic polymers. Polyzwitterions (PZs) garnered special interest for applications such as biocompatible surfaces and improving the efficiency of antifouling coatings.[75–80] The use of polyzwitterions like phosphobetaine phosphorylcholines (PC) as antifouling surface modifiers was inspired by the antifouling characteristics of cell surface phospholipids.[81] Various studies demonstrated the reduction of protein adsorption onto surfaces using materials with PC head groups, such as phosphatidylcholine.

It was believed that protein resistance was achieved through the generation of steric exclusion effects that formed a hydration layer via interactions with water,[82] and the virtually neutral net charge of the PC reduced long-range electrostatic attraction between proteins and the surface.[83–86] Poly(2-methacryloyloxyethyl phosphorylcholine) (PMPC) is one of the most commonly used PCs to date. This polyzwitterion had a large volume of free water fraction around its coil chain, which inhibited non-specific protein adsorption.[87,88] Research involving PCs explored various areas, from synthesising PC-terminated thiols to preparing pure self-assembled monolayers (SAMs) on gold surfaces to reduce protein adsorption,[83,84] as well as incorporating PC groups into polymers to attach them onto polymer surfaces.[88]

Additionally, polysulfobetaines and polycarboxybetaines, such as poly(sulfobetaine methacrylate) (PSBMA) and poly(carboxybetaine methacrylate) (PCBMA), have been studied for their protein-resistant properties. These polymers could be grafted onto surfaces or incorporated into other platforms like hydrogels or polyelectrolyte multilayers.[89–94] PSBMA

brushes showed resilience against non-specific adsorption of fibrinogen even under high salt concentration and pH conditions.[95] Ladd et al.[96] compared the antifouling properties of different polymer brush coatings—PSBMA, PCBMA, poly(PEG-co-MEMA) brushes, and PEG—finding that PCBMA coating was the most effective at preventing non-specific protein adsorption.

A comparison of the antifouling properties of PSBMA and PCBMA brushes underscores the significance of the spacing between positive and negative charges within the zwitterionic units for the antifouling effectiveness of the brush coating.[97] This study demonstrated that closer proximity of the charged groups enhances the hydration layer, making CBMA an excellent candidate for repelling proteins.

Figure 2.10 illustrates the structures of the most commonly used polyzwitterions to reduce adhesion applications. Polyzwitterions are categorised into three types: (A) Sulfobetaine (SB), (B) Carboxybetaine (CB), and (C) Phosphobetaine (PB).

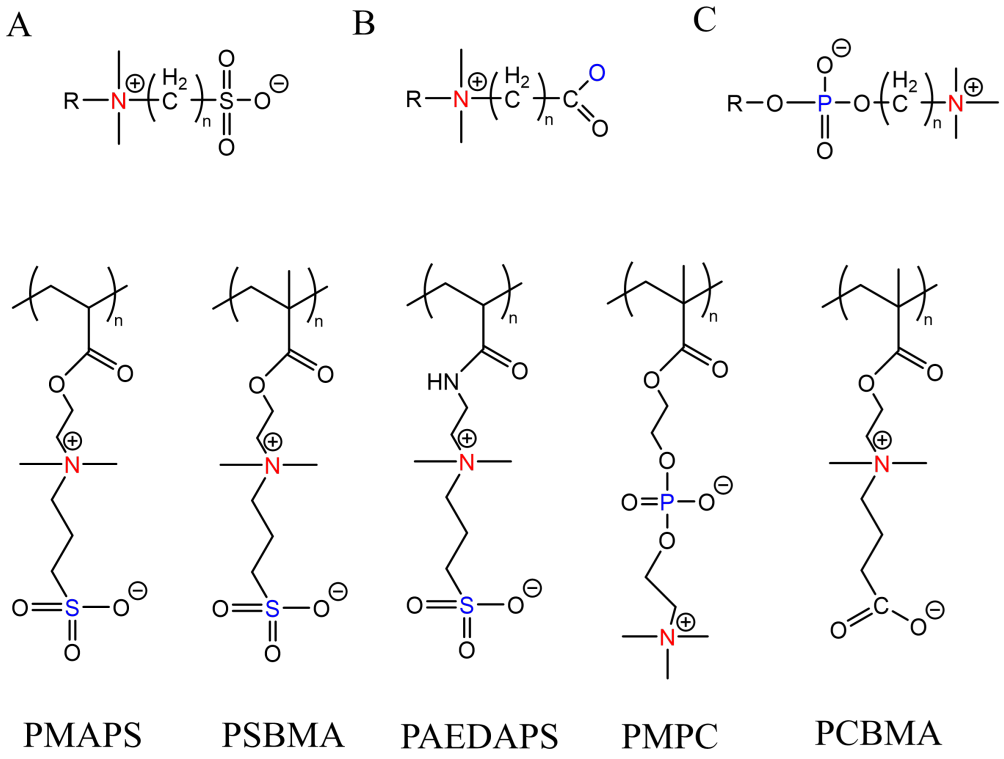



Figure 2.7: Zwitterionic polymers used for protein reduction applications included: A. Sulfobetaine (SB): Poly(3-[N-(2-methylacryloylethyl)-N,N-dimethylammonio] propanesulfonate) (PMAPS), poly(sulfobetaine methacrylate) (PSBMA), and poly(3-[2-(acrylamido)-ethyl dimethylammonio]propanesulfonate) (PAEDAPS); B. Carboxybetaine (CB): Poly(carboxybetaine methacrylate) (PCBMA); C. Phosphobetaine (PB): Poly(2-methacryloyloxylethyl phosphorylcholine) (PMPC).

## 2.4 Conclusions

Critical parameters in polymer chemistry have been briefly reviewed, highlighting the importance of modifying interfacial behaviour through polymer adhesion. The effectiveness of adhesion is determined by the chemical nature of the polymer, as well as the conditions of the bulk fluid and the interface. Changes in the chemistry and structure of the polymer can lead to variations in adhesion properties. For instance, block copolymers, where one

segment adheres to the surface while the other extends into the liquid, can serve as barriers to further adhesion. Consequently, the primary objective is to identify suitable copolymers demonstrating these characteristics. The remainder of this thesis will focus on examining the quantities of copolymer adsorption, the kinetics of adsorption, and their effects on interfacial properties and adhesion.

In Chapter 4, the block copolymers used were varying ratios of polyethylene oxide (PEO) and poly[2-(dimethylamino)ethyl methacrylate] (PDMAEMA). Throughout Chapter 4, this block copolymer is referred to as PEO-*b*-PDMAEMA. The ratios used were 5.0-*b*-2.5, 5.0-*b*-5.6, and 5.0-*b*-12.0. For more detailed information, see Chapter 4, Section 4.1.1.

In Chapters 5 and 6, the random copolymers utilised were poly[2-(dimethylamino)ethyl methacrylate] (PDMAEMA), and poly[2-(methacryloyloxy)ethyl trimethylammonium chloride] (PMAETAC) which are both polycations, the former consists of a permanent positive charge whilst the latter does not. The polyanion used was polyacrylic acid (PAA). Further information can be found in Chapter 5, Table 5.2.

# Chapter Three

# Methodology

This chapter outlines the methodology employed in the doctoral project. The aim of the chapter is to provide a detailed explanation of how the experiments were conducted and the rationale behind each method. In brief, the Quartz Crystal Microbalance (QCM) was utilised to monitor the real-time adsorption and desorption of molecules. Atomic Force Microscopy (AFM) was employed to measure film thickness and adhesion. Dynamic Light Scattering (DLS) was utilised to assess particle size and polymer solution charge. Contact angle measurements were conducted to determine the surface energy of the deposited polymer on various substrates. The FLuSHT test apparatus was constructed to observe polymer response to synthetic faeces in a real-world scenario, bridging the gap between microscopic and macroscopic testing. Lastly, the force board test was employed to gauge the force necessary to detach the coated glazed ceramic tile from the synthetic faeces. Chapter 3 describes the methodology of the instruments used in this project, elucidating the principles, data interpretation, limitations, and experimental setup of each instrument.

## 3.1 Quartz Crystal Microbalance - Dissipation (QCM-D)

The Quartz Crystal Microbalance (QCM) and its variations, such as the Quartz Crystal Microbalance with Dissipation monitoring (QCM-D), are advanced technologies that provide real-time, surface-sensitive detection of minute changes in mass at the sensor surface with nanoscale precision. Essentially, these devices operate as highly sensitive scales for detecting small masses in the nanogram range, where interactions between molecules and the surface are observed as alterations in mass, either through the absorption or release of molecules. In addition to providing information on changes in mass, QCM can also offer insights into the viscoelastic properties of the system under investigation. It can give information about structural changes, such as cross-linking, swelling, and collapsing of the molecular layer at the sensor surface.[98,99]. QCM is an instrument that holds promise in forecasting fouling at larger scales.[62]

### 3.1.1 Principle

The principles underlying QCM-D are based on the piezoelectric effect exhibited by quartz crystals.[62,100] Certain materials possess a property known as piezoelectricity, in which exposure to mechanical stress induces the generation of an electric charge. When subjected to a supplied voltage, a quartz crystal vibrates at a specific frequency. Factors such as the crystal's shape and thickness influence its vibrational frequency.[101] QCM-D offers real-time measurement of structural, viscoelastic properties, and mass changes with nano-sensitivity. The quartz crystal oscillates at its resonant frequency, and alterations in frequency correspond to mass changes occurring at the surface. When molecules adsorb onto the surface, there is a decrease in frequency resulting in an increase in mass, as described by the Sauerbrey equation in section 3.1.2. In addition to providing insights into the viscoelastic properties, such as the adsorbed layer's shear modulus and hydrodynamic thickness, QCM-D enables

the determination of the rigidity and mass of the adsorbed layer.[98]

Structural properties can be assessed through changes in dissipation (damping) of the oscillating crystal. Adding mass changes the weight of the system and thus the resonant frequency which is the inverse of dissipation. Figure 3.1 shows a schematic diagram of a typical result. It illustrates that in step A, molecules have been introduced into the system and are beginning to deposit onto the sensor surface, resulting in a decrease in frequency as the molecules adsorb. Stage B shows that the molecules have completely covered the sensor, resulting in an equilibrium of the change in frequency; there is no further change in frequency at this step. Lastly, stage C shows that molecules weakly bound to the surface are removed during the final rinse giving the quantitative final mass adsorbed onto the sensor. Further details are discussed in section 3.1.4.

At the core of the technology is an oscillating unit comprising a slender quartz crystal disk equipped with electrodes on both surfaces. When a voltage is applied, the crystal vibrates, and its frequency correlates with its mass. Variations in thickness induce shifts in resonance frequency, enabling the detection of subtle changes in mass, such as the adsorption or removal of molecules, as illustrated in Figure 3.1 Stage C. In addition to tracking frequency alterations ($\Delta f$), QCM-D also evaluates dissipation ($\Delta D$), providing valuable insights into energy dissipation, particularly useful for examining the properties of soft layers.

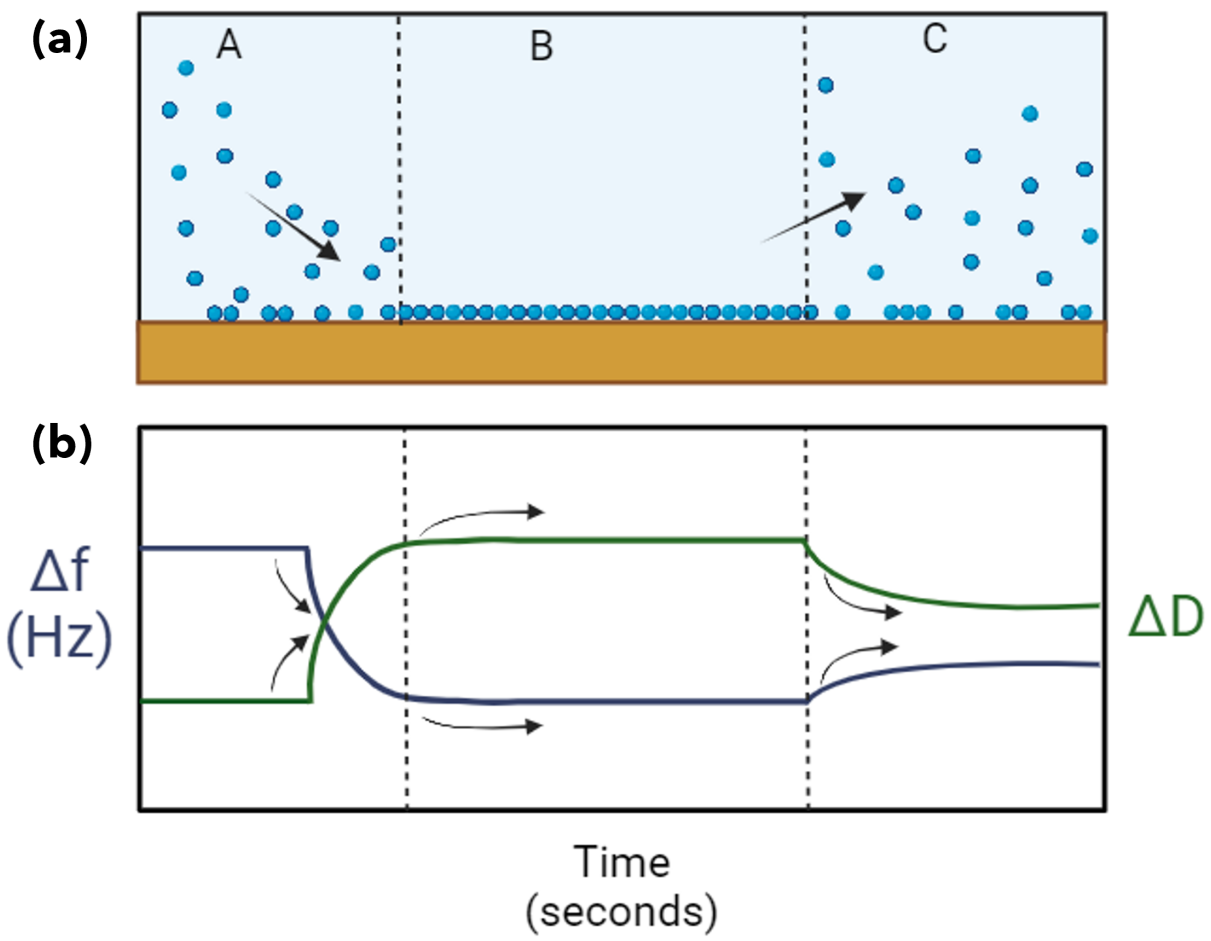



Figure 3.1: Schematic representation of a basic QCM output curve, Stage A is deposition, Stage B is adsorption and Stage C is desorption. Figure 3.1 (a) shows the molecular process occurring, whilst Figure 3.1 (b) shows the changes in factors measured by the QCM.

### 3.1.2 Data Interpretation

Günther Sauerbrey discovered in 1959 the direct relationship between frequency response and deposited mass, laying the fundamental basis for QCM methodology. The Sauerbrey equation, depicted below as Equation 3.1, articulates a linear relationship between frequency change and mass change.[102] The mass of the deposited layer undergoes alteration through the adsorption or desorption of molecules onto the QCM sensor, thereby inducing changes

in the crystal's vibration frequency.[99] Consequently, the frequency change can be utilised to gauge the change in mass of the deposited material; in

$$\Delta m = -\frac{C_{QCM} \cdot \Delta f}{n} \tag{3.1}$$

Where $\Delta m$ is expressed in ng $\cdot$ cm$^{-2}$ as the change in mass density on the sensor surface. The mass sensitivity constant, $C_{QCM}$ indicates the amount of material (in ng) per cm$^2$ of the sensor required to shift the resonance frequency by 1 Hz. A low value of C indicates higher mass sensitivity, which is determined solely by the fundamental resonant frequency of the crystal. $C_{QCM}$ in this study is 17.7 ng $\cdot$ cm$^{-2}$ Hz$^{-1}$ at an oscillation frequency of 5 MHz. Throughout this study, the sensor used was silicon dioxide as it has a chemistry closely related to the surface of a glazed ceramic tile. $\Delta f$ is expressed in Hz as the change in frequency on the sensor surface. Here, $n$ represents the odd overtone number.[98] The crystal resonates at different harmonics (n), predominantly odd ones (n = 1, 3, 5, etc.), in the thickness-shear mode for AT-cut QCM crystals.[103] The fundamental frequency (n = 1) establishes the baseline, while higher-order resonances (n = 3, 5, 7, etc.) are overtones.[62] Each harmonic offers unique insights into the studied system, enhancing QCM data interpretation. Throughout the QCM analysis, overtone 9 was taken as it was consistent throughout all measurements.[104]

### 3.1.3 Limitations of the QCM Method

QCM-D is a highly sensitive technique that measures mass changes in nanograms per square centimetre. It cannot detect mass changes below or above this measurement unit. Thus, it was not possible to use it to measure mass changes beyond its detection limits, which could be a barrier for some applications. The detection limit for QCM was 0.1 Hz. The Sauerbrey equation is only valid for rigid films; deviations from the Sauerbrey equation can

occur due to the viscoelastic properties of the deposited material. For example, certain biomolecular films could deposit in a non-rigid manner. When this occurs, the Voigt model can be used to analyse the change in mass deposited onto the sensor surface.[105] Furthermore, the heterogeneity of the sensor's surface can introduce errors in the data. As QCM-D assesses the viscoelastic and mass properties of the adsorbed material on the sensor, it is susceptible to variations in the surface properties of the sensor.[99] Another constraint of QCM-D is its susceptibility to environmental factors such as ambient noise, temperature variations, and humidity levels, which can impact data quality. Before each measurement, a meticulous cleaning protocol must be executed, detailed in section 3.1.5. Despite thorough cleaning procedures, the inherent sensitivity of QCM-D means that even minute contaminants can significantly influence measurement accuracy.

### 3.1.4 Experimental Setup

The QCM process was conducted utilising an X4 Advanced Multichannel QCM-D system (from AWSensors Scientific Technologies, Spain). Following the equilibration of the system with deionised water, the polymer solution was passed through the cell at a flow rate of 54.56 $\mu$L/min. Figure 3.2 depicts the setup of the AWS QCM instrument and the direction of flow. The peristaltic pump (Masterflex Ismatec UK), labelled in the image of Figure 3.2, pulls the liquid through the system, with the direction of flow from left to right. Figure 3.3 provides a detailed view of the interior of a chamber within the cell, highlighting the lid, the base, and the sensor.

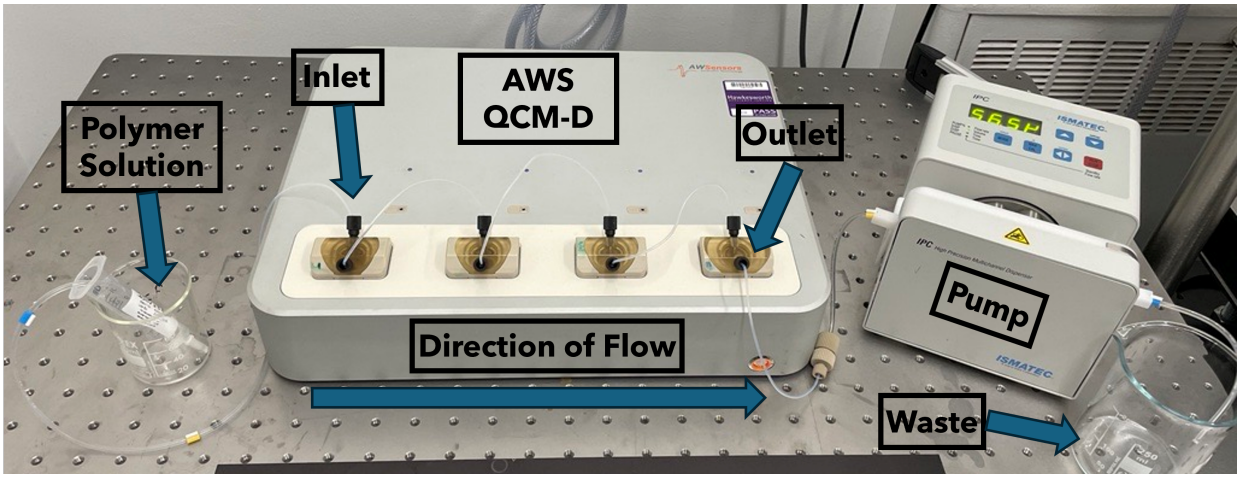



Figure 3.2: QCM instrument setup.

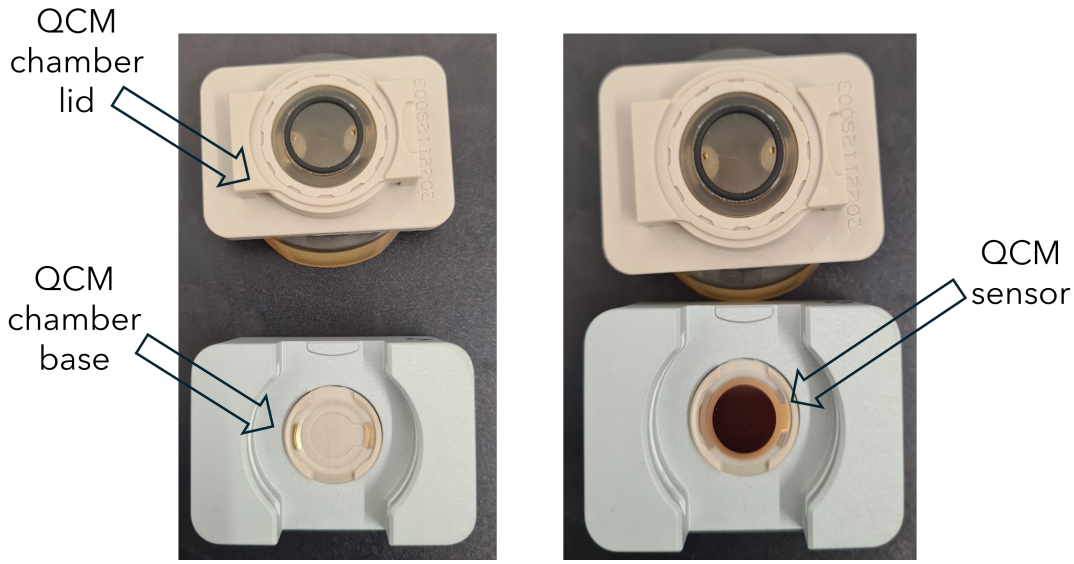



Figure 3.3: QCM 5 MHz 14 mm Cr/Au/SiO2 sensor setup and chamber.

Subsequently, once the frequency signal stabilised, as indicated by reaching a plateau with a change of $\pm 1Hz$, deionised water was flushed through the cell to remove weakly adsorbed polymers. The difference in frequency was then measured, and the mass was deduced from the frequency versus time plot. Each sample condition was repeated for a minimum of four runs to ensure the reliability and repeatability of the results. More information on how the data is obtained can be found in section 3.1.6.

Two measurement protocols were employed throughout this research. The first involved running deionised water, polymer, and then deionised water over the sensor, while the second included the same steps with two additional ones: Bovine Serum Albumin (BSA) followed by deionised water, aiming to investigate the fouling properties of the polymer in question. In the results chapters, when discussing QCM data, it will be indicated which protocol was followed for each dataset.

### 3.1.5 Cleaning Methodology: preparation of equipment

The sensors utilised throughout this project were QCM 5 MHz 14 mm Cr/Au/SiO2 sensors obtained from Quartz Pro (Sweden). Before each use, the sensors underwent cleaning using the following method:

1. Place sensors in 2% sodium dodecyl sulfate (SDS) solution for 15 minutes.
2. Rinse sensors with deionised water
3. Place sensors in Isopropyl alcohol (IPA) solution for 15 minutes
4. Dry with Nitrogen gas
5. Place in UV box for 10 minutes
6. Rinse with IPA
7. Dry with Nitrogen gas

The lids to the QCM chambers required cleaning before each measurement. The procedure used is as follows;

1. Place lids in 2% SDS for 15 minutes
2. Rinse with deionised water
3. Place lids in IPA solution for 15 minutes
4. Dry with compressed air

Given the QCM's extreme sensitivity, operating at a nanogram scale, thorough cleaning of the tubing was imperative. Two types of tubing were employed during the measurements: Ismatec Pump Tubing, 2-Stop, Tygon® S3™ E-LFL, 1.52 mm ID (12/PK) and Masterflex Transfer Tubing, PTFE, 1/32" ID x 1/16 " OD (25 ft). The cleaning procedure is outlined as follows:

1. Place the tubing in 2% SDS solution and sonicate for 15 minutes
2. Rinse with deionised water
3. Sonicate in deionised water for 15 minutes
4. Dry tubing with compressed air.

### 3.1.6 Data Analysis

Figure 3.4 illustrates a frequency versus time plot typically obtained from the QCM measurement, with mass adsorbed on the secondary y-axis. Step 1, labelled in the image below, depicts the baseline starting at zero, serving as the data analysis reference point. To determine the mass adsorbed from the measurement, the mass at point 1 is subtracted from the mass at point 2. This calculation provided the amount of mass adsorbed for the polymer under investigation. To assess the remaining mass adsorbed on the sensor after the final wash, the mass at point 3 is subtracted from the mass at point 2. The material was injected

at point A and built on the sensor until equilibrium was reached (stage 2). Water replaced the polymer in the flow at point B, reaching further equilibrium in stage 3. It was important to note that the system had to be equilibrated for each data point to obtain the mass adsorbed, ensuring consistency and accuracy in the results. There is no definitive duration for each experiment, as the system requires equilibration, which varies depending on the various polymer solutions investigated throughout this research project.

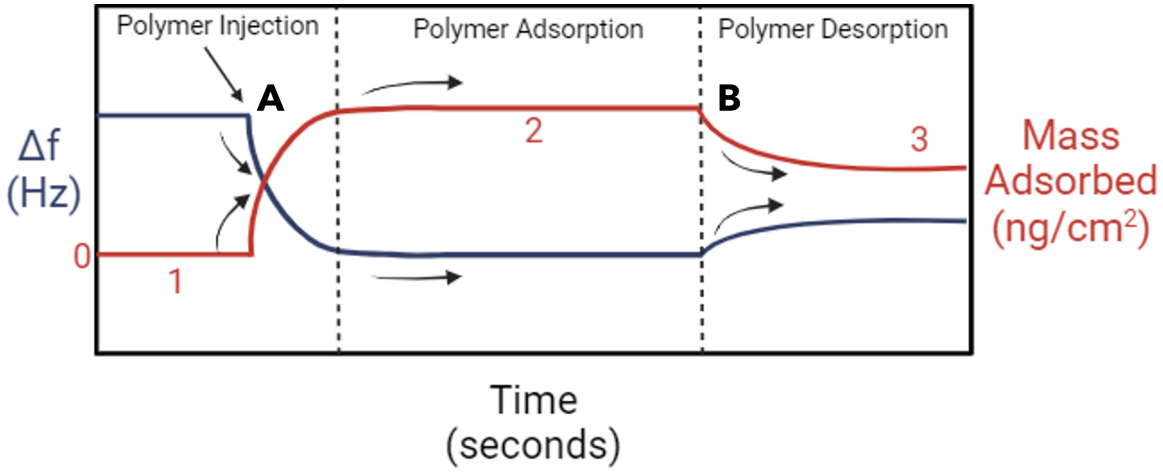



Figure 3.4: Frequency vs time plot with mass adsorbed (obtained from the Saurbrey equation) on the secondary y-axis.

It is also important to obtain the adsorption kinetics from the QCM measurements. This is achieved by fitting the data obtained to the Langmuir adsorption isotherm, allowing us to derive first-order adsorption kinetics data. The slope highlighted in Figure 3.5, referred to as "Climb," represents the initial part of the adsorption process. The data fitted to Equation 3.2 as described by Liu et al.[106] First-order kinetics provides data on how fast the polymer molecules reach the silicon dioxide surface.

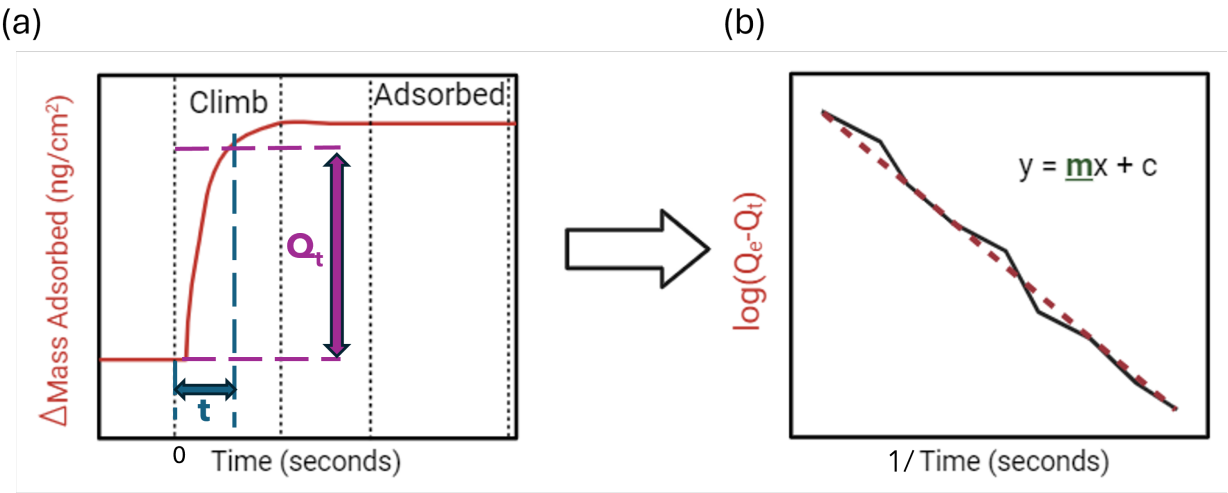



Figure 3.5: Illustrates a) Change in mass adsorbed in ng per $cm^2$ vs time in seconds which can then be converted to plot b)log vs time plot using the first-order Langmuir isotherm equation.

The first-order Langmuir isotherm equation is given by:

$$\log_{10}(Q_e - Q_t) = \log_{10}(Q_e) - \frac{2.303 \times K_{\text{ads}}}{t} \tag{3.2}$$

Where:

$Q_e$ = is the maximum mass adsorbed in ng

$Q_t$ = is the mass adsorbed at time t in ng

$K_{\text{ads}}$ = is the first-order adsorption kinetics in $s^{-1}$

$t$ = t is the time in seconds

Fitting the initial adsorption data to Equation 3.2 gives first-order adsorption kinetics, obtained from the gradient of the $\log_{10}(Q_e - Q_t)$ versus $1/t$ plot, as depicted in Figure 3.5 (b). Worked examples are shown in Chapter 4 section 4.1.

## 3.2 Atomic Force Microscopy

Binning, Quate and Gerber published a paper titled 'Atomic Force Microscopy' in 1986.[107] The idea originated from previous experiments on electron tunnelling, while the notion of utilising AFM for generating high-resolution images was inspired by the development of the Scanning Tunneling Microscope (STM).[107,108]

AFM has various modes known as 'spectroscopic' modes, these measure other properties of the sample at the nanometer scale. In these modes, AFM can be used as a multi-interdisciplinary tool to deliver quantitative high-resolution images, with great flexibility in the sample that can be studied. This versatility enables AFM to serve as a multidisciplinary tool, providing quantitative high-resolution images and offering flexibility in the types of samples that can be studied.

### 3.2.1 Principle

An AFM differs from typical optical or electron microscopes, as it does not form images by focusing light or electrons onto a surface. Instead, an AFM physically "feels" the sample surface using a small tip on a cantilever spring, as depicted in Figure 3.6. The cantilever is on the order of ten to hundreds of micrometres long, width of twenty to fifty micrometres and has a thickness between 0.4 and several micrometres[109] and can be moved on and over a surface, to construct an image of the sample surface height.[107,110] AFM allows observing materials at the nanoscale level.

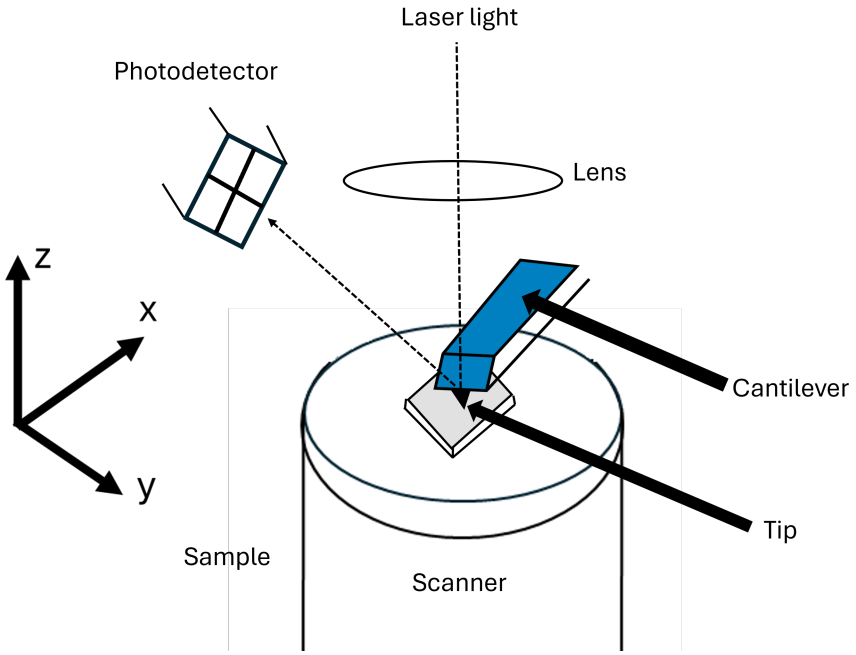



Figure 3.6: Schematic diagram of an atomic force microscopy unit.[110]

An AFM comprises a Z scanner that moves the cantilever up and down, an XY scanner that moves the sample back and forth underneath the cantilever, both of which can move several millimetres or greater, and a position detector that records the bending of the cantilever.[110] The cantilever can be moved a very small distance, so it can be lowered to nanometers above the surface. The position sensor operates by tracking a laser beam reflected off the flat top of the cantilever; any bending in the cantilever induces changes in the direction of the reflected beam. Subsequently, the position detector tracks and records these beam changes, as shown in Figure 3.6.

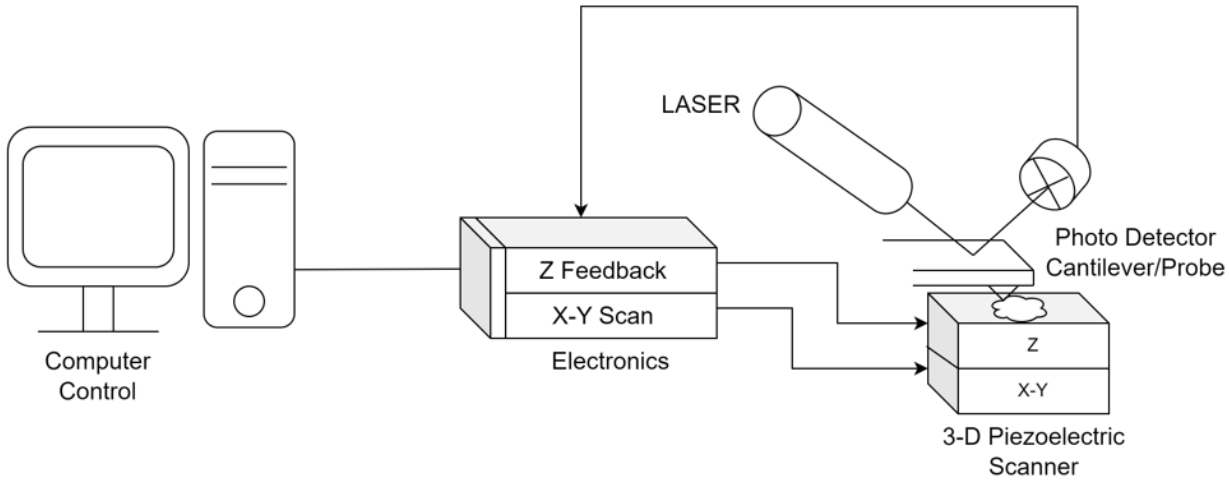



Figure 3.7: AFM components outside the cell.[107]

AFM can image the topography of a sample surface by scanning the cantilever over a region of interest. The raised and lowered features on the sample surface influence the bending of the cantilever, which is measured by the position detector, see Table 3.1 for more information on the tip-sample separation. By employing a feedback loop to control the height of the tip above the surface, AFM can generate an accurate topographic map of the surface data nanometer scale.[107,111]

There are two primary methods of AFM imaging: contact and non-contact AFM. In contact AFM, the cantilever scans across a sample with its tip in direct contact with the sample surface. The strong repulsive forces between the tip and the surface cause the cantilever to bend as it passes over surface features, measuring the sample surface roughness or topography.

In contrast, non-contact AFM involves oscillating the cantilever at much smaller amplitudes of 1 to 10 nm in the z-positioning just above the surface during scanning, ensuring that the tip does not touch the surface. A precise high-speed feedback loop is employed between the cantilever and the piezoelectric to prevent the cantilever tip from crashing into the surface, thus maintaining tip sharpness and preserving the sample surface integrity. As the tip nears

the surface, interactions between the tip and surface result in a reduction of the cantilever's oscillation amplitude. A feedback loop then adjusts for these amplitude changes, enabling the reconstruction of the surface topography at the nanometer scale.[111]

Non-contact AFM offers several advantages over contact AFM. It preserves the sample surface as the tip and surface do not make direct contact, prolonging the sharpness and lifespan of the tip and enabling high-quality imaging over multiple scans. Additionally, this approach reduces the total operating cost of the instrument, as tips are expensive to replace.[107,111]

AFM can also be utilised to acquire force-distance curves, achieved by bringing the cantilever into contact with the sample surface by moving closer and then further away from the sample. From this, the force between the sample surface and the probe tip can be quantified, as illustrated in Figure 3.7. Further details can be found in section 3.2.2. Table 3.1 describes the tip-sample interaction forces acting during force-distance measurements as a function of the distance.

Table 3.1: Types of Tip-sample separation and measurement in AFM.[112]

| **Tip-sample Distance** | **Dominant Forces** | **Typical force range** |
|---|---|---|
| When the tip is far from the sample (10 to 100 $\mu$m) | No Interaction | - |
| When the tip approaches the sample (Few $\mu$m) | Long-range interactions Electrostatic Forces | $\pm$ 1 nN - $\pm$ 1 $\mu$N |
| When the tip is close to the sample (Sub-nm to few nm) | Van der Waals (attractive) Capillary Forces (in moist air) | -100 nN - + 10 $\mu$N |
| When the tip contacts the sample (Indentation) | Pauli Interaction (repulsive) Mechanical Forces | +1 nN - + 10 $\mu$N |

### 3.2.2 Data Interpretation of force-distance curves

Measuring the spring constant and deflection sensitivity of the cantilever is crucial to derive the relationship between cantilever deflection and piezo movement, which can subsequently be converted into force versus tip-sample separation measurements, as demonstrated in Figure 3.7. This information is obtained from the built-in software of the AFM system.

In AFM, the deflection force (F) on the cantilever was determined by its deflection (d) according to Hooke's Law shown in equation 3.3:

$$F = k \cdot d \tag{3.3}$$

Where $k$ is the spring constant of the cantilever. The spring constant ($k$) measures the cantilever's calibrated stiffness. Deflection refers to the amount of bending in the cantilever, measured by the AFM system. The AFM measures the cantilever deflection caused by the interactions between the tip and the sample. This deflection is converted into force using the spring constant (k). This relationship allows for detailed nanoscale surface analysis by converting deflection into quantitative force measurements.

Force-distance curves are acquired using AFM, as the cantilever tip makes contact with the sample surface by approaching and retracting from the sample. The force between the sample surface and the probe tip can be quantified from these curves. Figure 3.8(a) illustrates a typical force-distance curve[113], where steps 1 - 5 are elucidated sequentially using Figure 3.8(b) to aid in the explanation. The experimental procedures necessary to achieve this are outlined below:

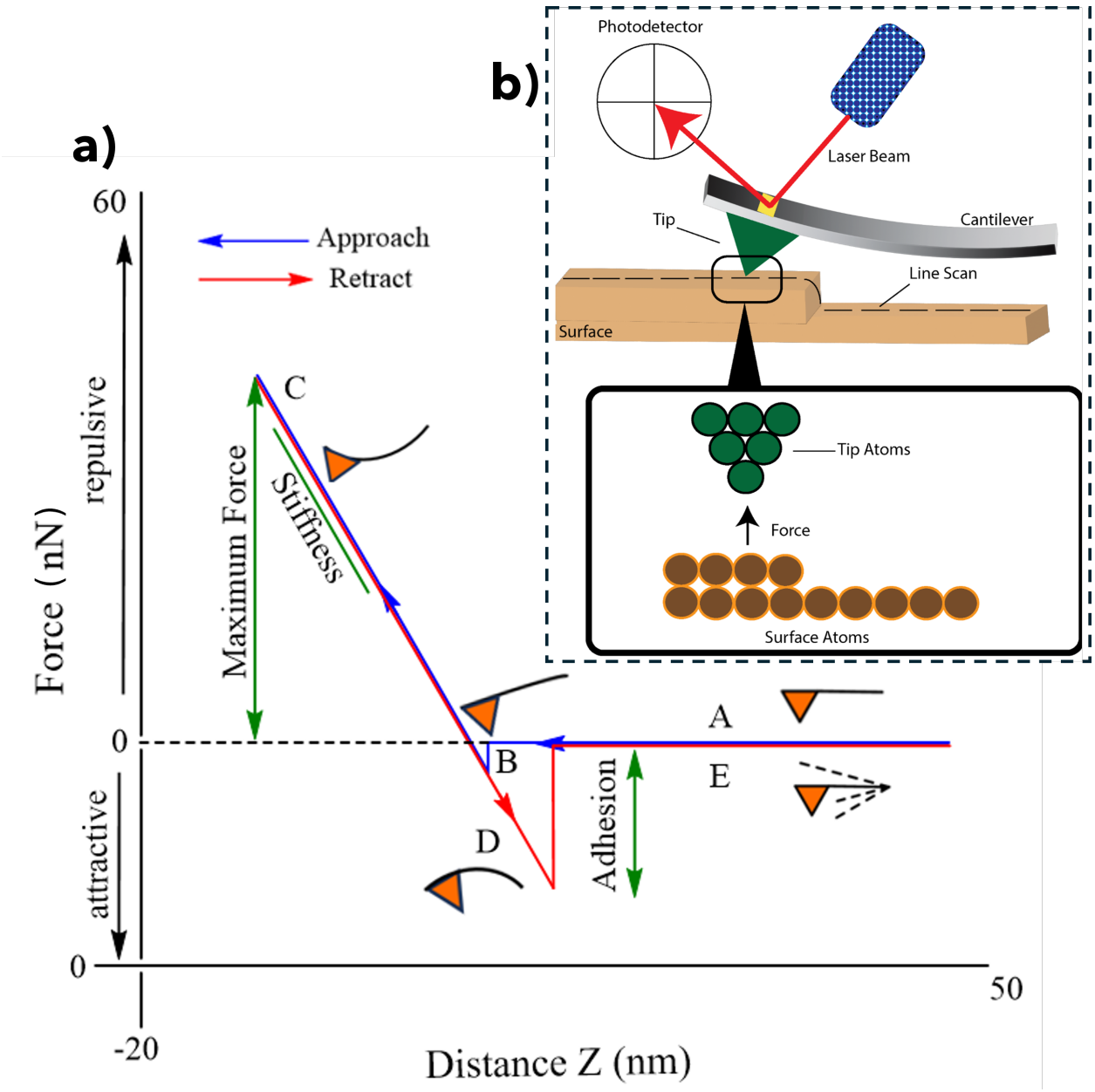



Figure 3.8: (a)Force distance curve data representation. Approach and retraction curves are shown in red and blue, respectively.[113] (b) The figure illustrates the tip atoms interacting with atoms of the sample surface, where the force is measured between the tip and the surface.

1. Region A in Figure 3.8. Utilising the piezoelectric scanner the cantilever is brought close towards the sample surface in a controlled manner at a controlled speed that may vary between a few nm $s^{-1}$ and dozens of $\mu$m.[114] There are no interactions between the tip and the sample surface at this point, so no force is measured.

2. In region B, long-range interactions such as electrostatic forces can be observed from a few micrometres away from the tip-sample interaction. As the tip approaches the sample surface, the cantilever begins to deflect due to attractive forces such as van der Waals forces in the region of sub-nm to a few nm.[115] Section 2.5.1 gives more information on the nature of these forces. Region B contains the "snap-into-contact" phase. This is primarily induced by capillary forces under ambient humid conditions, resulting in the formation of a thin layer of water covering both the tip and sample surfaces. Snap-in occurs when the attractive force gradient surpasses the spring constant of the cantilever.

3. In region C, as the Z scanner moves closer to the sample surface, the main repulsive force between the surface and tip gradually grows stronger until it matches a predetermined maximum force set. Once this setpoint is reached, the Z scanner withdraws the tip from the sample surface. As the tip nears contact with the sample surface, the cantilever bends to its maximum extent. The sample is then indented by the cantilever and repulsive forces such as Pauli interactions occur. The cantilever is then withdrawn.

4. As the distance between the tip and the surface increases, the deflection of the cantilever starts to decrease. Consequently, the cantilever bends in the opposite direction due to the attractive force between the surface and the tip, as indicated in point D. The adhesion between the tip and the surface can then be quantified.

5. The pull-off event occurs in region E, where the cantilever detaches from the surface as the Z scanner continues to retract, and the spring constant of the cantilever exceeds the adhesion force between the tip and the sample.

The information is captured in the form of tip-sample separation distance, enabling the recording of data detailing the force between the cantilever tip and the sample surface at each point (A-E). This data is visualised as the force curve depicted in Figure 3.7.

### 3.2.3 Limitations

The effectiveness of AFM is limited by the sample's shape, surface properties or size. In some cases, the AFM tip can be damaged if the sample surface is too sticky, rough or soft, for example with polymers[116], quartz[117] or biotin.[118] Another disadvantage of the AFM is that when it comes to imaging the instrument is very slow with experiments taking anywhere from minutes to hours which can cause issues when the experiment aims to capture dynamic processes. Other instruments such as optical and scanning electron microscopy would need to be carried out to overcome this limitation. A further limitation of the AFM tip is that it can wear down over time, affecting the measurement's accuracy and reproducibility. If the tip is not sharp or aligned perfectly with the sample surface this can cause issues when interpreting the data. It is also difficult to study a large area on a sample as AFM has a limited field of view commonly in the range of micrometres.[107,111]

Another limitation of AFM was its impracticality for measuring areas larger than approximately 100 micrometres. This limitation arose from the need to mechanically scan the probe over the surface, requiring very slow scanning speeds for large areas. Exceptions to this included parallel AFMs, which measured small areas with multiple probes to create a large dataset, and 'fast scanning' AFMs that could expedite the scanning process.[107]

### 3.2.4 Cleaning of Cantilevers

For adhesion force curves to be obtained the cantilever used was a PNP-TR-TL also known as Pyrex-Nitride AFM Probe – TRiangular AFM - TipLess cantilever at 0.32 $\mathrm{N\,m^{-1}}$ spring

constant and to obtain thickness measurements of the polymers. The cleaning method before use for the cantilever is listed below:

1. Place cantilevers in ethanol for 2 minutes.
2. Place cantilevers in deionised water for 2 minutes.
3. Dry with nitrogen gas.
4. Place in UV box for 10 minutes.
5. Place cantilevers in ethanol for 2 minutes.
6. Place cantilevers in deionised water for 2 minutes.
7. Dry with Nitrogen gas.

It must be noted that cantilevers that have been functionalised with borosilicate or polystyrene beads cannot be placed in the UV box as it would degrade the epoxy glue used to attach the spheres.

### 3.2.5 Experimental Setup

An atomic force microscope (Dimension 3100, Veeco, UK) with a Nanoscope 4 controller was used for characterising the materials used throughout this research project. Gold-coated cantilevers with a nominal spring constant of 5 N $m^{-1}$ (Tap150 GB-G, Budget Sensors, Bulgaria) were used to acquire surface morphology. Adhesion force measurements were carried out using a colloidal probe prepared by glueing a borosilicate glass microsphere (Dukes Standards, Thermo Fisher Scientific, USA) with a diameter of 10 µm onto a tipless silicon nitride cantilever with a nominal spring constant of 0.08 N $m^{-1}$ (PNP-TR-TL, Nanoworld, Switzerland). A two-component epoxy resin was used (Araldite, Switzerland). The prepared

colloidal probe was left for 24 hours to ensure the adhesive was fully set before use. Adhesion force measurements were carried out by obtaining 100 force curves from 3 different 1 $\mu m^2$ areas each curve 100 nm apart in a 10 x 10 grid in liquid. The adhesion force was taken as the pull-off deflection from the force curves in Figure 3.8 point D.

### 3.2.6 Data Analysis

Data analysis was carried out using a Python script that allowed all force curves to be analysed. The Python code enabled each of the 300 force curves to be examined. The Python script was designed to automatically calculate the adhesion force along with the standard deviation. The full script is provided in Appendix One, Section A.

## 3.3 Dynamic Light Scattering (DLS) - Measurement of Particle Size

DLS was employed as a quality control measurement, primarily for determining the size and zeta potential of the polymer samples. DLS was conducted to ascertain whether the samples were undergoing aggregation over time and to assess how pH changes influenced the size and charge of the polymer samples. Further details are discussed in Chapter 5, which focuses on the effect of random copolymer composition on its surface deposition. See Table 5.2 for the random copolymer composition and Figure 5.4 for the chemical structures of the compositions.

### 3.3.1 Principle

Dynamic Light Scattering (DLS) measures objects dispersed in a medium based on the signal collected by the detector. Light scattering is a versatile technique employed for characterising particles or macromolecules suspended in a solution. When a particle absorbs a photon from an incident beam, it re-emits it in all directions. DLS uses the Brownian motion of particles within a dispersion to ascertain their hydrodynamic size. Brownian motion, resulting from collisions with solvent molecules like water, induces random movement of particles. This motion, in turn, is influenced by Rayleigh scattering, where light is scattered by particles or molecules smaller than the wavelength of light.[119] Rayleigh scattering disperses the light from individual particles, while DLS aggregates the scattering collectively. Rayleigh scattering contributes to the intensity and size distribution of DLS. Smaller particles exhibit faster diffusion, whereas larger ones diffuse more slowly through the medium. The rate of Brownian motion is quantified by the translational diffusion coefficient, commonly denoted as 'D'. In dynamic light scattering (DLS), the hydrodynamic size refers to the size of a sphere that diffuses at the same rate as the particle under observation. This sphere includes the core particle along with any surface-bound entities, such as ions or adsorbed polymers.[120]

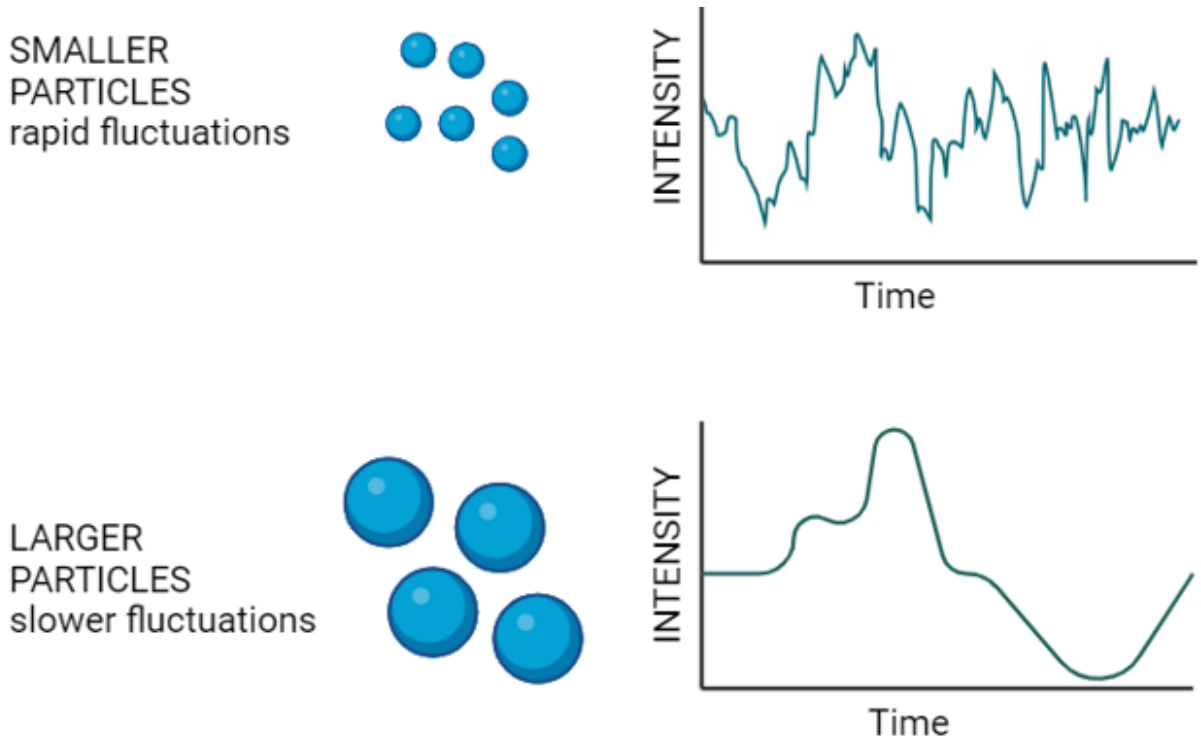



Figure 3.9: Influence of Particle Size on Intensity in DLS Measurements. Figure shows the impact of smaller and larger particles on the intensity distribution obtained from Dynamic Light Scattering (DLS) measurements. The data highlights how particle size variations affect the overall intensity profile.

In DLS, particles are illuminated by a laser, which they scatter. If the particles were stationary, the scattered light would maintain a constant intensity. However, due to diffusion caused by dispersion, the intensity of scattered light fluctuates over time. The detected light from many randomly diffusing particles combines, resulting in a fluctuating intensity signal. These fluctuations occur because of the interference between light scattered by individual particles, with intensity changes corresponding to ongoing diffusion.[121] The rate of these intensity fluctuations is determined by the diffusion speed of the particles: smaller particles diffuse more quickly, causing faster fluctuations in scattered light, and vice versa, as depicted in Figure 3.9.

DLS can measure size distributions of particles ranging from less than a nanometer up to several microns in size. It is a rapid and non-invasive technique which is extremely versatile and used widely. For example, DLS has been used to help characterise and optimise the pigments used in paints, dyes and inks,[122] to advance research into drug delivery systems such as liposomes,[123] and to improve the formulation of emulsions and colloidal systems.[124]

### 3.3.2 Data Interpretation

In DLS, snapshots of the light scattering signal are rapidly captured one after another, each compared to the original signal measured. Over consecutive snapshots, which occur on the scale of nano- or microseconds, the intensity signals exhibit high similarity or correlation. However, as the time gap between snapshots increases, the similarity or correlation decays. Eventually, the intensity signal undergoes complete change, resulting in no correlation with the original signal. This process is known as autocorrelation, Malvern includes software which autocorrelates these signals through a mathematical approach which is built into the Malvern software. Larger particles, which diffuse more slowly, take longer to lose correlation with the original signal. Small particles undergoing rapid diffusion experience a rapid decay in signal correlation as shown in Figure 3.10. The auto-correlation function can be used

to calculate the size distribution. The Zetasizer software uses an algorithm to analyse and extract the decay rates for several size classes to produce a size distribution.[121]

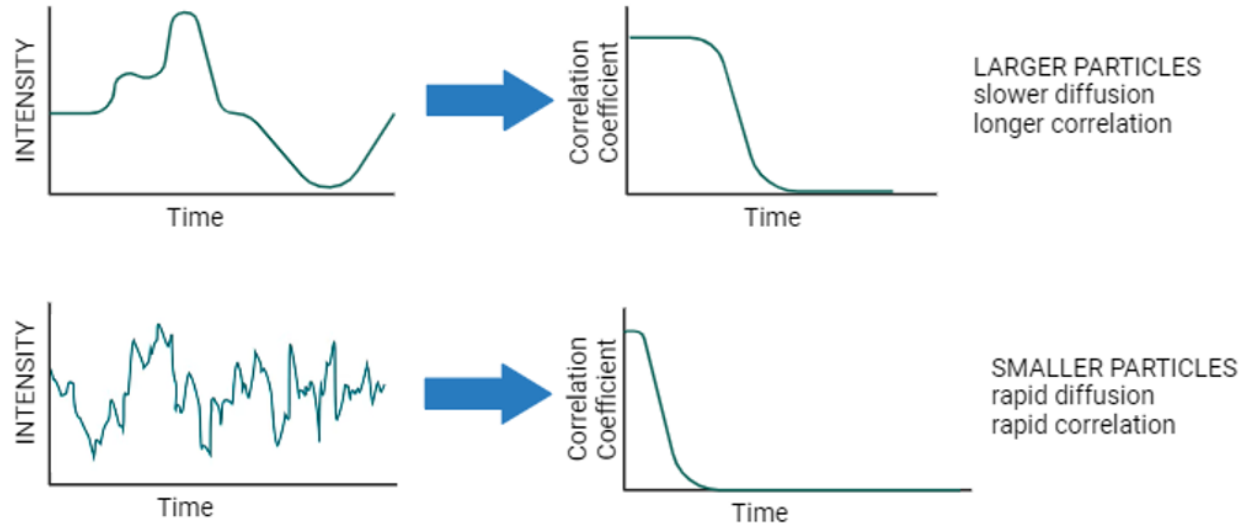



Figure 3.10: Schematic diagram of DLS autocorrelation function. Larger particles diffuse more slowly than small ones, resulting in a longer time to lose correlation with the original signal, while smaller particles diffuse rapidly, causing a quicker decay in signal correlation.

From the autocorrelation function the translational diffusion coefficients, D, can be extracted. These values are used in the Stokes-Einstein equation 3.4 to obtain the hydrodynamic size of the particle in question.

$$d_h = \frac{k_B T}{3\pi\eta D} \tag{3.4}$$

where:

- $d_h$ is the hydrodynamic diameter of the particle,
- $k_B$ is Boltzmann's constant,
- $T$ is the absolute temperature,
- $\eta$ is the viscosity of the medium, and

- $D$ is the diffusion coefficient.

Variables such as solvent viscosity and temperature must be known as they will affect the particle's diffusion. Using DLS, the size of the particles in the sample can be measured. Size distribution can be calculated as an intensity distribution, representing the intensity of scattered light from each size population in the sample. Additionally, these results can be converted into a volume or number size distribution if necessary.[121]

### 3.3.3 Limitations

DLS can measure particles ranging from 1 nanometer to 10 micrometres; particles outside this range are challenging to measure. In polydisperse systems where a sample consists of particles of varying sizes, DLS provides data on the average size across the sample rather than individual particle sizes, as it is a bulk measurement technique. DLS sensitivity to concentration[125] means that impurities or aggregates in a colloidal system can affect particle size measurements by scattering light, leading to interference with the DLS signal and unreliable data.[121] Additionally, if the sample concentration is too low or too high, it can result in excessive or insufficient light scattering, leading to inaccuracies in the dataset.

Another limitation of DLS is its inability to measure different particle shapes in solution. Since DLS measures the hydrodynamic size of particles, which is an average of particle shape and size in the bulk solution, particles with similar hydrodynamic sizes but different shapes, such as rod-shaped or spherical particles, may produce similar signals, making it difficult to distinguish between them.[125,126]

Although DLS primarily produces an intensity-based size distribution of the particles being analysed, this can be converted into a volume distribution using Mie theory, as demonstrated in equations 3.5 and 3.6.[121] This volume distribution can also be further converted to a number distribution.

To convert an intensity distribution $I(r)$ obtained from Dynamic Light Scattering (DLS) to a volume distribution $V(r)$ using Mie theory, the final equation is:

$$V(r) \propto I(r) \tag{3.5}$$

This proportionality can be expressed more explicitly as:

$$V(r) = k \cdot I(r) \tag{3.6}$$

where $k$ is a proportionality constant that depends on the specific experimental setup and calibration.

DLS may struggle to distinguish between particles measuring 90 and 110 nm, resulting in a broad peak with a high Polydispersity Index (PDI). Achieving peak resolution with DLS necessitates particles that differ in size by at least a factor of 3 (e.g., 10 and 30 nm, or 50 and 150 nm). This poses a challenge for polydisperse samples. One approach to enhancing resolution is to perform size separation of particles before analysis. Additionally, modern DLS instruments can be integrated with analytical tools, enabling precise size determination for each fraction.[125]

### 3.3.4 Cleaning Method

Before each DLS size measurement, the cuvette, DTS0012, a disposable 45 x 12 x 12 mm plastic cell purchased from Malvern Panalytical (United Kingdom), was rinsed three times with ethanol to remove organic contaminants followed by three rinses with deionised water to remove ethanol. This procedure ensured that the sides of the cuvette were wetted to remove bubbles, which could interfere with the measurement.

### 3.3.5 Experimental Setup

Figure 3.11 illustrates a standard DLS system consisting of six primary components. Initially, a laser is employed to provide illumination for the sample particles within the cuvette. While the majority of the laser beam traverses the sample directly, a portion is scattered by the particles within. A detector is then used to gauge the intensity of this scattered light. Since particles scatter light in all directions, theoretically, the detector can be positioned anywhere and still detect the scattering. In the Zetasizer Nano series, the detector position varies depending on the specific model, either at 175° or 90°. The detector can effectively measure the scattered light only within a particular range of intensity. If the detected light exceeds this range, the detector may become overloaded. To mitigate this, an attenuator is utilised to decrease the intensity of the laser, consequently reducing the scattering intensity. The zetasizer automatically determines the optimal attenuator position during the measurement sequence. The scattering intensity signal from the detector is transferred to a digital signal processing board, known as a correlator, that analyses the scattering intensity over successive time intervals to calculate the rate of intensity variation. Subsequently, this correlator data is transmitted to a computer, where the specialised zetasizer software analyses the data and extracts size information. "A" and "B" designate the detection path, as depicted below, leading back to the correlator for data acquisition.[127]

The intensity of the scattered light is measured as a function of time, and this data is used to calculate the size and size distribution of the particles in the sample.

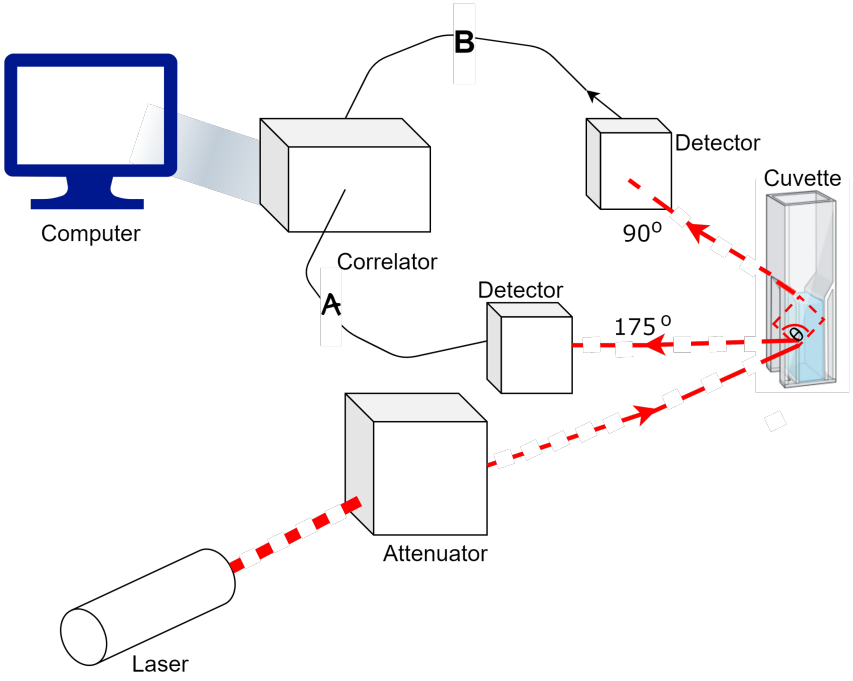



Figure 3.11: Principle of DLS Operation: A laser light is directed at suspended particles, and a high-time-resolution detector measures the intensity of the light scattered at a specific angle, $\theta$. These fluctuations in scattered light intensity over time are caused by the Brownian motion of the particles.[127]

Dynamic Light Scattering, Zetasizer Ultra (Malvern Panalytical, United Kingdom) was used for characterising the materials' size. The light source used in this DLS was a monochromatic laser, which is a single laser light, in the visible range, directed onto the sample during the measurement run. The sample was prepared at a chosen concentration and dispersed in deionised water all samples looked visibly transparent. The sample is then placed in a cuvette and placed into the DLS, the sample is then exposed to the monochromatic laser. A detector is used to detect the scattered light from the sample. The detector is typically positioned at a fixed angle, backscattering was used for the DLS measurements which were placed at an angle of 175 degrees. It must be noted that before running a DLS size measurement the sample's refractive index and absorbance must be known.[127]

### 3.3.6 Data Analysis

The data was exported from the ZS Explorer software, which is used to analyse DLS data. Subsequently, the data was exported to an Excel file, and the average of the five DLS measurements was calculated. These averaged values were then plotted using Python; graphs representing parameters such as Intensity, Number, or Volume against size were plotted in Python.

## 3.4 Zeta Potential

### 3.4.1 Principle

Figure 3.12 presents a schematic of a particle in solution. The surrounding liquid layer is divided into two regions: the Stern layer, where ions are tightly bound, and an outer diffuse layer, where ions are less firmly attached. This arrangement results in the formation of an electrical double layer around each particle. Within the diffuse layer, there is a boundary where ions and particles create a stable structure. When the particle moves, due to gravity or other forces, the ions within this boundary move with it, while those outside it do not. This boundary is known as the surface of hydrodynamic shear or the slipping plane, and the zeta potential is the electrical potential at this boundary, as illustrated in Figure 3.12.[120,125,128,129]

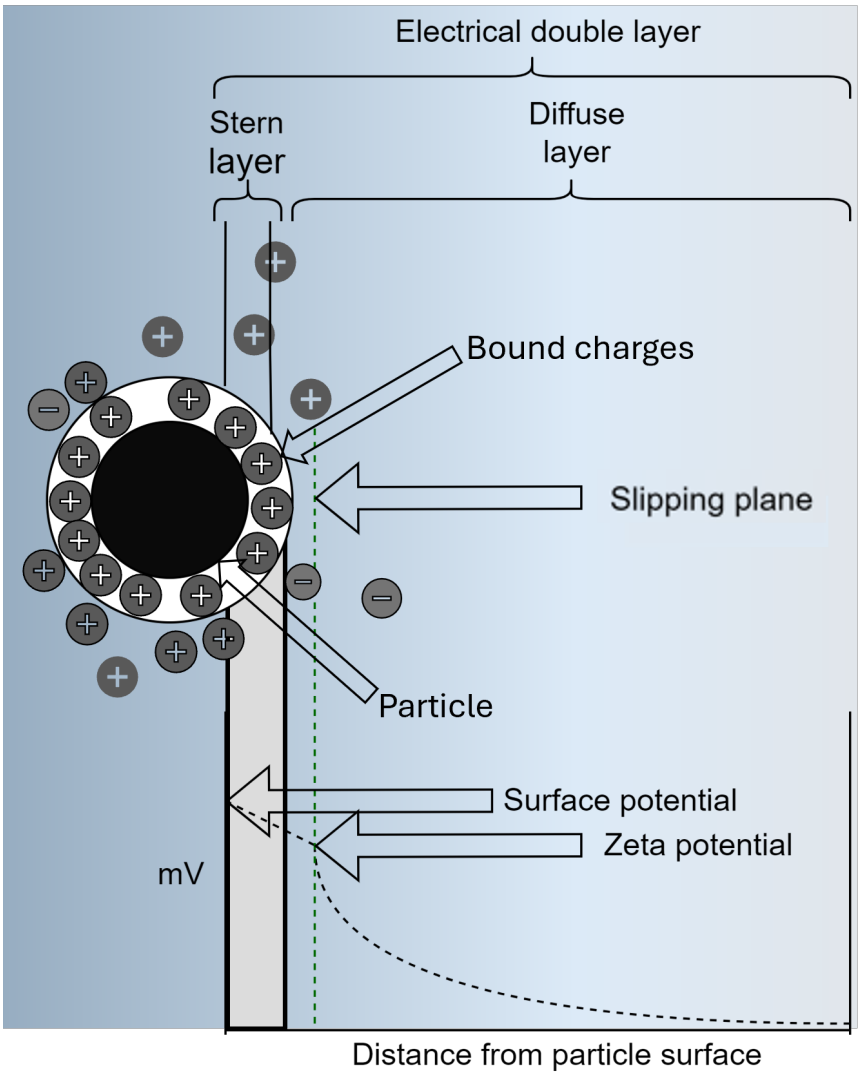



Figure 3.12: Schematic representation of zeta potential.

The Zetasizer Nano (Malvern Panalytical, United Kingdom) series computed the zeta potential through the assessment of Electrophoretic Mobility. Electrophoretic Mobility was derived from an electrophoresis experiment conducted on the sample, where the velocity of particles was measured using Laser Doppler Velocimetry (LDV).[120]

The pH served as the paramount factor influencing zeta potential. Without a specified pH value, a zeta potential measurement lacks contextual meaning. Consider a particle in sus-

pension with a negative zeta potential. Upon adding alkali to the suspension, the particles would tend to acquire an even more negative charge. Conversely, the addition of acid could neutralise the negative charge, eventually leading to a buildup of positive charge. Consequently, a zeta potential versus pH curve typically exhibits positive values at low pH levels and decreases or becomes negative at high pH.

The presence of electrical charges on particle surfaces leads to specific responses when subjected to an applied electric field. These responses are collectively referred to as electrokinetic effects, encompassing four distinct phenomena based on how motion is induced. These included:[130,131]

- Electrophoresis: The motion of a charged particle in relation to the liquid in which it was suspended, driven by an applied electric field.
- Electroosmosis: The movement of a liquid in relation to a fixed charged surface, induced by an electric field.

When an electric field is applied across an electrolyte, charged particles within the electrolyte are drawn towards the electrode of opposite charge. However, viscous forces acting on the particles resist this movement. Once a balance is achieved between these opposing forces, the particles move at a constant velocity.

The particle velocity depends on several factors:

- The strength of the electric field or voltage gradient.
- The dielectric constant of the medium.
- The viscosity of the medium.
- The zeta potential.

This particle velocity in an electric field is often termed as its Electrophoretic mobility.[130]

### 3.4.2 Data Interpretation

The magnitude of the zeta potential serves as an indicator of the potential stability of colloidal systems. When all particles in suspension possess either a significantly negative or positive zeta potential, they tend to repel each other, thus preventing aggregation. Conversely, if particle zeta potentials are low, there is insufficient repulsive force to prevent particles from aggregating and flocculating.

Typically, the threshold for distinguishing between stable and unstable suspensions lies around +30 or -30 mV. Particles with zeta potentials exceeding +30 mV or falling below -30 mV are generally considered stable. However, particles with a higher density than the dispersant may eventually settle and form a densely packed bed, even if they are initially dispersed.[120] Therefore, the zeta potential is influenced by both the nature of the dispersant and the surface properties. Consequently, when comparing the zeta potential of different materials, it is essential to consider not only the characteristics of the surface but also the definition of the dispersant's nature.

In a classical micro-electrophoresis setup, a cell contains electrodes at both ends and a potential is applied. Particles migrated toward the oppositely charged electrode as shown in Figure 3.13, and their velocity was measured. This velocity was then expressed in units of field strength as their mobility.

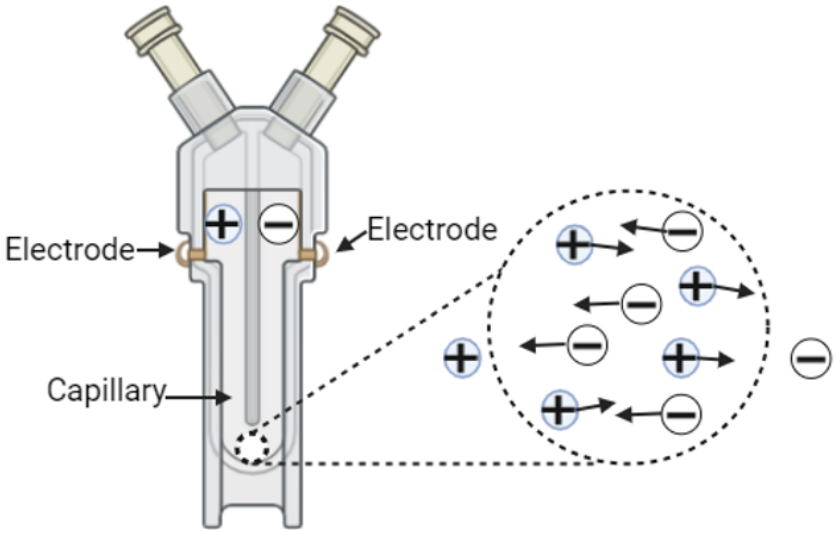



Figure 3.13: Measuring Electrophoretic Mobility of a sample placed in a DTS1070 cuvette, indicating the movement with the effect of the positive and negative electrodes.

The method used to determine this velocity was Laser Doppler Velocimetry (LDV), which is a widely used technique in engineering to investigate fluid flow in diverse scenarios, ranging from the supersonic airflow around turbine blades in jet engines to the flow velocity of sap within plant stems. In these instances, LDV measures the velocity of minuscule particles within the fluid streams, which moved at the same velocity as the fluid. Hence, LDV was suitable for determining the velocity of particles moving through a fluid in an electrophoresis experiment. The receiving optics are precisely focused to capture the scattering of particles within the cell. Figure 3.14 shows light scattered at a 17° angle was merged with the reference beam, generating a varying intensity signal. The frequency of these fluctuations was directly linked to the particles' speed.[120]

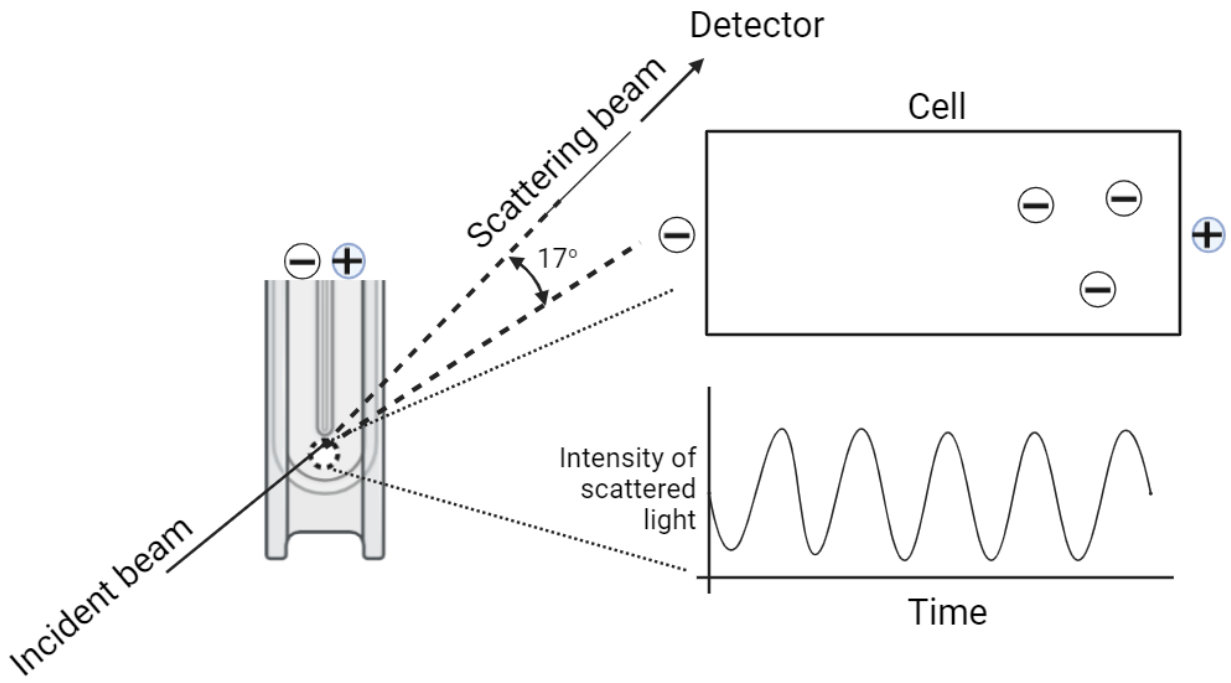



Figure 3.14: Schematic of Zeta Potential Measurement Process. Illustration of how light scattered at a 17° angle merges with a reference beam to produce a varying intensity signal. The frequency of these fluctuations corresponds to the particles' speed, which is analysed by a digital signal processor to identify characteristic frequencies in the scattered light.

### 3.4.3 Limitations

The Zeta potential (ZP) technique has limitations, especially when dealing with high concentrations and intricate nanostructures. Changes in particle surface chemistry can greatly impact measurements. Samples relevant to therapy often experienced shifts in viscosity, pH, dielectric constant, and refractive index, making diluted sample ZP measurements insufficient for representing in vivo formulations. Thus, solely relying on ZP analyses to progress nanoformulations to in vivo studies was not recommended. Furthermore, these analyses typically occurred under controlled laboratory conditions using aqueous dispersants, which may not faithfully mirror the intricate environment of in vivo settings, such as blood.[125]

### 3.4.4 Cleaning Method

The cuvette DTS1070 Zetasizer NanoSeries disposable folded capillary cells were utilised for conducting zeta potential measurements. Before measurements, the cells were rinsed with deionised water three times to wet the inner walls of the cuvette, thus preventing the formation of bubbles.

### 3.4.5 Experimental Setup

Similar to the DLS system outlined in section 3.3.5, a zeta potential measurement system consists of six main components, shown in Figure 3.15. A laser (1) shown in Figure 3.15 served as a light source to illuminate particles within the sample. For zeta potential measurements, this light source was divided into an Incident (A) and Reference beam (B). The Reference beam was modulated to induce the Doppler effect.[128]

The laser beam traversed through the centre of the sample cell (2), while the scattering beam (C) was detected at an angle of 12.8°.[128]

When an electric field was applied to the cell, any particles moving through the measurement volume caused fluctuations in the detected light intensity, with a frequency proportional to the particle speed. This information was transmitted to a digital signal processor (4) by a detector (3), then further processed by a computer (5) running Zetasizer software to derive frequency spectrum data, facilitating the calculation of electrophoretic mobility and subsequently, the zeta potential.[128]

To ensure successful measurement, the intensity of scattered light within the cell had to fall within a specific range; otherwise, detector overload could occur. An attenuator (6) was employed to mitigate this issue by reducing laser intensity and, consequently, scattering intensity. For samples with minimal light scattering, such as very small particles or low-

concentration samples, the attenuator permitted increased light transmission to the sample. Conversely, for samples with higher light scattering, like large particles or high-concentration samples, the attenuator regulated light transmission by reducing intensity.[128]

Compensation optics (7) were integrated within the scattering beam path to address discrepancies in cell wall thickness and dispersant refraction, thereby ensuring the alignment of scattering beams.[128]

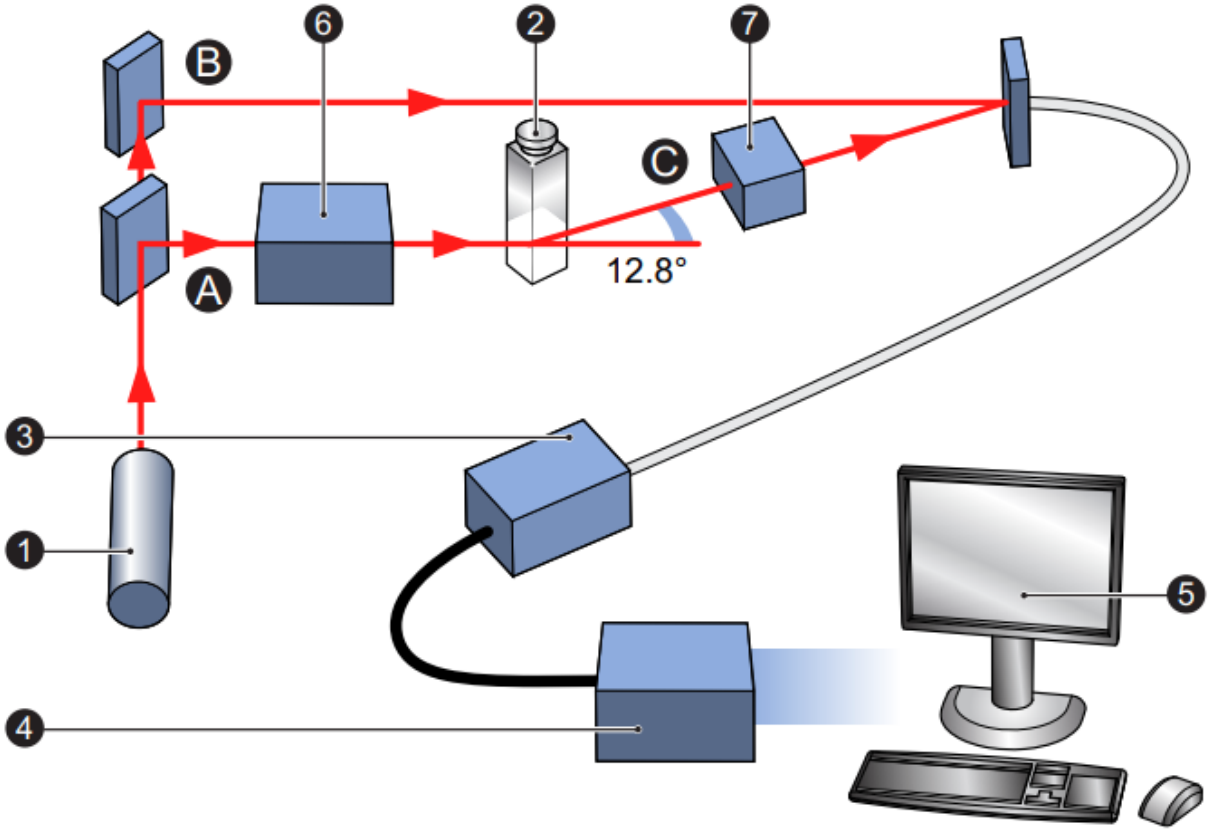



Figure 3.15: Operation of the Zetasizer Nano - Zeta potential measurements. (A) Incident, (B) Reference beam and (C) Scattering beam. 1 - Laser, 2 - Sample cell, 3 - Detector, 4 - Digital signal processor, 5 - Computer, 6 - Attenuator and 7 - Compensation optics.[129]

### 3.4.6 Data Analysis

The data analysis was conducted in the same manner as described in Section 3.3.6.

## 3.5 Surface Tension Measurement

### 3.5.1 Principle

Surface tension indicates how well or how poorly a liquid spreads over a surface. When formulating coatings, inks, or paints, the contact angle indicates how a modification to the ink or paint would affect its spreading over the solid surface. It also provides a strong indication of the performance of the product as well as the success of the process. Contact angle expresses the effects of surface tension, and can be readily measured as how a liquid interacts with a solid surface.[132] A contact angle is an angle formed by a liquid at the three-phase boundary where a liquid, gas, and solid intersect, illustrated in Figure 3.16.

Figure 3.16 shows a solid surface with a drop of liquid on it. The level of interaction between the solid and liquid is determined by the angle theta, known as the contact angle.

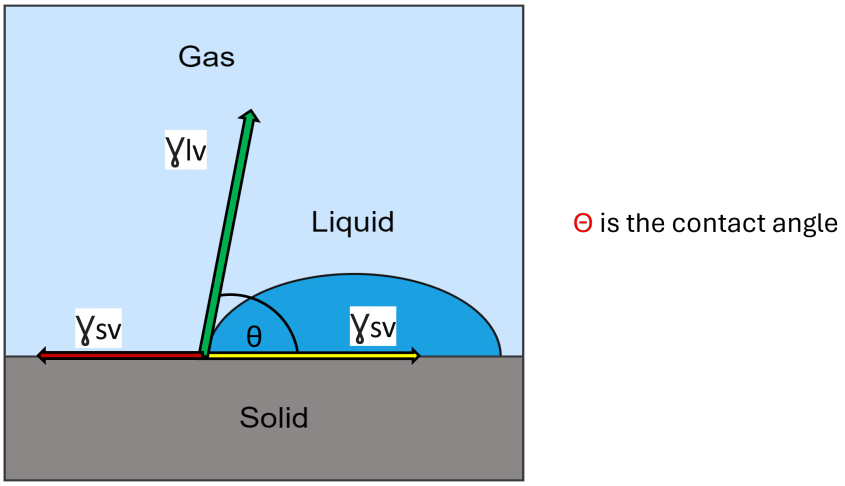



Figure 3.16: Water droplet interaction between solid, liquid and gas, showing surface energies. Red arrow indicates the phase boundary between solid and vapour interface, Green arrow indicates the phase boundary between the liquid and vapour interface and yellow arrow indicates the phase boundary between the solid and liquid interface.[132]

Figure 3.17, shows a drop that does not wet the surface and appears as a ball on a lotus leaf, with a contact angle of 180 degrees. This represents something that is completely non-wetting. Wetting refers to a liquid's ability to maintain contact with a solid surface. The smaller the contact angle, the better the wettability. Consequently, the higher the contact angle, the lower the wettability. Hence, no wetting indicates that the liquid would stay on the solid surface in droplet form, without spreading. In such instances, the liquid droplet can easily roll over the surface due to poor wettability and a high contact angle.[132,133]

An example of a non-wetting surface is the lotus leaf, depicted in Figure 3.17. The contact angle between the water droplet and the lotus leaf is much higher than 90 degrees, resulting in water droplets forming a nearly spherical shape. Conversely, when water is dropped on a piece of cotton fabric also shown in Figure 3.17, it forms a zero contact angle with the fabric and spreads out completely, demonstrating complete wetting. This phenomenon is attributable to surface tension; when water or any other liquid forms a spherical shape, it is

because water molecules in the liquid are attracted to each other. Surface tension is a result of the forces between molecules in fluids and between molecules and surfaces.[132,133]



Figure 3.17: Illustration of lotus leaf vs cotton fabric, showing a lotus leaf having a hydrophobic surface and the cotton fabric having a hydrophilic surface.

Water molecules can form hydrogen bonds with other water molecules around them. This attraction among water and other liquid molecules is known as cohesion, and the corresponding attractive force is termed cohesive force. In liquid water molecules tend to aggregate or form groups due to cohesive forces, each molecule is pulled equally in all directions by neighbouring molecules, resulting in a net force of zero. However, at the surface, there are no water molecules above them, allowing surface water molecules to group more effectively and form a stronger, tighter bond.[134]

This gives rise to a surface energy effect commonly discussed in terms of surface tension. Surface tension is the tendency of a liquid surface to minimise its surface area and thus surface energy enabling liquid molecules to maintain a spherical shape. When comparing liquids with high and low surface tension, the high surface tension liquid will form a high or large contact angle and remain in a spherical droplet form, whereas the low surface tension liquid will exhibit a low contact angle compared to the high surface tension liquid and tend to wet, spreading out on the solid surface as shown in Figure 3.18.[133]

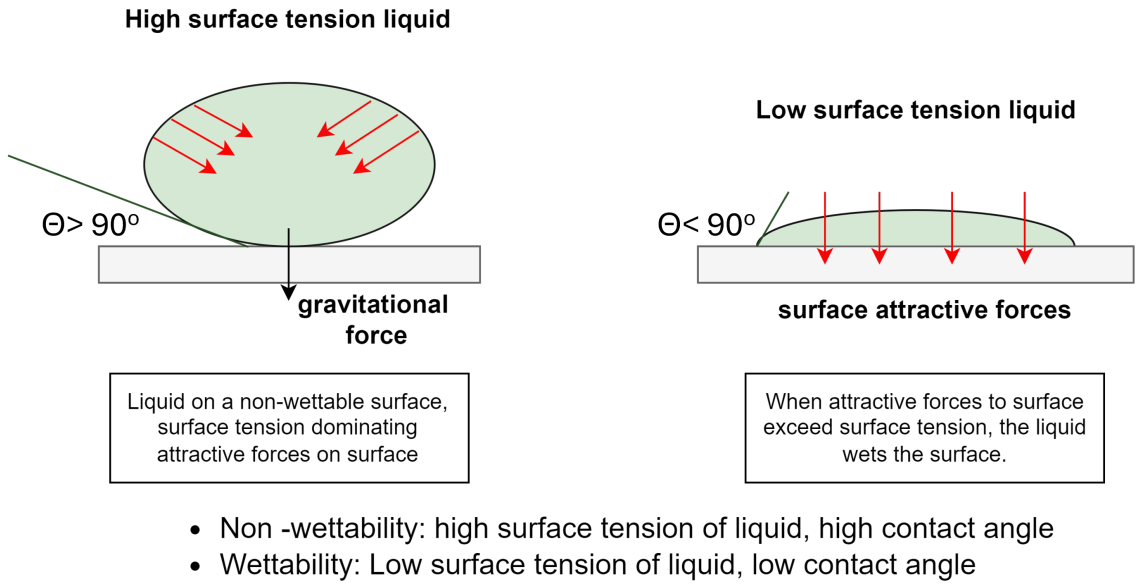



Figure 3.18: Surface behaviour of high surface tension liquid vs. low surface tension liquid, giving high and low contact angles respectively.

Fundamentally, contact angles are a function of the interactions of the surface tensions involved. When a droplet is in contact with a solid surface, three boundaries exist the solid, the liquid, and the vapour surrounding them, usually air, as depicted in Figure 3.20; there are three surface tensions, of the liquid against vapour; the solid against air vapour; and finally, the surface tension of the liquid against the solid. Figure 3.19 illustrates a force diagram at the point where all three phases met. The three arrows represent the force exerted by three interfaces: liquid-solid, liquid-vapour, and solid-vapour.[132–134]

If the droplet is in equilibrium, the forces are balanced, meaning the leftward force is equal to the rightward force. Several factors, such as surface roughness, impurities, functional groups on the surface, etc., affect the contact angle.

The force balance can be expressed in terms of surface tension and the contact angle through the Youngs equation shown in Equation 3.7 and Figure 3.19.

$$\gamma_{SV} = \gamma_{SL} + \gamma_{LV} \cos\theta \tag{3.7}$$

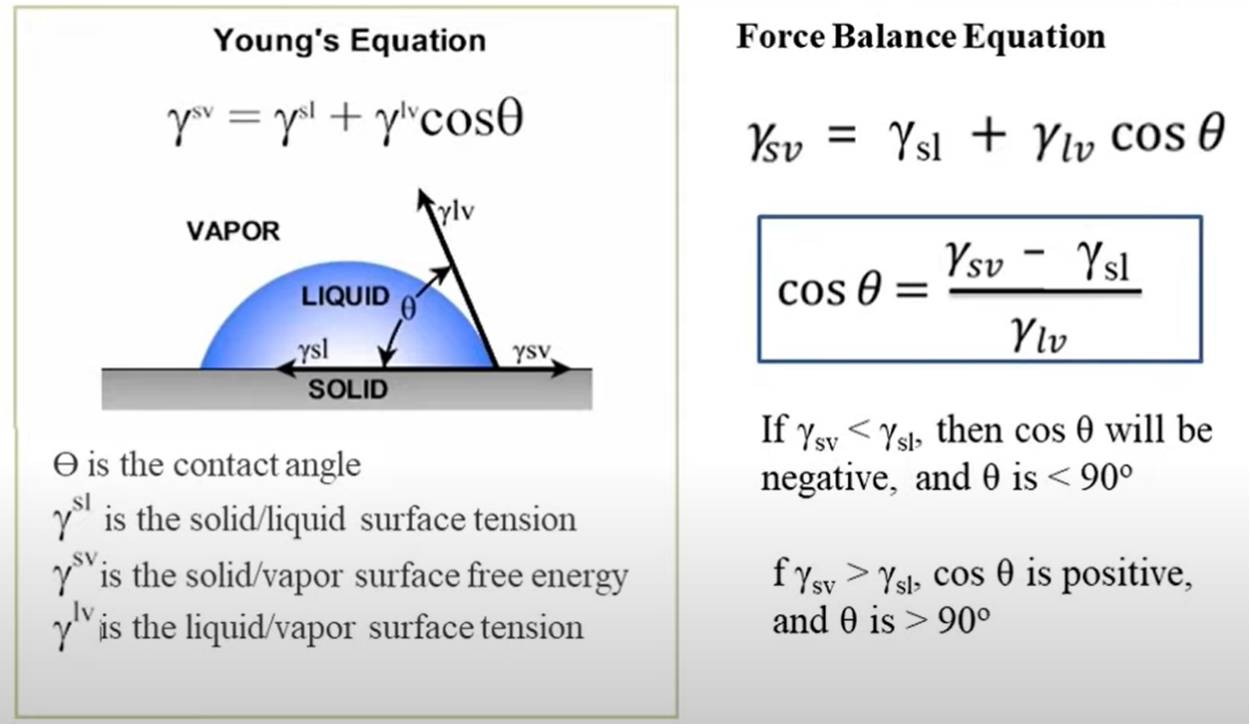



Figure 3.19: Illustration of a force balance can be written as $\gamma_{SV} = \gamma_{SL} + \gamma_{LV} \cos\theta$ known as the Youngs Equation.[132,133]

### 3.5.2 Data Interpretation

If fully wetting, a drop of liquid can spread out completely and cover the surface, denoted by a contact angle of zero degrees, representing complete wetting as shown in Figure 3.20. For perfect wetting, $\theta = 0°$, whereas for non-wetting, $\theta = 180°$. Typically, the contact angle falls between zero and 180 degrees: a contact angle less than 90 degrees denoted wetting, while one greater than 90 degrees indicated non-wetting, reflecting the nature of the surface. For instance, for water, if the contact angle is less than 90 degrees, the surface is hydrophilic; if greater, it is hydrophobic, as depicted in Figure 3.20. Additionally, if the

contact angle approaches the theoretical limit of 180 degrees, the surface can be considered super hydrophobic.

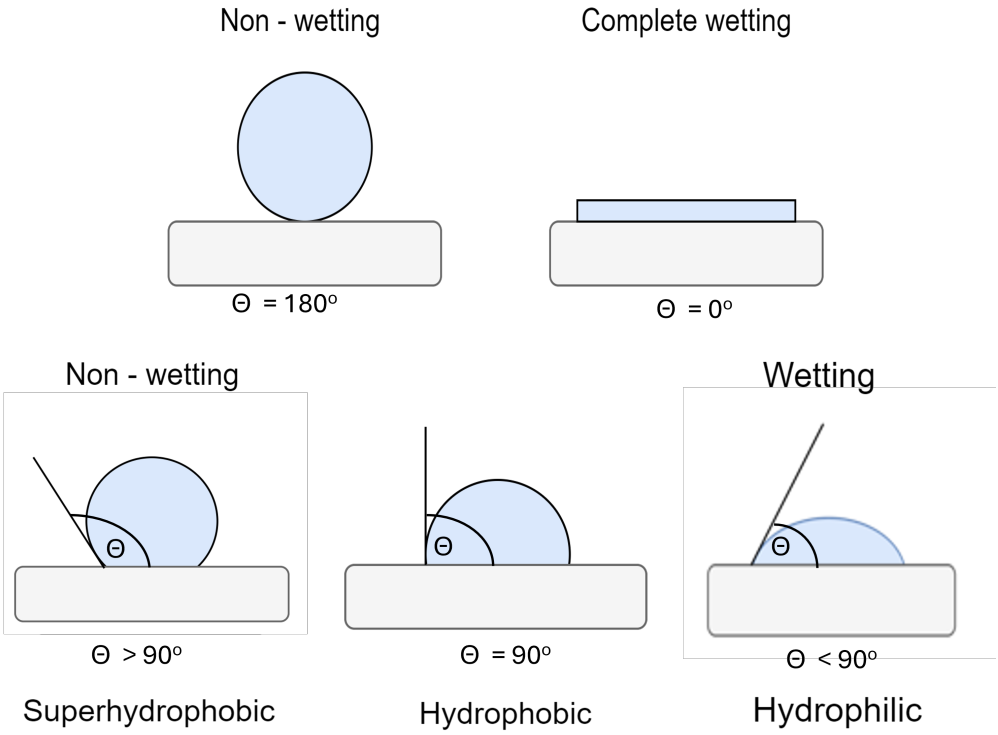



Figure 3.20: Illustration of different contact angle measurement scenarios for non-wetting and complete wetting along with their respective angles.

### 3.5.3 Limitations

Many factors influence the contact angle and wettability of the solid surface, including surface roughness, functional groups present on the surface, impurities, porosity, and surface energy. Surface roughness can cause variations in the measured contact angle because it affects the wetting behaviour of the liquid on the surface. If the surface is rough, the liquid might not be able to wet the surface uniformly, leading to variations in the measured contact angle. Surface contamination can alter the surface energy and wettability of the material being studied, affecting the contact angle measurements. For example, if the surface is

contaminated with a hydrophobic substance, it can reduce the surface energy and make the surface less wettable, increasing the measured contact angle.[135]

Contact angle measurements can be time-dependent because the contact angle might change over time due to factors such as evaporation or absorption of the liquid. For example, if the liquid slowly evaporates from the surface, the contact angle might increase over time as the liquid volume decreases. Hysteresis occurs when the advancing and receding contact angles differ due to differences in the energy required to create or break contact between the liquid and the surface.[136] An advancing contact angle is when the angle is formed by a liquid as it spreads outward on a surface when additional liquid is added. A receding contact angle is when the angle is formed by a liquid droplet as it retracts inwards on a surface when liquid is removed. This can occur when the surface is not perfectly smooth or when there are chemical or physical interactions between the liquid and the surface. Hysteresis could make it difficult to interpret contact angle measurements and can lead to errors in the calculated surface properties.[135]

Contact angle measurements can be affected by temperature because temperature changes can alter the surface energy and wettability of the material being studied. For example, as the temperature increases, the surface energy of some materials might decrease, making them less wettable and increasing the contact angle.[135]

### 3.5.4 Cleaning Method

The Glazed ceramic tiles used in this study were Utopia White Gloss Ceramic Wall Tile, Pack of 25, 100mm(L) 100mm(W) purchased from B&Q. The samples were cut by the physics workshop at the University of Birmingham into 1 cm squares so that the tiles could fit into the contact angle instrument and to carry out the measurement with ease. All the samples were first cleaned using the QCM cleaning method shown in section 3.1.5.

### 3.5.5 Experimental Setup

A static drop of deionised water was imaged on a pre-deposited coated substrate. A high-speed camera was used to capture a video of the droplet falling, forming and spreading. Measurements were carried out at room temperature for each surface measurement and an average of four readings were taken at different locations and reported.

To measure surface tension, a custom-built setup was employed. This setup involved directing light from a fibre optic light source from Dual Fiber Unit LED (Germany) through a Thor Labs (UK) DG20-600-MD light diffuser, which then passed to a camera from First Ten Angstroms (UK), as depicted in Figure 3.21.

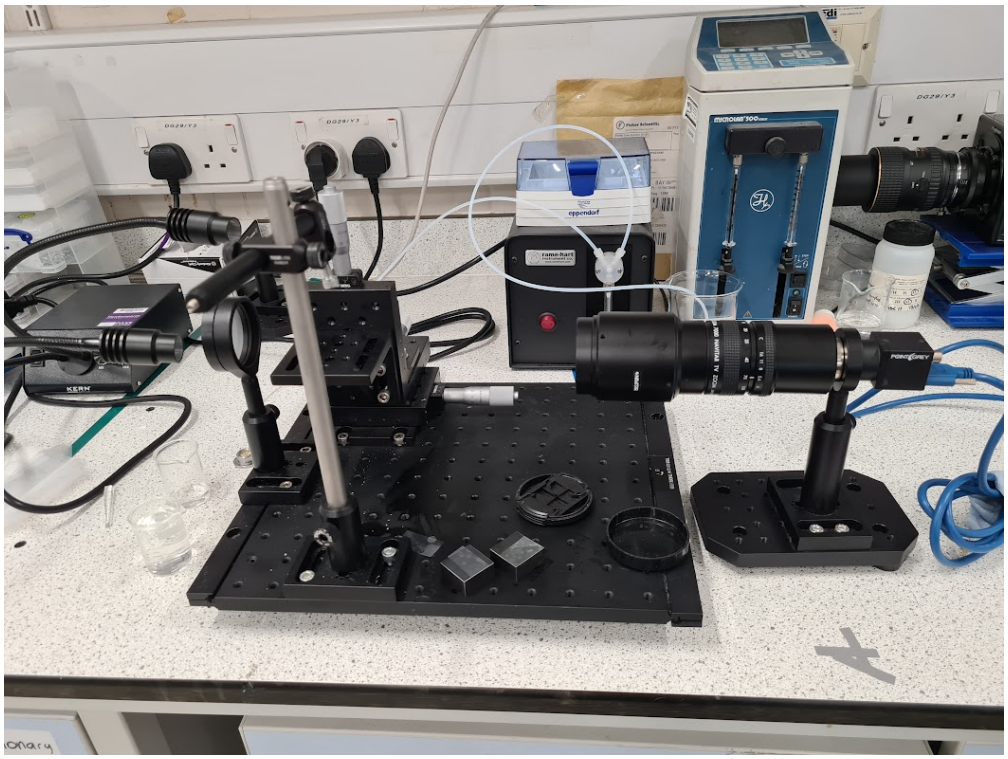


Figure 3.21: Image of surface tension setup.

To measure the surface tension, a syringe containing the solution under investigation was positioned between the light source and the camera. A 21 GA blunt-tipped needle was attached to the syringe. A specific volume of liquid was dispensed from the syringe, forming a droplet, which was captured in a photograph.

### 3.5.6 Data Analysis

To analyse the contact angle data, a Python-based software tool called PyDSA was utilised. Designed specifically for drop shape analysis, PyDSA enables the measurement of droplet properties when in contact with solid surfaces, such as contact angle, droplet volume, evaporation rate, and displacement velocity, all through an intuitive, user-friendly interface. Developed in Python, PyDSA employs the Qt5 framework to build its graphical interface, allowing users to interact with the software visually without requiring coding skills. Although PyDSA was not tailored exclusively for image analysis, it can be integrated with other Python libraries, such as OpenCV, or scikit-image, to conduct advanced image processing tasks. Examining the form of a droplet typically involves analysing an image to identify important characteristics such as the contact angle or overall droplet shape.

## 3.6 Flow Lubricating Solution for Household Toilets (FLuSHT)

### 3.6.1 Principle

The concept for this technique was inspired by Wang et al.[5] Its purpose was to assess the impact of different coatings on synthetic faecal matter. The setup was custom-built in-house using a 3D printer. This setup's principle was to replicate a real toilet flushing process while maintaining control over all associated parameters. An amount of synthetic faeces could be placed on a surface at an angle, and water onto and around it. The liquid flow required to displace the faeces could be measured, giving some quantification of parameters that could be varied the flow rate, deposition angle, tile coating, and water composition utilised for the measurements. The system replicated the flow dynamics of a toilet flush; using a peristaltic pump to generate the flow. A series of coatings were applied to the glazed ceramic tiles to study their effect on flushing efficiency and cleanliness.

In essence, the underlying concept of an open-channel toilet system for research revolves around furnishing a meticulously controlled experimental environment. This facilitates the exploration and comprehension of the intricate dynamics inherent in toilet flushing processes. Additionally, it enables the assessment of various design attributes, coatings, and flushing technologies in terms of their performance.

Figure 3.22 illustrates a side view of the FluSHT setup, indicating where the synthetic faecal matter was deposited onto the testing surface, also known as the coated glazed ceramic tile, as well as the holding pins for the adjustable movement of the substrate in question.

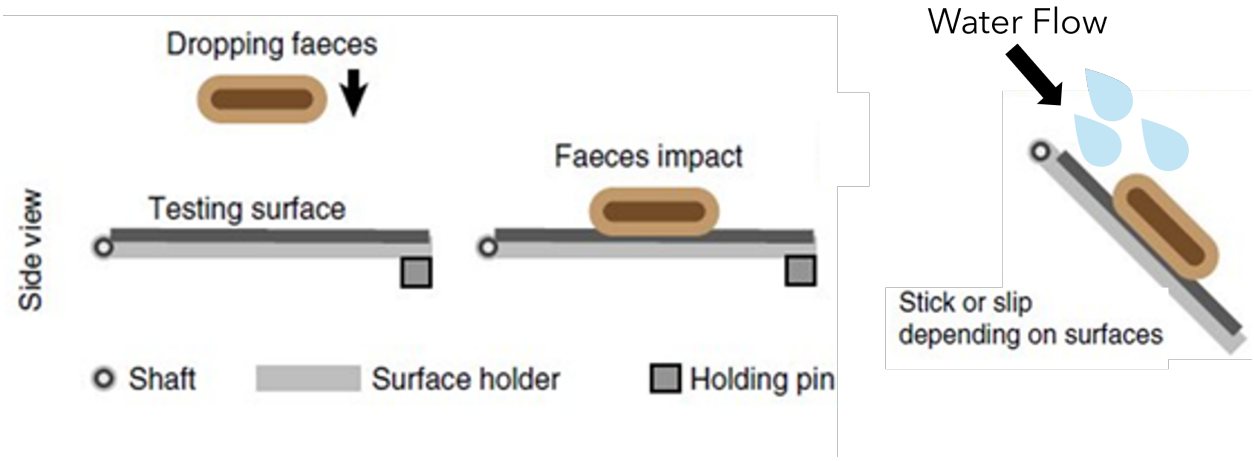



Figure 3.22: Side View of FLuSHT setup.

### 3.6.2 Data Interpretation

In analyses, the time it took for the synthetic faecal matter to traverse down the tile and the corresponding distance it covered was considered. From this, velocity in mm/s against the various polymer coatings was plotted. If one coating exhibits greater lubricity than another, it implies that faecal matter will slide down the tile more rapidly, thereby indicating a superior anti-fouling coating.

### 3.6.3 Limitations

There are several limitations inherent in constructing an in-house open-channel toilet system, despite its capacity to provide valuable insights into the toilet flushing process. The FLuSHt system does not consider the interaction between synthetic faeces and water, nor does it account for the bowl geometry or dynamics of waste removal. This system is highly simplified and, consequently, not designed to accommodate the complexities of an actual toilet. The FLuSHt system does not incorporate environmental factors that can influence toilet flushing, such as temperature, pH of the water, and humidity. These factors are significant in real-life

toilet flushing scenarios and can affect the process accordingly. Lastly, FLuSHT does not consider the variety of toilet materials used worldwide. Glazed ceramic tiles were used for this project, it's important to note that materials such as stainless steel are common in certain regions, such as America. However, the decision to use glazed ceramic tiles as the substrate was made at the project's outset, restricting the ability to test other substrate materials.

### 3.6.4 Cleaning Method

Before carrying out the FLuSHT measurements, the substrates had to be cleaned the following steps were used to clean the glazed ceramic tiles.

1. Rinse with IPA.
2. Rinse with tap water.
3. Rinse with DI water.
4. Sonicated in IPA for 180 seconds.
5. Air dried.
6. Polished with a microfiber cloth.
7. Rinse with tap water.
8. Rinse with DI water.
9. Sonicated in IPA for 180 seconds.
10. Rinse with tap water.
11. Rinse with DI water.

12. Sonicated in DI water for 180 seconds.

13. Air dried.

14. Left to adjust to room humidity.

15. Fully cover the tile with the chosen polymer solution.

16. Leave to dry and then test tiles' response in the FLuSHT measurement.

### 3.6.5 Experimental Setup

Firstly, it was important to identify the flow rate used for the FLuSHT setup; it had to simulate the flow rate of an actual toilet flushing. A flow rate of 5460 mL $min^{-1}$. was used during the FLuSHT measurements. Below is a clear outline of how this flow rate was achieved.

4-7 seconds (average toilet flush time)
5.5 seconds was the average flush time considered for the calculation
Average water used for toilet flushing = 5 Litres
5 Litres/5.5 seconds = 0.91 L/s X 1000 ml/L
= 910 mL/s x 60 min/s
54600 mL/min
= 5460 mL $min^{-1}$ (scaled down to the size of the tile)

Once the flow rate had been established, the next step was to organise the setup for the FLuSHT measurements. The placement of the deionised water, either above or below the rest of the components, affected the flow rate. After finalising the setup, the pump was calibrated by selecting multiple flow rates ranging from 250 mL/min to 2000 mL/min and measuring the amount of water dispensed over a minute. A graph of the flow rate versus the

volume in mL/min was plotted, yielding a linear relationship. This resultant flow rate was utilised throughout the FLuSHT measurements. Importantly, this flow rate closely simulated an actual toilet flushing system. Figure 3.4 illustrates the FLuSHT setup. Subsequently, the tile in question was placed into the FLuSHT device for investigation. The flow rate had to closely simulate that of an actual toilet flushing because the project's end application is for toilet bowls and for the coating to be applied in a toilet bowl.

Figure 3.23 shows the FLuSHT setup, clearly illustrating the FLuSHT device. This device was 3D-printed to ensure the tile could sit securely within it, allowing a blade of water to run over the tile. The angle of the device was also adjustable. A pump was used to generate the flow rate, and deionised water was utilised to control the water's composition.

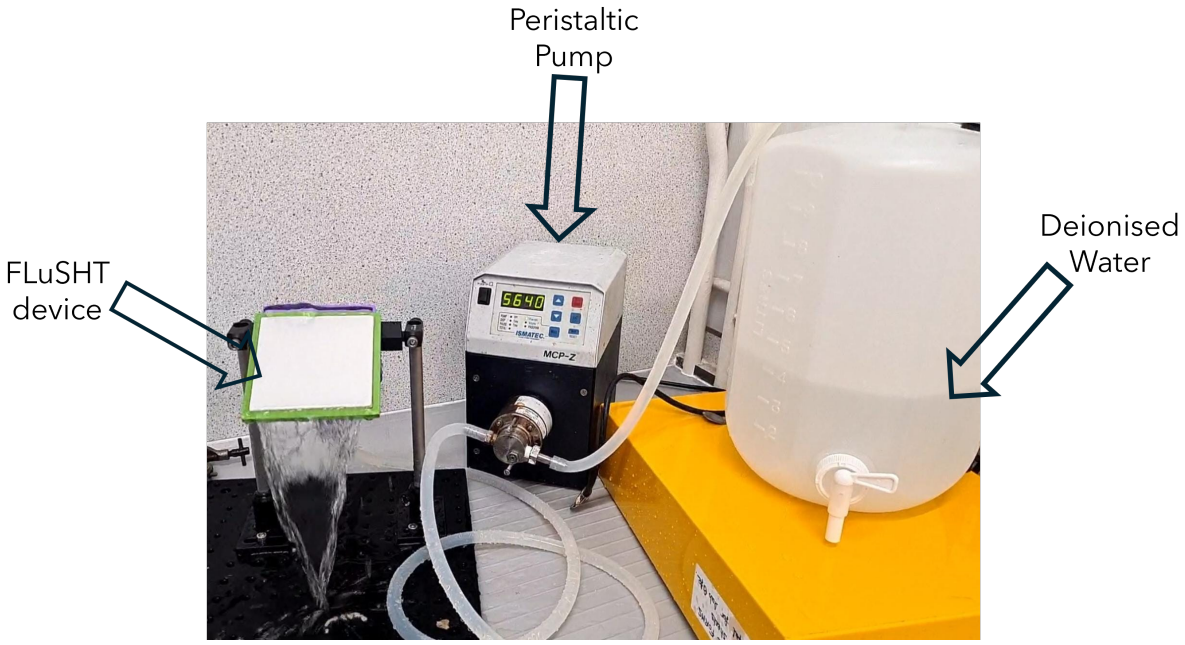



Figure 3.23: FLuSHt Setup, showing the FLuSHT device, peristaltic pump and the deionised water.

The recipe for synthetic faeces was originally obtained from the University of KwaZulu-Natal in South Africa.[5], The recipe comprises the components specified in Table 3.2 and their respective amounts. To enhance the representation of viscoelastic properties, the water

percentage was adjusted from 77.6% to 65%. The remaining ingredients were proportionally increased using a linear scale factor to maintain ingredient ratios. The components were mixed in a food processor to obtain the viscoelastic consistency replicating faecal matter.

Table 3.2: Composition of synthetic faeces.[5]

| **Chemical Name** | **Mass (g)** |
|---|---|
| Yeast | 227.4 |
| Water | 1300 |
| Psyllium Husk | 75.9 |
| Peanut Oil | 121.2 |
| Miso Paste | 75.9 |
| Polyethylene glycol | 84.96 |
| Calcium Phosphate | 75.9 |
| Cellulose | 38.73 |
| Total Weight (g) | 2000 |

Once the tiles were cleaned and coated with their respective dried polymer coatings, the synthetic faeces were prepared, and 10 grams of synthetic faeces were placed onto the tile in an oval shape with dimensions of 1cm in diameter. A weight of 164 grams was applied to the synthetic faeces for 5 seconds to ensure control over the system. The tile was then tilted to a 45° angle, as shown in Figure 3.5, and the pump was activated at a flow rate of 5640 mL/min. The time taken for the synthetic faeces to slide down the tile was recorded and converted to velocity. All measurements were video recorded.

### 3.6.6 Data Analysis

Python was used to analyse the data as well as plot the graphs. The full script is provided in Appendix Two, Section B.

## 3.7 Force Board

### 3.7.1 Principle

ForceBoard™, developed by Industrial Dynamics Sweden AB, located at Veddestavagen 19, 17562 Järfälla, Sweden, is a force measurement system tailored for laboratory and research use. This system can concurrently measure forces in both vertical and horizontal orientations, making it useful and versatile for various research and development testing settings.

Initially conceived for measuring coefficients of friction between different materials, the ForceBoard™ functions on a simple principle. The coefficient of friction (represented as $\mu$) between two materials or objects A and B is determined by the ratio of the frictional force (horizontal) to the normal force (vertical) both measured by the ForceBoard, as illustrated in Equation 3.8.[137]

$$\mu_{A,B} = \frac{F_{\text{friction}}}{F_{\text{normal}}} \tag{3.8}$$

### 3.7.2 Experimental Setup & Data Interpretation

In Figure 3.24a, the grey rectangular box represents a glazed ceramic tile, affixed to the instrument holder with double-sided sticky tape to ensure the stability of movement for the tile when interacting with synthetic faeces, depicted as an orange sphere. For consistency,

5g of synthetic faeces were weighed out for each measurement. As time progressed, the orange sphere depicted in Figure 3.24 as synthetic faeces underwent deformation due to the ceramic tile applying a vertical force of roughly 1 Newton upon contact. Stage a) showed the tile nearing but not yet touching the synthetic faecal matter. Stage b) depicted the tile making contact with the material, increasing the vertical force. Stage c) illustrated the vertical force diminishing as the tile moved away from the synthetic faeces, known as the pull-off force, a significant point of interest due to variations in tile coatings. Consequently, the pull-off force between the different coating types on the tile and the synthetic faecal matter was measured. Stage d) marked when the tile was no longer in contact with the material, requiring no additional force for separation. Stage d) mirrored stage a) as both indicated the absence of contact between the tile and the material, resulting in identical baseline conditions.

The random copolymer composition discussed in Chapter 5 (see Table 5.2 for the random copolymer composition and Figure 5.4 for the chemical structures of the compositions) was deposited onto the clean glazed ceramic tiles and left overnight to dry. Once the tiles were visibly dry, they were taped to the adjustable motor head via double-sided sticky tape, as shown in Figure 3.24b. Step a) in Figure 3.24b shows the glazed ceramic tile approaching the synthetic faeces but not yet touching the material; the coated side of the tile is facing the synthetic faeces. The velocity of the tile approaching the synthetic faeces was set to 10.05 mm $s^{-1}$, and the vertical force was set to 1 Newton (N). Step b) shows the tile in contact with the material and compressing it at a set force of 1 N. Step c) indicates the tile being pulled away from the synthetic faeces; this is when the adhesion force can be determined between the coated tile and the synthetic faeces at the point of separation. Step d) shows the complete detachment of the coated tile from the material at a velocity of 10.05 mm $s^{-1}$. Each random copolymer sample was repeated at least three times to ensure the reliability of the data obtained which was the adhesion between the coated tile and the synthetic faeces.

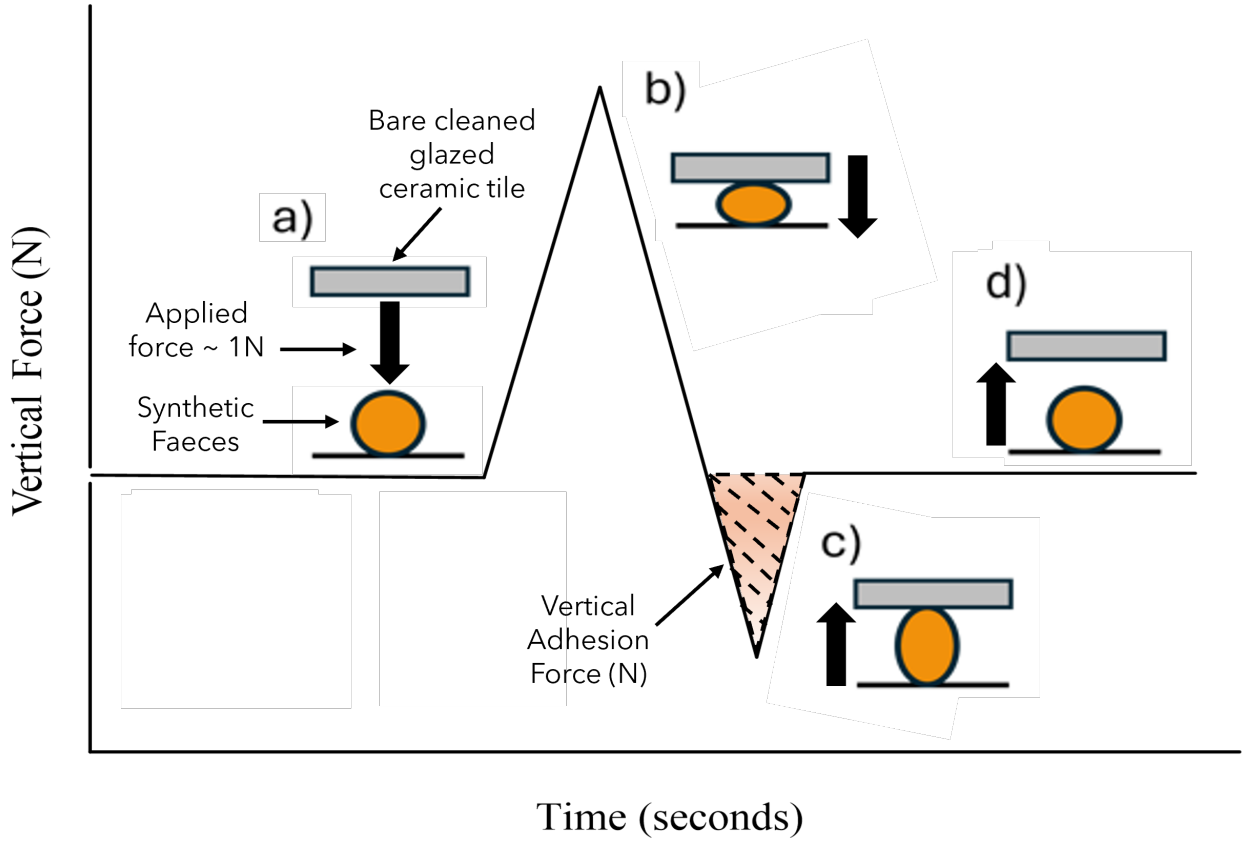



Figure 3.24a: The plot depicts the Vertical Force (N) against time (seconds) obtained from force board measurements. Step (a) shows the tile approaching synthetic faeces, step (b) indicates the tile in contact with synthetic faeces, step (c) illustrates the tile being pulled away from synthetic faeces, and step (d) marks the tile no longer in contact with the synthetic faeces.

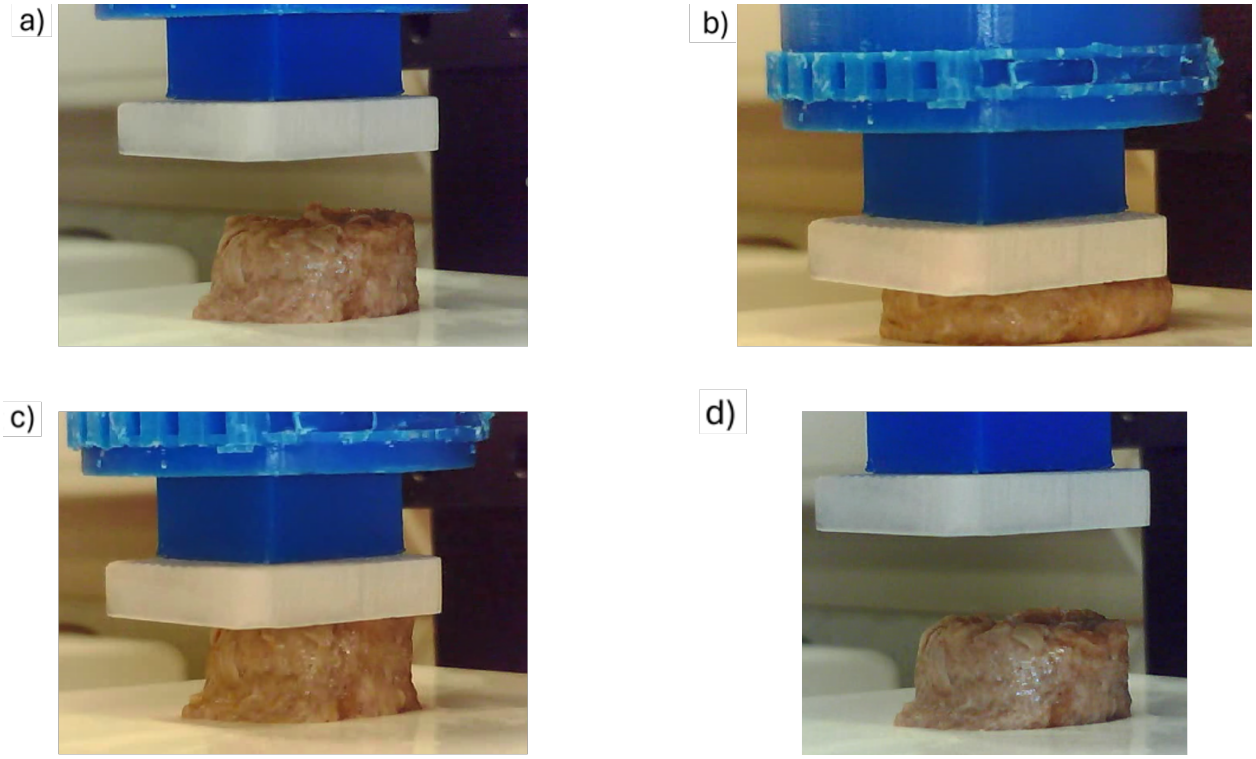



Figure 3.24b: Plot showing vertical force (N) against time (s) for the bare control tile and random copolymers.

The experimental setup for the synthetic faecal recipe can be found in section 3.6.5.

The software used to conduct the experiments included DAQFactory, which was used to save the data and take measurements, and Kinesis, which was used to control the movement of the tile to bring it into contact with the synthetic faeces and pull it away from the synthetic faeces.

### 3.7.3 Limitations

The force board can only accommodate large-scale setups for grams; it cannot carry out small-scale setups like atomic force microscopy for micrograms. The force board is thus not sensitive enough for small-scale experiments. Another limitation of the force board

was encountered while preparing synthetic faecal matter; maintaining consistency of the synthetic faeces was difficult, leading to fluctuations in dimensions. Consequently, ensuring constant force during the contact between the tile and the synthetic faeces was challenging, as the fluctuating dimensions affected the contact area. Additionally, the temperature and humidity of the lab were not controlled during the measurements, potentially resulting in inconsistency in the measurements

### 3.7.4 Cleaning Method

The Glazed ceramic tiles used from this study were Utopia White Gloss Ceramic Wall Tile, Pack of 25, 100mm(L) 100mm(W) purchased from B&Q. The samples were cut into 1 cm squares so that the tiles could fit into the force board instrument and to carry out the measurement with ease. All the samples were cleaned using the Innospec cleaning method as mentioned in section 3.6.4.

### 3.7.5 Data Analysis

Data was obtained from DAQFactory in an Excel file. This Excel file was then imported into Python to analyse and plot the data.

## 3.8 Conclusions

A series of experimental techniques have been identified and described to investigate polymer adsorption, with a focus on quantifying adsorption, analysing the kinetics involved, and assessing the impact on interfacial properties. These methods integrate nanoscale measurements with macroscale observations, aiming to establish a correlation between the properties

observed at the nanoscale and those at the full scale. The subsequent chapters will utilise these techniques to explore various combinations of polymers and interfaces.

Quartz Crystal Microbalance (QCM) was used to monitor the real-time adsorption and desorption of molecules. Chapters 4 and 5 discuss in detail the data obtained from the QCM. Atomic Force Microscopy (AFM) was employed to measure film thickness and adhesion of the block copolymers, which is the focus of Chapter 4. Dynamic Light Scattering (DLS) was used to assess particle size and polymer solution charge, as detailed in Chapter 5. Contact angle measurements were conducted to determine the surface energy of the deposited polymer on various substrates, which is discussed in Chapter 6. The FLuSHT test apparatus was constructed to observe polymer response to synthetic faeces in a real-world scenario, bridging the gap between microscopic and macroscopic testing, also covered in Chapter 6. Lastly, the force board test was employed to gauge the force necessary to detach the coated glazed ceramic tile from the synthetic faeces, as described in Chapter 6. Chapter 3 describes the methodology of the instruments used in this project, elucidating the principles, data interpretation, limitations, and experimental setup and data analysis of each instrument. Chapter 4 focuses on the effect of block copolymer architecture on its surface deposition.

# Chapter Four

# The Effect of Block Co-polymer Architecture on its Surface Deposition

## 4.1 Introduction

Chapter 2 examined and evaluated various antifoulant candidates and their effectiveness in preventing the build-up of foulants on biomedical devices. This background sets the stage for the current chapter, which focuses on identifying the most effective polymer among three block copolymers. The chapter aims to understand the molecular architecture responsible for surface adsorption and subsequent antifouling applications, as well as the methodologies used to investigate these properties.

This chapter aimed to explore the surface interactions between a negatively charged surface and a block copolymer composed of polyethylene oxide (PEO) and varying ratios of Poly(2-(dimethylamino)ethyl methacrylate) (PDMAEMA). Surface adsorption is primarily driven by electrostatic interactions for the materials used in this thesis, which provided the foundational knowledge for designing the block copolymers used in this chapter.

The aim of this research was to develop a surface protective additive designed to repel dirt and minimise soil attachment on coated surfaces, a functionality that has not been thoroughly studied on glazed ceramic surfaces. While extensive literature (see Chapter 2) supports PEG as an effective antifoulant for biomedical devices,[59–62] the focus here was on creating a similar solution for toilet bowl systems.

The primary objective of this chapter was to investigate the relationship between block copolymers and the negatively charged surface. QCM was used to monitor the mass adsorption of the block copolymer samples in real-time and at varying concentrations. QCM also helped to examine the adsorption kinetics of the block copolymer samples, which was crucial for understanding the speed and extent of polymer adsorption onto the surface. Additionally, BSA was introduced into the QCM system to evaluate the antifouling potential of the block copolymers. The thickness of the block copolymers on the sensor surface was measured using atomic force microscopy (AFM).

Previous research, discussed in Chapter 2, has demonstrated that polyethylene glycol (PEG), also known as polyethylene oxide (PEO), significantly contributes to antifouling. When exposed to an aqueous solution, PEG segments form a disordered structure that creates a hydration layer, repelling the foulant in question, for example, BSA.[138–141]
Poly(2-(dimethylamino)ethyl methacrylate) (PDMAEMA) contains a tertiary amine group that can protonate under acidic conditions, rendering the polymer positively charged and allowing it to adhere to anionic surfaces.[142] In this chapter, we investigate three block copolymers composed of PEO and PDMAEMA. Given PEO's effectiveness as an antifouling agent, the goal of this project was to develop an antifouling coating that can repel viscoelastic substances in toilets. Therefore, PEO was used in the block copolymer system, and PDMAEMA served as the anchoring segment of the block copolymer, adhering to the QCM sensor via electrostatic forces as discussed in Chapter 2.

It is hypothesised that as the ratio of the PDMAEMA segment increases in the block copolymer chain, the mass adsorbed onto the silicon dioxide sensor surface would also increase due to enhanced electrostatic interactions from the greater number of positively charged groups. This study examined both the mass and the number of molecules adsorbed onto the surface.

Through these experiments, we aimed to determine whether the block copolymers could effectively repel viscoelastic materials and minimise soil attachment on surfaces. By understanding the adsorption behaviour and surface interactions of the copolymers, we hoped to identify promising candidates for antifouling applications in toilet bowl systems.

### 4.1.1 Materials

The block copolymers used in this chapter came from Polymer Source (Dorval, Canada). Figure 4.1 presents the differences between the generated three-block copolymers, illuminating their molecular structures. Different ratios of the two monomers, ethylene oxide and 2-(dimethylamino)ethyl methacrylate, were combined to synthesise Poly(ethylene oxide-*b*-2-(dimethylamino)ethyl methacrylate) (PEO-*b*-PDMAEMA) via anionic polymerisation was used throughout this chapter.

Every molecule was created in 500 parts per million solutions. To do this, 0.125 g of the polymer was carefully weighed and placed into individual 500 mL Duran bottles. These bottles were then filled with deionised water. These starting solutions were used to produce different concentrations of 10, 50, 100, 150, 200, and 300 parts per million. After every solution was created in its container, 10 µL of 1M NaCl was added to reduce the electrostatic interactions between the charges in the solution. Figure 4.1 illustrates the chemical structures of the three-block co-polymers.

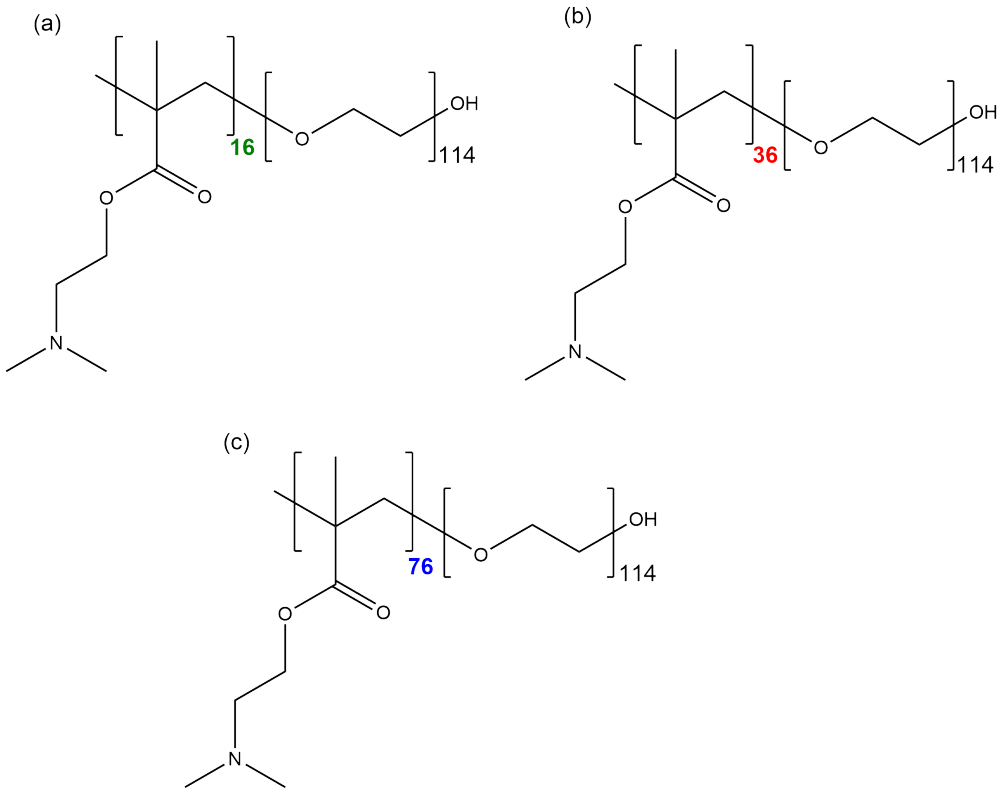



Figure 4.1: The chemical structures of the three-block co-polymers - PEO-*b*-PDMAEAMA (a) 5.0-*b*-2.5 (b) 5.0-*b*-5.6 and (c) 5.0-*b*-12.0. Numbers in colour show the repeat units of DMAEMA in the DMAEMA block.

To study the effect of molecular architecture on adsorption, three block copolymers, shown in Figure 4.1, were analysed in this chapter. Figure 4.2 illustrates a schematic representation of the PEO-*b*-PDMAEMA block copolymer structure and its adsorption on a silicon dioxide sensor. It was anticipated that the positively charged segment of the block copolymer would adhere to the negatively charged sensor, resulting in the PEO strands extending from the surface as depicted in Figure 4.2.

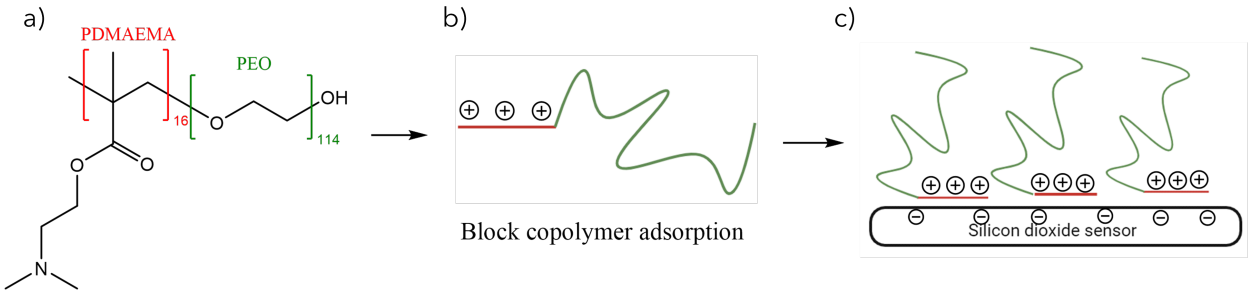



Figure 4.2: (a)Molecular structure of 5.0-*b*-2.5 (PEO-*b*-PDMAEAMA), (b) Schematic illustration of the block copolymer and (c) Schematic illustration of block copolymer adsorption onto the QCM sensor.

Table 4.1 illustrates the differences between the block copolymers tested here. The first column in the table specifies the ratio of each monomer in the block copolymer chain. For example, 5.0-*b*-2.5 indicates that PEO has twice the number of blocks in the chain compared to PDMAEMA. The table also displays the molecular weight of each block copolymer, obtained from the data sheet supplied by Polymer Source when purchasing the materials. PEO has a constant molecular weight of 5000 in all three block copolymers, while the molecular weight of PDMAEMA increases progressively down the column. Notably, in all three compounds, the PEO segment consistently outweighs the anchoring group, the PDMAEMA segment, shown in the last two columns of the table. The number of repeat units for each monomer was calculated by dividing each block's molecular weight by the repeat unit's molecular weight. The data sheet also provided the polydispersity index (PDI) of the block copolymers. Samples 5.0-*b*-2.5 and 5.0-*b*-5.6 had a PDI of 1.20, while sample 5.0-*b*-12.0 had a PDI of 1.30.

Table 4.1: Molecular weight and repeat units calculated for all three block copolymers.

| **Block Copolymers** | | | |
|---|---|---|---|
| **Mn x $10^3$ PEO-b-PDMAEMA** | **Molecular weight of each block** | **Repeat units of DMAEMA in DMAEMA block** | **Repeat units of PEO in PEO block** |
| 5.0-b-2.5 | 5000:2500 | 16 | 114 |
| 5.0-b-5.6 | 5000:5600 | 36 | 114 |
| 5.0-b-12.0 | 5000:12000 | 76 | 114 |

Figure 4.3 illustrates the structure of the materials. The red spheres represented the PDMAEMA molecules, also known as the anchoring molecules. These molecules possess a positive charge due to the tertiary amine being protonated under acidic conditions, which caused them to have a positive charge in solution. The blue spheres represented the PEO molecules within the block copolymer samples, referred to as the functional molecules. The structure illustrates the block copolymer at the substrate surface, as shown in Figure 4.3. Figure 4.3 shows the block copolymer structure, where blue spheres were followed by red spheres, rather than a random arrangement such as blue-red-blue-blue-red-blue-blue, which would indicate a random copolymer.

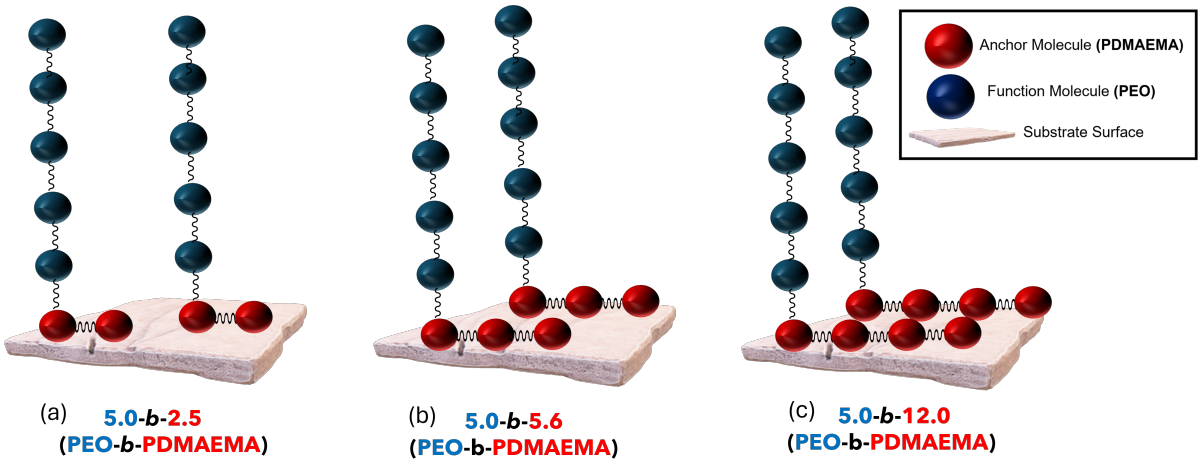



Figure 4.3: Illustration of the theoretical deposition of three-block co-polymers - PEO-*b*-PDMAEAMA onto the substrate surface: (a) 5.0-*b*-2.5, (b) 5.0-*b*-5.6, and (c) 5.0-*b*-12.0. Red spheres illustrate the anchoring molecule - PDMAEMA, and blue spheres illustrate the functional molecule - PEO. The white slab illustrates the substrate surface. The illustration is not an accurate depiction of the system but is intended to provide a conceptual layout of molecular adsorption.

## 4.2 Results & Discussion

### 4.2.1 Effect of varying concentration on surface adsorption

To study the effect of varying concentrations on surface adsorption, QCM was used to determine the mass adsorbed, adsorption kinetics, and binding energy of the three-block copolymer samples at varying concentrations. To obtain the mass adsorbed data from the QCM, deionised water was first injected into the system, followed by the block copolymer under investigation, and then deionised water again. Figure 4.4 illustrates a schematic representation of a typical QCM mass adsorbed experimental plot and the data acquisition process.

Further information can be found in Section 3.1.2.

Section A (blue region) in Figure 4.4 indicates the point of deionised water injection into the system, allowing the system to establish a baseline where it equilibrated and stabilised. This baseline facilitated accurately determining the mass absorbed data for the block copolymers. Region 1 shown in Figure 4.4 shows a region that consisted of 100 data points, from which an average was taken during the QCM measurement to act as a baseline. At the end of Section A, the block copolymer was injected into the system as shown in Figure 4.4.

Section B in Figure 4.4 shows the response of the QCM in the polymer adsorption process. At the start of Stage B, there is an increase in mass adsorbed, indicating that the polymer had adsorbed onto the sensor surface. Once the polymer molecules have equilibrated on the sensor surface, 100 data points were taken from Region 2 and averaged, yielding the mass adsorbed data (pre-wash) as indicated in Figure 4.4.

Finally, Section C shows the polymer desorption stage, where deionised water was reintroduced into the system to determine how much polymer remained on the sensor surface (post-wash) as indicated in Figure 4.4. To obtain the post-wash data, 100 data points were taken from Region 3 where the reading is essentially constant and averaged.

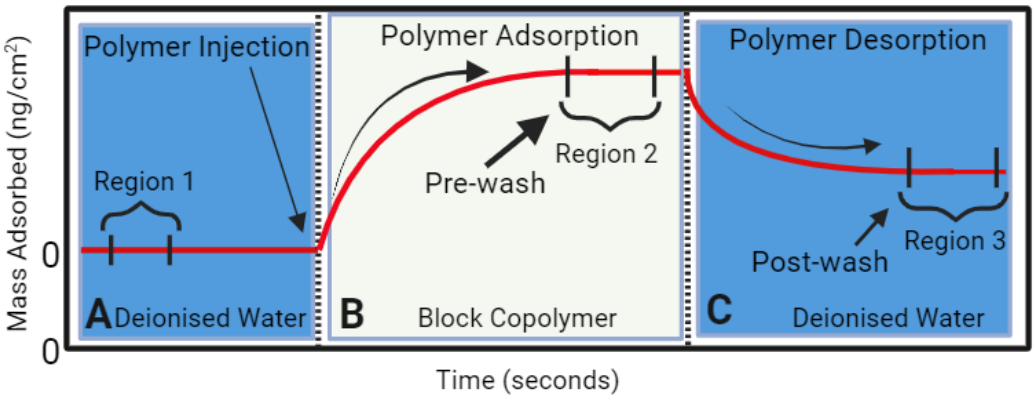



Figure 4.4: A typical QCM experimental plot of mass adsorbed versus time illustrated the different stages of the QCM measurement. Stage A involved deionised water, Stage B involved the block copolymer, and Stage C involved deionised water again.

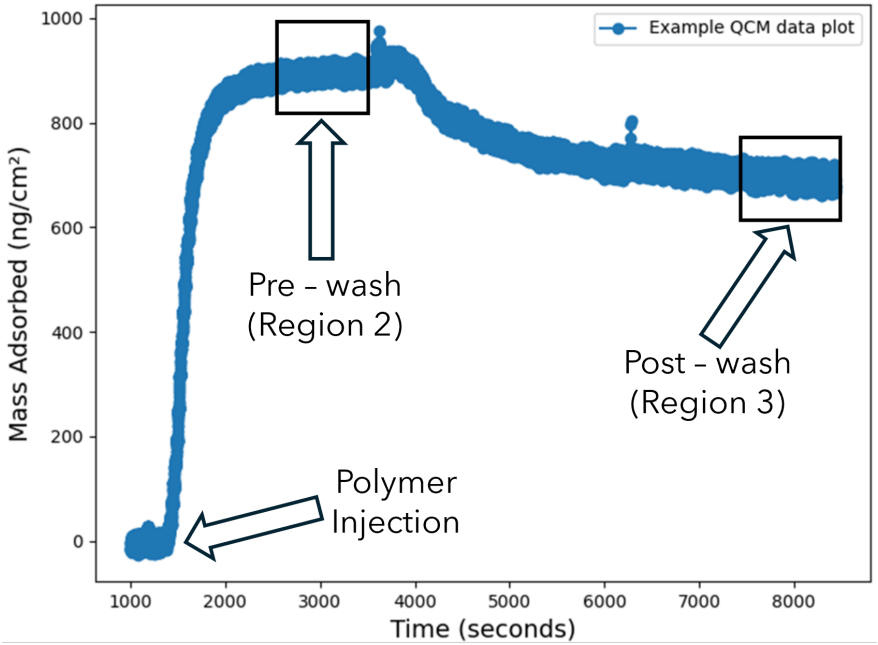



Figure 4.5a: Example representation of QCM plot, indicating polymer injection, pre-wash (Region 2) and post-wash (Region 3).

Figure 4.5a presents a real-time plot of a QCM (Quartz Crystal Microbalance) curve, depicting the mass adsorbed in ng/cm$^2$ against time in seconds. This figure illustrates the polymer injection phase and the pre-wash stage, designated as Region 2, which corresponds to the same stage shown in Figure 4.4. Additionally, Figure 4.5a includes the post-wash phase, labelled as Region 3, which is also consistent with the representation in Figure 4.4. The data displayed in Figure 4.5a has been utilised to calculate the results shown in Figure 4.5b.

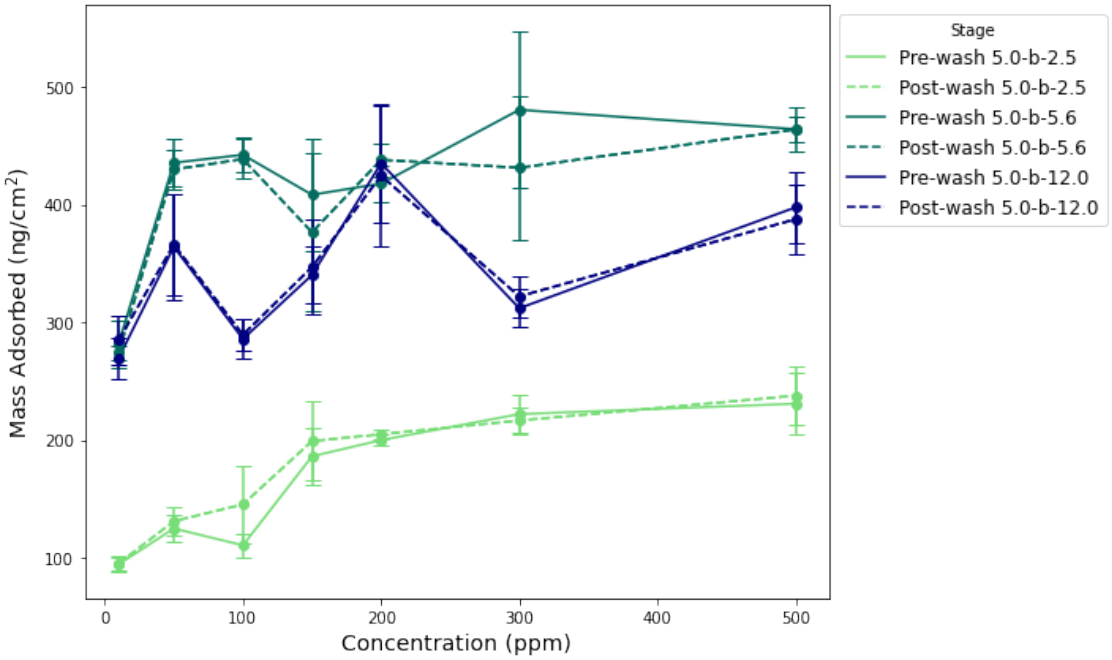



Figure 4.5b: Plot of mass adsorbed vs. concentration of the three-block co-polymers pre and post-deionised water wash. Error bars show the standard error over five repeats and the line is added to clarify trends.

Figure 4.5b displays mass adsorbed data in ng/cm$^2$ of the three block copolymers: 5.0-*b*-2.5, 5.0-*b*-5.6, and 5.0-*b*-12.0, both pre-and post-wash, against the concentration of the block copolymers in parts per million (ppm). Error bars depict the average standard error across five repetitions, and a trend line has been added to facilitate visual interpretation. It can be seen that sample 5.0-*b*-2.5 exhibited the lowest adsorption levels in both pre-and post-wash stages across all concentrations tested during the measurements. For 5.0-*b*-2.5, adsorption increased with concentration, reaching a plateau of approximately 200 ng/cm$^2$ after 300 ppm. Overall, the adsorption was much lower than that for 5.0-*b*-5.6 and 5.0-*b*-12.0. This can be attributed to the smaller PDMAEMA anchoring segment in 5.0-*b*-2.5, resulting in less adsorption onto the silicon dioxide surface, given that it contained only 16 repeat units of DMAEMA in the DMAEMA block, as shown in Table 4.1. It thus was expected that the block copolymer sample 5.0-*b*-2.5 would have the lowest amount of mass adsorbed onto

the QCM sensor, as it consisted of the lowest amount of PDMAEMA molecules within the chain. Consequently, there were fewer positive charges within the solution to adsorb onto the sensor, resulting in a lower overall mass being detected on the surface.

The block copolymer sample 5.0-*b*-5.6, which consisted of almost equal amounts of anchoring and functioning molecules (see Figure 4.3), adsorbed the highest amount onto the silicon dioxide surface, both pre-and post-wash, across all concentrations. Sample 5.0-*b*-12.0 consisted of 76 DMAEMA repeat units in the block. Block copolymer sample 5.0-*b*-12.0 exhibited maximum adsorption of approximately 415ng/cm$^2$ on the silicon dioxide sensor. However, block copolymer sample 5.0-*b*-5.6, at 300 ppm during the pre-wash stage, had maximum adsorption of approximately 475 ng cm$^{-2}$. Despite having a DMAEMA repeat unit of 36, this sample showed a maximum amount of adsorption across all the concentrations measured. There is a finite number of sites on the surface onto which the PDMAEMA can adhere. For the short chain (5.0-*b*-2.5, light green lines) system, more molecules can adhere to the surface per unit area, resulting in a larger number of moles adsorbed. Although 5.0-*b*-12.0 contains the highest number of DMAEMA repeat units, total adsorption is determined not only by the magnitude of surface interaction and the number of repeat units involved but also by the interfacial conformation and the occupation of adsorption sites.

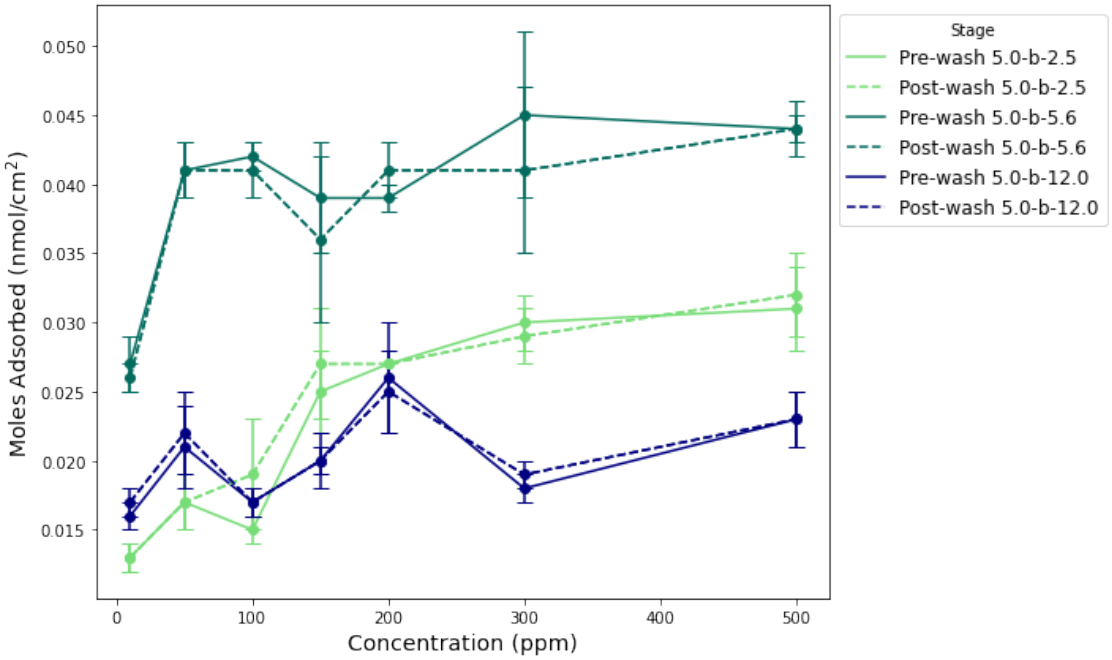



Figure 4.6: Plot of moles adsorbed vs. concentration of the three-block co-polymers pre and post-deionised water wash. Error bars show the standard error over five repeats and the line is added to clarify trends.

Figure 4.6 displays data of Figure 4.5b replotted in terms of the moles adsorbed in nmol cm$^{-2}$ of the block copolymers as a function of their concentration in ppm for the pre and post-wash. A trend line was added to improve the visualisation of patterns, while the error bars represent the average standard error derived from five independent repetitions.

Notably, when 5.0-*b*-5.6 was contrasted with the other two block copolymer samples, it showed the highest moles adsorbed across all concentrations in Figure 4.6. Conversely, the block copolymer sample with the least moles adsorbed onto the sensor surface was 5.0-*b*-12.0. This behaviour may be explained by the high number of repeat units in the anchoring segment of the block copolymer, as shown in Table 4.1, resulting in an extended PDMAEMA section. Consequently, PDMAEMA maximised its spatial occupancy as it interacted with the surface, reducing the ability of new molecules to adsorb.

Although in Figure 4.5b the block copolymer sample 5.0-*b*-12.0 exhibited a relatively high amount of mass adsorbed onto the sensor surface, Figure 4.6 indicates that in terms of moles adsorbed, it adsorbed the least. It was anticipated that as the PDMAEMA anchoring segment increased, both the mass and moles adsorbed onto the surface would increase linearly due to more electrostatic interactions between the PDMAEMA positive segment and the negatively charged sensor surface. However, with more PDMAEMA in the chain, there was less available space for the chains to adsorb onto the surface, leading to competition for space and ultimately resulting in less overall adsorption onto the sensor. For sample 5.0-*b*-12.0, the molecules adopt a train-like conformation at the interface, occupying a larger surface area compared to the other block copolymers, such as 5.0-*b*-2.5, due to fewer active sites available for adsorption. This is shown schematically in Figure 4.3.

As the pre-wash data (indicated in section B in Figure 4.4) represents the stage before the final rinse of deionised water onto the sensor's surface, the post-wash data (indicated in Section C) involves deionised water washing over the surface of the sensor. Figure 4.5b shows that, for all pre-wash and post-wash data, there was no statistical difference as the data overlapped in some places, especially for 5.0-*b*-2.5, indicating that the surface had been fully saturated. Overall, there was minimal removal of the block copolymer samples during the post-wash stage, suggesting that the polymers were not removed from the surface, resulting in physisorption of the polymers rather than chemisorption.

### 4.2.2 Effect of varying concentration on adsorption kinetics

To study the effect of varying concentrations on adsorption kinetics, QCM was used to estimate the adsorption kinetics of the block copolymers. The Langmuir isotherm equation, shown in Equation 4.1, was employed to obtain the first-order rate constants, as depicted in Figure 4.8. It is crucial to determine the adsorption kinetics for the block copolymers at different concentrations to achieve part of the project's aim. This determination was

important to identify which block copolymer, and at which concentration, reached the sensor surface most rapidly. This information is vital for Innospec, as it would inform the decision on which polymer to proceed with and at what concentration. Ideally, the aim was to identify a polymer that stays on the surface, as quantified by the Sauerbrey equation and a polymer that quickly adsorbs onto the surface, as quantified by the Langmuir isotherm equation. Further information on Langmuir isotherm equation can be found in Chapter 3, section 3.1.6.

The data in Figures 4.5 and 4.6 demonstrate that adsorption is irreversible. If a Langmuir-type process is assumed, i.e., that there are an infinite number of adsorption sites on the surface, then the deposition will follow Langmuir adsorption kinetics. The rate of formation of the monolayers can be expressed as:

$$\frac{d\theta}{dt} = k_a(1-\theta)C - k_d\theta \tag{4.1}$$

where $\theta$ is a dimensionless quantity representing the fraction of available sites that have reacted (or equivalently, the fraction of a monolayer formed), $C$ is the concentration of the block copolymers in the solution, and $k_a$ and $k_d$ are the rate constants for the adsorption and desorption processes, respectively.

Integration of equation 4.1 leads to:

$$\theta(t) = \frac{C}{C + \frac{k_d}{k_a}}\left(1 - e^{-(k_aC + k_d)t}\right) \tag{4.2}$$

Setting:

$$k_{obs} = k_aC + k_d \tag{4.3}$$

and

$$k' = \frac{C}{C + \frac{k_d}{k_a}} \tag{4.4}$$

results in the equation:

$$\theta(t) = k'\left(1 - e^{-k_{obs}t}\right) \tag{4.5}$$

To determine the values of $k_{\text{obs}}$ and $k'$, the fractional coverage $\theta$ is measured as a function of time $t$ and this experimental data is fitted to Equation 5. By repeating the experiment at different block copolymer concentrations and plotting $k_{\text{obs}}$ against $C$, a line is obtained with a slope of $k_a$ and a y-intercept of $k_d$ (Equation 3).

Figure 4.7(a) illustrates a typical QCM experimental plot of mass adsorbed in ng cm$^{-2}$ against time in seconds. Both $q_e$ (equilibrated mass adsorbed) and $q_t$ (increase in adsorption, purple dotted line) are indicated in Figure 4.7(a). Once these values were obtained, the logarithm of $q_e - q_t$ was calculated and plotted against time in seconds, as shown in Figure 4.7(b). This plot indicated a linear relationship. The equation of the straight line, depicted as a green dashed line in Figure 4.7(b), is provided as an example to explain how the kinetics data were obtained.

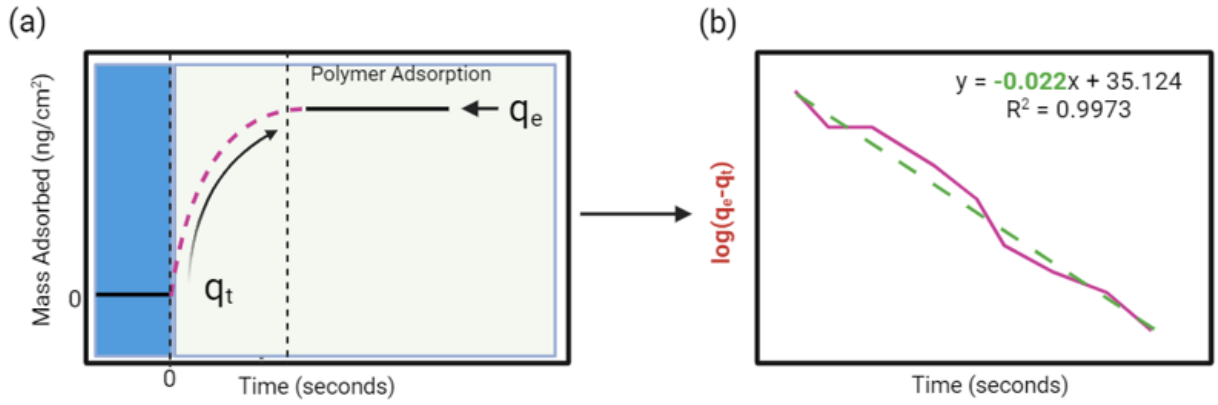



Figure 4.7: a) A typical QCM experimental plot of mass adsorbed versus time, illustrating the stage of polymer adsorption. b) Applying $\log(q_e - q_t)$ to the 'climb' section of the plot (a) to obtain the gradient of a straight line.

Once the gradient of the straight line was obtained, it was used in Equation 4.6. By rearranging the equation, the first-order kinetics rate was determined.

$$\begin{array}{ccccc} \log(q_e - q_t) & = & \log q_e & - & \frac{k_{\text{obs}}}{2.303} t \\ \downarrow & & \downarrow & & \downarrow \\ y & & c & & mx \end{array} \tag{4.6}$$

**Step 1:** The maximum point of adsorption was identified, and this value was subtracted from every single point on the incline in Figure 4.7 (a) to obtain $q_e - q_t$.

**Step 2:** The values of $\log(q_e - q_t)$ were plotted against time in seconds.

**Step 3:** The gradient of the resulting line was determined.

**Step 4:** Using the equation

$$m = -\frac{k_{\text{obs}}}{2.303},$$

the gradient $m$ was fitted to the line.

**Step 5:** Given that

$$-0.022 = -\frac{k_{\text{obs}}}{2.303},$$

it was found that

$$k_{\text{obs}} = 0.051\,\text{s}^{-1}.$$

Figure 4.7 shows how the data is obtained: the plateau gives the mass adsorbed at full occupation of sites (i.e. $\theta = 1$) and that at time t gives $\theta_t$. Figure 4.8 shows a plot of the first order rate constants ($s^{-1}$) obtained by fitting the Langmuir isotherm equation (see section 3.1.6. equation 3.2) to the change in mass adsorbed data vs. time in seconds against the concentration of block copolymers (ppm) of 5.0-*b*-2.5 (light green), 5.0-*b*-5.6 (green), and 5.0-*b*-12.0 (dark blue) with their respective trend lines. The plot shows that irrespective of concentration, the block copolymer sample 5.0-*b*-2.5 exhibited similar adsorption kinetics across all concentrations from 10 to 500 ppm. This indicates that as the concentration increased for 5.0-*b*-2.5, with molecules within the solution, adsorption occurred at the same

rate onto the silicon dioxide surface regardless of concentration. The block copolymer sample 5.0-*b*-5.6 displayed an increase in adsorption constant as concentration increased, suggesting that as the concentration increased, the rate of adsorption also increased across all concentrations from 10 to 500 ppm. As the concentration of 5.0-*b*-5.6 increased, it meant that there was more of the PDMAEMA segment, which was adsorbing rapidly onto the silicon dioxide surface. Lastly, the block copolymer sample 5.0-*b*-12.0 exhibited an increase in adsorption kinetics from 300 to 500 ppm, with the adsorption kinetics constant increasing from 0.0105 $s^{-1}$ to 0.0487 $s^{-1}$. Below 300 ppm, the adsorption kinetics increased very slightly from 10 to 200 ppm, indicating that as the concentration increased from 10 to 200 ppm, the adsorption kinetics for 5.0-*b*-12.0 also increased. This may be due to the adsorption of the PDMAEMA segment (anchoring group) increasing with concentration. Additional experimental data are required to thoroughly assess whether the materials conform to the expected Langmuir behaviour, as outlined in Equation 3.2. This need is particularly evident for the 5.0-*b*-2.5 sample, where the rate constant remains unchanged despite variations in concentration. This inconsistency suggests a potential deviation from the Langmuir adsorption model, underscoring the necessity for further investigation to determine the applicability of this theoretical framework to the materials under study.

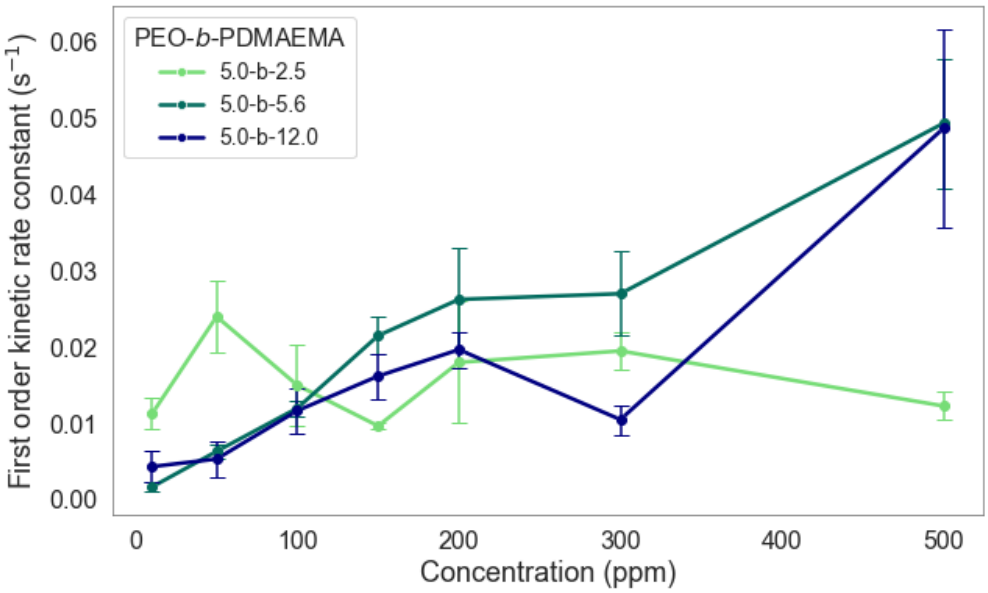



Figure 4.8: Plot of first-order rate constant ($s^{-1}$) against concentration (ppm) of 5.0-*b*-2.5 (light green), 5.0-*b*-5.6 (green) and 5.0-*b*-12.0 (dark blue) with their respective trend lines. Binding energy was obtained by utilising the trendlines and equation 4.1.

Figure 4.9 depicts the relationship between first-order kinetics rate constant and mass adsorbed for three different types of PEO-*b*-PDMAEMA block copolymers: 5.0-*b*-2.5, 5.0-*b*-5.6, and 5.0-*b*-12.0. The data is divided into two stages: "Pre-wash" and "Post-wash," represented by circle and square symbols respectively.

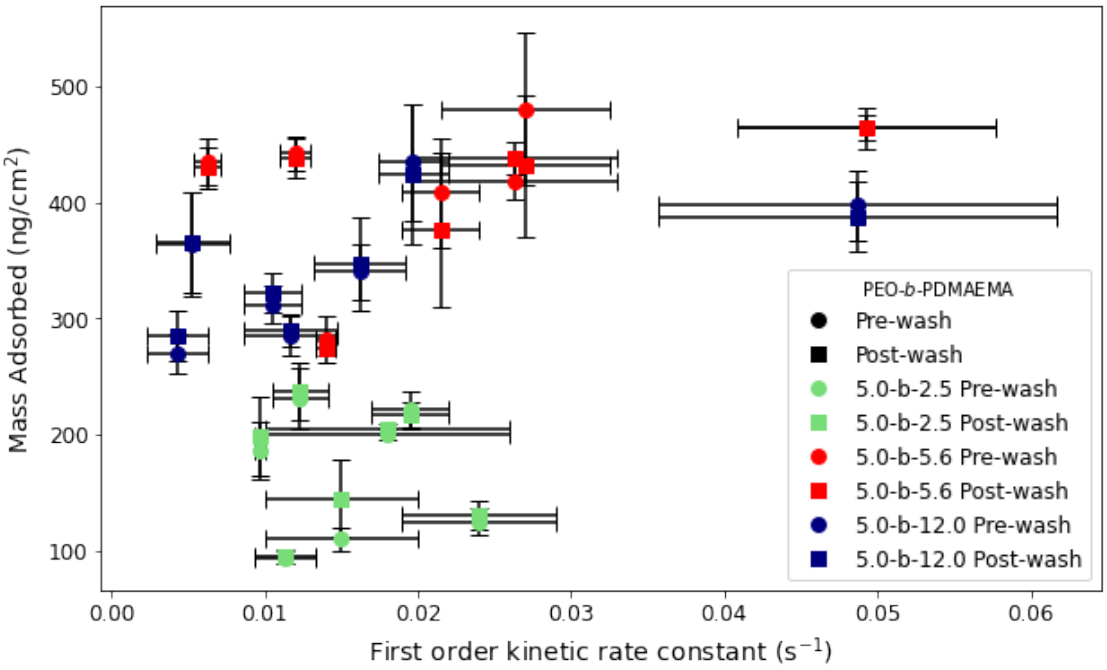



Figure 4.9: Correlation between the first-order kinetic rate constant ($s^{-1}$) and mass adsorbed (ng/cm$^2$) for PEO-*b*-PDMAEMA samples. The plot shows pre-wash (circle symbols) and post-wash (square symbols) data for three block copolymer compositions: 5.0-*b*-2.5 (green), 5.0-*b*-5.6 (red), and 5.0-*b*-12.0 (blue). This highlights the effect of washing and polymer composition on adsorption behaviour and kinetic properties. Note that a colour change has been implemented to emphasise the spread of data for clarity.

From the plot, it is evident that there is no real general trend of increasing mass adsorbed with increasing rate constant across all samples. However, there are noticeable variations between the pre-wash and post-wash stages, which are crucial for understanding the effect of the washing process on the adsorption behaviour of the copolymers.

For the 5.0-*b*-2.5 (green) sample, both pre-wash and post-wash data points (light green) are clustered towards the lower end of the rate constant spectrum, with mass adsorbed values ranging from approximately 100 to 250 ng/cm$^2$. There is little reduction in mass adsorbed post-wash, indicating that the washing process does not affect the adsorption stability of

this copolymer.

The 5.0-*b*-5.6 sample (red) shows a broader distribution across the rate constant range. Pre-wash data points are scattered between 275 and 450 ng/cm$^2$, while post-wash data points are less scattered and slightly lower in rate constant, suggesting a moderate reduction in mass adsorbed after washing.

For the 5.0-*b*-12.0 sample (blue), pre-wash data points show a significant spread with higher mass adsorbed values, up to 450 ng/cm$^2$. Post-wash data points also exhibit a wide distribution but generally show a slight decrease in mass adsorbed, particularly at higher adsorption kinetics values.

Figure 4.9 highlights distinct adsorption behaviours and the impact of the washing process on different PEO-*b*-PDMAEMA block copolymers. The 5.0-*b*-2.5 sample demonstrates the most significant reduction in mass adsorbed after washing, indicating lower stability of adsorption. This suggests that the 5.0-*b*-2.5 copolymer may not be as effective in applications requiring high adsorption stability post-wash.

The 5.0-*b*-5.6 sample shows a moderate reduction in mass adsorbed post-wash, with a more consistent distribution of data points. This indicates a relatively stable adsorption behaviour with moderate resistance to washing, making it a potentially better candidate for applications where some degree of post-wash stability is required.

The 5.0-*b*-5.6 sample exhibits high adsorption values pre-wash and retains relatively high mass adsorbed values post-wash. The high mass adsorbed values indicate a strong adsorption capacity and good post-wash stability. This suggests that the 5.0-*b*-5.6 copolymer could be the most suitable for applications demanding high adsorption performance and stability after washing.

### 4.2.3 Binding Energy

Figure 4.10 shows a plot of first-order adsorption constant versus concentration, fitted to the equation of a straight line. This was done to determine the binding energy of the block copolymer samples using equations 4.1 and 4.2. As illustrated in Figure 4.6, the equation of a straight line ($y = mx + c$) allowed the values of $K_a$ and $K_d$ to be obtained from the relationship between m and c, giving $k_e q$ as shown in equation 4.6. The results of the reaction rate calculations, the equilibrium constant shown in Figure 4.1, and the free energy of adsorption shown in Equation 4.2 were utilised to obtain the binding energies of the block copolymers.

Data for the block copolymer sample 5.0-*b*-2.5 showed that the Langmuir model for adsorption kinetics did not show the expected linear relationship with increasing concentration. Therefore, modifying the mechanism and applying a different equation to fit the data might have been necessary. For the sake of this study, it was assumed that the binding energy was low for the block copolymer 5.0-*b*-2.5 and it was not considered when comparing the binding energies among the block copolymers. The results of 5.0-*b*-2.5 confirm that the surface adsorption is independent of the concentration as seen in Figure 4.8.

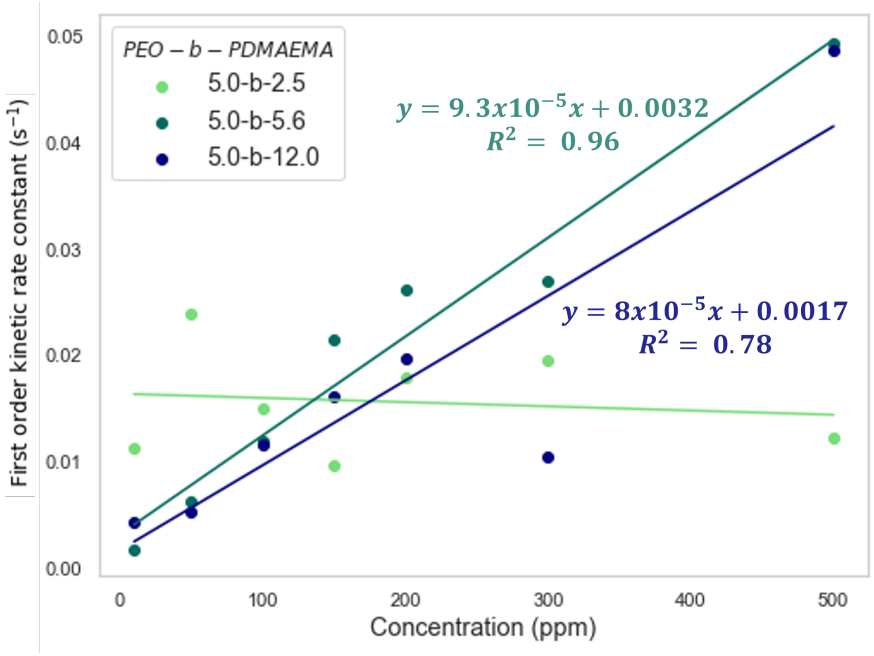



Figure 4.10: Determination of binding energy for 5.0-*b*-2.5 (light green), 5.0-*b*-5.6 (green) and 5.0-*b*-12.0 (dark blue) also the relationship of a straight line for 5.0-*b*-5.6 and 5.0-*b*-12.0 is illustrated.

The adsorption process can be considered as an equilibrium one, from equation 4.1. The equilibrium constant for absorption is

$$k_{\text{obs}} = \frac{k_a}{k_d} \tag{4.7}$$

and this can be written in terms of the free energy change $\Delta G$ for the process

$$\Delta G = -RT \ln k_{\text{obs}} \tag{4.8}$$

where:

- $R$ is the universal gas constant ($8.314\,\text{J}\,\text{mol}^{-1}\,\text{K}^{-1}$),

- $T$ is the absolute temperature in Kelvin, here 298 K.

Utilising Figure 4.6 and equations 4.8, the binding energy for block copolymer samples 5.0-*b*-5.6 and 5.0-*b*-12.0 was determined, obtaining Gibbs free energy values of 8.8 kJ/mol and 7.5 kJ/mol, respectively. These positive values suggest desorption is slightly favoured in the process. Block copolymer, 5.0-*b*-12.0 attained a Gibbs free energy only slightly lower than the 5.0-*b*-5.6.

### 4.2.4 Effect of foulant on block co-polymer

Figure 4.11 shows the effect of adsorbing Bovine Serum Albumin (BSA) on the QCM sensor surface established by adsorbing the block copolymers. In Region 1 of Figure 4.11, from 100 to 2230 seconds, the block copolymers were introduced into the system. Once they reached the sensor surface, there was an increase in mass adsorbed onto the surface, indicated by a change in the QCM signal as discussed in the previous sections. 5.0-*b*-2.5 (light green line) exhibited the lowest mass adsorption onto the surface, followed by 5.0-*b*-12.0 (dark blue line), with 5.0-*b*-5.6 (green line) exhibiting the highest amount of mass adsorbed onto the surface. Polymer injection occurred at approximately 100 seconds, and polymer adsorption onto the surface took place at approximately 200 seconds.

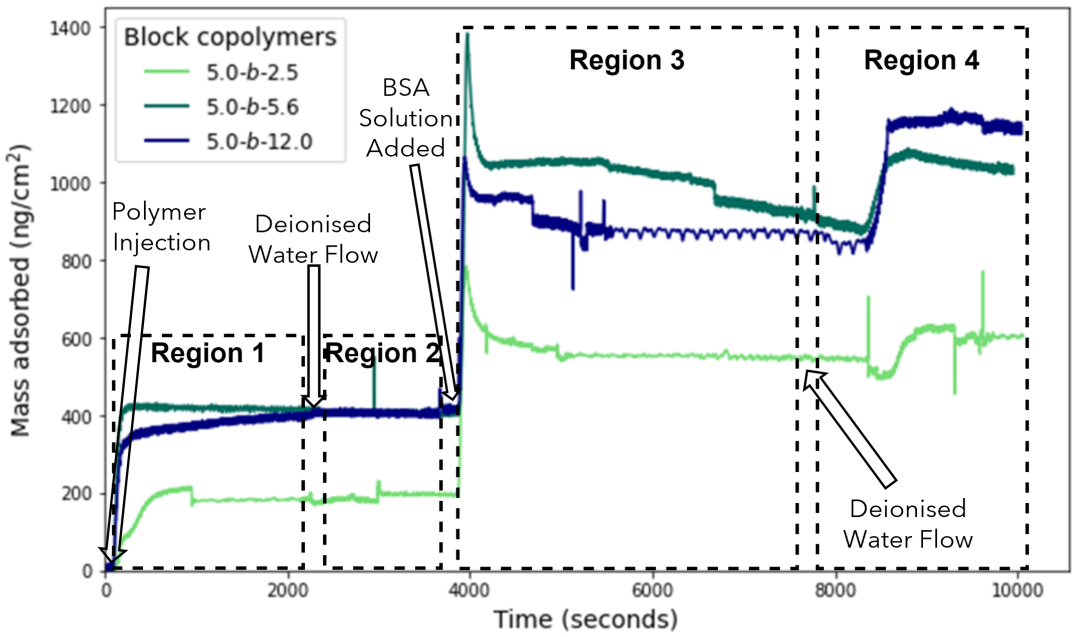



Figure 4.11: Plot overlaying the change in mass adsorbed in ng cm$^{-2}$ against time in seconds for the block copolymers at a concentration of 200 ppm. Region 1 represents the polymer adsorption, region 2 is the deionised water rinse, region 3 is the BSA adsorption, and Region 4 is the final deionised water rinse.

Block copolymer 5.0-*b*-5.6 adsorbed the most, with a mass of $417 \pm 15$ ng cm$^{-2}$ at a concentration of 200 ppm. This may be due to the PDMAEMA anchoring segment of the block copolymer having a strong electrostatic attraction to the silicon dioxide surface from the tertiary amine group. Block copolymer 5.0-*b*-12.0 adsorbed $414 \pm 50$ ng cm$^{-2}$ at a concentration of 200 ppm, while block copolymer 5.0-*b*-2.5 adsorbed $200 \pm 5$ ng cm$^{-2}$ at 200 ppm. The lower adsorption of 5.0-*b*-2.5 may be attributed to its having fewer PDMAEMA anchoring segments on the surface, resulting in a decrease in the mass adsorbed.

In Region 2 of Figure 4.11, deionised water was introduced into the system from approximately 2260 to 3660 seconds, with adsorption onto the surface occurring at approximately 3000 seconds. This region constitutes the first deionised water wash in the system. All

three block copolymers showed no change in mass adsorbed on the surface when deionised water was introduced. This suggests that the polymers are being adsorbed irreversibly onto the sensor's surface, indicating no further polymer adsorption during Region 2. This may also suggest that the block copolymers were physisorbed onto the surface, meaning that the polymers had strong electrostatic interactions with the silicon dioxide surface.

At the start of Region 3 in Figure 4.11, BSA was introduced into the system, from approximately 3850 to 7780 seconds. BSA did not reach the sensor surface until approximately 3950 seconds. Upon interaction with the surface, the mass adsorbed onto the surface increased significantly for each polymer sample, indicating that none of the polymers were suitable candidates for anti-fouling performance.

In all cases, there was a substantial increase in the amount of deposition when the surfaces were first contacted with BSA, taking approximately 88 seconds to occur. This amount then decreased initially rapidly over about 144 seconds and then more slowly. The mass adsorbed on 5.0-*b*-2.5 decreased smoothly to approximately 544 ng $cm^{-2}$ over 3200 seconds, while the mass for the other two systems decreased at first smoothly and then in some discontinuous jumps. All block copolymers formed a fairly uniform concentration, significantly higher than the block copolymer alone, after approximately 1500 seconds. The data suggested that at the 200 ppm concentration, the block copolymers did not exhibit an antifouling effect. When deionised water was passed over the sensor's surface at approximately 8345 seconds, the mass adsorbed increased further, suggesting the formation of a hydration layer formed from the deposition of the BSA in region 3.

Region 4 constituted the final wash, occurring between 7800 to 9650 seconds, with deionised water adsorption occurring at approximately 8590 seconds. For all three block copolymers, there was an increase in mass adsorbed onto the surface, indicating that a hydration layer may have formed on the surface upon the BSA wash.

The results demonstrate that under the conditions studied here, there was no inhibition of adsorption as measured by the QCM probe; for all three block copolymers, the addition of BSA led to an increase in deposition. Despite the findings discussed in Chapter 2, these block copolymers did not resist deposition. The reasons for this are unclear; it may be that the polymers did not fully cover the surface leaving space for further adsorption. Another factor could be the concentration levels: the polymers were investigated in parts per million (ppm), whereas the BSA concentration used was 2g/L (0.1 g in 50 mL of deionised water). This means the polymer has been exposed to a much higher concentration of BSA, which is one million times greater than the 200 ppm concentration of the block copolymers.

### 4.2.5 Hydration Layer - QCM

As shown here, the block copolymer samples used did not prove to be ideal candidates for antifouling, despite earlier literature suggesting that PEO is highly effective for this purpose (Chapter 2). However, the data shown here suggests that the block copolymer PEO-*b*-PDMAEMA there is strong adsorption of the PDMAEMA segment to the silicon dioxide surface. Consequently, attention turned to exploring the potential of the PEO segment. As highlighted in Chapter 2, PEO is known to create a hydration layer that effectively prevents fouling. This section will therefore focus on experiments that densely pack the surface with polyethylene glycol chains to maximise their antifouling properties; a fully packed surface is then studied to analyse its properties.

To achieve optimal anti-fouling properties, PEG needed to be densely packed onto the gold QCM sensor surface. Uniform monohydroxyterminated PEG (PEG-OH) and uniform monothiolterminated PEG (PEG-SH), were purchased from Sigma and Jenkem, respectively, were dissolved together in deionised water, with PEG-OH at a concentration of 40% and PEG-SH at 0.01 g/mL. The material was left for 24 hours to allow the dissolution process to occur, and the solution was left to dissolve overnight at room temperature on a stirrer

plate, the solution took one day to dissolve and was very viscous so was left overnight to ensure complete homogeneity. Gold-coated silicon sensors were then immersed in these PEG solutions for 24 hours. PEG-SH irreversibly adsorbed to the gold surface, while PEG-OH effectively filled the excluded volume, enabling higher grafting densities than would otherwise be feasible.

After immersion, the samples were removed from the solution, rinsed with water, and dried with nitrogen. They were subsequently treated with chloroform and sonicated for 10 minutes to eliminate any unbound PEG. Following another rinse with deionised water, the samples were dried under nitrogen and stored in degassed ethanol. Before measurements, thorough rinsing with ethanol and drying with nitrogen was conducted. Figure 4.12 illustrates the procedural steps taken to achieve the desired grafting density of PEG on the gold sensors. The method was adopted by Zhang *et al*[143], the specific amount of PEG was unknown as the aim of this measurement was to prove that PEG is good at antifouling and to not quantify how much PEG had been adsorbed onto the gold QCM sensor.

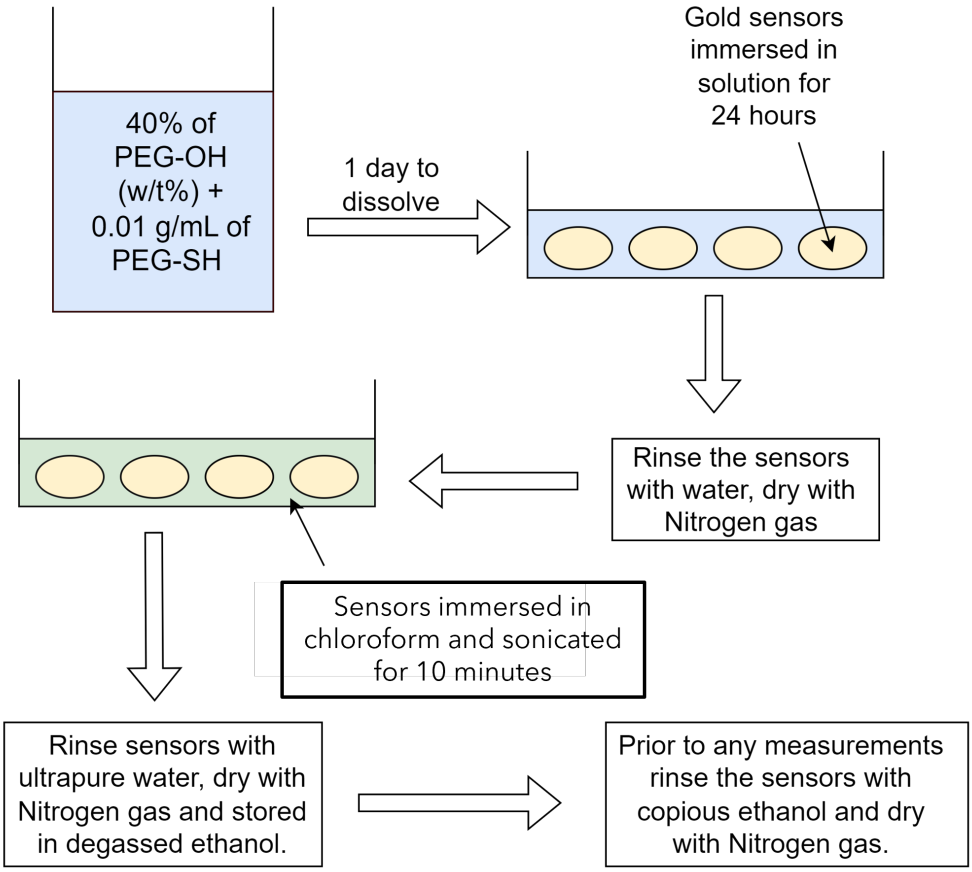



Figure 4.12: Experimental procedure for densely packing PEG-OH and PEG-SH onto a gold QCM sensor in order to maximise surface coverage of PEG.

QCM was used first to confirm that PEG is an effective candidate for antifouling applications, as suggested in Chapter 2. This will help to test the hypothesis that block copolymers did not fully pack onto the QCM surface—hence their poor performance in repelling BSA (concentration of 2 g/L).

Figure 4.13 illustrates one out of four QCM data plots of mass adsorbed (ng $cm^{-2}$) against time (seconds) for the densely packed PEG-OH/SH terminated polymer on the QCM gold sensor surface. The plot shows a lot of scatter demonstrating the sensitivity of the QCM instrument.

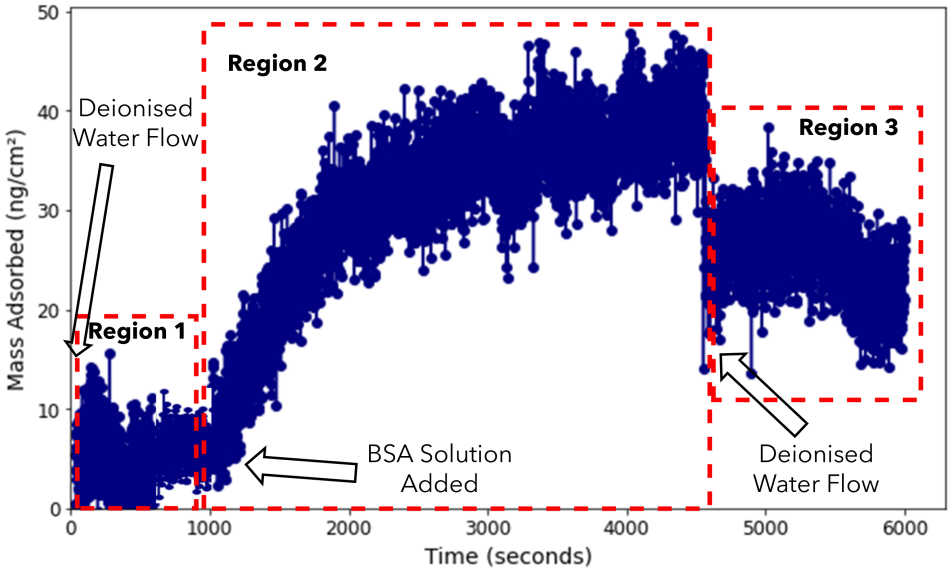



Figure 4.13: QCM measurement of densely packed PEG-OH/SH onto a gold QCM sensor at a constant flow rate of 56.54 $\mu$L min$^{-1}$. Region 1 is deionised water flow, Region 2 is BSA solution added and Region 3 is deionised water flow again.

Region 1 in Figure 4.13, the first 1000 seconds of the experiment, involved the flow of deionised water over the gold QCM sensor's surface at a constant flow rate of 56.54 µL/min. Deionised water was used to establish a baseline and to observe the impact of BSA on the mass adsorbed of the PEG-OH/SH chains.

Region 2, extending from approximately 1100 seconds to 4700 seconds, involved the introduction of BSA (concentration of 2 g/L) into the system. The data shows that very little BSA managed to adsorb onto the sensor's surface, approximately 45 ng cm$^{-2}$. This is significantly less than the amount of BSA deposited on the block copolymer samples (see Figure 4.11). This finding indicates that PEG is indeed a suitable candidate for antifouling.

Region 3 indicates the results of another deionised water wash, between approximately 4750 to 5900 seconds. During this stage, about 15 ng cm$^{-2}$ of BSA was washed off, further indicating that not much BSA had deposited onto the surface. Approximately 30 ng cm$^{-2}$ of

BSA remained on the surface after the final deionised water flow in region 3.

This QCM measurement confirms that PEG is an adequate candidate for antifouling applications. The results suggest it is possible to generate effective antifouling properties by densely packing the surface with polymer chains to prevent BSA from adsorbing onto the sensor's surface. However, this preparation method is complex and is not feasible for realistic systems. The data also suggests that the block copolymers were less than fully adsorbed on the surface - that should full adsorption have occurred greater inhibition of adsorption of BSA would have been found.

### 4.2.6 Hydration Layer - AFM

The reason for this measurement is to demonstrate that deionised water acts as a hydration layer that repels proteins (foulants). To validate this, two systems were compared: one using deionised water and the other using an organic solvent, specifically hexadecane.

To elucidate the molecular mechanism behind PEG's antifouling efficacy, as demonstrated by the QCM data (Figure 4.13), AFM-based force spectroscopy was used to measure the surface adhesion between a borosilicate sphere (8 $\mu$m) and the PEG surfaces in both water and hexadecane. The removal measure results are presented in Figure 4.14(b), the curves shown are for the withdrawal of the sphere from the surface. The findings reveal that the adhesion in water is significantly lower, nearly 0 nN, compared to hexadecane, which exhibits an average adhesion value of 8 nN. This indicates adhesion between PEG and the borosilicate sphere in hexadecane, demonstrating strong attractive interactions such as Van der Waals forces between the borosilicate probe and the PEG chains when the two surfaces are separated.

Figure 4.13(a) illustrates how terminally attached PEG chains form on a solid substrate, showing a water layer amongst the PEG chains and protein, which resists protein adsorption.

Jeon et al.[74] modelled proteins as finite spherical particles and found that increasing the chain length of a polymer with a known surface density resulted in higher protein resistance. This figure demonstrates how PEG chains are oriented on the substrate surface in water and how this affects protein deposition, indicating that a high surface density and long chain length of PEG are desirable for protein resistance. PEG has long been proposed as an effective antifouling material because of its strong hydration properties.[61] The hydration layer creates a repulsive force when a foulant (protein) approaches the PEG chains. When polyethylene glycol (PEG) molecules are exposed to a good solvent such as water, the brush layer becomes solvated, meaning that polymeric molecules and water molecules co-exist in the so-called 'hydration layer'. While water molecules are, of course, present in the bulk phase, the resistance to protein adsorption is primarily due to the steric repulsion of the hydrated polymer layer, not the presence of the water layer itself as shown in Figure 4.13(a).

Thus, Figure 4.14(b) indicates that there is no attraction between the two surfaces in contact, showing that the water acts as a barrier, preventing the borosilicate sphere from attracting to the PEG chains. Since there is no attraction, steric repulsion is present.

Figure 4.14 (b) displays an AFM adhesion force curve of thiol PEG in deionised water (shown in red dashed line) and thiol PEG in hexadecane (shown in blue line). Both systems were tested on a gold-coated QCM sensor with a functionalised borosilicate cantilever tip to determine the adhesion force during the retract curve. Figure 4.14 (c) provides a quantitative representation of Figure 4.14 (b), illustrating the adhesion force in nanonewtons.

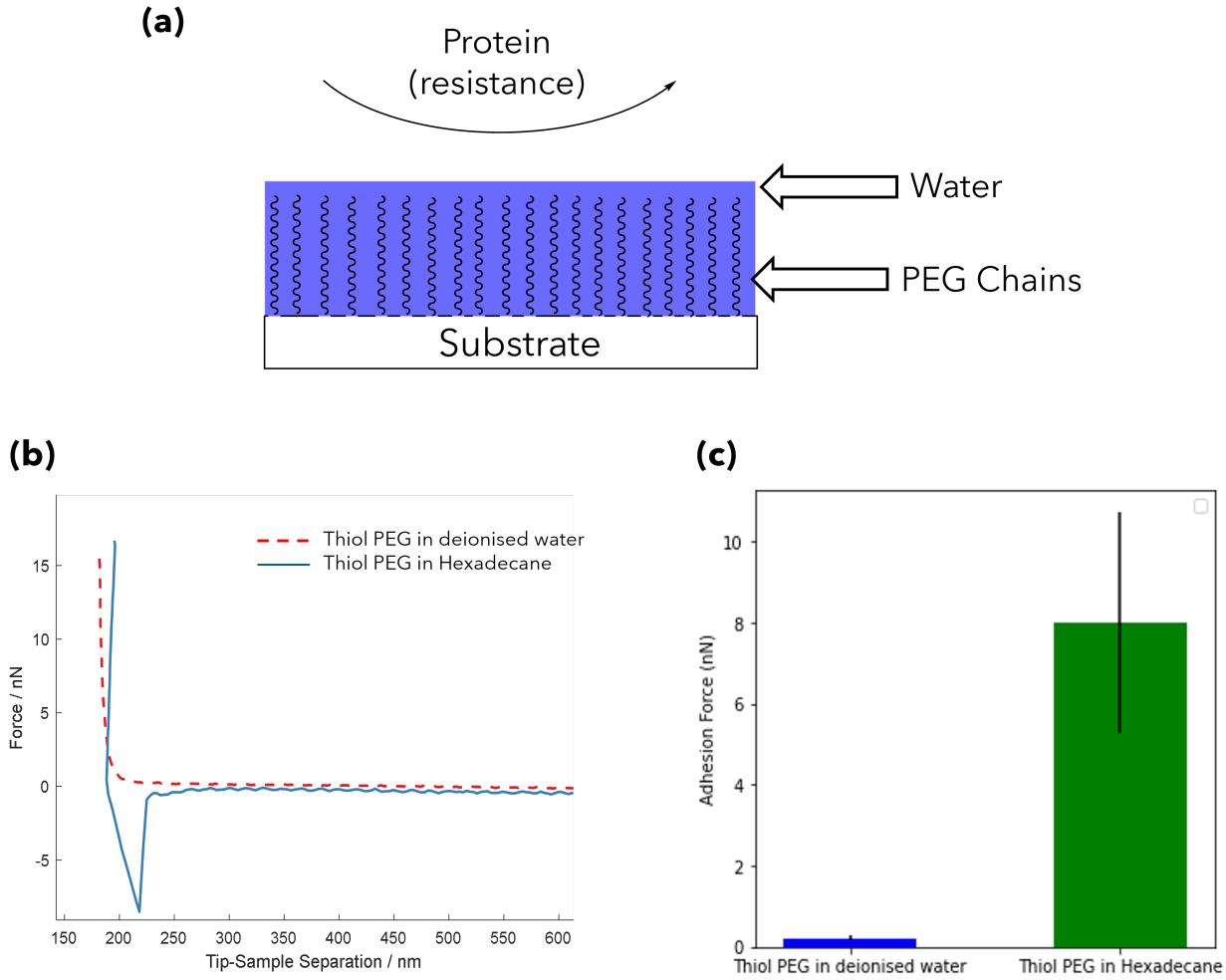



Figure 4.14: (a) Effect of hydration layer on protein adsorption. (b) AFM Adhesion Force curve (retract curve) of Thiol PEG in deionised water (red) and Thiol PEG in hexadecane (blue) on a gold QCM sensor coming into contact with a functionalised borosilicate cantilever tip. (c) A quantified approach of (b) showing the measured adhesion of the borosilicate cantilever tip being pulled away from the coated surface. The adhesion of an average of 300 force curves was plotted for part (c).

### 4.2.7 Thickness of block copolymer samples in deionised water

It is not clear from the previous data what confirmation the block copolymers form on the surface. The thickness of the adsorbed block copolymer chains on a silicon dioxide QCM sensor was thus measured using AFM. Measurement was carried out on a silicon dioxide sensor because this surface closely resembles that of a glazed ceramic tile, which is used in toilet bowl applications. The purpose of this measurement was to understand, at a nanoscale level, the thickness at which the block copolymers had deposited onto the surface and the configuration of deposition. As shown in Figure 4.11, none of the block copolymers exhibited effective antifouling properties. Therefore, it was essential to determine the extent of their deposition. Unlike PEG, which adheres efficiently to the sensor surface (as discussed on page 123), the block copolymers may not adhere as effectively. Consequently, measuring the thickness of the block copolymer samples in deionised water could provide insight into the extent of deposition onto the sensor surface.

Measurements were carried out in deionised water to allow the chains to elongate from the substrate surface, the silicon dioxide QCM sensor. A functionalised polystyrene (purchased from Cospheric) cantilever tip was used to isolate the charge interactions between the block copolymer chains, which are electrostatic, and the cantilever tip. This ensured that no extraneous factors impacted the data, allowing accurate measurement of the thickness of the deposited polymers in solution on the QCM sensor surface. Figure 4.15(a) illustrates the approach curves of the block copolymers in a wet film (in a deionised water environment), with an uncoated silicon dioxide sensor acting as the control. Figure 4.15(b) shows a diagrammatic representation of how the cantilever comes into contact with the elongated block copolymer chains.

A quantitative evaluation of the block copolymer deposition layer's thickness was performed by measuring the onset of repulsion upon contact. Figure 4.15(a) presents representative approach curves for all three block copolymers, along with the control, an uncoated silicon

dioxide sensor. Wherever the curves differ from the uncoated control this can be attributed to the block copolymers layer. Notably, the block copolymer 5.0-*b*-2.5 exhibited the largest wet thickness, approximately 60 nm, as shown in part (a) of Figure 4.15: at *ca.* 60 nm from the surface the force curve separates from the control. This thickness is more pronounced compared to the other two block copolymers, suggesting that the 5.0-*b*-2.5 film was well solvated in deionised water, causing the chains to extend far from the supporting substrate and thus inducing steric repulsion.

As shown in Figure 4.15(a), the block copolymer 5.0-*b*-5.6 has a wet film thickness of approximately 40 nm, while 5.0-*b*-12.0 exhibited the smallest wet thickness at around 25 nm. Despite 5.0-*b*-2.5 having the smallest anchoring segment, it possesses the largest PEO group, which does not bind to the surface but rather faces the bulk solution. This indicates that the PDMAEMA segment is the primary factor involved in surface deposition.

It can be observed that as the anchoring segment, which is the PDMAEMA group within the block copolymer chains, increases, the thickness decreases in a wet film environment. Additionally, it can be said that the block copolymer sample 5.0-*b*-2.5, which has the highest wet film thickness, is also the most effective polymer at antifouling BSA. This is evidenced by Figure 4.11, where it absorbed the least amount of BSA in ng/cm2 during region 3 of the plot compared to the other two block copolymers.

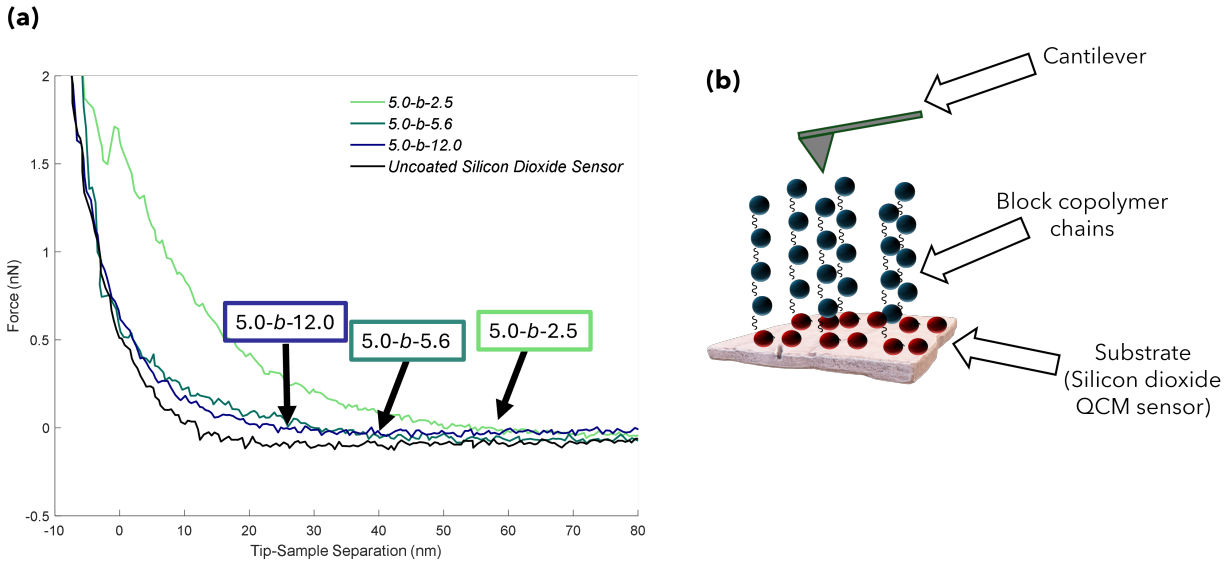



Figure 4.15: (a) Interfacial interactions are measured by the AFM when approaching a polystyrene particle of 9.5 - 11.5 $\mu$m towards the block copolymer samples at 200 ppm. (b) Schematic illustration of the configuration of the block copolymer deposited onto the surface as the cantilver tip is approaching the block copolymer chains.

## 4.3 Conclusions

This chapter delves into the intricate surface interactions between negatively charged surfaces and block copolymers composed of polyethylene oxide (PEO) and varying proportions of poly(2-(dimethylamino)ethyl methacrylate) (PDMAEMA). The primary aim was to develop a surface protective additive capable of repelling dirt and minimising soil attachment, with a focus on antifouling applications in toilet bowl systems—an area currently underserved by commercial additives.

The study employed Quartz Crystal Microbalance (QCM) and Atomic Force Microscopy (AFM) to monitor the mass adsorption of the block copolymers in real time and at different concentrations. QCM provided insights into adsorption kinetics, essential for understanding

the rate and extent of polymer adhesion to the sensor surface. AFM enabled the measurement of copolymer thickness and the adhesion of PEG-OH/SH on the sensor surface. Together, these techniques offered a comprehensive view of how various copolymer architectures impact surface coverage, adsorption kinetics, binding energies, and antifouling behaviour.

The results underscored the significant role of electrostatic interactions in the adsorption process. The hypothesis was that increasing the PDMAEMA segment in the block copolymer would lead to higher mass adsorption onto the silicon dioxide sensor surface due to stronger electrostatic interactions from the positively charged groups. However, a linear correlation between the PDMAEMA ratio and adsorption mass was not consistently observed. This discrepancy suggests that factors such as molecular configuration, steric hindrance, and the dynamic behaviour of the solution copolymers play substantial roles in influencing adsorption behaviour.

Adsorption kinetics provided crucial information about the interaction rate of the block copolymers with the surface, while the data on mass and moles adsorbed offered a quantitative measure of polymer adherence.

Figure 4.8 illustrates that the 5.0-*b*-5.6 copolymer displayed the fastest adsorption rate for concentrations greater than 100 ppm, indicating strong early interactions with the surface, likely due to an optimal balance between the hydrophilic PEO segments and the anchoring PDMAEMA segments. The adsorption kinetics followed a typical trend, with the rate decreasing as the surface approached saturation.

The mass adsorption data, shown in Figure 4.5b, revealed that the 5.0-*b*-5.6 copolymer achieved the highest mass adsorption. This substantial uptake correlates with its favourable adsorption kinetics, suggesting that the copolymer's architecture supports both rapid and significant surface interaction. The moles adsorbed data further corroborates this, showing that the 5.0-*b*-5.6 copolymer had the highest number of moles adsorbed per unit area, indicating effective surface coverage.

In contrast, the 5.0-*b*-12.0 copolymer, despite slower initial kinetics, ultimately reached a comparable level of mass adsorption but exhibited a distinct adsorption profile. The slower initial adsorption likely resulted from steric hindrance due to the higher PDMAEMA content, which may have delayed surface interaction. Nonetheless, the continued mass uptake over time suggests that once initial adsorption occurs, the copolymer can achieve substantial surface coverage, though the moles adsorbed were slightly lower than those of the 5.0-*b*-5.6 copolymer.

The 5.0-*b*-2.5 copolymer, with its lower PDMAEMA content, demonstrated the least mass adsorption and the fewest moles adsorbed. This indicates that insufficient PDMAEMA content may result in weaker interactions with the surface, leading to lower mass uptake and fewer moles adsorbed, which translates to less effective surface coverage.

Analysis of adsorption behaviour for the three PEO-*b*-PDMAEMA block copolymers (5.0-*b*-2.5, 5.0-*b*-5.6, and 5.0-*b*-12.0) relative to rate constants revealed no consistent trend of increasing mass adsorbed with higher rate constants. Washing affected each copolymer differently: the 5.0-*b*-2.5 copolymer showed minimal change in mass adsorbed post-wash, indicating lower adsorption stability and making it less suitable for applications requiring high post-wash stability. The 5.0-*b*-5.6 copolymer experienced a moderate reduction in mass adsorbed after washing, with relatively consistent data distribution, suggesting moderate stability and suitability for applications needing some post-wash stability. Conversely, the 5.0-*b*-12.0 copolymer maintained high mass adsorbed values even after washing, with a broad distribution indicating strong adsorption capacity and good post-wash stability.

Introducing Bovine Serum Albumin (BSA) into the QCM system provided a thorough evaluation of the block copolymers' antifouling potential. The data showed that these copolymers did not exhibit promising antifouling properties. Despite the initial irreversible adsorption of these copolymers, no antifouling effect was observed with the introduction. Each copolymer showed increased mass deposition upon BSA interaction, indicating ineffective resistance

to protein fouling. Additionally, the presence of a hydration layer, indicated by a further mass increase during the final wash, suggests that BSA deposition led to increased surface hydration. The lack of antifouling performance may be due to inadequate surface coverage by the polymers or the high concentration of BSA used in the experiments, which may have overwhelmed the copolymers' adsorption capabilities. Under the conditions studied, these block copolymers did not demonstrate effective antifouling properties.

QCM measurements confirm that PEG is a viable candidate for antifouling applications. The results suggest that effective antifouling properties might be achieved by densely packing the surface with polymer chains to prevent BSA adsorption onto the sensor's surface. However, this preparation method is complex and impractical for realistic systems. The data also suggest that the block copolymers were not fully adsorbed on the surface—greater inhibition of BSA adsorption might have been observed with full adsorption.

AFM was used to measure the thickness and configuration of block copolymer deposits on a silicon dioxide QCM sensor, aiming to understand their nanoscale deposition and antifouling properties. The results indicated that none of the block copolymers exhibited effective antifouling characteristics, as none could prevent BSA adsorption. AFM measurements revealed that the 5.0-*b*-2.5 copolymer formed the thickest wet film, approximately 60 nm, due to its larger PEO group extending further from the substrate. In contrast, the 5.0-*b*-5.6 and 5.0-*b*-12.0 copolymers had smaller wet film thicknesses of about 40 nm and 25 nm, respectively. This suggests that the PDMAEMA segment, which anchors the copolymer to the surface, significantly influences deposition extent, with a larger PEO group contributing to greater film thickness. Notably, despite having the smallest anchoring segment, the 5.0-*b*-2.5 copolymer showed the highest antifouling efficacy by absorbing the least BSA. This implies that the thickness of the copolymer film and surface coverage are crucial factors in its antifouling performance.

These findings have significant implications for developing advanced ceramic coatings for sanitary applications. The detailed analysis of mass and moles adsorbed, kinetics, binding energies, and interactions with foulants provides valuable insights for selecting and designing block copolymers tailored to specific needs.

For instance, the 5.0-*b*-5.6 copolymer stands out as a strong candidate for coatings requiring high adsorption efficiency and rapid kinetics, crucial for robust and swift film formation on toilet ceramics. Additionally, the thermodynamic favourability observed in the binding energy calculations suggests that this copolymer has the potential for long-term stability, making it ideal for applications demanding durability and longevity.

The study also emphasises the need to address antifouling capabilities. The interaction with foulants, particularly with PEG functionalisation, highlights the necessity for further modifications to improve resistance to biofouling—a common issue in toilet ceramics.

In conclusion, this chapter provides an in-depth investigation into the adsorption and antifouling potential of PEO-*b*-PDMAEMA block copolymers on negatively charged surfaces. Utilising QCM and AFM, the study elucidates how copolymer architecture influences surface coverage, adsorption kinetics, and antifouling behaviour. The results reveal that 5.0-*b*-5.6 copolymer enhances mass adsorption due to stronger electrostatic interactions, effective antifouling properties were not achieved, likely due to inadequate surface coverage and high BSA concentrations. Notably, the 5.0-*b*-5.6 copolymer demonstrated the best balance of adsorption efficiency and rapid kinetics, suggesting its potential for applications requiring quick film formation and stability. These findings highlight the need for further refinements to improve antifouling capabilities and provide valuable insights for developing advanced coatings in sanitary environments.

Using QCM, the molecular properties influencing surface deposition were identified, allowing for the quantification of copolymer adsorption onto the sensor surface and the determination of adsorption rates. These techniques were instrumental in developing the protocols necessary

to achieve the objectives aligned with Innospec's aims. Subsequently, Innospec supplied random copolymers (see Table 5.2) to identify which additives could effectively prevent fouling in toilet bowls. The methods developed in this chapter are applied to candidate chemistry supplied by Innosoec.

# Chapter Five

# The Effect of Random Co-polymer Architecture on its Surface Deposition

## 5.1 Introduction

Following the block copolymer study in the previous chapter which developed a range of experimental techniques for studying the adsorption behaviour of chemicals on a nanoscale, Innospec provided four samples as outlined in Table 5.1. A study was designed in which samples were provided without prior knowledge of their composition before conducting the QCM measurements. These mixtures were based on the PEO-*b*-PDMAEMA block copolymer samples studied in the previous chapter but with additional Innospec additives incorporated into the mix. The polymers in the study were selected by Innospec to span a variety of chemical functionalities, demonstrating differing cleaning abilities during testing. This selection made them suitable for evaluating using QCM to compare results with Innospec's testing standards.

The samples were examined at a concentration of 200 ppm, a concentration recommended by Innospec based on typical operating concentrations of commercial cleaning products. At

least four QCM measurements were performed for each of the four random copolymers listed in Table 5.1 to observe the adsorption and desorption of molecules in a real-time system. For experimental details, refer to Chapter 3, section 3.1.5.

The random copolymers provided by Innospec were tested on silicon dioxide sensors in the QCM measurements. The choice of silicon dioxide as the substrate was deliberate because its surface closely resembles the glazed ceramic surface of a toilet bowl. This similarity ensures that the test conditions are relevant to the intended application environment.

This study aimed to determine which polymer exhibited the best antifouling properties by introducing Bovine Serum Albumin (BSA) to the system after the post-wash. Once the behaviour was established, the findings were reported back to Innospec, after which another experimental matrix was constructed as shown in Table 5.2. The polymers in the study were provided by Innospec, encompassing a variety of chemical functionalities. They exhibited varying cleaning abilities during testing.

In this chapter, the focus is solely on DLS and QCM techniques. DLS was employed both to ascertain the size of the random copolymer molecules and to examine whether changes in pH affected the size of the random copolymer molecules in the solution, considering that this analysis had been conducted in a bulk solution. Since the polymer molecules were not spherical, the Stokes-Einstein equation (that assumes a spherical molecule) did not directly apply.

Zeta Potential measurements were also conducted to assess the charge of the solutions as a function of pH. This enabled the determination of the charge of the molecules as the environment transitioned from acidic to basic, covering the pH range from 2 to 10. pH served as the primary determinant of zeta potential. A zeta potential value without a corresponding pH reference lacks substantial significance on its own.[120]

QCM was utilised as this project emphasised the deposition aspect of the polymer behaviour. QCM enabled a deeper exploration of the absorption and desorption dynamics of the polymer molecules in a real-time, dynamic system, which could be determined using the Saurbrey equation. Additionally, the rate constant of the polymer molecules onto the surface can be analysed, which could be modelled using the first-order Langmuir isotherm equation[98,106] given in section 3.1.6.

Overall, this chapter investigates the effect of pH on random copolymers in solution using Dynamic Light Scattering (DLS) to determine the size and charge of the polymers at different pH levels in bulk solution. Quartz Crystal Microbalance (QCM) was employed to evaluate the impact of pH on the mass adsorbed onto the silicon dioxide sensor and to determine the rate constant of adsorption, all samples were tested at a concentration of 200 ppm.

## 5.2 Results and Discussion

### 5.2.1 Study of random copolymers provided by Innospec

Figure 5.1 describes the chemical structures of the monomers in the study. The acronyms represent the following monomers: 2-(dimethylamino) ethyl methacrylate known as DMAEMA (blue), Acrylic acid known as AA (red), 2-(methacryloyloxy)ethyl[trimethylammonium chloride] known as MAETAC (black), Iso-octyl acrylate (green) known as i-OA, Ethylene glycol dimethacrylate (purple) known as EGDMA, and Dodecanethiol known as DDT (pink).

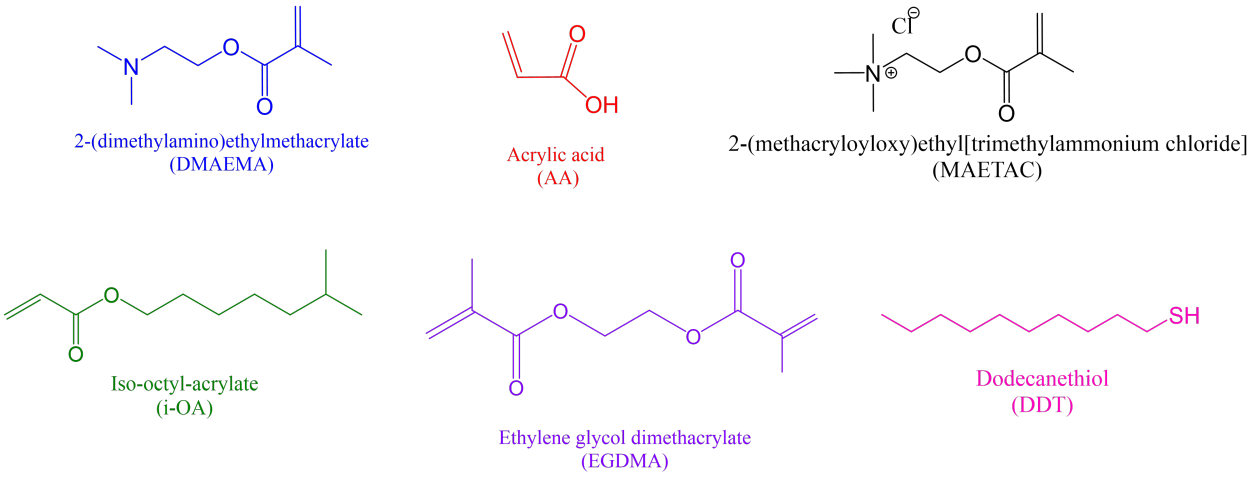



Figure 5.1: Chemical structures of the monomers in the study. 2-(dimethylamino) ethyl methacrylate known as DMAEMA (blue), Acrylic acid known as AA (red), 2-(methacryloyloxy)ethyl[trimethylammonium chloride] known as MAETAC (black), Iso-octyl acrylate (green) known as i-OA, Ethylene glycol dimethacrylate (purple) known as EGDMA, and Dodecanethiol known as DDT (pink).

Table 5.1 shows the initial composition of the random copolymer samples provided by Innospec, detailing their weight (Wt) ratios, Mol ratios and acronyms for the monomers as part of the study. The ratios listed alongside the acronyms indicate the weight ratios of the monomers used during the synthesis process which have then been converted into mol ratios.

Table 5.1: Initial compositions of the random co-polymer samples provided by Innospec illustrating their weight (Wt) ratios, Mol ratios, and chemical structures for the study.

| Random Co-polymer | Wt Ratio | Mol Ratio |
|---|---|---|
| DMAEMA:AA | 95:5 | 90:10 |
| MAETAC:AA | 90:10 | 86:14 |
| i-OA:MAETAC | 10:90 | 10:90 |
| MAETAC:AA:EGDMA:DDT | 40:40:10:10 | 22:66:6:6 |

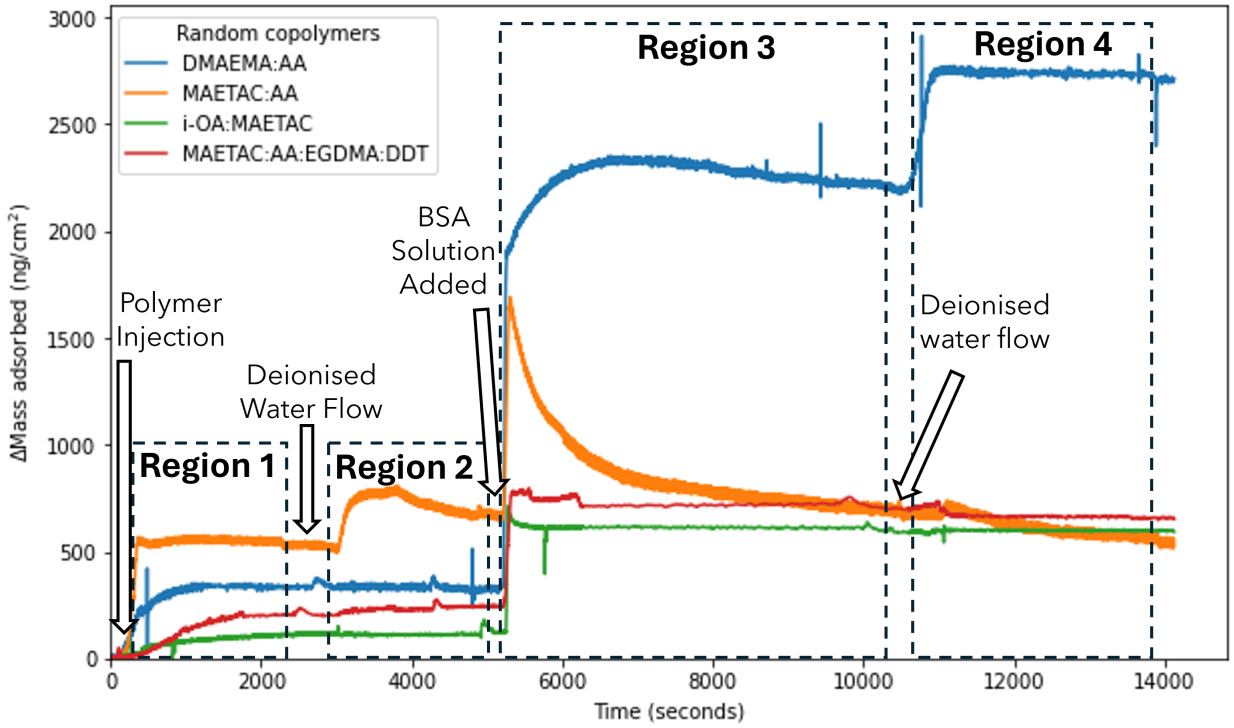



Figure 5.2: Plot overlaying the change in mass adsorbed in ng $cm^{-2}$ against time in seconds for the initial random copolymers supplied (composition given in Table 5.1) by Innospec at a concentration of 200 ppm. Region 1 represents the polymer adsorption, region 2 is the deionised water rinse, region 3 is the BSA adsorption, and region 4 is the final deionised water rinse.

Figure 5.2 illustrates the change in mass of the random copolymers adsorbed onto the sensor throughout the QCM measurements. The plots have been overlaid to visualise how each polymer responded to different stages in the QCM measurement process. All plots have been normalised to facilitate the explanation of the figure.

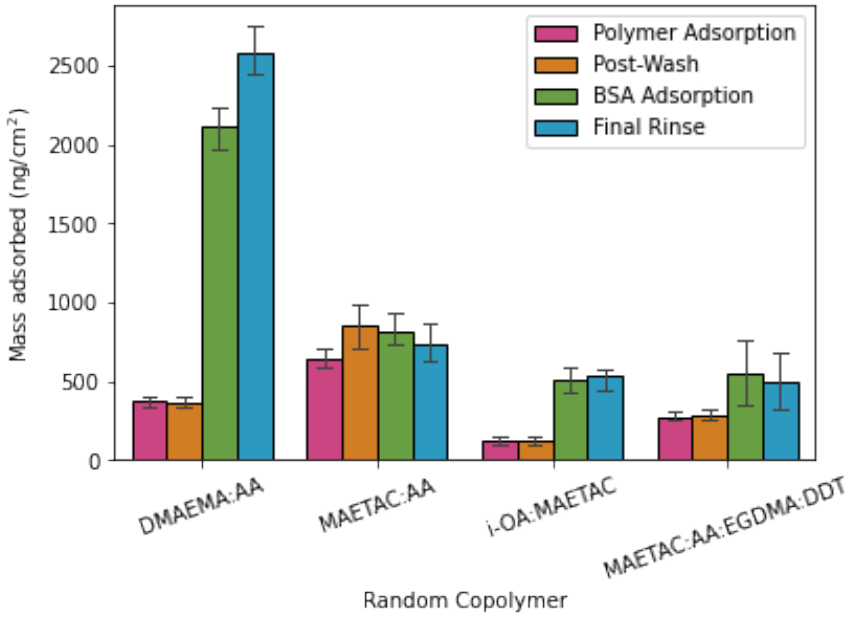



Figure 5.3: Mass adsorption of the random copolymer samples obtained *via* QCM measurements at the different stages of adsorption (see Figure 5.2). One hundred data points were collected for the mass adsorbed when the system was equilibrated. (i) Pink represented polymer adsorption in Region 1, 1800 to 1900 seconds; (ii) orange represented post-wash in Region 2, 4560 to 4660 seconds; (iii) green represented BSA adsorption in Region 3, 9660 to 9760 seconds; (iv) and blue represented the final rinse in Region 4, 13000 to 14000 seconds. The error bars represent the standard error of the mean (SEM).

In Region 1, from 150 to 2000 seconds, polymer is introduced into the system. The polymer injection occurred at approximately 109 seconds, and polymer adsorption onto the surface took place at approximately 150 seconds. Once the polymers have reached the sensor surface, there is an increase in mass adsorbed onto the surface shown by a change in QCM signal.

MAETAC:AA (orange line) exhibits the highest adsorption onto the surface, followed by DMAEMA:AA (blue line), then MAETAC:AA:EGDMA:DDT (red line), and the polymer with the least adsorption during Region 1 was i-OA:MAETAC.

MAETAC:AA adsorbed the most, with a mass of $646 \pm 36$ ng cm$^{-2}$ (error method calculated by the standard error of the mean (SEM)) as shown in Figure 5.3, which plots polymer adsorption in region 1, 1800 to 1900 seconds. This may be attributed to the fact that it contained a permanent quaternary ammonium cation within the MAETAC. This renders it more positively charged than DMAEMA:AA, which adsorbed $378 \pm 21$ ng cm$^{-2}$, as shown in Figure 5.3. As MAETAC contains a permanent positive charge, it strongly interacts with the negative charges from the silanol groups on the silicon dioxide sensor surface, resulting in a strong electrostatic force. Although DMAEMA contains a tertiary amine group, it does not possess a permanent positive charge, thus exhibiting a less strong electrostatic interaction with the $SiO_2$ surface.

MAETAC:AA:EGDMA:DDT adsorbed $275 \pm 15$ ng cm$^{-2}$ at region 1, with i-OA:MAETAC adsorbing $123 \pm 15$ ng cm$^{-2}$, illustrated in Figure 5.3.
As MAETAC:AA:EGDMA:DDT contains dodecanethiol, which contains of an inherently insoluble hydrocarbon chain, this may lower the amount of mass adsorbed onto the surface. Additionally, Ethylene glycol dimethacrylate (EGDMA) consists of two alkene chains, both of which can propagate with the alkene group in MAETAC, resulting in crosslinking within the polymer chains. This crosslinking induces structural rigidity, which may also reduce the polymer's adsorption onto the silicon dioxide surface.

Deionised water was introduced into the system from approximately 2900 to 4800 seconds, and adsorption of deionised water onto the surface took place at approximately 3000 seconds. Region 2 thus constitutes the first deionised water wash in the system. DMAEMA:AA, MAETAC:AA:EGDMA:DDT, and i-OA:MAETAC all showed no significant change in mass adsorbed onto the surface when deionised water was introduced, possibly due to the polymer

already being adsorbed onto the sensor's surface, resulting in no change in polymer adsorption during region 2. However, MAETAC:AA exhibited a clear change in mass adsorbed onto the surface upon deionised water rinsing. The mass on the surface increased from $646 \pm 36$ ng cm$^{-2}$ to $849 \pm 79$ ng cm$^{-2}$, as shown in Figure 5.3. This increase may be attributed to the polymer swelling on the surface from the deionised water wash.

Region 3 is the time when BSA was introduced into the system. BSA was added to the system from approximately 4900 to 10500 seconds but did not reach the sensor's surface until approximately 5200 seconds. As soon as BSA interacted with the surface, the mass adsorbed onto the surface increased significantly for each polymer sample, suggesting that each polymer was not a good candidate for anti-fouling performance. However, as time progressed, BSA slowly began to be removed from the sensor's surface, particularly in the case of MAETAC:AA. A spike in MAETAC:AA (orange line) to 1690 ng cm$^{-2}$ can be observed at 5300 seconds, after which the mass adsorbed gradually decreased, indicating a reduction in the mass adsorbed onto the surface over the time between *ca.* 5300 seconds to 10500 seconds. This suggests that BSA was being removed from the sensor surface in the MAETAC:AA sample over time. The removal of BSA may be attributed to the formation of a hydration layer formed during Region 2, which could have prevented BSA adsorption onto the surface, causing it to detach slowly. The hydration layer, composed of water molecules closely interacting with the polymer surface, forms a protective barrier that prevents foulants from adhering to the surface. This layer effectively shields the surface from contaminants, enhancing the polymer's antifouling properties.[61,138]

Upon introducing BSA to the DMAEMA:AA system, there was a significant increase in mass adsorption onto the surface between 5210 seconds to 10560 seconds. This suggests that DMAEMA:AA is unsuitable for anti-fouling, as BSA remained on the surface over time. Similar observations were made for the MAETAC:AA:EGDMA:DDT and i-OA:MAETAC polymer systems, where BSA remained on the surface over time. Although there is much less adhesion for these two polymers, BSA is still adsorbed onto the sensor surface, thus they

were not considered for further investigation.

Region 4 constituted the final wash, occurring between 10500 to 14100 seconds. For the polymer systems MAETAC:AA:EDGMA:DDT and i-OA-MAETAC, there was no significant change in mass adsorbed onto the surface, indicating that the BSA remained on the surface and none was washed away. However, for DMAEMA:AA, during the final rinse, there was another increase in mass adsorbed onto the surface. This may have been due to a hydration layer forming from the BSA deposition in the previous region.

For the MAETAC:AA polymer system during region 4, the mass adsorbed continued to decrease during the final rinse stage. If the measurement had been allowed to continue, it was assumed that the mass adsorbed at region 4 would return to the level of the mass adsorbed at region 2, which was the polymer adsorption stage. This suggests that it was a good candidate for anti-fouling properties.

As i-OA:MAETAC and MAETAC:AA:EGDMA:DDT adsorbed the least onto the surface, they were not considered for further studies. Although Bovine Serum Albumin (BSA) adsorbed the least onto the surface when exposed to i-OA:MAETAC and MAETAC:AA:EGDMA:DDT, it did not completely detach from the sensor's surface during the wash step (region 4), unlike MAETAC:AA. This work aimed to elucidate why certain polymers exhibited efficacy and to understand the underlying mechanism of adsorption. MAETAC:AA demonstrated the highest adsorption onto the silicon dioxide QCM sensor, while DMAEMA:AA showed less adsorption onto the QCM sensor in comparison to MAETAC:AA. However, DMAEMA:AA absorbed the most BSA onto the sensor surface, as shown in Figure 5.2.

The next objective was to combine polymers with differing adsorption characteristics at various weight ratios to determine if there was a discernible relationship between MAETAC and DMAEMA. Since MAETAC:AA and DMAEMA:AA adsorbed the most onto the QCM sensor surface and DMAEMA:AA adsorbed the most BSA onto the surface, as illustrated in

Figure 5.2, region 3, the next aim was to understand whether combining all three homopolymers to create random copolymers at varying ratios of MAETAC and DMAEMA (as shown in Table 5.2) would reveal a relationship between MAETAC and DMAEMA and clarify how polymer adsorption occurs as the DMAEMA content increased as shown in Table 5.2. Table 5.2 displays the compositions of the random copolymer matrix samples provided by Innospec. Innospec supplied PolyMAETAC, while PolyAA and PolyDMAEMA were purchased from Sigma Aldrich (United Kingdom).

Table 5.2: The compositions of the random copolymer matrix samples provided by Innospec were determined based on the QCM results of the blind study. These compositions are illustrated by their weight (Wt) ratios and molar (Mol) ratios. The rows highlighted in blue are the polymers used in Chapter 6, Section 6.2.1, to facilitate cross-referencing when discussing the results in Chapter 6.

| **Monomers AA:MAETAC:DMAEMA** | |
|---|---|
| **Wt Ratios** | **Mol Ratios** |
| 100:0:0 | Pure AA |
| 0:100:0 | Pure MAETAC |
| 0:0:100 | Pure DMAEMA |
| 10:90:0 | 24:76:0 |
| 10:80:10 | 24:66:11 |
| 10:60:30 | 22:47:31 |
| 10:45:45 | 22:34:45 |
| 10:30:60 | 21:22:57 |
| 10:10:80 | 20:07:73 |
| 10:0:90 | 20:00:80 |

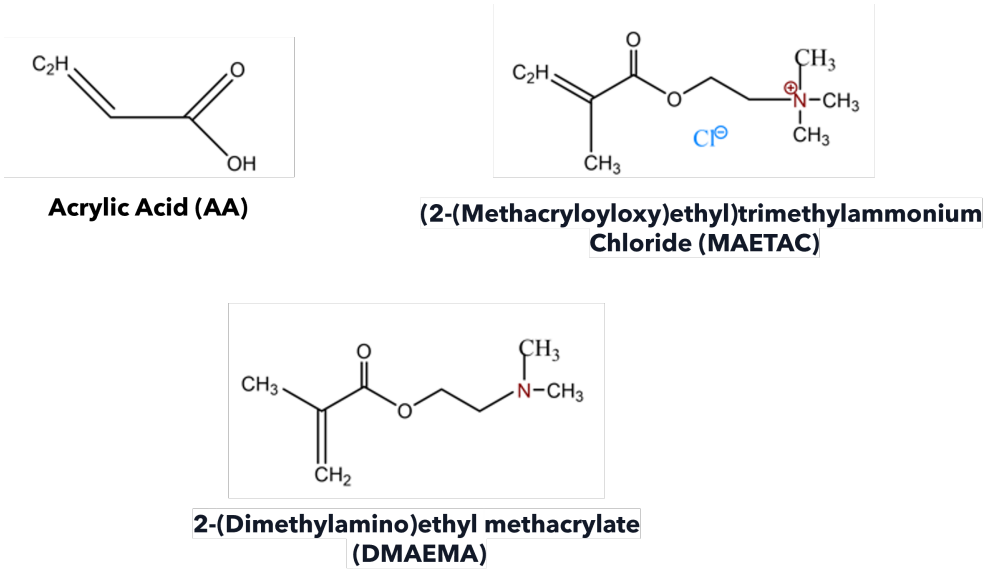



Figure 5.4: Chemical structures of the random copolymers: Acrylic Acid (AA), [2-(methacryloyloxy)ethyl]trimethylammonium chloride (MAETAC), and [2-(dimethylamino)ethylmethacrylate] (DMAEMA).

To study the effect of random copolymer architecture on its surface deposition, seven random copolymers along with three homopolymers, shown in Figure 5.4, were analysed here. Figure 5.5 illustrates a schematic representation of the AA:MAETAC:DMAEMA random copolymer structure and its adsorption on a silicon dioxide sensor. It was anticipated that the positively charged segment of the random copolymer would adhere to the negatively charged sensor.

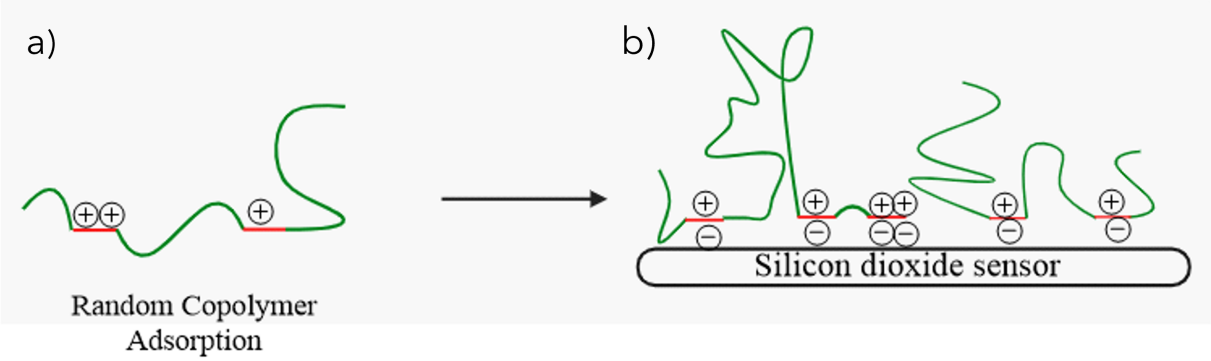



Figure 5.5: (a) Schematic illustration of the random copolymer and (b) Schematic illustration of the random copolymer adsorption onto the QCM sensor.

### 5.2.2 The Effect of pH Change on the Random Copolymers' Size in Bulk Solution

This section examines how pH influences the surface deposition of random copolymers composed of acrylic acid (AA), (methacryloyloxy)ethyl[trimethylammonium chloride] (MAETAC), and 2-(dimethylamino)ethyl methacrylate (DMAEMA), examples of the homopolymers and random copolymers are shown in Table 5.2. Understanding the pH-dependent behaviour of these copolymers is crucial for evaluating their effectiveness in various applications, especially those involving surface deposition. This is particularly relevant for interactions with surfaces such as silicon dioxide, which are similar to the surface of a toilet bowl.

Stock solutions were prepared to adjust the pH of the random copolymers. This involved preparing a 1M solution of sodium hydroxide (NaOH) to make the solutions basic and a 1M hydrochloric acid (HCl) to make the solutions more acidic. To prepare the 1M NaOH solution, 10 grams of NaOH was weighed into a weighing boat and transferred into a 250 mL flat-bottomed flask. The flask was then filled to the 250 mL mark with deionised water

and inverted several times to ensure complete dissolution. This process resulted in the preparation of 1M NaOH, which served as the base. The stock solution was subsequently used to adjust the pH of the random copolymer solutions to a pH of approximately ten as shown in Table 5.3. Ambient pH in Table 5.3 refers to the pH of the random copolymers in deionised water, without the addition of any other substances, resulting in an uncontrolled environment. The pH values for the random copolymers vary, as they represent the natural pH each copolymer adopts in deionised water at a concentration of 200 ppm, without the influence of any added acids or bases.

Table 5.3: Composition of the random copolymer mixtures of acrylic acid (AA), (methacryloyloxy)ethyl[trimethylammonium chloride] (MAETAC), and 2-(dimethylamino)ethyl methacrylate (DMAEMA), along with their respective pH values at $2 \pm 0.08$, ambient and $10 \pm 0.08$ .

| **AA:MAETAC:DMAEMA** | **pH 2** | **Ambient pH** | **pH 10** |
|---|---|---|---|
| 100:0:0 | 1.72 | 3.16 | 10.12 |
| 0:100:0 | 1.76 | 3.64 | 10.64 |
| 0:0:100 | 1.44 | 8.55 | 10.23 |
| 10:90:0 | 2.03 | 2.81 | 9.86 |
| 10:80:10 | 2.16 | 3.04 | 10.38 |
| 10:60:30 | 1.95 | 4.27 | 9.78 |
| 10:45:45 | 2.27 | 4.16 | 10.19 |
| 10:30:60 | 1.86 | 7.21 | 10.25 |
| 10:10:80 | 1.94 | 4.99 | 10.41 |
| 10:0:90 | 1.75 | 8.01 | 9.92 |

To prepare an acidic stock solution to adjust the random copolymer samples to pH 2, 20.83 mL of 37% hydrochloric acid (HCl) was measured out. 37% HCl corresponds to approximately 12 mol/L. To obtain a 1M solution, 250 mL was divided by 12, resulting in 20.83 mL. Therefore, 20.83 mL (measured by a micropipette) of the 37% HCl solution was added to a 250 mL flat-bottomed flask and then filled to the mark with deionised water. The flask was then gently shaken and inverted several times to ensure thorough mixing.

To create a solution with a concentration of 200 ppm, 0.01 g of 10:90:0 (AA:MAETAC:DMAEMA) was placed in a 100 mL Duran bottle. The Duran bottle was then filled with 50 mL of deionised water, resulting in a concentration of 200 ppm. Two separate solutions were prepared, one adjusted to pH 2 and the other to pH 10 using 1M HCl and NaOH respectively.

The 10:90:0 sample was used to create two pH samples, one at pH 2 and the other at pH 10. However, this resulted in unanticipated polymer aggregation in solution, as shown in Figure 5.6. To address this issue, a titration was conducted following the procedure outlined by Zhang et al.[144] The 200 ppm polymer solution was initially rendered extremely acidic by adding 740 $\mu$L of HCl. Subsequently, a 1M NaOH solution was employed for the titration, with simultaneous monitoring of pH changes as NaOH was gradually added dropwise. Deionised water served as the control, with pH adjusted to 2, followed by a dropwise addition of 1M NaOH to the solution. The titration procedure commenced by slowly adding 1M NaOH drop by drop, while pH readings were recorded as a function of the volume of NaOH added, as depicted in Figure 5.7.




Figure 5.6: Aggregation of random copolymer 10:90:0 both at pH2 (left) and pH 10 (right).

A basic titration was conducted on the homopolymers in Table 5.2, namely, polyacrylic acid (PAA), poly methacryloxy ethyl trimethyl ammonium chloride (PMAETAC), and poly 2-(dimethylamino)ethyl methacrylate (PDMAEMA). To initiate this, the preparation of solutions was necessary. This involved measuring 8 mg of the respective polymer and introducing it into 40 mL of deionised water, allowing dissolution to occur naturally. Upon achieving full polymer dissolution, pH measurements were promptly recorded. Subsequently, 740 µL of 1M HCl was introduced into the solution, followed by thorough mixing, and a pH measurement was taken, denoted as the 'initial pH.'

Figure 5.7 depicts data on pH as a function of the sequential addition of NaOH for the different systems. The data indicated an aggregated 10:90:0 solution (illustrated by the red line with red triangles), displayed a remarkably swift response to NaOH, resulting in a rapid change in pH. The 10:90:0 solution also exhibited a more rapid response to NaOH, which suggested a lower electrolyte concentration in the system due to aggregation. Consequently, less NaOH was required for this sample, as shown by the response to NaOH addition shown in Figure 5.7.

The titration for PolyDMAEMA is represented by the black line in Figure 5.7, demonstrating that less NaOH was needed to shift the solution from acidic to basic. Subsequently, a fresh 10:90:0 solution was prepared a couple of days later from the aggregated pH to assess if the random copolymer would still aggregate, which was found not to be the case. The behaviour of the fresh 10:90:0 solution closely resembled that of PolyMAETAC, as observed in Figure 5.7. Given that 90% of the random copolymer solution consisted of PolyMAETAC, this correlation was consistent with our expectations.

Notably, compared to PolyAA (depicted by the purple line), both the fresh 10:90:0 and PolyMAETAC solutions exhibited faster reactions to NaOH. This accelerated reaction implied that less NaOH was needed to elevate the pH of the solutions to a basic level. As PolyAA inherently carries a negative charge of the hydroxyl group, in solution, more NaOH was added to the solution, giving a longer time for PolyAA to become basic.

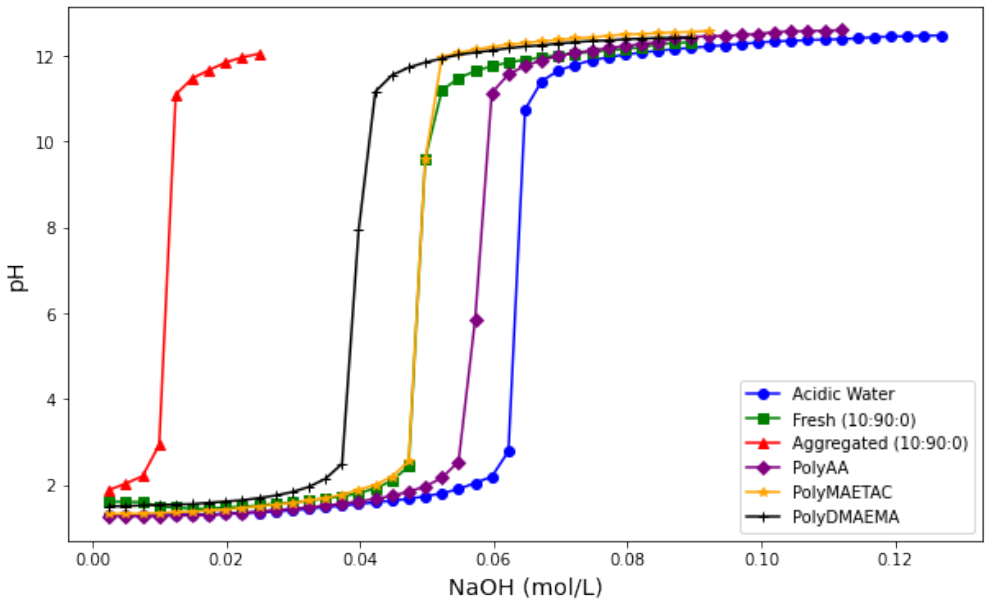



Figure 5.7: A basic titration curve, showing the pH change whilst adding 1M NaOH drop by drop to the homopolymer and random copolymer solution. All solutions under investigation were set to approximately pH 2. This data was subsequently used to generate a pH-versus-NaOH-added graph using Python.

Table 5.3 and Figure 5.8 present a range of random copolymers composed of acrylic acid (AA), (methacryloyloxy)ethyl[trimethylammonium chloride] (MAETAC), and 2-(dimethylamino)ethyl methacrylate (DMAEMA), along with their respective pH values and z-average size in nanometres measured by Dynamic Light Scattering (DLS).

Table 5.3 illustrates the pH values of various random copolymer mixtures composed of acrylic acid (AA), (methacryloyloxy)ethyl]trimethylammonium chloride (MAETAC), and 2-(dimethylamino)ethyl methacrylate (DMAEMA) at different composition ratios. The measurements are taken at three distinct pH conditions: pH 2, ambient pH, and pH 10. For example, a ratio of 100:0:0 indicates a composition of 100% AA, 0% MAETAC, and 0% DMAEMA, while a ratio of 0:100:0 indicates 0% AA, 100% MAETAC, and 0% DMAEMA. The table provides a clear view of how the composition of the copolymer mixtures affects their pH values in different environments.

To adjust the pH of the random copolymers, 1M hydrochloric acid (HCl) was used to lower the pH from their ambient pH to approximately pH 2, adding more protons to the mixture. To increase the pH to approximately 10 from the ambient pH, 1M sodium hydroxide (NaOH) was added to introduce more hydroxide ions to the mixtures. A Mettler Toledo pH probe, a benchtop device, was used to measure the pH of the random copolymers accurately and reliably. Before each measurement, the pH meter was calibrated using three buffer solutions, for pH 4, 7 and 10. The reason for choosing pH 2 and pH 10 was to expose the random copolymers to two extreme ends of the pH scale. This approach helps to understand how different environments affect the polymers' overall size, charge, mass adsorbed, and the rate at which the polymers reach the surface of the silicon dioxide sensors.

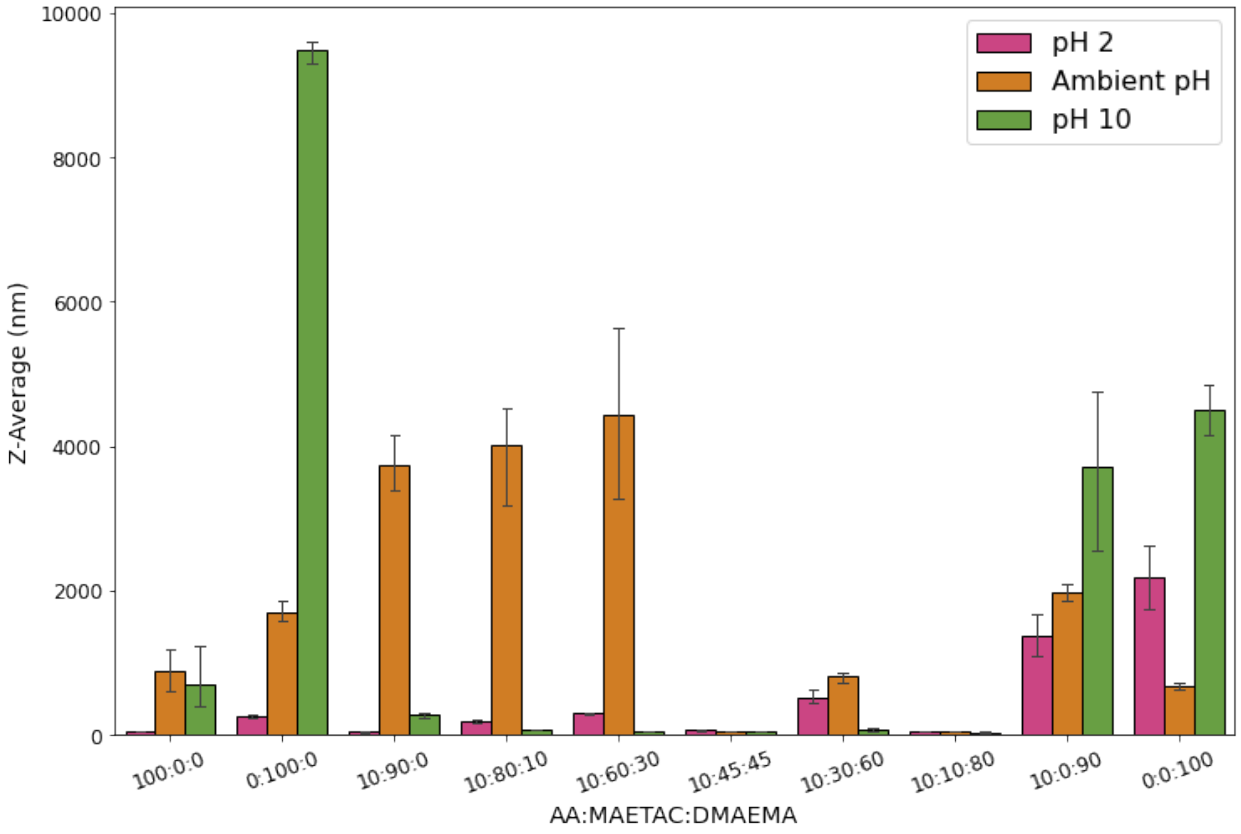



Figure 5.8: Z-Average in nm (measured by DLS) against AA:MAETAC:DMAEMA (random copolymer samples) at pH 2 (pink), ambient (orange) and 10 (green) along with their respective errors. Thus, 100:0:0 is 100% acrylic acid.

Figure 5.8 shows the average particle size (also known as z-average size) in nanometers of the random copolymers in bulk solution with an increase in DMAMEMA content at a concentration of 200 ppm. The size of the block copolymers was measured at three different pH levels (Table 5.3): *ca.* pH 2, set using 1M HCl; ambient pH, representing the natural pH of the random copolymers without any influence of acid or base, in deionised water at 200 ppm; and *ca.* pH 10, set using 1M NaOH. These measurements showed how the random copolymers change under different environments and how they affect their overall size in deionised water.

It must be noted that the z-average measurement assumes the particles are spherical. However, this assumption may not hold true for this system with random copolymers due to the presence of three different components.

Figure 5.8 shows that the size of pure AA (100:0:0) remains relatively small across all pH values, suggesting that the polymer chains are well-solvated and exhibit minimal aggregation. The slight increase in size at ambient pH and pH 10, compared to pH 2, is likely due to ionisation and electrostatic repulsion, which slightly expands the polymer chains. This behaviour aligns with existing literature, indicating that protonation at acidic pH reduces the negative charge density on AA, leading to a more compact polymer structure.

For MAETAC, the size at pH 10 is significantly larger, *ca.* 9000 nm, indicating substantial aggregation, while the sizes at pH 2 and ambient pH are much smaller. Pure DMAEMA has a small size at ambient pH, with a moderate increase at both pH 2 and pH 10.

Random copolymer samples 10:90:0, 10:80:0, and 10:60:30 show an increase in size at ambient pH, with much smaller sizes at pH 2 and pH 10. The 10:45:45 sample maintains a relatively low size of $54.10 \pm 2.69$ nm for all three pH values. The 10:30:60 sample exhibits an increase in size at pH 2 and ambient pH but remains relatively small at pH 10. For the 10:0:90 random copolymer, the size increases as the pH increases.

At acidic pH, the carboxyl groups of AA are protonated for the random copolymers shown in Figure 5.8, reducing electrostatic repulsion among polymer chains and leading to smaller sizes. This is consistent with literature indicating that protonation reduces the negative charge density on AA, causing the polymer chains to become more compact.

MAETAC, being a quaternary ammonium salt, maintains a positive charge regardless of pH as shown in Figure 5.4. This positive charge can lead to moderate aggregation due to electrostatic attraction between the negatively charged AA units and positively charged MAETAC units, even at low pH.

At alkaline pH, the carboxyl groups of AA are deprotonated, increasing electrostatic repulsion and potentially leading to larger aggregates due to increased solubility and swelling.

For DMAEMA, the increase in size at pH 10 can be attributed to the decreased protonation of the tertiary amine groups, reducing the positive charge and increasing hydrophobic interactions, leading to moderate aggregation.

The copolymers exhibit diverse behaviours depending on their composition and the pH of the solution. Sizes at ambient pH are generally larger due to complex interactions between the different monomer units. At pH 10, polymers show moderate aggregation due to increased electrostatic repulsion and decreased protonation of amine groups. Conversely, at pH 2, polymers are more compact due to reduced repulsion and increased protonation.

Overall, the hydrodynamic size of the copolymer samples is heavily influenced by their composition and the pH of the solution. MAETAC-rich compositions exhibit significant aggregation, especially at higher pH levels, resulting in larger hydrodynamic sizes. Acrylic acid (AA) tends to reduce aggregation due to its anionic nature, while DMAEMA, which can be protonated, generally decreases aggregation at lower pH levels. The balance among these components ultimately determines the size and behaviour of the copolymer in solution.

### 5.2.3 The Effect of pH on the Random Copolymers' Zeta potential in Bulk Solution

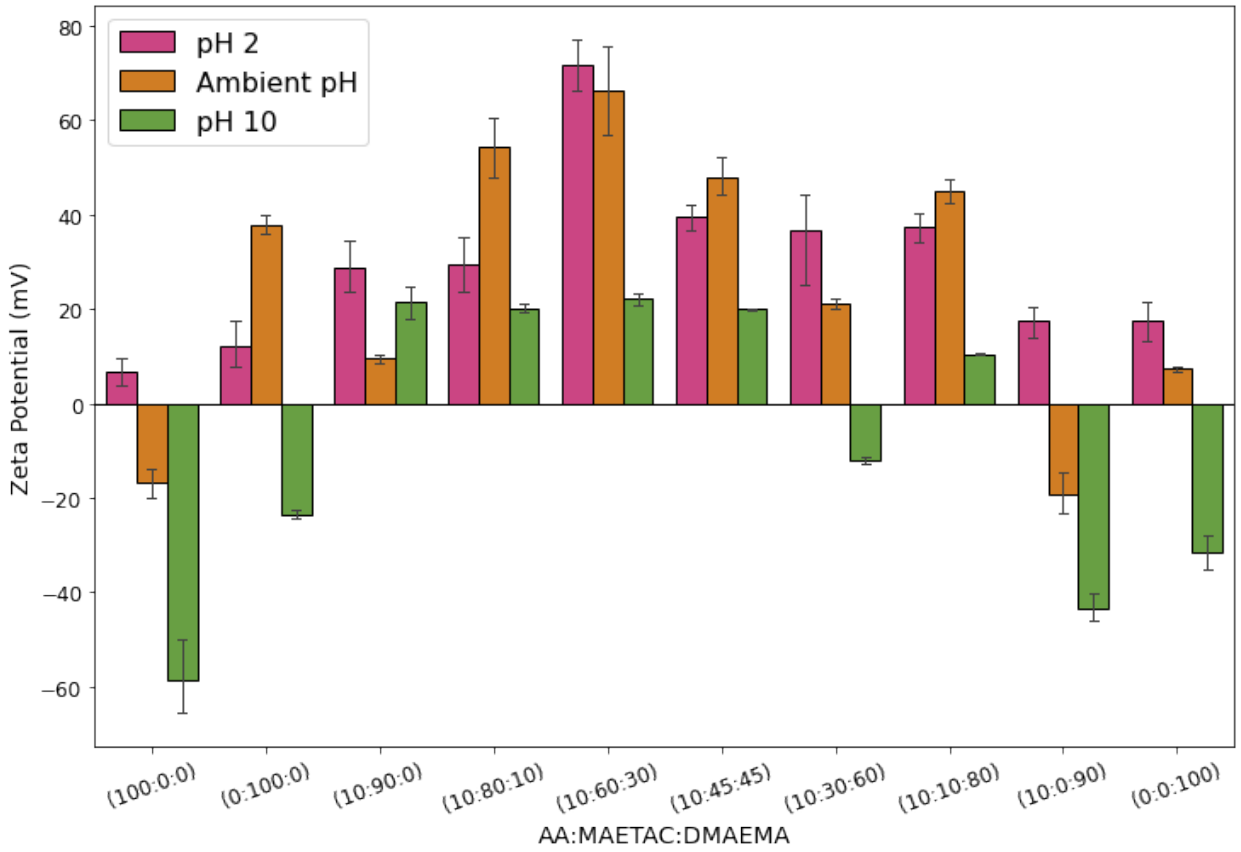



Figure 5.9: Zeta potential in millivolts (mV) (measured by DLS, see section 3.4) for the AA:MAETAC:DMAEMA random copolymer samples at pH 2 (pink), ambient (orange) and 10 (green) along with their respective errors.

Figure 5.9 illustrates the zeta potential (mV) of the various polymer compositions at three different pH levels: pH 2, ambient pH, and pH 10. The compositions are displayed as ratios of AA along the x-axis, with the zeta potential measured in millivolts (mV). Zeta potential measures the magnitude of electrostatic charge repulsion or attraction between particles, with higher positive or negative values indicating greater stability in the random copolymer mixture.

For most compositions, the zeta potential is positive at pH 2 and ambient pH, indicating that the surface of the particles is protonated in acidic and neutral conditions, leading to positive charges on the random copolymers. These positive zeta potentials suggest particle repulsion from the other particles within the bulk solution, typically preventing aggregation and enhancing the stability of the random copolymer mixtures. At pH 10, however many compositions exhibit negative zeta potentials, indicating deprotonation where surface groups lose protons in basic conditions, resulting in negative charges. The negative zeta potentials suggest particle repulsion under basic conditions, similarly preventing aggregation and maintaining the stability of the random copolymers in solution.

For the 100% acrylic acid (AA) (100:0:0) composition in Figure 5.9, the zeta potential is slightly positive at pH 2, slightly negative at ambient pH, and highly negative around -60 mV at pH 10. This significant shift indicates strong deprotonation, leading to enhanced stability due to electrostatic repulsion in basic conditions of AA.

The 0:100:0 composition, 100% MAETAC, consistently shows positive zeta potentials of around +15 mV at pH 2 and +40 mV at ambient pH, with a slight drop to around -20 mV at pH 10, reflecting minor deprotonation effects. For the 10:90:0 composition, the zeta potential remains positive at pH 2, ambient pH and at pH 10. The 10:80:10 composition exhibits positive zeta potentials across all pH levels, peaking at around +55 mV at ambient pH, suggesting stable colloidal behaviour with minimal pH-induced charge alteration. In contrast, the 10:60:30 composition has a high positive zeta potential of +70 mV at pH 2, which drops to +60 mV at ambient pH and remains slightly positive at pH 10, indicating strong protonation at low pH and stable random copolymer mixture. The 10:45:45 composition shows a high positive zeta potential at pH 2 and ambient pH, and about +20mV at pH 10, reflecting balanced protonation and deprotonation effects. For the 10:30:60 composition, the zeta potential is positive at pH 2 and ambient pH but shifts to slightly negative at pH 10, indicating deprotonation. The 10:10:80 composition demonstrates positive zeta potentials at all three pHs. The 10:0:90 composition has a slightly positive zeta potential at pH 2,

slightly negative at ambient pH, and highly negative around -50 mV at pH 10, indicating substantial deprotonation and enhanced stability in basic conditions. Finally, the 0:0:100 composition, which is 100% DMAEMA, exhibits a slightly positive zeta potential at pH 2, slightly positive at ambient pH, and highly negative around -40 mV at pH 10, reflecting significant pH-induced charge shifts. The net effect is that the mixed copolymers have higher zeta potentials than the pure components, and as the fraction of the DMAMEMA increases the zeta potential becomes more negative. Overall, whether positive or negative, compositions with high absolute values of zeta potential indicate stable colloidal systems due to electrostatic repulsion preventing particle aggregation.

### 5.2.4 Effect of varying pH on the Random Copolymers' Adsorption

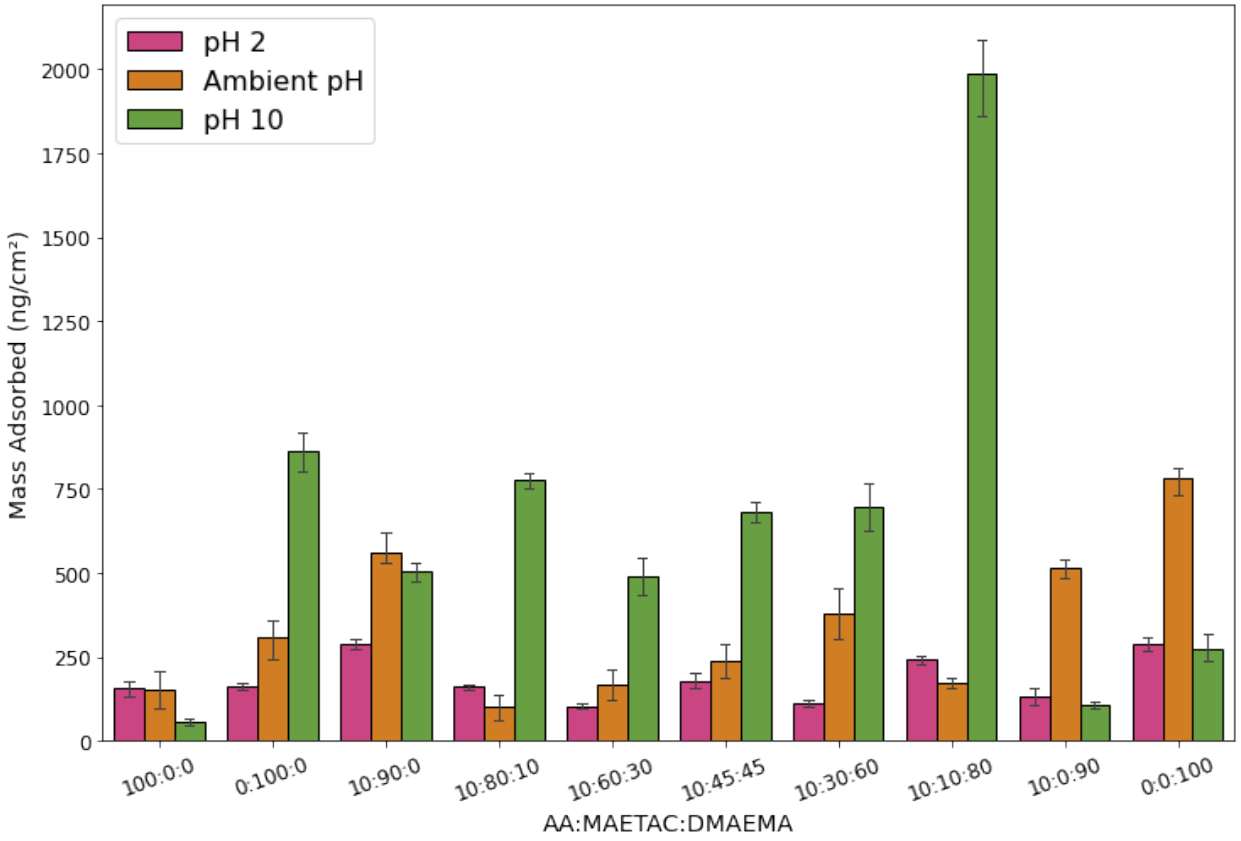



Figure 5.10: Mass Adsorbed of random co-polymers at pH 2, ambient pH and pH 10 at 200ppm.

Figure 5.10 depicts the mass adsorbed by the random copolymers in ng/cm$^2$ under three pH conditions: pH 2, ambient pH, and pH 10 (see Table 5.2). Generally, at pH 2, the mass adsorbed is low for all compositions. The adsorption behaviour significantly varies with pH and copolymer composition.

At pH 10, the mass adsorbed is generally higher compared to pH 2 and ambient pH across most compositions. Specifically, at pH 2, the adsorbed mass is consistently lower than at ambient pH and pH 10 for all compositions, while the adsorption at ambient pH tends to be

intermediate between pH 2 and pH 10.

For the 100% AA (100:0:0) composition, the mass adsorbed decreases as pH increases, suggesting more effective interaction with the sensor surface under acidic conditions. For 100% MAETAC (0:100:0), the mass adsorption increases from pH 2 to pH 10, indicating enhanced interaction with the sensor surface in alkaline conditions. The 100% DMAEMA (0:0:100) composition shows the highest adsorption at ambient pH. The 10:10:80 composition exhibits particularly high adsorption at pH 10, significantly higher than at pH 2 and ambient pH. Compositions with a balanced ratio of MAETAC and DMAEMA (e.g., 10:45:45) demonstrate higher adsorption at pH 10 than at pH 2 and ambient pH. This significant increase in adsorbed mass at pH 10 indicates stronger interactions between the copolymers and the silicon dioxide QCM sensor surface in alkaline conditions. This is likely due to the increased ionisation of functional groups on the copolymers at higher pH, leading to stronger electrostatic interactions with the sensor surface. Conversely, the lower adsorption at pH 2 can be attributed to the protonation of functional groups, resulting in reduced electrostatic attraction between the copolymers and the QCM sensor surface. Ambient pH results indicate moderate interaction, likely due to partial ionisation of functional groups.

The compositions 10:90:0 and 10:80:10 show higher adsorption at pH 10, indicating that a higher proportion of MAETAC in the copolymer leads to stronger interaction with the sensor in alkaline conditions. The 10:10:80 composition shows significantly higher adsorption at pH 10 compared to other pH levels, indicating a unique synergistic interaction between the three monomers under alkaline conditions.

The composition 10:10:80 (AA:MAETAC:DMAEMA) shows the highest adsorption at pH 10, possibly due to a unique balance of hydrophilic and hydrophobic interactions facilitated by the presence of all three monomers. At pH 10, DMAEMA groups become more ionised, enhancing electrostatic interactions with the sensor surface. Meanwhile, the presence of MAETAC contributes to strong ionic interactions, and AA might provide additional sta-

bilisation through hydrogen bonding and ionic interactions. The specific ratio of 10:10:80 creates an optimal environment where the different functional groups can interact synergistically with the QCM sensor surface, leading to higher mass adsorption compared to other compositions.

The data shows that adsorption of random copolymers on a silicon dioxide QCM sensor is significantly influenced by the pH of the solution and the copolymer composition. Higher adsorption at pH 10 suggests favourable conditions for stronger interactions between the copolymers and the sensor surface in alkaline environments. The 10:10:80 composition stands out with the highest adsorption at pH 10, indicating a potential optimal formulation for applications requiring strong adsorption under alkaline conditions.

### 5.2.5 Effect of Varying pH on the Random Copolymers' Rate Constant for Adsorption

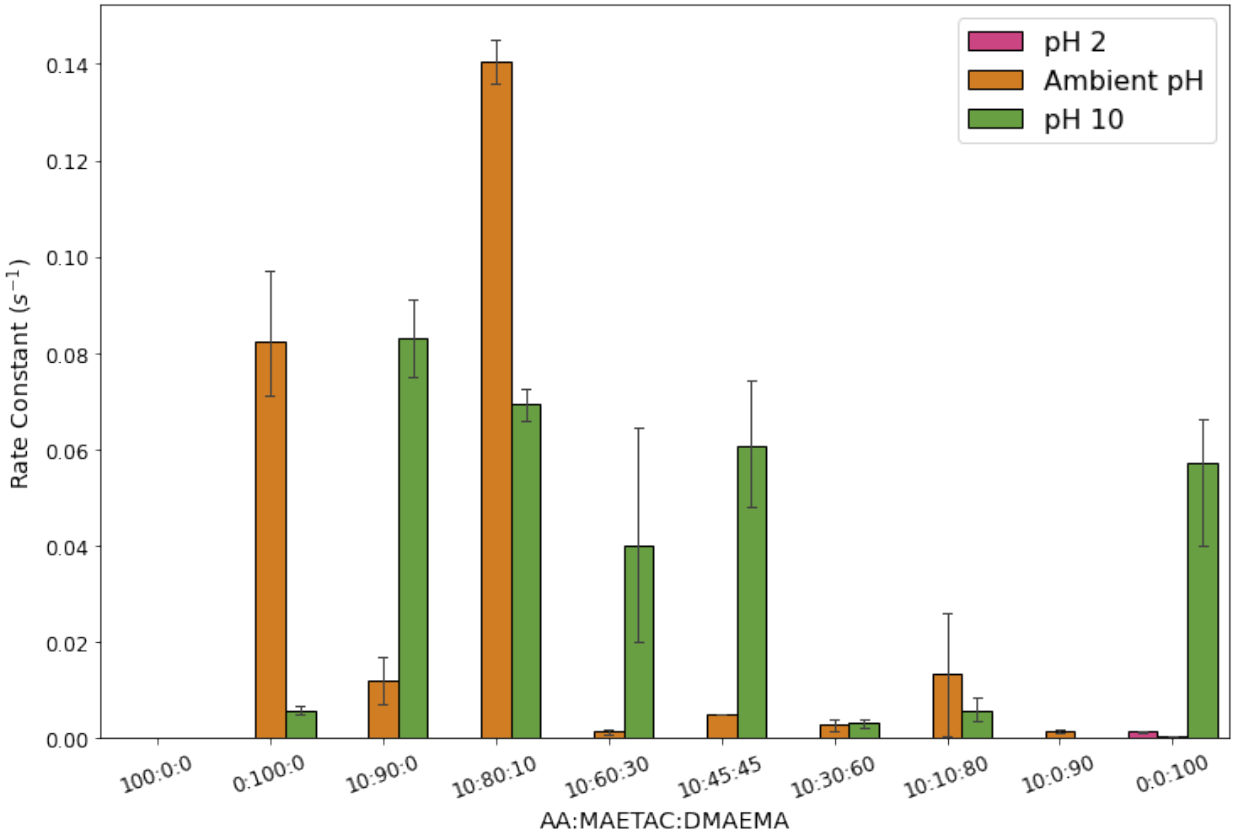



Figure 5.11: Rate constant of random co-polymers at pH 2, ambient pH and pH 10 at 200ppm.

Figure 5.11 presents the rate constants ($s^{-1}$) for various random copolymer compositions of AA:MAETAC:DMAEMA, determined using the Langmuir isotherm at different pH levels: pH 2, ambient pH, and pH 10. The polymers consist of different ratios of Acrylic Acid (AA), Methacryloyloxyethyltrimethyl Ammonium Chloride (MAETAC), and Dimethylaminoethyl Methacrylate (DMAEMA). Prior to adsorbing the random copolymers onto the silicon dioxide ($SiO_2$) QCM sensor, the sensor was pre-exposed to deionised water adjusted to the respective pH levels, influencing the sensor's surface charge and interaction potential with

the polymers.

The rate constants for pH 2 could not be obtained as the slope of the mass adsorbed and the rate of adsorption were too low to be fitted to the Langmuir isotherm equation. The highest rate constant was observed for the 10:80:10 composition. Compositions with higher MAETAC content (e.g., 0:100:0 and 10:80:10) display relatively high rate constants under ambient pH conditions, indicating strong interaction. At pH 10, the random copolymers adsorb more quickly onto the silicon dioxide sensor compared to pH 2 and ambient pH, with the highest rate constant observed for the 10:90:0 composition.

The variations in rate constants across different pH levels can be attributed to the chemical behaviour and interactions of the polymer components under acidic, neutral, and basic conditions. At pH 2, the silicon dioxide surface is less negatively charged due to protonation, leading to reduced electrostatic interaction. AA is protonated, resulting in weaker electrostatic interactions with the less negatively charged sensor surface. MAETAC, being positively charged, has reduced interaction with the less negatively charged surface. DMAEMA is also protonated, leading to limited interaction. The overall low rate constants at pH 2 reflect these limited electrostatic interactions.

At ambient pH, typically around pH 5-7, the silicon dioxide surface is moderately negatively charged. AA is partially ionised, providing some negative charge for electrostatic interaction. MAETAC remains positively charged, interacting strongly with the negatively charged surface. DMAEMA is partially protonated, providing moderate electrostatic interactions. High rate constants for compositions like 10:80:10 suggest that MAETAC has a strong affinity for the moderately negatively charged surface, with the combination of partially ionised AA and positively charged MAETAC enhancing surface adsorption.

At pH 10, the silicon dioxide surface is highly negatively charged due to deprotonation. AA is fully ionised, providing a strong negative charge that interacts effectively with the positively charged sites on the sensor surface. MAETAC retains its positive charge, maintaining strong

interactions with the highly negatively charged surface. Higher rate constants for mixed compositions like 10:60:30 and 10:45:45 indicate strong electrostatic interactions between fully ionised AA, positively charged MAETAC, and the sensor surface, leading to enhanced adsorption.

For the 100:0:0 composition (high AA content), the low rate constants across all pH levels indicate that AA alone, even when fully ionised, does not provide sufficient interaction strength with the sensor surface. The 0:100:0 composition (high MAETAC content) shows high rate constants at ambient pH, consistent with MAETAC's strong interaction potential due to its positive charge aligning well with the moderately negatively charged surface. The 0:0:100 composition (high DMAEMA content) has a moderate rate constant at pH 10, showing steady but not exceptional reactivity, possibly due to reduced interaction strength compared to compositions with MAETAC.

Interestingly, some of the mixed compositions, such as 10:80:10 and 10:60:30, show high rate constants at basic pH, suggesting that a balanced mixture of AA, MAETAC, and DMAEMA maximises interaction with the highly negatively charged surface, leveraging electrostatic attractions. The 10:10:80 composition has lower rate constants compared to 10:80:10 at ambient pH, indicating that a higher MAETAC content enhances the rate constant due to its strong positive charge interacting effectively with the sensor surface.

### 5.2.6 Relationships Between Measured Data

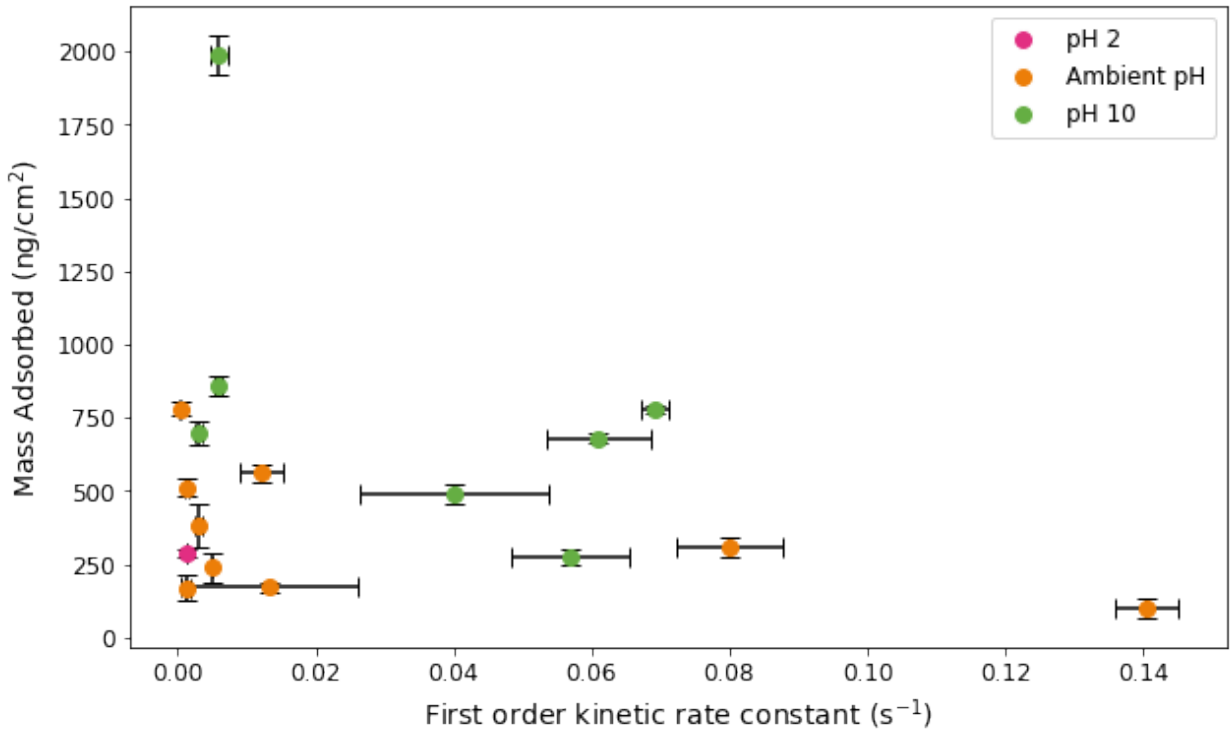



Figure 5.12: Correlation plot of mass adsorbed vs. rate constant of the random co-polymers at pH 2, ambient pH and pH 10 at 200ppm.

A series of calculations were carried out to relate the data shown in Figures 5.8 - 5.11, to identify any effects. Figure 5.12 illustrates adsorption kinetics, with the x-axis denoting the first-order kinetic rate constant ($s^{-1}$) and the y-axis showing mass adsorbed ($ng/cm^2$). Each data point is colour-coded by pH: pink for pH 2, orange for ambient pH, and green for pH 10, with error bars indicating measurement variability.

Across different pH levels, observations reveal distinct patterns. At pH 2 (pink points), minimal adsorption and slow adsorption is evident with only one data point showing a low rate constant ($\sim$0.001 $s^{-1}$). The highest adsorption is for 10:10:80, but this also showed a slow adhesion rate. Adsorption at ambient pH (orange) exhibits a broader range of rate constants, primarily clustering at low values ($<$0.08 $s^{-1}$), albeit with greater variability in

mass adsorbed. As noted in the discussion of Figure 5.11, the pH 2 adsorption data is mostly so low that the kinetics cannot be identified. pH 10 (green points) displays a wider spectrum of rate constants, with some points indicating significantly higher mass adsorbed (up to $\sim$2000 ng/cm$^2$).

Regarding rate constants, low values (0.00 to 0.04 s$^{-1}$) correspond to substantial mass adsorption at both ambient pH and pH 10, with pH 10 showing the highest levels. Intermediate rate constants (0.04 to 0.08 s$^{-1}$) are predominantly observed at pH 10 and result in moderate adsorption. The highest rate constants (>0.08 s$^{-1}$) are shown at ambient pH, indicating faster adsorption rates with lower mass adsorbed compared to pH 10 at lower rate constants. Error bars highlight variability, particularly notable at pH 10 and ambient pH, underscoring reliable measurements across different pH conditions.

At pH 2, the single data point with a low rate constant and minimal adsorption suggests acidity inhibits adsorption, likely due to protonation effects hindering interactions. At ambient pH, the wider range and higher variability in adsorption reflect environmental complexity. Higher rate constants with moderate adsorption at pH 10 suggest a balance between rapid adsorption and equilibrium dynamics. At pH 10, higher mass adsorption at lower rate constants suggests alkalinity enhances adsorption, possibly due to deprotonation effects facilitating adsorbate-adsorbent interactions. However, very rapid kinetics may limit complete adsorption due to reduced interaction time between the polymer and sensor surface.

It is clear that the relationship between the first-order rate constant and mass adsorbed is influenced by pH, indicating complex adsorption mechanisms involving chemical interactions, surface availability, and diffusion effects. Mechanistic insights suggest that at lower pH, protonation may inhibit adsorption sites or adsorbate binding. Variability at ambient pH suggests competing processes such as adsorption and desorption or varying surface charges. At higher pH, deprotonation enhances adsorption, but rapid kinetics may restrict equilibrium mass adsorption due to inadequate interaction time. Suggesting that fast rates lead to low

adsorption as there is some indication that an increase in mass adsorbed onto the surface relates to a decrease in rate constant as shown in Figure 5.12.

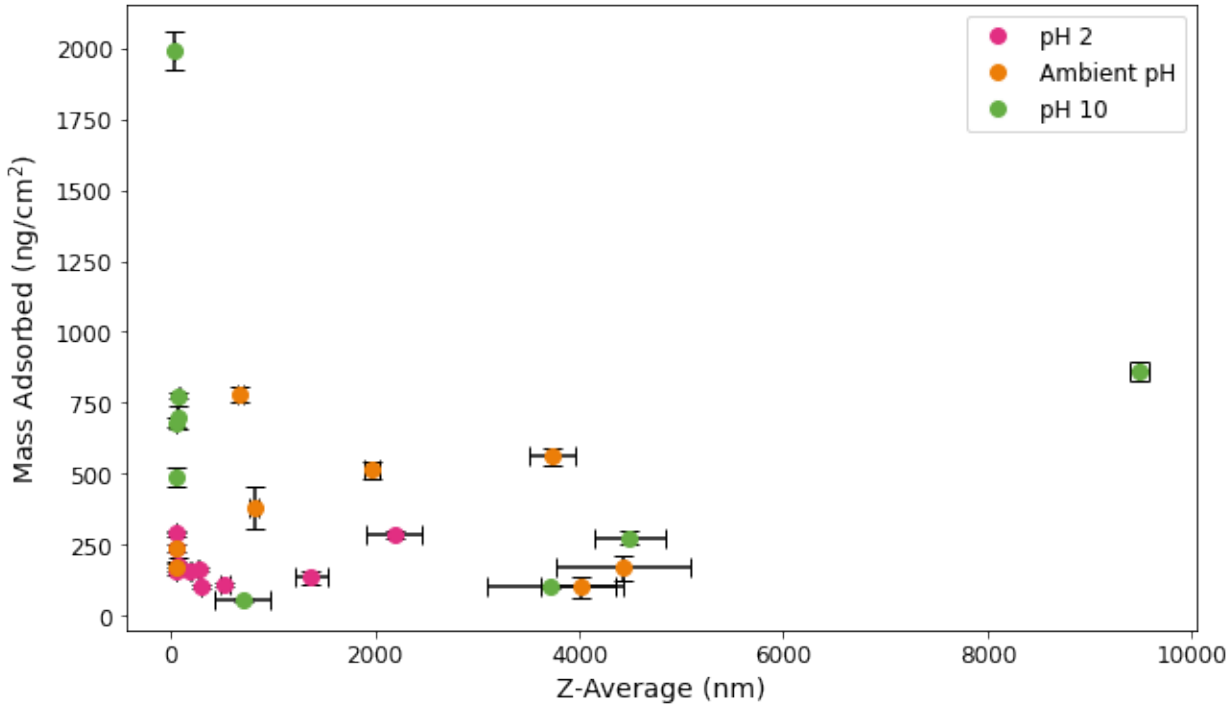



Figure 5.13: Correlation plot of mass adsorbed vs. z-average of the random co-polymers at pH 2, ambient pH and pH 10 at 200ppm.

Figure 5.13 correlates the the mass adsorbed (ng/cm$^2$) on the y-axis, measured using Quartz Crystal Microbalance (QCM), plotted against the Z-average size of polymers on the x-axis, determined *via* Dynamic Light Scattering (DLS).

At pH 2 (pink), data points are concentrated around smaller z-average sizes, correlating with relatively low mass adsorption. At ambient pH (orange points), the data covers a spectrum of polymer sizes, indicating moderate mass adsorption. pH 10 (green points) displays data points across a wide range of polymer sizes, with prominent outliers indicating both high mass adsorption associated with a large polymer size, and one where high adsorption is associated with a low polymer size.

For smaller polymer sizes, both pH 2 and ambient pH exhibit some level of adsorption, whereas pH 10 shows higher mass adsorption for a subset of points in comparison to pH 2 and ambient pH. Intermediate polymer sizes, particularly observed at ambient pH, indicate moderate adsorption levels. Larger polymer sizes observed at pH 10 include a significant outlier with notably high mass adsorption, suggesting distinct adsorption behaviour under alkaline conditions.

At pH 2, data points highlight smaller polymer sizes and lower mass adsorption, implying that acidic conditions restrict the effective adsorption of larger polymers. Protonation effects likely hinder the formation, stability, or surface interaction of larger polymer structures. At ambient pH, a moderate correlation between polymer size and adsorption suggests that polymer size influences adsorption to some degree. The interplay between polymer stability and surface interactions modulates adsorption capacity. At pH 10, a notable data point with very high mass adsorption at a large polymer size suggests that alkaline conditions significantly enhance adsorption. Deprotonation effects may improve polymer-surface interactions or stabilise larger polymer structures. The non-linear relationship between Z-average size and mass adsorbed across pH levels indicates complexity influenced by polymer stability, surface interactions, and pH conditions.

Lower pH levels favour the adsorption of smaller polymers due to limitations in stability and interaction. At neutral pH, a range of polymer sizes exhibit moderate adsorption, reflecting a dynamic equilibrium between polymer formation and surface interaction. At higher pH, larger polymers demonstrate notably higher adsorption, likely due to enhanced stability and stronger interaction capabilities.

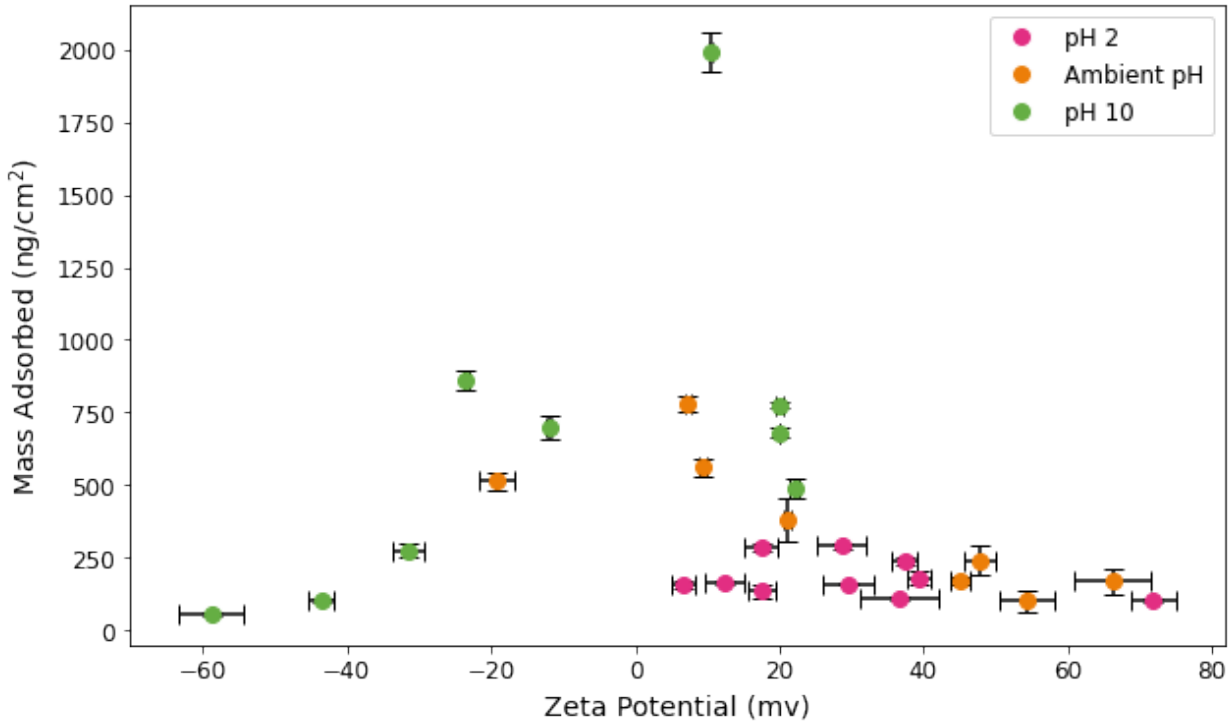



Figure 5.14: Correlation plot of mass adsorbed vs. zeta potential of the random co-polymers at pH 2, ambient pH and pH 10 at 200ppm.

Figure 5.14 correlates the behaviour between mass adsorbed in ng/cm$^2$ (y-axis) and zeta potential in mV (x-axis) across different pH levels. The data points are categorised into three pH conditions: pH 2, ambient pH, and pH 10, represented by pink, orange, and green markers, respectively. Error bars are included for both axes, indicating the variability and uncertainty in the measurements.

At pH 2 (pink), the data points show relatively low mass adsorption and are spread over a range of positive zeta potentials. At ambient pH (orange), the data points cluster around neutral and positive zeta potential values with moderate mass adsorption. At pH 10 (green), the data points are dispersed across a wide range of negative and positive zeta potentials, with some points showing very high mass adsorption values. Notably, there is a significant spread in the data points at pH 10, with some points showing high mass adsorption at both

positive and negative zeta potentials. In contrast, at ambient pH, the data points are more clustered around neutral/positive zeta potentials, indicating less variability compared to the other pH conditions.

Mass adsorption varies with pH, indicating that adsorption is influenced by the surface charge of the particles. At pH 2, lower mass adsorption could be due to repulsive forces between positively charged surfaces and may be due to the QCM sensor being pre-exposed to deionised water adjusted to pH 2. At pH 10, the higher mass adsorption might be due to attractive forces between the positively charged MAETAC and negatively charged sensor surface. The plot suggests a complex relationship between mass adsorption and zeta potential. At higher zeta potentials (both positive and negative), mass adsorption tends to be higher, indicating that extreme surface charges enhance adsorption. Neutral or low zeta potentials correspond to moderate mass adsorption, suggesting less effective adsorption. Overall, the adsorption is highest at low zeta potential, both positive and negative, suggesting that high zeta potentials of both charges reduce the mass adsorbed. The greatest adsorption occurs at a zeta potential of +18 mV, and all the points for mass adsorbed $> 500$ ng/cm$^2$ have zeta potentials in the range of +25 to -25 mV. Figure 5.14 also shows a clear effect of low zeta potential, as pH increases the zeta potential decreases.

The variability in mass adsorption, especially at high pH, may be due to differences in particle size, aggregation, or experimental conditions such as ionic strength and temperature. The plot demonstrates the significant influence of pH on both zeta potential and mass adsorption.

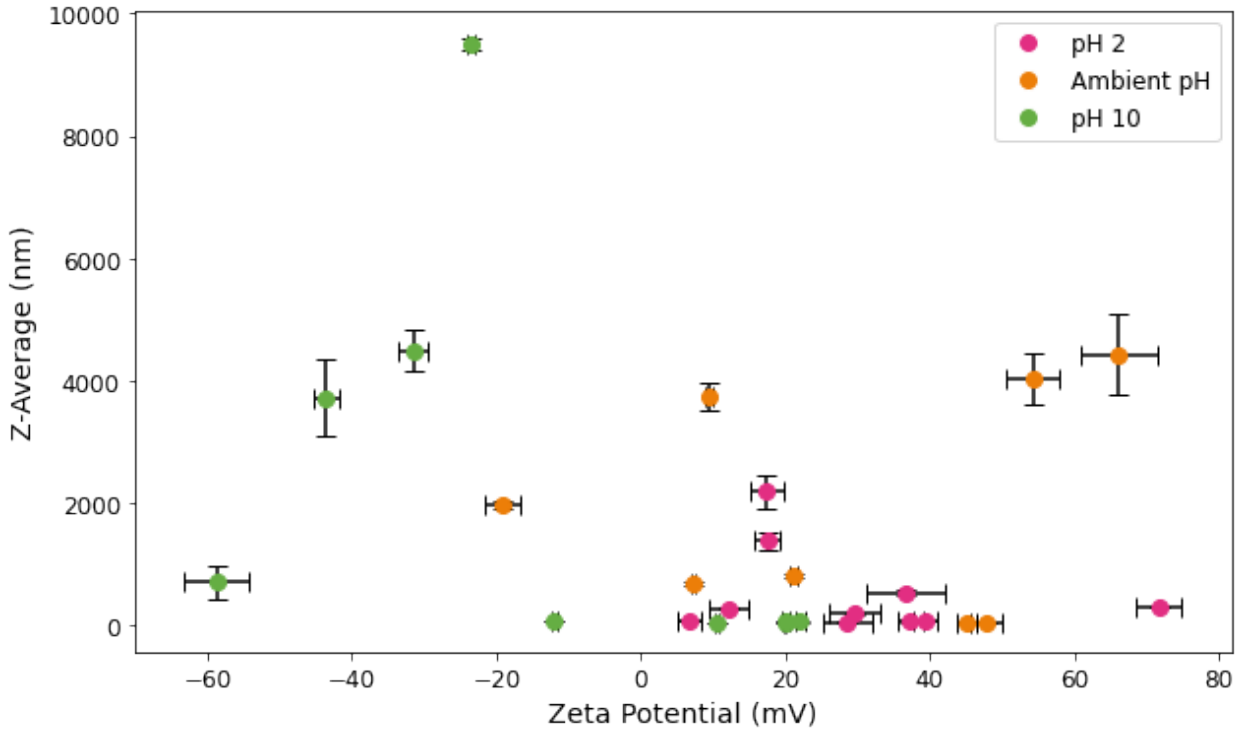



Figure 5.15: Correlation plot of z-average vs. zeta potential of the random co-polymers at pH 2, ambient pH and pH 10 at 200ppm.

Figure 5.15 shows the correlation between z-average (y-axis) in nanometers and zeta potential (x-axis) in millivolts (mV), both measured using Dynamic Light Scattering (DLS). The z-average represents the average hydrodynamic diameter of particles, while the zeta potential indicates the bulk charge. Data points are categorised into three pH conditions: pH 2 (pink), ambient pH (orange), and pH 10 (green).

At pH 2, data points show positive zeta potentials, mostly clustered around low to moderate z-average values. For ambient pH, the points are distributed around moderate zeta potentials with moderate to high z-average values. In contrast, at pH 10, data points exhibit negative zeta potentials and a wide range of z-average values, including some very high values.

The distribution of data points further highlights distinct characteristics across pH conditions. At pH 2, z-average values are generally low, with positive zeta potentials. At ambient

pH, z-average values range from moderate to high, with zeta potentials varying from slightly negative to highly positive. At pH 10, z-average values are highly variable, with negative zeta potentials, including some points with very high z-average values, indicative of large particle sizes or aggregation.

The effect of pH on zeta potential is evident. At pH 2, the zeta potential is positive, suggesting protonation of surface groups leading to a positively charged surface. At ambient pH, the zeta potential varies around neutral to positive, indicating balanced surface charge conditions. At pH 10, the zeta potential is negative, likely due to the deprotonation of surface groups, resulting in a negatively charged surface.

Regarding the effect of pH on z-average, at pH 2, the low z-average values suggest smaller, stable particles in acidic conditions. At ambient pH, particle sizes range from moderate to high, indicating possible aggregation or growth in a neutral pH environment. At pH 10, z-average values are highly variable, with some points indicating large particle sizes or aggregation under alkaline conditions.

The correlation between z-average and zeta potential reveals that at pH 2, positive zeta potentials correspond to smaller particle sizes, indicating stable conditions without significant aggregation. At ambient pH, variable zeta potentials correlate with moderate to high particle sizes, suggesting varying degrees of particle stability and aggregation. At pH 10, negative zeta potentials correlate with a wide range of particle sizes, including very large sizes, indicating potential instability and aggregation under alkaline conditions.

The data suggest that pH significantly impacts both zeta potential and particle size. Acidic conditions (pH 2) lead to smaller, positively charged particles, while alkaline conditions (pH 10) result in larger, negatively charged particles with a tendency towards aggregation. Overall there is no strong correlation between the particle size and zeta potential. Figure 5.15 again, shows that as pH increases the zeta potential decreases.

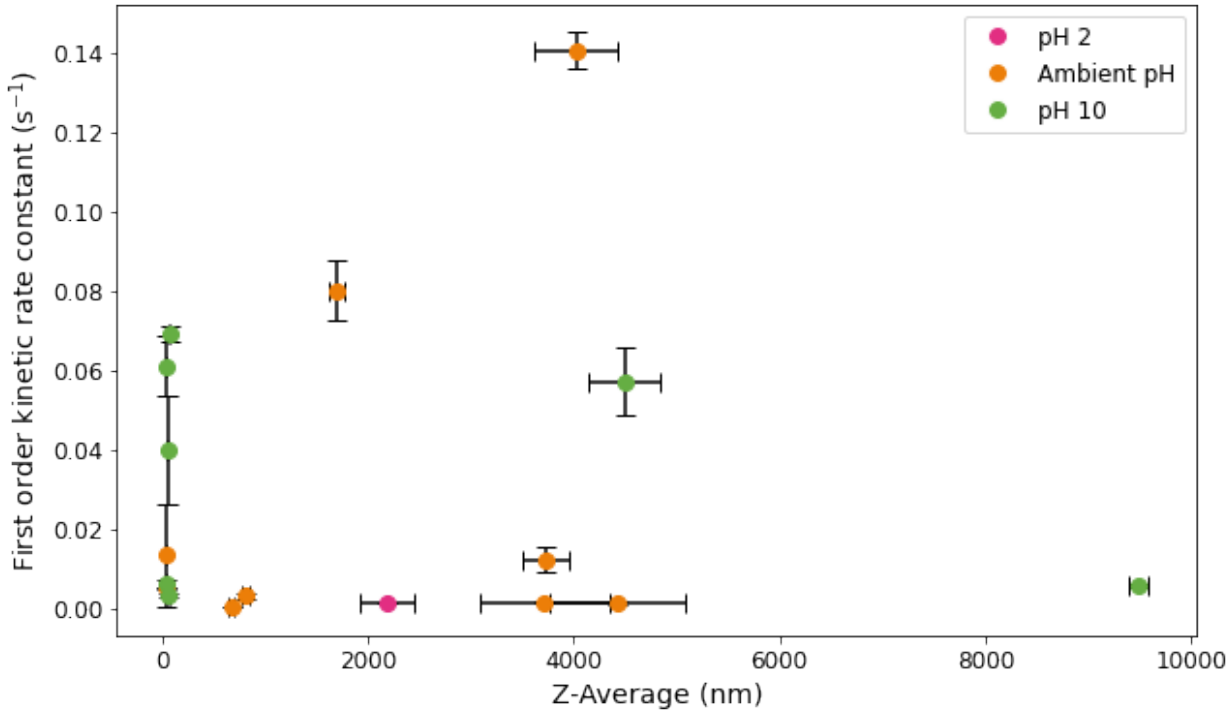



Figure 5.16: Correlation plot of rate constant vs. z-average of the random co-polymers at pH 2, ambient pH and pH 10 at 200ppm.

Figure 5.16 correlates the first-order kinetic rate constant (y-axis) in $s^{-1}$ and the z-average (x-axis) in nanometers, with data obtained using Quartz Crystal Microbalance (QCM) and Dynamic Light Scattering (DLS), respectively. The kinetic rate constants were derived using the Langmuir isotherm model, discussed in Chapter 3. The data points are categorised into three pH conditions: pH 2 (pink), ambient pH (orange), and pH 10 (green).

At pH 2, the data point shows a low z-average value with low first-order kinetic rate constants. For ambient pH, data points spread across a range of z-average values, generally showing higher first-order kinetic rate constants. In contrast, at pH 10, data points exhibit a wide range of z-average values with variable first-order kinetic rate constants.

The distribution of data points highlights distinct characteristics across pH conditions. At pH 2, both the z-average value and the first-order kinetic rate constant is low. At ambient

pH, z-average values range from low to moderate, with higher kinetic rate constants. At pH 10, the z-average values vary widely, with moderate kinetic rate constants.

The effect of pH on the kinetic rate constant is evident. At pH 2, a low kinetic rate constant indicates slower reaction kinetics, correlating with smaller particle sizes. At ambient pH, higher kinetic rate constants suggest faster reaction kinetics, correlating with moderate particle sizes. At pH 10, moderate kinetic rate constants indicate intermediate reaction kinetics, correlating with a wide range of particle sizes.

Regarding the effect of pH on z-average, at pH 2, a low z-average value suggests smaller, stable particles under acidic conditions. At ambient pH, particle sizes are moderate, indicating a balanced environment conducive to faster kinetics. At pH 10, z-average values are highly variable, with some points indicating large particle sizes or aggregation under alkaline conditions.

The correlation between the kinetic rate constant and z-average reveals that at pH 2, the positive correlation between smaller z-average values and lower kinetic rate constants suggests that smaller particles have slower reaction kinetics. At ambient pH, higher kinetic rate constants correspond to moderate particle sizes, suggesting an optimal size range for faster reaction kinetics. At pH 10, the wide range of z-average values and moderate kinetic rate constants indicate variability in reaction kinetics, potentially due to aggregation.

The data suggest that pH significantly impacts both the kinetic rate constant and particle size. Acidic conditions (pH 2) result in smaller particles with slower kinetics, while ambient pH conditions yield moderate particle sizes with faster kinetics. Alkaline conditions (pH 10) produce a wide range of particle sizes with intermediate kinetics.

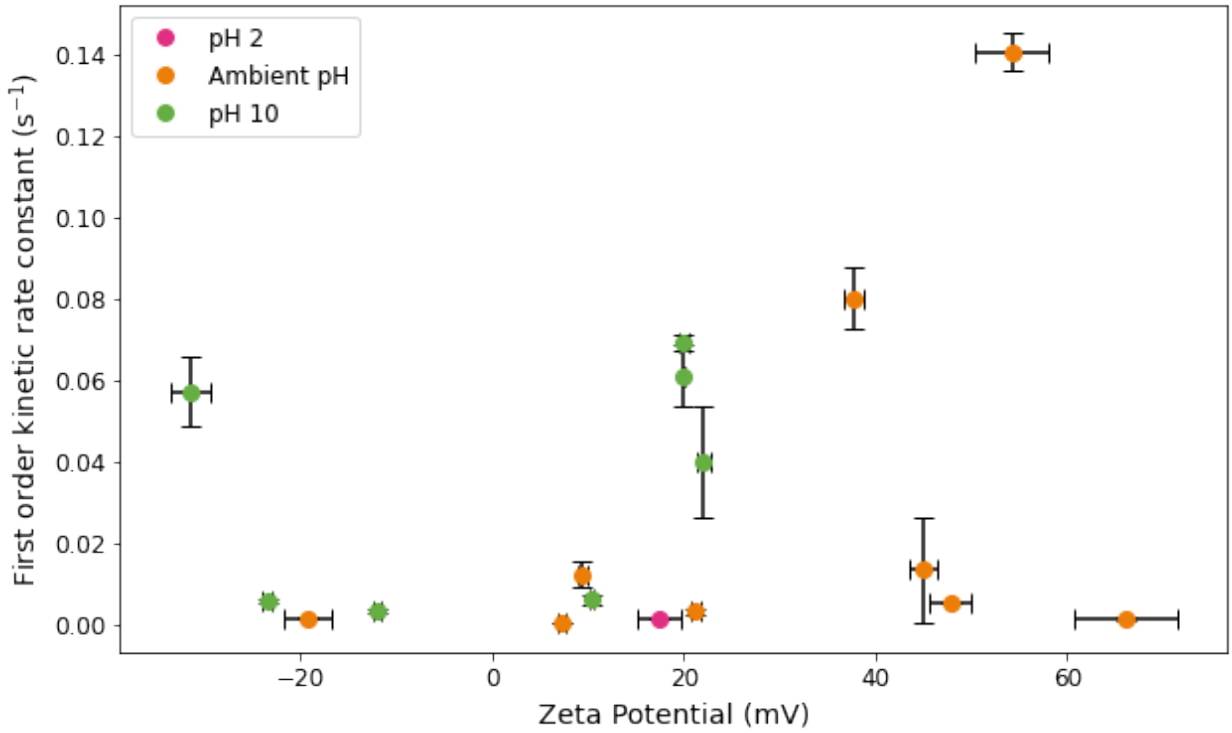



Figure 5.17: Correlation plot of rate constant vs. zeta potential of the random co-polymers at pH 2, ambient pH and pH 10 at 200ppm.

Figure 5.17 correlates the behaviour between the first-order kinetic rate constant (y-axis) in $s^{-1}$ and the zeta potential (x-axis) in millivolts (mV), both measured using Quartz Crystal Microbalance (QCM) and Dynamic Light Scattering (DLS), respectively. The kinetic rate constants were derived using the Langmuir isotherm model. The data points are categorised into three pH conditions: pH 2 (pink), ambient pH (orange), and pH 10 (green).

At pH 2, the data point shows a low zeta potentials with low first-order kinetic rate constants. For ambient pH, data points are distributed across a range of zeta potentials, generally showing higher first-order kinetic rate constants. At pH 10, data points show a wide range of zeta potentials with variable first-order kinetic rate constants.

The distribution of data points highlights distinct characteristics across pH conditions. At pH 2, the zeta potential value and first-order kinetic rate constant is low. At ambient pH,

zeta potential values range from low to high, with higher kinetic rate constants. At pH 10, zeta potential values vary widely, with kinetic rate constants showing moderate to high values.

The effect of pH on the kinetic rate constant is evident. At pH 2, the low kinetic rate constant indicates a slower reaction kinetic, correlating with a lower zeta potential value. At ambient pH, higher kinetic rate constants suggest faster reaction kinetics, correlating with a wide range of zeta potential values, mostly positive. At pH 10, the kinetic rate constants are moderate to high, indicating intermediate to fast reaction kinetics, correlating with a wide range of zeta potential values, both negative and positive.

Regarding the effect of pH on zeta potential, at pH 2, the zeta potential value is low and positive, suggesting protonation of surface groups leading to a positively charged surface. The zeta potential varies widely at ambient pH, ranging from slightly negative to highly positive, indicating balanced surface charge conditions. At pH 10, zeta potential values are highly variable, with both negative and positive values, likely due to the deprotonation of surface groups affecting surface charge.

The correlation between the kinetic rate constant and zeta potential reveals that at pH 2, a lower zeta potential value corresponds to a slower reaction kinetic. At ambient pH, higher kinetic rate constants correspond to a wide range of zeta potential values, suggesting an optimal surface charge for faster reaction kinetics. At pH 10, the wide range of zeta potential values and moderate to high kinetic rate constants indicate variability in reaction kinetics, potentially influenced by changes in surface charge.

The data suggest that pH significantly impacts both the kinetic rate constant and zeta potential. Acidic conditions (pH 2) result in lower zeta potentials with slower kinetics, while ambient pH conditions yield a wide range of zeta potentials with faster kinetics. Alkaline conditions (pH 10) produce highly variable zeta potentials with intermediate to fast kinetics.

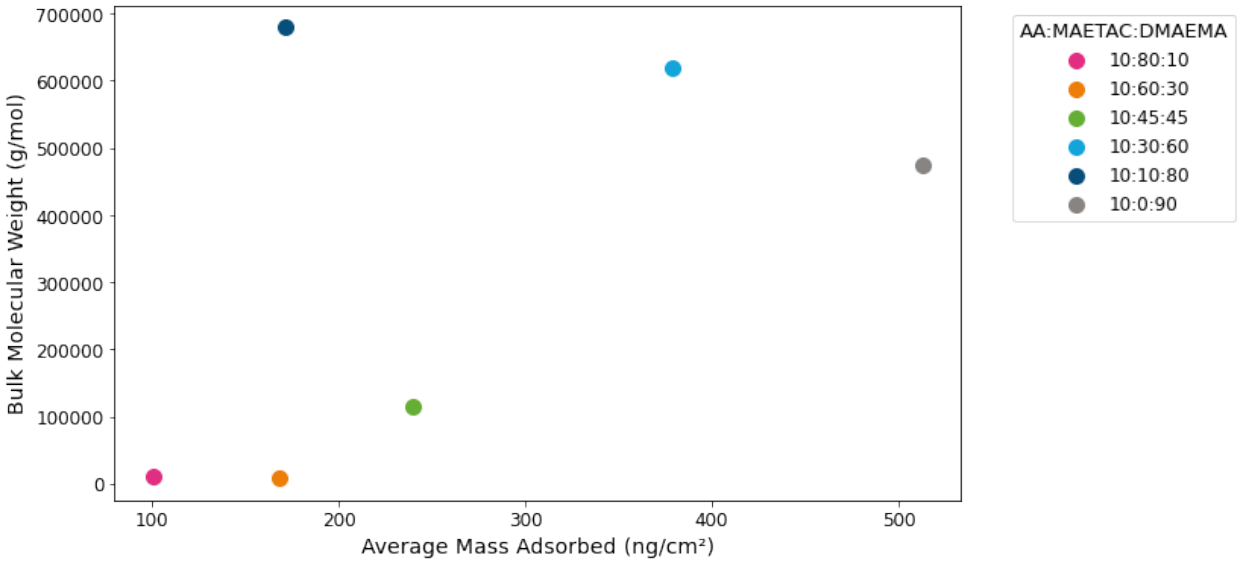



Figure 5.18a: Correlation plot of bulk molecular weight vs average mass adsorbed at 200ppm.

Figure 5.18(a) illustrates the relationship between bulk molecular weight (in g/mol) and average mass adsorbed (in ng/cm$^2$) for the various random copolymer compositions (AA:MAETAC:DMAEMA). As the average mass adsorbed increases, there is a general trend of increasing bulk molecular weight across the different compositions, suggesting a positive correlation between molecular weight and mass adsorbed. The data points form distinct clusters corresponding to each copolymer composition, suggesting that each composition has a unique adsorption behaviour. For example, the 10:80:10 composition (pink) shows both the lowest molecular weight and the lowest average mass adsorbed, while the 10:0:90 composition (grey) exhibits the highest values for both parameters. There is one outlier, with the highest molecular weight giving a low mass adsorbed.

This implies that as the molecular weight of the copolymer increases, its adsorption capacity also tends to increase. This effect could be attributed to larger molecules having more interaction sites and a greater surface area for adsorption, allowing them to cover more space on the surface. Consequently, this leads to an increased average mass adsorbed onto the sensor's

surface. The specific copolymer composition significantly affects adsorption behaviour. For instance, increasing the DMAEMA content (from 10:80:10 to 10:0:90) generally results in higher molecular weights and higher mass adsorbed, suggesting that DMAEMA-rich copolymers have a higher affinity for the surface, possibly due to electrostatic interactions or better conformational adaptability.

The increase in adsorption with molecular weight might also be attributed to entropic factors, where larger polymers adopt more favourable configurations upon adsorption, leading to higher overall adsorption. Additionally, specific interactions between the polymer functional groups and the surface could be contributing factors.

In summary, the data indicates a slight positive correlation between the bulk molecular weight of the random copolymers and their average mass adsorbed. Different copolymer compositions exhibit distinct behaviours, with DMAEMA-rich compositions (e.g., 10:0:90) showing higher molecular weights and greater adsorption.

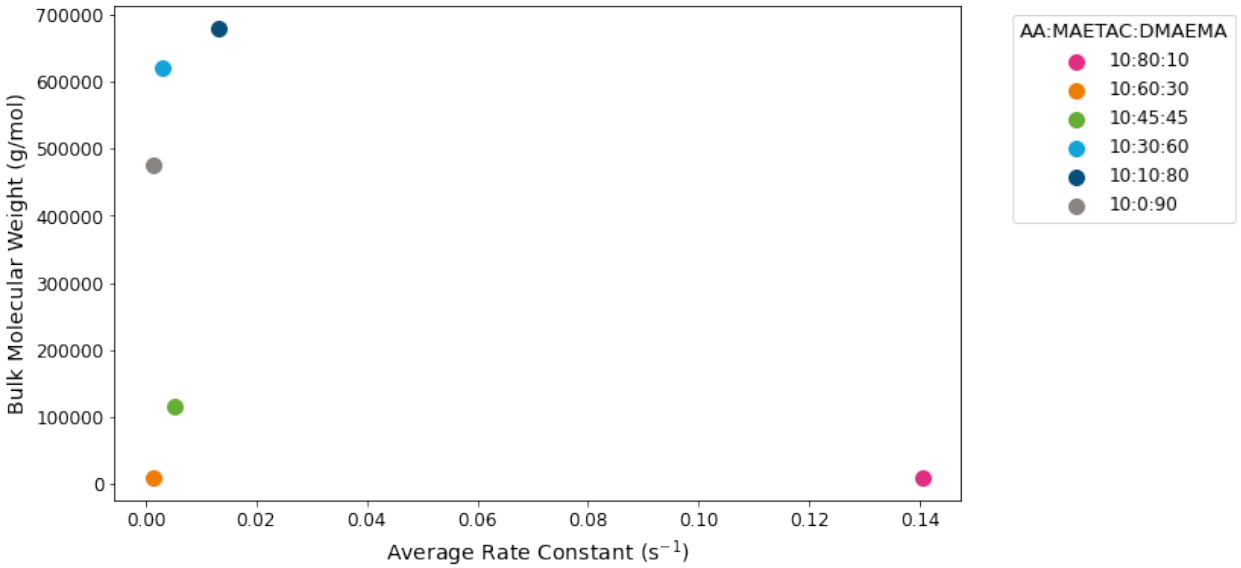



Figure 5.18b: Correlation plot of bulk molecular weight vs average rate constant at 200ppm.

Figure 5.18(b) plots bulk molecular weight (in g/mol) on the y-axis against the average rate constant (in $s^{-1}$ ) on the x-axis for various random copolymer compositions (AA:MAETAC:DMAEMA).

The data shows that there is no strong relationship between molecular weight and the rate constant. suggests that copolymers with lower molecular weights adsorb faster. There is one outlier, the 10:80:10 composition has a high rate constant, indicating rapid adsorption kinetics, here likely due to its lower molecular weight. Conversely, compositions like 10:0:90, with higher molecular weights, exhibit lower rate constants, indicating slower adsorption due to the larger size of the molecules, which might reduce their diffusion rate and increase steric hindrance during adsorption.

The data suggests that the adsorption kinetics could be diffusion-limited for higher molecular weight copolymers. The larger size reduces their diffusion coefficients, making their adsorption slower. Additionally, different copolymer compositions might interact differently with the surface, affecting their adsorption kinetics. The functional groups in the copolymers and their ability to interact with the surface could play a significant role. As sample 10:80:10 shows a low molecular weight, this may suggest that its particles experience more rapid Brownian motion, moving more quickly through the medium due to their smaller size. In general, smaller particles tend to move faster in solution because they are more easily affected by the random collisions with molecules in the medium.

In summary, the graph shows that there is no strong relationship between the bulk molecular weight of random copolymers and their average rate constant. Different copolymer compositions display distinct behaviours, with higher molecular weight compositions generally showing slower adsorption kinetics.

## 5.3 Conclusions

Chapter 5 explored the development and evaluation of innovative additives for glazed ceramics, focusing on the deposition characteristics of various random copolymers on silicon dioxide surfaces and the impact of pH on their behaviour. This research simulated conditions analogous to those found on glazed ceramic surfaces in toilet bowls, providing insights into how these copolymers might enhance antifouling properties.

The study employed Dynamic Light Scattering (DLS) and Quartz Crystal Microbalance (QCM) to analyse the interaction of the random copolymers with surfaces under varying pH conditions. The findings reveal that pH levels significantly affect the zeta potential and particle size of the copolymers in solution. At acidic pH (2), the copolymers form smaller, positively charged particles, indicating stable conditions with minimal aggregation. The particles exhibit moderate to high sizes in neutral pH environments with balanced surface charges, reflecting a dynamic equilibrium between stability and aggregation. Alkaline conditions (pH 10) lead to larger, negatively charged particles that are prone to aggregation, suggesting potential instability in such environments.

The mass adsorption of copolymers on silicon dioxide surfaces was closely related to pH levels. Acidic conditions hindered the effective adsorption of larger polymers due to protonation effects, while neutral pH facilitated moderate adsorption levels, suggesting a balance between polymer formation and surface interaction. Alkaline conditions, on the other hand, significantly enhanced adsorption, likely due to deprotonation effects that stabilise larger polymer structures and improve polymer-surface interactions.

Figure 5.2 illustrates the mass adsorption curves, highlighting that different copolymers exhibit varying affinities for the silicon dioxide surface. The copolymer MAETAC:AA, in particular, demonstrated the highest initial adsorption ($646 \pm 36$ ng/cm$^2$) in the first phase, suggesting that copolymers with high MAETAC content are more likely to form stable coat-

ings on ceramic surfaces. This stability could potentially enhance the copolymer's ability to prevent biofilm formation in toilets. During the deionised water rinse phase, MAETAC:AA's mass adsorption increased, likely due to polymer swelling. This swelling could either improve or diminish its antifouling effectiveness, depending on subsequent contamination. In the BSA adsorption phase, all polymers allowed some degree of fouling, as evidenced by increased mass on the surface. However, MAETAC:AA showed a significant reduction in BSA mass over time, indicating superior long-term antifouling performance. In the final rinse phase, MAETAC:AA continued to lose mass, suggesting better resistance to long-term fouling compared to other tested copolymers. This is crucial for designing self-cleaning toilet surfaces.

Figure 5.3 provides a detailed analysis of adsorption at specific time points, confirming that MAETAC:AA not only has the highest initial adsorption but also significant mass loss after BSA introduction, reinforcing its potential for reducing fouling over time. In contrast, DMAEMA:AA exhibited lower initial adsorption but higher BSA fouling, making it less effective for maintaining a clean surface. Copolymers such as MAETAC:AA:EGDMA:DDT and i-OA:MAETAC showed the lowest initial adsorption, indicating that these materials might not provide adequate surface coverage, leading to reduced fouling resistance. However, their lower initial adsorption might be advantageous in contexts where minimal interaction with the ceramic surface is preferred.

The schematic in Figure 5.5 illustrates the interaction between copolymer segments and the negatively charged silicon dioxide surface. It suggests that polymers with a higher proportion of positively charged segments, such as MAETAC, could form more robust coatings on ceramic surfaces. This is crucial for developing toilets with enhanced antifouling properties.

Overall, the study underscores that copolymers with high MAETAC content are the most promising candidates for antifouling applications on glazed ceramic surfaces. The strong adsorption characteristics of MAETAC-based copolymers could lead to surfaces that are more resistant to foulant formation and easier to clean, thereby reducing maintenance needs

and improving hygiene. Conversely, DMAEMA-based copolymers may not offer as effective antifouling properties, although optimising the balance between adsorption and fouling removal could be beneficial depending on specific design requirements. For instance, surfaces requiring frequent refreshing might benefit from different copolymer compositions.

In summary, incorporating MAETAC-rich copolymers into toilet surface design could significantly enhance long-term cleanliness and reduce biofilm formation. These findings provide valuable guidance for material selection in the development of advanced self-cleaning toilets, ultimately improving both user experience and hygiene standards. In the next chapter, the effects of these polymers on adhesion will be studied at the macroscale.

# Chapter Six

# The Effect of Deposited Polymer on the Attachment of Viscoelastic Material

## 6.1 Introduction

The previous chapter has shown that changing the structure of the block copolymers affects their adhesion to surfaces. Following the random copolymer study of the previous chapter, a top-down approach was employed to investigate the effect of deposited polymers on the attachment of viscoelastic material. In this context, a top-down approach involves beginning with a macroscopic system and progressively reducing its size and complexity to examine its components. This methodology includes analysing the entire system first and then deconstructing it into smaller, more manageable parts to investigate interactions at various scales.

The random copolymers examined in this chapter were the same as the ones investigated in the previous chapter (see Table 5.2) and analysed by contact angle, force board and FLuSHT measurements. The primary objective of the work described in this chapter is to evaluate the deposition behaviour of random copolymers supplied by Innospec in real-life applications.

Consequently, the random copolymers were deposited onto glazed ceramic tiles rather than the silicon dioxide sensors extensively discussed in Chapters 4 and 5. This substrate was selected because it is commonly used in toilet bowl applications, allowing for the assessment of the random copolymers' performance in a practical context. This investigation aligns with Innospec's original proposal for this project and forms the basis of this doctoral research.

The work in this chapter was conducted to understand how the random copolymers supplied by Innospec behaved in a real-life application. Contact angle measurements, force board tests, and the FLuSHt test were carried out to achieve this.

Contact angle measurements were employed to simulate the washing process of the quartz crystal microbalance (QCM) and to replicate the behaviour of a toilet bowl on a glazed ceramic tile, rather than using a silicon dioxide sensor. These measurements also quantified the spreading kinetics of water droplets on the coated tiles. This approach provided an opportunity to adopt a top-down perspective and assess the performance of polymer coatings in real-life applications. Consequently, this chapter serves as a practical investigation into the behaviour of polymer coatings, offering insights into their efficacy in actual applications, as initially proposed by Innospec and forming the foundation of this doctoral research.

The force board measurement, as discussed in Section 3.7, was utilised to assess the adhesion between the coated tile and the synthetic faeces. This measurement was conducted on a macro scale, corresponding to the scale used in real-life applications. Additionally, the FLuSHT setup, described in Section 3.6, was developed to examine the behaviour of the random copolymer in a toilet application with a constant water flow rate. The polymers used for the force board and FLuSHT measurements are listed in Table 5.2. The polymers employed in the contact angle measurements are also included in Table 5.2, highlighted in blue.

## 6.2 Results & Discussion

### 6.2.1 Static Contact Angle

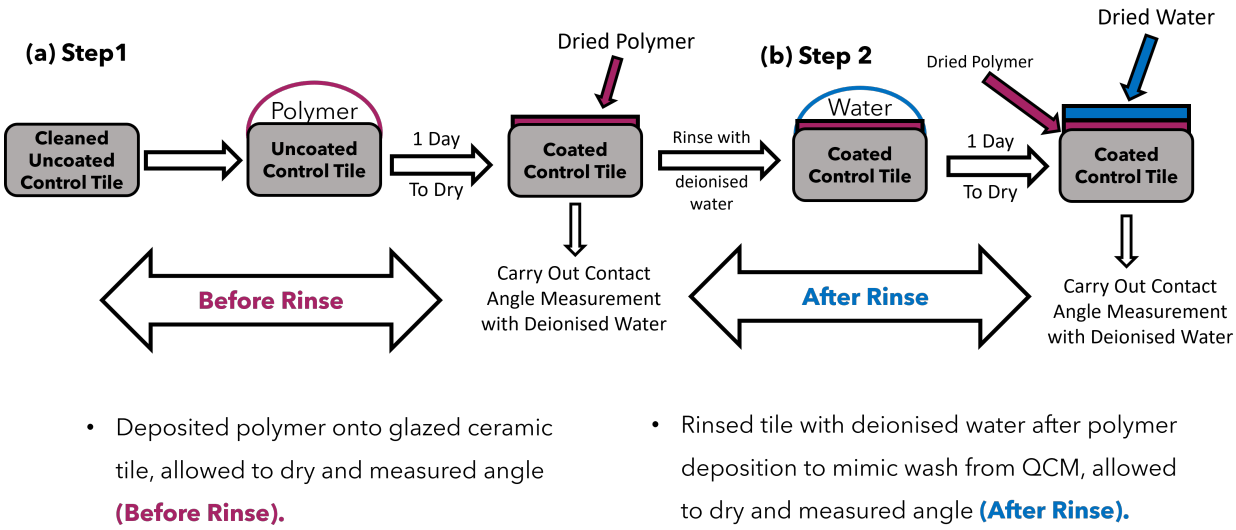
A contact angle method was developed to study the effects of coatings on surface energy. Figure 6.1 depicts the contact angle methodology used to test the effects of adhesion measured using the QCM in the previous two chapters. The ceramic tiles were first cut into 1 cm squares (see Chapter 3) and cleaned as described below. The tile was:

1. Rinsed with IPA.
2. Rinsed with tap water.
3. Rinsed with DI water.
4. Sonicated in IPA for 180 seconds.
5. Air dried.
6. Polished with a microfiber cloth.
7. Rinsed with tap water.
8. Rinsed with DI water.
9. Sonicated in IPA for 180 seconds.
10. Rinsed with tap water.
11. Rinsed with DI water.
12. Sonicated in DI water for 180 seconds.
13. Air dried.

14. Left to adjust to room humidity.

Once the tiles were cleaned, a controlled amount of 200 ppm random copolymer, approximately 2.3 mL in solution, was uniformly deposited across the entire surface of the ceramic tile using a Pasteur pipette. The copolymers were chosen to cover the full range of compositions. The copolymers selected are highlighted in blue in Chapter 5, Table 5.2.

The tiles were then left to dry for a day under ambient conditions, as shown in step (a) in Figure 6.1. After the polymer had dried, contact angle measurements were conducted using deionised water. Five contact angle measurements were taken on each polymer-coated tile to ensure the reliability and repeatability of the data. A 5 µL droplet was deposited onto the surface of the coated tiles. The behaviour of this droplet was used to identify the wettability of the surface by analysing how much it spread on the surface. A Python script, described in Section 3, was used to analyse the data. Stage (b) in Figure 6.1 illustrates the after-rinse step. Once the contact angle measurements were taken in step (a), the surface was rinsed with deionised water, and then 2.3 mL of deionised water was deposited onto the tile's surface and allowed to dry overnight. Allowing water to dry on the samples was done to replicate a flush setup and closely simulate the QCM protocol described in Chapter 5. Once the deionised water had dried overnight, contact angle measurements were carried out in the same manner as in step (a). An average of the five contact angle measurements was taken and the data is plotted in Figure 6.2.




- Deposited polymer onto glazed ceramic tile, allowed to dry and measured angle **(Before Rinse).**
- Rinsed tile with deionised water after polymer deposition to mimic wash from QCM, allowed to dry and measured angle **(After Rinse).**

Figure 6.1: Schematic of the experimental protocol to measure contact angle on 200 ppm Random Co-polymer samples of AA:MAETAC:DMAEMA. Step 1 represents the pre-rinse stage, while step 2 signifies the post-rinse stage.

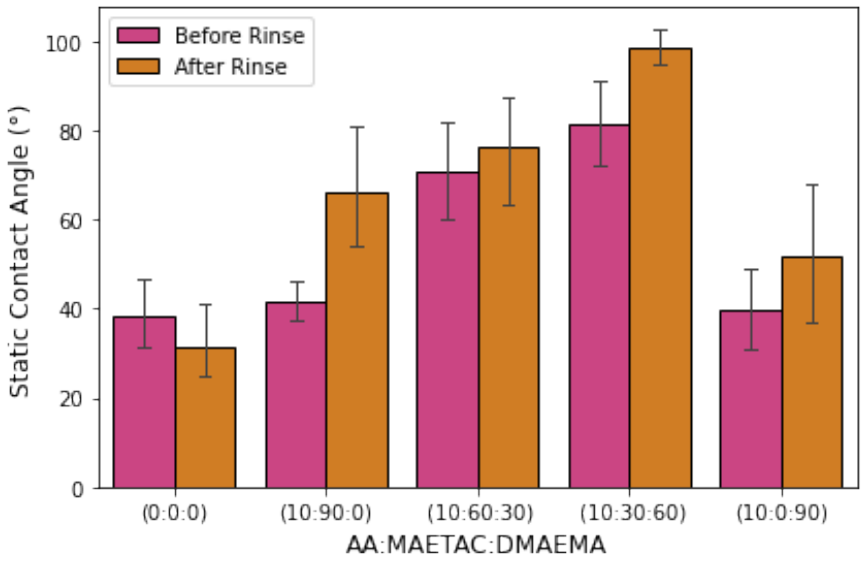



Figure 6.2: Static Contact Angle of 200 ppm Random Co-polymer samples before and after deionised water rinse. Sample 0:0:0 is the bare ceramic surface contact angle. An average of five measurements were taken for each sample. The error bars represent the standard error of the mean (SEM), calculated for the five repeats of each polymer.

Figure 6.2 displays the static contact angle data before and after rinsing the random copolymer samples. The static contact angle was recorded as soon as the water was deposited and settled on the surface, typically within the first 5 to 10 seconds (see Chapter 3 for further information). Sample 0:0:0 served as the control, representing the bare tile, with an average contact angle of $38 \pm 4.3°$. This matches the contact angle measured by Innospec using the same cleaning method. The random copolymer samples were tested at 200 ppm.

It can be observed that before rinsing, the samples exhibit more hydrophilic behaviour compared to the contact angle data after rinsing. For instance, sample 10:90:0 showed an average contact angle measurement of $42 \pm 2.7°$ before rinsing. Sample 10:60:30 had a contact angle of $71 \pm 7.3°$ before rinsing, while sample 10:30:60 had a contact angle of $82 \pm 6.8°$ before rinsing. Sample 10:0:90 had a contact angle of $40 \pm 6.7°$ before rinsing, similar to that of the control.

In Figure 6.2, the statistically different samples are 10:90:0 and 10:30:60 for before and after rinse. This is evident as the error bars for the measurements before and after rinsing do not overlap, suggesting a significant change in the random copolymer architecture due to rinsing with deionised water. The rinsing process notably alters the surface properties of the 10:90:0 and 10:30:60 samples, making them more hydrophobic. There is a clear increase in the static contact angle.

Contact angles measured increased with decreasing MAETAC content, suggesting that the molecular architecture of the polymer made a significant difference. The random copolymers altered the surface, changing the surface energy of the tile. This electrostatic attraction between the positively charged nitrogen and the partially negative oxygen atoms will facilitate the interaction between MAETAC and water. Since the quaternary ammonium group in MAETAC was hydrophilic, it will interact with water. It might also be possible that the alkyl group to which the quaternary group was attached within MAETAC's structure had folded to expose the hydrophobic alkyl chains to the air. Therefore, during the post-rinse

stage, the alkyl chains in the MAETAC group might have been oriented outward to the non-surface side, causing the water droplet to become hydrophobic upon contact with the surface.

Figure 6.2, shows that as the MAETAC components decreased within the random copolymer ratio and the DMAEMA component increased, the hydrophobicity of the static water contact angle increased. This could be attributed to MAETAC not having to compete with other MAETAC groups for water molecules, resulting in more alkyl groups facing towards the water droplet.

Figure 6.2, shows also that Sample 10:0:90 exhibited a notable decrease in static water contact angle before and after rinsing compared to the other random copolymer samples. Again this difference could be attributed to the absence of MAETAC components within the sample. While DMAEMA carried a positive charge, it was not as positively charged as MAETAC. The amino group in DMAEMA could form hydrogen bonds with water molecules, facilitating some level of solubility. However, the methacrylate backbone of DMAEMA was hydrophobic due to nonpolar carbon-carbon double bonds and carbonyl groups, which tended to repel water molecules. Although DMAEMA molecules could form hydrogen bonds with water, leading to partial dissolution, the hydrophobic nature of the methacrylate backbone may have prevented complete solubility in water.

### 6.2.2 Dynamic Contact Angle

An increase in contact angle after rinsing was observed in samples 10:90:0 and 10:30:60. As the MAETAC component decreased and the DMAEMA component increased in the random copolymer samples, the surface became more hydrophobic. However, the static contact angle before and after rinsing for sample 10:0:90 was lower.

Further work was conducted to examine the dynamic contact angle both to understand

this observation better and to identify the spreading kinetics of the random copolymers on the tile. The dynamic contact angle was particularly interesting to examine, as it could indicate whether the polymers deposited a uniform layer. Figure 6.3 illustrates a schematic representation of the evolution of a dynamic contact angle.

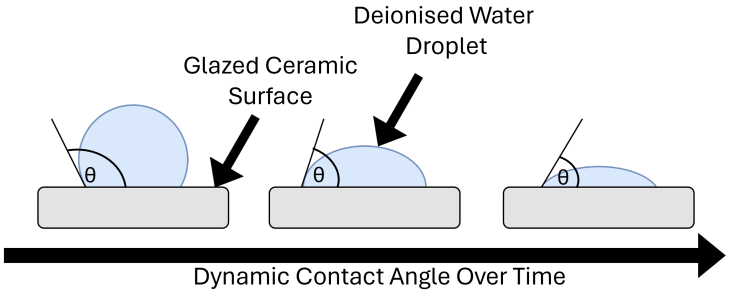



Figure 6.3: Schematic diagram of dynamic contact angle, illustrating how the angle of the deionised water droplet decreases over time.

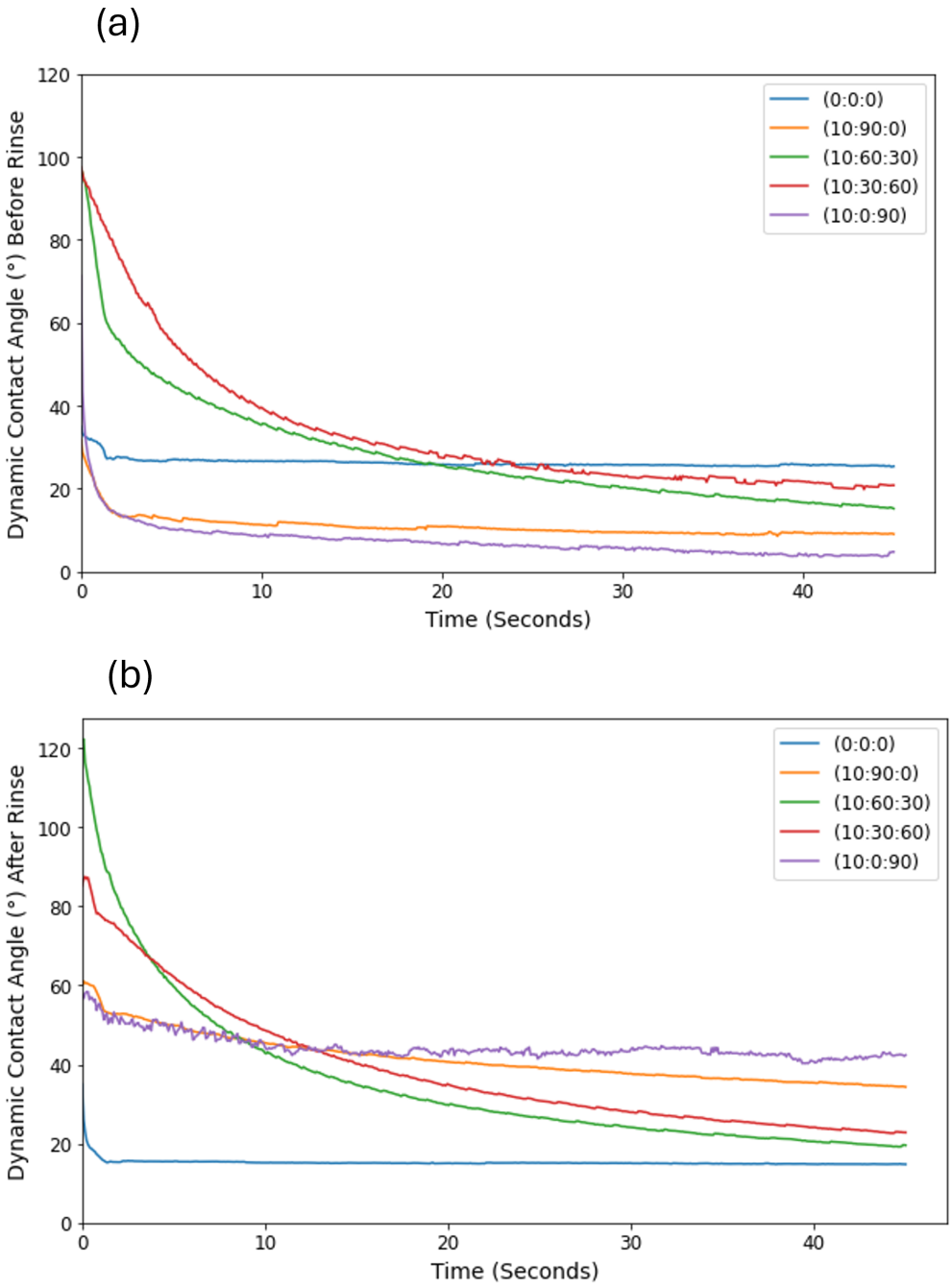



Figure 6.4: Evolution of the water contact angle during the 45-second analysis period: dynamic contact angles of 0:0:0 (blue line), 10:90:0 (orange line), 10:60:30 (green line), 10:30:60 (red line), and 10:0:90 (purple line) are shown in (a) before rinsing and (b) after rinsing with deionised water. All random copolymer samples were deposited on a glazed ceramic tile at a concentration of 200 ppm. The plots represent individual measurements.

Figure 6.4a illustrates the dynamic contact angle of the bare-glazed ceramic tile without coating (0:0:0) and the random copolymers 10:90:0, 10:60:30, 10:30:60, and 10:0:90 before rinsing with deionised water. Sample 0:0:0 had a starting contact angle of approximately 37 degrees and quickly reached its equilibrium contact angle, plateauing very rapidly, with a constant value after approximately 2 seconds. There was no change in the dynamic contact angle over after this, both before and after rinsing, as the contact angle stayed uniform. The figure shows that for all the other systems the contact angle significantly decreased as time progressed and then plateaued towards the end, indicating that the contact angle stabilised over time. Examining Figure 6.4a, it is evident that 10:30:60 (red line) and 10:60:30 (green line) had the highest starting values, ca. 90°, for the contact angle before rinsing with deionised water, while 10:0:90 (purple line) and 10:90:0 (orange line) had a lower starting contact angle before rinsing with deionised water.

Figure 6.4b shows the dynamic contact angle of the bare-glazed ceramic tile without coating (0:0:0) and the random copolymers, 10:90:0, 10:60:30, 10:30:60, and 10:0:90 after rinsing with deionised water. The data shows that the random copolymer 10:60:30 (green line) started with a very high static contact angle of approximately 120 degrees, which then dropped significantly over time; a final value had not been reached after 45 seconds. In comparison to the conditions before rinsing, sample 10:30:60 (red line) did not start at the same initial contact angle as 10:60:30. Interestingly, this time random copolymer samples 10:90:0 and 10:0:90 also had the same initial contact angle. However, both of these polymers reached equilibrium quickly. To quantify the kinetics of the dynamic contact angle, equation (6.1)[145] was used to fit the slope to the curve.

Figure 6.4a shows that all the random copolymer samples initially have a higher contact angle than the uncoated control tile (0:0:0) at the beginning of the measurement. Over time, the random copolymers exhibit a decrease in contact angle, resulting in lower contact angles compared to the control tile. The control tile has the highest final contact angle over time, suggesting that it becomes the most hydrophobic, while the random copolymers become

more hydrophilic when in contact with the water droplet over time. Thus, before rinsing, all the dynamic contact angles for the random copolymers are less than the bare tile (0:0:0).

In Figure 6.4b, a similar trend is observed: the random copolymers exhibit the highest contact angles at the beginning of the measurement. However, over time, the random copolymers maintain their hydrophobic behaviour after rinsing, and the water droplet retains its hydrophobicity when in contact with these copolymers post-rinse, the opposite is observed for sample 0:0:0. Sample 10:0:90, which has the lowest contact angle before rinsing, shows the highest contact angle at the end of the measurement. This indicates that, after rinsing, the surface of the 10:0:90 sample becomes hydrophobic, with the water droplet maintaining its hydrophobicity over time compared to the other samples. Thus, after rinsing, all the dynamic contact angles for the random copolymers are higher than that of the bare tile (0:0:0).

### 6.2.3 Contact Angle Kinetics

Farris et al[145] analysed contact angle kinetics using the equation provided below. Equation (6.1) is a three-parameter decay equation, which was fitted to the experimental contact angle data to characterise the kinetics of contact angle change for each random copolymer. To extract the kinetics from fitting the equation to the slopes depicted in Figure 6.4, a Python script was developed. Figure 6.5 gives an example of the evolution of water contact angle over time. The red solid line represents the result of fitting Equation 6.1 to the experimental data using Python.

$$\theta(t) = \theta(0)exp(-kt)^{\,n} \text{ for } n = 1 \text{ (two-parameter system)} = \theta(0)\exp(-kt) \tag{6.1}$$

- $\theta(t)$: Contact angle at time $t$. It denotes an angle that depends on $t$.
- $\theta(0)$: Contact angle at time, when $t = 0$, i.e. the initial contact angle.

- $\exp(kt)$: Exponential function where $k$ is a constant, and time, $t$ was the independent variable.

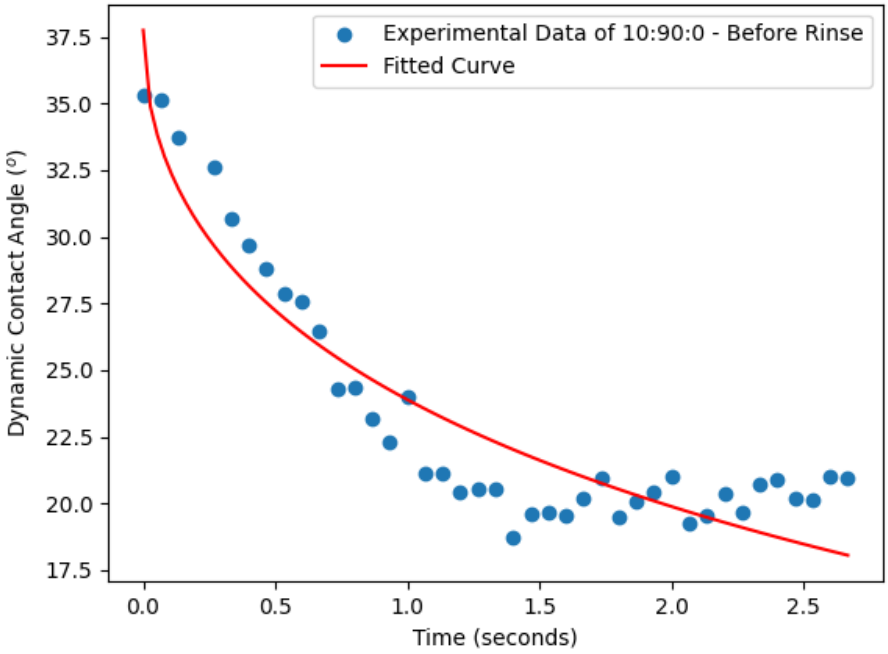



Figure 6.5: Example of water contact angle evolution over time of analysis for 10:90:0 which is 10% AA and 90% MAETAC. Blue dots are the experimental data for 10:90:0 before rinse. The red solid line was obtained by fitting equation 6.1 to the experimental data.

Figure 6.6 depicts the dynamic contact rate constant *'k'* (also referred to as spreading kinetics constant) of the random copolymer samples before and after rinsing, fitted from equation 6.1. For sample (0:0:0), the spreading kinetics constant before rinsing was -0.24, and after rinsing, it was -0.70. This indicates that deionised water droplets spread rapidly on the surface after the rinsing stage. Furthermore, Figure 6.2 corroborated this observation, as the contact angle after rinsing was lower than the contact angle before rinsing, suggesting lower surface energy and increased hydrophilicity.

All of the random copolymer samples exhibited faster spreading (i.e. a higher $k$) before rinsing, indicating that the deionised water droplet spread more quickly upon contact with the surface. After rinsing, the rate constants decreased for the random copolymer samples, suggesting that the water droplet did not spread rapidly in the forced water deposition state, suggesting the surface had rendered itself more hydrophobic. Overall, there was no discernible trend among the random copolymers themselves, but there was a clear difference before and after rinsing.

The kinetic constant for Sample 10:90:0 before rinsing was significantly higher compared to the other random copolymer samples, with an average value of -1.08, indicating rapid spreading of the deionised water droplet over the surface.

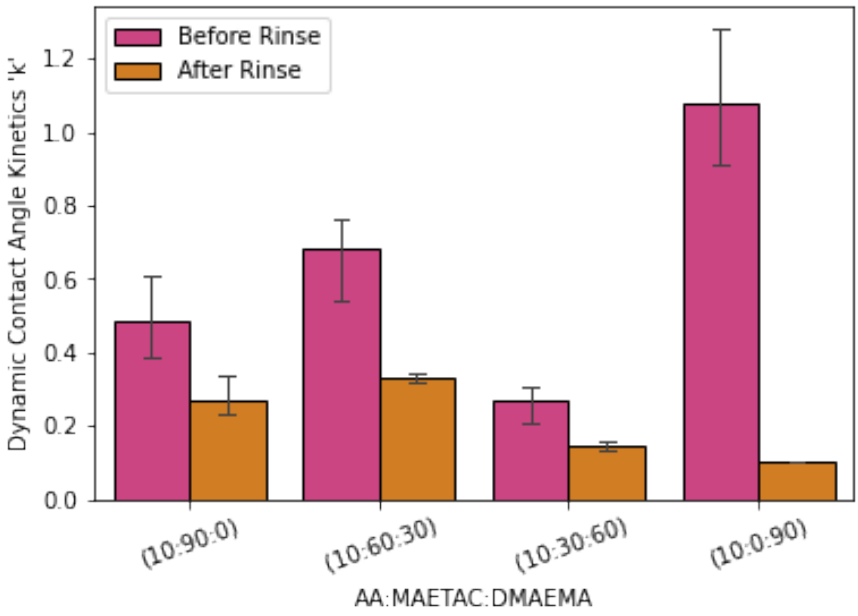



Figure 6.6: Plot showing kinetic constant *'k'* against AA:MAETAC:DMAEMA (random copolymer components), before and after rinse.

Figure 6.7 plots the static contact angle (in degrees) on the y-axis against the kinetic constant $k$ on the x-axis for various random copolymer compositions (AA:MAETAC:DMAEMA). The data points represent measurements taken both before and after rinsing.

The static contact angles observed range from approximately 30° to 100°, indicating a wide spectrum of surface wettabilities among the copolymers. Notably, the highest contact angle, around 100°, is observed for the 10:30:60 composition after rinsing (green square). The kinetic constant $k$ also varies significantly among different copolymer compositions, with values ranging from approximately 0.1 to 1.2. The highest value of $k$, approximately 1.1, is seen in the 10:0:90 composition before rinsing, marked by a red circle.

Before rinsing, indicated by circles, the contact angles are generally lower, and the range of kinetic constants is broad. The changes effected by rinsing are shown by arrows on the plot. After rinsing, for all samples tested the contact angles increase and the rate constants decrease, suggesting alterations in surface properties.

The static contact angle serves as an indicator of surface wettability; higher contact angles suggest more hydrophobic surfaces, while lower angles indicate hydrophilicity. The variation in contact angles among different compositions points to differences in surface energy and the hydrophilic/hydrophobic balance of the polymer coatings. The kinetic constant $k$ relates to the rate of droplet spreading on the surface, influenced by the interaction between the liquid and the surface. Higher $k$ values indicate faster spreading, potentially due to lower surface energy or higher wettability. For example, the 10:0:90 composition before rinsing, with the highest $k$ value, suggests a more hydrophilic nature, allowing for rapid spreading.

Rinsing appears to influence both the static contact angle and the kinetic constant $k$, indicating changes in surface properties. This effect could be due to the removal of loosely bound polymer chains or surface contaminants, revealing more intrinsic surface characteristics. For instance, the 10:30:60 composition shows a significant increase in contact angle after rinsing, indicating increased hydrophobicity.

There is no simple linear correlation between static contact angle and kinetic constant $k$, but certain trends are noticeable. Compositions with lower $k$ values, such as 10:0:90 after rinsing, generally have higher contact angles, indicating slower spreading on more hydrophobic

surfaces. Conversely, some cases show higher $k$ values associated with lower contact angles, suggesting faster spreading on hydrophilic surfaces.

Rinsing significantly alters the surface energy and wettability of the random copolymers. The statistical significance of these changes can be inferred from the error bars; non-overlapping error bars between measurements before and after rinsing suggest substantial changes in surface properties due to rinsing.

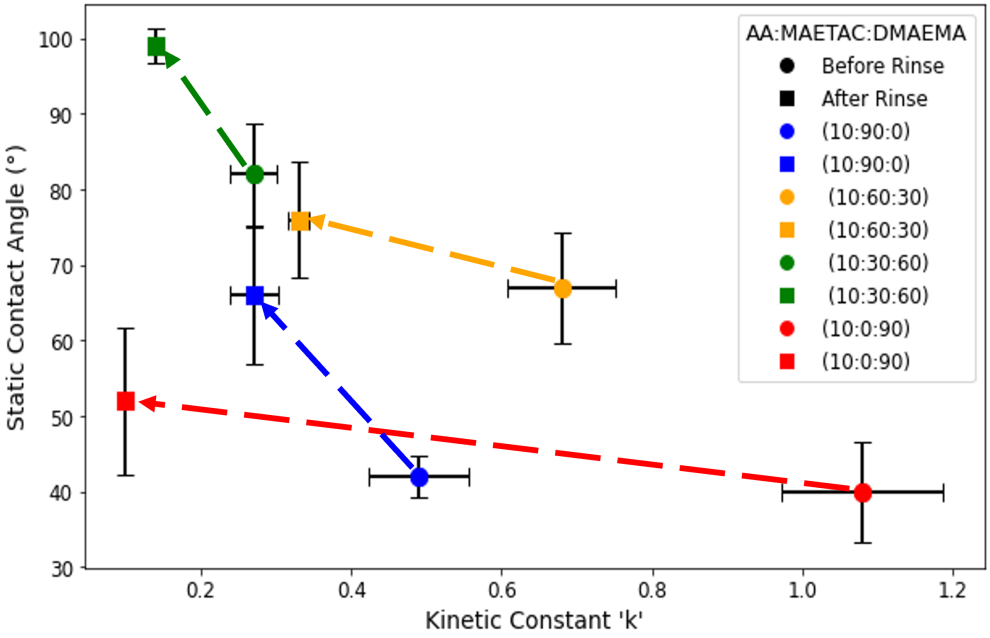



Figure 6.7: Plot correlating static contact angle against Kinetic constant 'k' before and after rinse. Arrows indicate the difference between before rinse and after rinse samples of the random copolymers.

### 6.2.4 Adhesion of viscoelastic material on different random copolymer samples - Forceboard experiments

The force board measurement, as detailed in Chapter 3, was employed to assess the adhesion between the coated tile and synthetic faeces (discussed in section 3.7). This assessment was conducted on a macroscopic scale, analogous to the scale used in practical applications. The force board measurement was used to determine whether the coating of the random copolymer supplied by Innospec (see Table 5.2) facilitated the detachment of synthetic faeces with less force compared to an uncoated tile (0:0:0).

Glazed ceramic tiles used from this study (discussed in Chapter 3) were Utopia White Gloss Ceramic Wall Tile, Pack of 25, 100mm(L) 100mm(W) purchased from B&Q. The samples were cut into 1 cm(L) and 1cm(W) so that the tiles could fit into the force board machine and to carry out the measurement with ease. All the samples were cleaned using the Innospec cleaning method mentioned in section 6.1.1. See Chapter 3 for the description of the force board and its method.

Figure 6.8 presents a plot of vertical force in newtons against time in seconds for a bare-cleaned glazed ceramic tile stated as the control (0:0:0).

The experiments were conducted in four stages, shown schematically in Figure 6.8.

(a) The tile approached the faecal matter but stopped 1 cm away.

(b) Tile made contact with the synthetic faecal matter, compressing it until a vertical compressive force of 1 Newton was reached.

(c) The tile was then moved away from the synthetic faeces at a speed of $10.05\,\mathrm{mm\,s^{-1}}$, and the vertical adhesion force reported. The information acquired at this stage provided insights into the adhesion between the control tile and the synthetic faeces, determined by the lowest vertical force measured from the zero baseline.

(d) At this point, there is complete detachment of the tile from the synthetic faeces.

In the figure, bare cleaned glazed ceramic tile shows a maximum adhesion force of approximately -0.39 N. This variation in adhesion force between the faecal matter and the random copolymer samples is an interesting parameter that will facilitate comparison against the bare-cleaned glazed ceramic tile. Figures 6.9 and 6.10 show the variation in measured parameters.

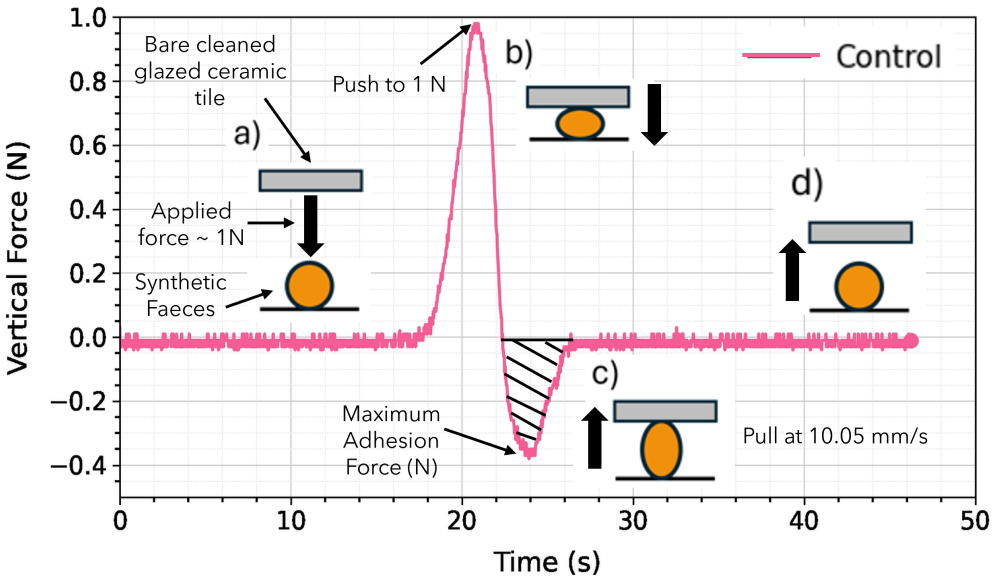



Figure 6.8: Vertical force (N) against time (s) for the bare cleaned glazed ceramic tile. The grey rectangle represents the bare-cleaned glazed ceramic tile, while the orange sphere represents the synthetic faecal matter, and the thick black arrows indicate the direction in which the tile was headed and the applied force. In Step (a), the tile approached the synthetic faecal matter. In Step (b), the tile touched the synthetic faecal matter at a vertical force of 1N. Step (c) involved the tile being pulled away from the synthetic faecal matter to determine the vertical adhesion force (N), and Step (d) represented the complete detachment of the tile from the synthetic faecal matter.

### 6.2.5 Effect of random copolymer structure on adhesion force

Figure 6.9 presents plots of vertical force in newtons (N) against time in seconds for a bare-cleaned glazed ceramic tile, designated as the control, along with the random copolymer samples. A variation in adhesion force was observed among all samples during the stage when the tile was removed from the synthetic faecal matter. The figure illustrates a clear variation in the maximum vertical force, between the synthetic faeces and the uncoated and the different coated tiles. In all cases the maximum adhesion force for coated tiles is less than that for the bare tile, this suggests that the coatings all reduce the adhesion between the tile and synthetic faeces. This demonstrates that the macroscale data reflects the changes in the micro and nanoscale information on surface charge and contact angle.

Additionally, there is variation in the rate of the rise of the compressive vertical force when the tile begins to come into contact with the synthetic faeces and compresses to a set force of 1 N. The variation in data may be attributed to the consistency of the synthetic faeces; as it was made (described in Chapter 3), it was quite difficult to remove the lumpy parts. Therefore, the synthetic faeces were not all of the same consistency; however, they were set to a constant dimension of $0.5 \pm 0.01$ cm.

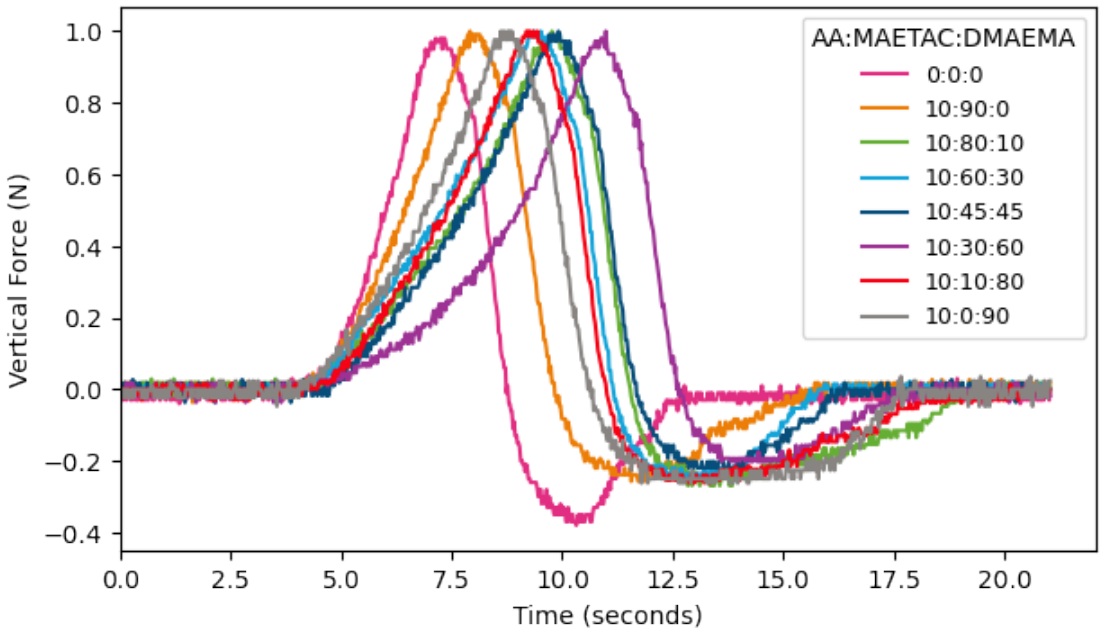



Figure 6.9: Plot showing vertical force (N) against time (s) for the bare control tile (0:0:0) and random copolymers. The plot shows a single experiment, however, three of each measurement were carried out to assess reproducibility.

Figure 6.10 represents the vertical adhesion force in newtons (N) on the y-axis, while the x-axis lists the copolymer compositions, denoted by their respective AA:MAETAC:DMAEMA ratios. Each bar in the graph corresponds to a specific copolymer composition and shows the mean vertical adhesion force measured across three replicates, with error bars indicating the standard error of the mean (SEM) to account for measurement variability.

The uncoated glazed ceramic tile (composition 0:0:0) exhibits the highest vertical adhesion force, approximately 0.33 N, suggesting that the strongest adhesion of the material to the bare tile surface. All the coated samples show lower adhesion force. The copolymer with the composition 10:30:60 shows the lowest vertical adhesion force, around 0.25 N, indicating this coating has the greatest effect on adhesion. A general trend is observed where the adhesion force decreases as the MAETAC content in the copolymer decreases, particularly noticeable from the 10:90:0 to the 10:80:10 and then to the 10:60:30 compositions. However,

an increase in adhesion force is seen in the 10:0:90 sample compared to the 10:30:60 and 10:10:80 samples, suggesting that increasing DMAEMA content does not consistently lead to lower adhesion.

The variations in vertical adhesion force can be attributed to differences in copolymer composition, which likely affect surface properties such as hydrophobicity, surface roughness, and charge distribution. The 10:30:60 composition, characterised by relatively higher DMAEMA and moderate AA and MAETAC content, results in the lowest adhesion force. This suggests that the surface characteristics imparted by this composition, potentially balancing hydrophilicity and electrostatic interactions, are particularly effective at minimising adhesion. In contrast, the high adhesion force observed in the uncoated sample underscores the coatings' effectiveness in reducing adhesion compared to bare tiles, highlighting the utility of these copolymer films.

The error bars on the graph emphasise the statistical difference of the results. Non-overlapping error bars between certain samples, such as between 0:0:0 and 10:30:60, suggest statistically different differences in adhesion forces. This validation confirms that the observed effects of different copolymer compositions on adhesion reduction are genuine and not merely due to random variability. Specifically, where error bars do not overlap, it suggests that the differences in adhesion force are attributable to the specific effects of the copolymer compositions.

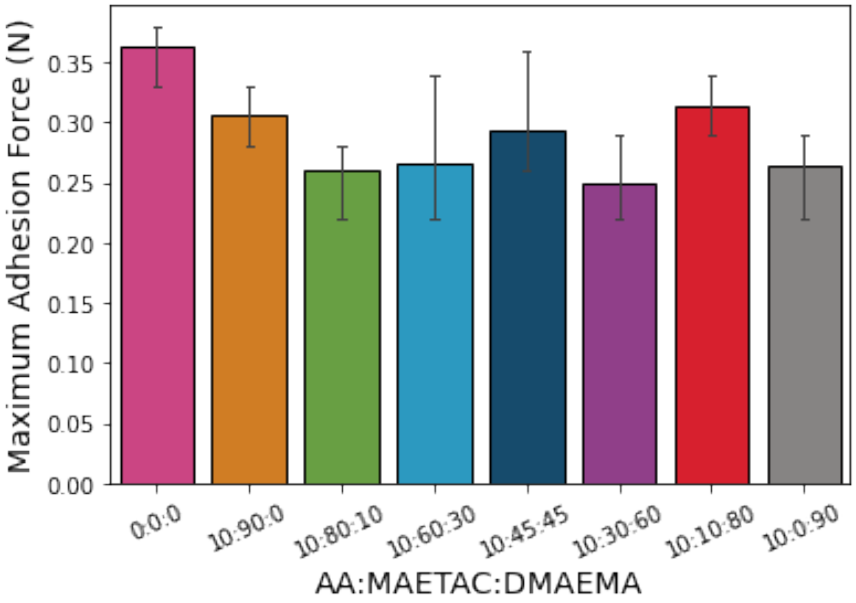



Figure 6.10: Illustrates average maximum adhesion force (N) for different copolymer compositions with standard error bars. The copolymer compositions are represented as ratios of AA:MAETAC:DMAEMA. Each bar represents the mean value from three measurements for each copolymer, with the error bars indicating the standard error of the mean.

### 6.2.6 Effect of random copolymers on the work of adhesion

When the tile is withdrawn from the surface, an adhesion force between the tile and the synthetic faeces is measured using the force board. The variation in force over time is illustrated in Figure 6.9, where the area under the curve represents the total work required for removal. This area can be correlated to the total work of removal as follows:

$$W = \int F \, dx \tag{6.2}$$

In this equation:

Where $W$ is the work of removal (in Joules), $F$ is the force (in Newtons), and $dx$ is the infinitesimal displacement.

Figure 6.11 displays the work of removal obtained from equation 6.2 (in Joules, J) on the y-axis, which is calculated by integrating the force over the distance (area under the force-displacement curve) and multiplying by velocity (10.05 mm/s). The x-axis shows various random copolymer compositions (AA:MAETAC:DMAEMA) in different ratios. Each bar represents the average work of removal for a specific copolymer composition, with error bars indicating the standard error of the mean (SEM), for three measurements.

Unlike the peak adhesion force, the work of removal for the different copolymer compositions is sometimes greater than that for the bare tile. There is a substantial effect of composition on the energy required to remove adhered material. Certain compositions demand notably more work of removal than others, indicating differences in adhesion strength and surface interactions. For example, the copolymer composition 10:10:80 exhibits the highest work of removal, suggesting strong adhesion that requires more energy to detach. In contrast, the 10:90:0 composition shows the lowest work of removal, indicating weaker adhesion. Intermediate values are observed in compositions like 10:60:30 and 10:45:45, reflecting varying degrees of adhesion strength. There are some copolymer compositions for which the work of removal is less than that of the bare tile.

Overlapping error bars in some compositions (e.g., 10:60:30 and 10:45:45) imply that the differences in the work of removal may not be statistically significant. Conversely, non-overlapping error bars (e.g., between 10:10:80 and 10:60:30) suggest statistically different differences in the work of removal, reinforcing the reliability of the observed trends.

The work of removal measures the energy required to overcome the adhesive forces between the copolymer coating and the adhered material. Differences in copolymer composition likely

influence surface energy, roughness, and chemical interactions, affecting adhesion strength. Compositions with higher work of removal may exhibit stronger van der Waals forces, hydrogen bonding, or other intermolecular interactions requiring more energy to break.

Understanding the relationship between copolymer composition and adhesion properties can inform the design of coatings for specific applications. Compositions with lower work of removal may be suitable for applications requiring easy cleaning or low-fouling surfaces. Conversely, compositions with higher work of removal may be desirable for applications where strong adhesion is necessary, such as in protective coatings or adhesives.

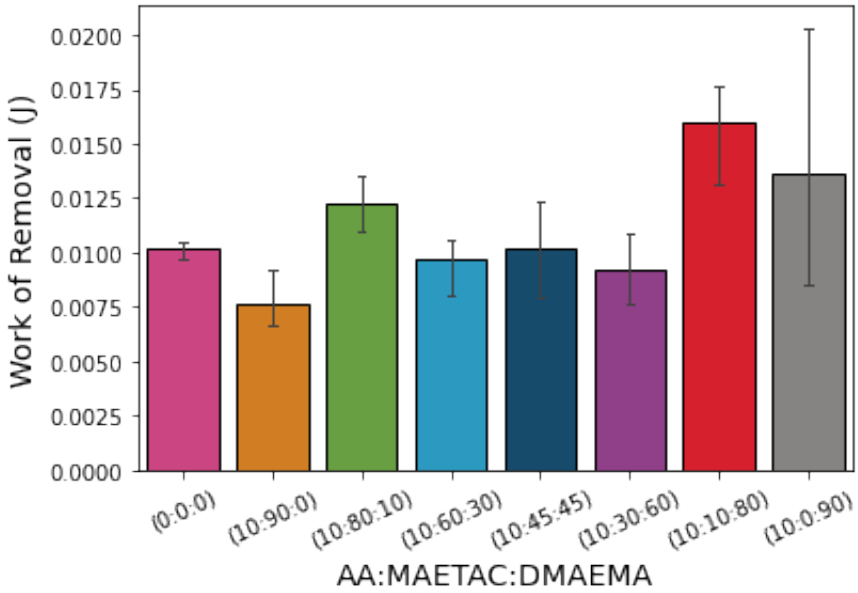



Figure 6.11: Work of removal (J) calculated from equation (6.2) for different copolymer compositions with standard error bars. The copolymer compositions are represented as ratios of AA:MAETAC:DMAEMA. Each bar represents the mean value from three measurements for each copolymer, with the error bars indicating the standard error of the mean.

### 6.2.7 Preliminary experiments with FLuSHT

The aim of the FLuSHT test was to expose synthetic faeces to flow similar to those found in toilets. Time did not permit full investigation of the equipment, but it was possible to study how faeces were removed by the water flow. Experiments were conducted in which the velocity of the model faeces was measured during removal. It would be expected that the less adhesion, the faster the sliding velocity, i.e. the lower the coefficient of friction.

Figure 6.12 displays preliminary data from the FLuSHT test. The y-axis shows the sliding velocity in millimetres per second (mm/s), while the x-axis shows various random copolymer compositions (AA:MAETAC:DMAEMA). Pink bars indicate the sliding velocity before rinsing, and orange bars show the sliding velocity after rinsing.

It can be seen that most of the copolymers covered surface show sliding velocities that are greater than those for the clean tiles, suggesting that the polymers do lower the coefficient of friction. The sliding velocities exhibit significant variation across different copolymer compositions, highlighting the substantial impact of composition on surface properties. Additionally, notable differences in sliding velocities are observed before and after rinsing for most compositions. Some compositions show a significant decrease in sliding velocity post-rinsing (e.g., 10:90:0 and 10:80:10), suggesting that rinsing has given the surface a higher coefficient of friction. Conversely, other compositions show a decrease or minimal change in sliding velocity after rinsing (e.g., 10:30:60 and 10:45:45), indicating that rinsing may not have affected the coefficient of friction significantly.

The sliding velocity is influenced by the surface properties of the copolymer samples, which are affected by their composition and the treatment they undergo, such as rinsing. Rinsing can remove surface contaminants or loosely bound molecules, which might smooth the surface, resulting in increased sliding velocity or exposing underlying layers with different properties, changing the coefficient of friction. Increased sliding velocity after rinsing could

be due to the removal of a rough or sticky surface layer, resulting in a smoother, more uniform surface with lower friction. Conversely, decreased sliding velocity after rinsing might occur if rinsing exposes a rougher or chemically different layer, increasing friction and resistance to sliding.

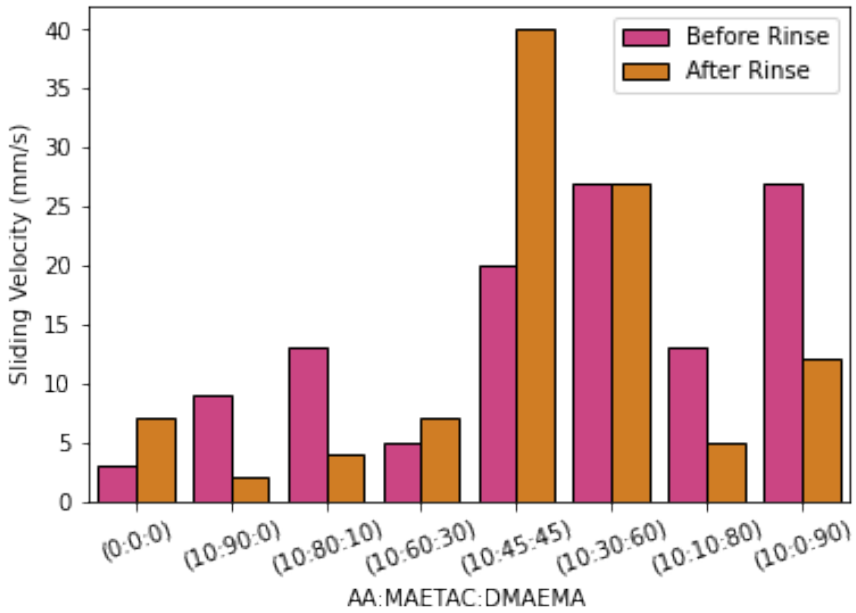



Figure 6.12: A comparison of preliminary data on sliding velocity (in millimetres per second, mm/s) before and after rinsing for various AA:MAETAC:DMAEMA polymer ratios. Pink bars represent the sliding velocity before rinsing, while orange bars depict the sliding velocity after rinsing.

The method thus seems to be able to discriminate between different coatings and maybe develop into a test method. Some improvements are possible:

(a) Redesign the flow system to achieve more uniform water distribution.

(b) Explore additional experimental approaches. Measuring the static coefficient of friction could be accomplished by:

(i) Keeping the tile at a constant angle, gradually increasing the water flow from zero and recording the flow rate at which the material begins to move.

(ii) Maintaining a constant flow rate while varying the angle of the tile relative to the horizontal, and recording the angle at which the material starts to move. At this angle, the force exerted by the water balances the static frictional force of the adhered material.

The method needs further development, but the preliminary experiments suggest that it could be modified to create a rapid way of testing formulation at a realistic scale.

## 6.3 Conclusions

Chapter 6 has investigated the development of innovative random copolymer additives designed to reduce adhesion forces on glazed ceramic surfaces. By synthesising various copolymer compositions and employing comprehensive testing methods—including contact angle measurements, the force board test, and the FLuSHT test. The findings underscore the critical role of surface properties, particularly wettability, in influencing adhesion forces, as evidenced by the contact angle and force board data. The surface energetics and the resulting adhesive behaviour of the samples has been addressed using contact angle and force board measurements.

The random copolymers synthesised in this study, consisted of acrylic acid (AA), methacryloyloxyethy ltrimethylammonium chloride (MAETAC), and dimethylaminoethyl methacrylate (DMAEMA) in varying ratios shown in Table 5.2. These compositions have been designed to investigate how different monomer ratios influence adhesion properties on glazed ceramic surfaces.

The contact angle measurements yielded essential insights into the surface wettability of

the copolymer-coated ceramics. Static contact angle data revealed that copolymers with higher MAETAC content created more hydrophilic surfaces, resulting in lower static contact angles. These hydrophilic surfaces reduce the interfacial energy between the ceramic surface and adhering substances, facilitating their removal. (See Figure 6.2 for static contact angle results across different copolymer compositions). Faster wetting kinetics were observed with higher MAETAC content, indicating quicker surface wetting as shown in Figure 6.6.

The force board test provided quantitative data on the force required to displace materials adhered to the copolymer-coated surfaces. The results of this test showed a clear correlation with the contact angle data. Copolymers exhibiting lower static contact angles (indicating more hydrophilic surfaces) show a reduction in the force required to move adhered materials in the force board test. This relationship indicates that increased hydrophilicity, as quantified by contact angle measurements, translates to reduced adhesion strength, facilitating the displacement of adhered materials. This can be seen in Figure 6.10 for the force board test results and Figure 6.2 for static contact angle data. The dynamic contact angle data, particularly the low hysteresis observed, suggests that these surfaces maintain consistent wettability during movement. This consistency is reflected in the force board test results, where less force was needed to initiate movement on these low-hysteresis surfaces, further supporting the notion that uniform surface energy leads to reduced adhesion forces. (See Figure 6.10 for the analysis of force board results and Figure 6.6 for dynamic contact angle data). The rapid wetting kinetics observed in certain copolymers correlate with a quicker reduction in adhesion forces in the force board test. This suggests that in real-world applications where surfaces encounter liquids, these copolymers can swiftly alter their wettability to reduce adhesion, thereby enhancing performance in environments with dynamic interactions.

In addition to the force board test, the vertical adhesion tests and FLuSHT provided further evidence of the copolymer coatings' effectiveness. The vertical adhesion tests confirmed that surfaces treated with copolymers, particularly those with higher MAETAC content, exhibited reduced adhesion forces, aligning with the contact angle and force board data.

(See Figure 6.10 for vertical adhesion test results). The FLuSHT results demonstrated that these copolymer coatings maintained their anti-adhesion properties under flow conditions, which is crucial for applications where surfaces are exposed to fluid flow.

The correlation between contact angle data and force board results highlights the importance of fine-tuning copolymer compositions. Achieving the right balance of hydrophilic and hydrophobic monomers, as demonstrated by MAETAC's role, is key to optimising adhesion reduction. However, the study also indicated that higher DMAEMA content could introduce inconsistencies in performance, necessitating careful optimisation to ensure uniform surface energy and reliable adhesion reduction.

This thesis makes a significant contribution to surface engineering by linking contact angle measurements to practical adhesion outcomes, as demonstrated by the force board test. The integration of static, dynamic, and kinetic wettability data with other performance metrics offers a comprehensive understanding of how these copolymer coatings function.

# Chapter Seven

# Final Conclusions and Future Work

The research detailed in this thesis focuses on the development and evaluation of innovative polymer additives to enhance the anti-fouling properties of glazed ceramic surfaces, specifically in sanitary ware such as toilets. Through an extensive exploration of polymer science, experimental methodologies, and detailed analyses of polymer behaviour in solution and at surfaces, this work provides valuable insights into optimising polymer coatings for practical applications. This chapter summarises the key findings, discusses the overall implications of the research, identifies the most effective polymer for the project, and outlines the broader impact on toilet design and manufacturing.

Chapter 2 lays the groundwork by exploring polymer behaviour in various environments, with a particular emphasis on polyelectrolytes. The interaction of these polymers with surfaces and their ability to modify surface properties are central to this discussion. Key findings highlight the critical role of polymer structure, especially in polyelectrolytes, in influencing surface interactions. Block copolymers' ability to form stable, hydrated layers on ceramic surfaces emerged as a significant factor in their effectiveness as anti-fouling agents. The balance between hydrophilic and hydrophobic segments within the polymer architecture was found to be crucial for optimal surface coverage and fouling minimisation. Additionally, the chapter underscores the importance of polymer solubility and interfacial conformation in

determining the efficacy of surface coatings, essential for long-term anti-fouling performance.

Chapter 3 details the experimental techniques used to assess polymer performance, including Quartz Crystal Microbalance with Dissipation (QCM-D), Atomic Force Microscopy (AFM), and Dynamic Light Scattering (DLS) on the nanoscale. QCM-D was key in measuring the mass of polymer adsorbed onto surfaces, while AFM provided insights into the uniformity and thickness of the polymer layers, which are critical indicators of their anti-fouling potential. DLS and Zeta Potential measurements contributed to understanding the size distribution and charge characteristics of the polymers in solution, influencing their adsorption behaviour and the stability of the resulting coatings. Together, these methodologies offered a comprehensive understanding of how polymer structure affects surface interactions, which is crucial for evaluating the effectiveness of different polymer architectures.

A series of experimental techniques were identified and outlined to investigate polymer adsorption, with a focus on quantifying adsorption, analysing the associated kinetics, and evaluating the effects on interfacial properties. These methods integrate nanoscale (QCM, AFM, DLS) measurements with macroscale (Surface Tension, Force Board and FLuSHT measurements) observations to establish a correlation between properties observed at the nanoscale and those at the full scale. The subsequent chapters will apply these techniques to examine various polymer-interface combinations.

Chapter 4 delves into the interactions between negatively charged surfaces and block copolymers composed of polyethylene oxide (PEO) and poly(2-(dimethylamino)ethyl methacrylate) (PDMAEMA). The objective was to create a surface additive for toilet bowls that repels dirt and reduces soil attachment, addressing a gap in current commercial products. Using QCM and AFM, the study examined how these copolymers adsorb onto surfaces, focusing on adsorption kinetics, surface coverage, and antifouling properties. The findings indicate that increasing PDMAEMA content generally led to higher adsorption due to stronger electrostatic interactions, though the relationship was complex, influenced by molecular configuration and

steric hindrance.

The copolymer 5.0-*b*-5.6 showed the fastest initial adsorption rate and highest mass adsorption, making it a strong candidate for applications requiring quick and effective surface coverage. In contrast, the copolymer with lower PDMAEMA content (5.0-*b*-2.5) exhibited the least adsorption and weakest surface interactions. Despite promising adsorption characteristics, none of the copolymers demonstrated effective antifouling properties against Bovine Serum Albumin (BSA), likely due to insufficient surface coverage or high BSA concentrations. The study suggests that denser polymer packing might be necessary for effective antifouling, though achieving this in practical applications could be challenging. These findings provide insights into developing advanced coatings for sanitary applications, particularly in improving adsorption efficiency and stability, though further refinements are needed to enhance antifouling capabilities.

Chapter 5 investigates the development and evaluation of innovative additives for glazed ceramics, focusing on how various random copolymers (see Table 5.2) interact with silicon dioxide surfaces under different pH conditions. The study aims to enhance the antifouling properties of ceramic surfaces, particularly in toilet bowls, using techniques like DLS and QCM. The findings reveal that pH significantly influences the behaviour of copolymers. At acidic pH (2), copolymers form small, positively charged particles that are stable and show minimal aggregation. Neutral pH results in a dynamic equilibrium with moderate particle sizes, while alkaline pH (10) produces larger, negatively charged particles prone to aggregation.

The study also demonstrates that pH levels affect the mass adsorption of copolymers on silicon dioxide surfaces. Acidic conditions reduce adsorption due to protonation, neutral pH allows moderate adsorption, and alkaline conditions enhance adsorption due to deprotonation effects. Among the copolymers, MAETAC:AA exhibited the highest initial adsorption and superior long-term antifouling performance, making it a promising candidate for self-

cleaning toilet surfaces. In contrast, DMAEMA-based copolymers showed lower effectiveness in preventing fouling.

Environmental pH is a critical factor influencing polymer performance. Alkaline conditions favoured better polymer adsorption due to deprotonation effects on the polymer chains, leading to larger and more stable structures that enhanced interaction with ceramic surfaces. Polymers with strong electrostatic interactions, such as those containing the MAETAC monomer, exhibited the highest adsorption efficiencies. These polymers maintained their integrity and functional properties even after multiple wash cycles, essential for practical applications. The random copolymer composition, specifically MAETAC:AA, was particularly effective in reducing surface fouling. This composition provided a balanced combination of electrostatic and hydrophobic interactions, contributing to superior anti-fouling performance.

Chapter 6 focused on the development of random copolymer additives designed to reduce adhesion on glazed ceramic surfaces. The study involved random copolymers with varying proportions of acrylic acid (AA), MAETAC, and DMAEMA (see Table 5.2), and assessed their effects using contact angle measurements, force board tests, and FLuSHT tests.

The key findings indicated that increasing the MAETAC content enhanced surface hydrophilicity, leading to lower static contact angles and reduced adhesion forces. This correlation between hydrophilicity and decreased adhesion was consistently observed across multiple tests, suggesting that these copolymers can improve performance by rapidly altering wettability in dynamic environments. The study underscores the importance of optimising copolymer compositions to achieve effective adhesion reduction.

Based on the findings from this research, the ideal polymer coating to repel foulants would densely pack the surface to maximise its anti-fouling properties. Given that this research is sponsored by Innospec, it is important to incorporate their additives into the formulation. MAETAC should be included in the formulation for an ideal polymer coating, as it demonstrated strong adsorption onto the sensor's surface, as discussed in Chapter 5. Additionally,

PEO should be incorporated into the formulation, as it was shown in Chapter 4 to repel BSA, but only when densely packed onto the surface. To ensure significant adsorption, a pH of 10 should be considered, as indicated in Chapter 5.

The findings have significant implications for the ceramics industry. By tailoring polymer formulations, manufacturers can enhance the durability and functionality of ceramic coatings, reducing maintenance costs and improving user satisfaction with cleaner and more resilient surfaces. The research also highlights the potential for these innovative additives to be applied in various other industries, such as biomedical devices, marine coatings, and food packaging, where anti-fouling properties are highly desirable.

## 7.1 Future Work

Building on the significant findings from this research, several promising avenues for future work are proposed to further advance the field of polymer additives for ceramic coatings. While the work conducted thus far has laid a strong foundation, numerous opportunities remain to deepen our understanding and enhance the practical applications of these materials.

Future research should focus on optimising polymer architectures for specific applications by thoroughly investigating various factors such as monomer ratios, molecular weights, and copolymer configurations. Understanding how these variables influence the performance of polymer additives in ceramic coatings could lead to the development of more effective and specialised materials. For example, by exploring different monomer ratios, researchers can fine-tune the balance between hydrophobic and hydrophilic properties, which is crucial for applications such as anti-fouling or self-cleaning surfaces. Additionally, varying molecular weights can affect the polymer's mechanical strength and flexibility, both of which are important factors in the durability of the coating.

Advanced computational modelling and simulations offer powerful tools for predicting and tailoring polymer behaviour at interfaces. By leveraging these technologies, researchers can gain insights into the most effective polymer structures for various applications. For instance, simulations can predict how a polymer will adsorb onto a ceramic surface, helping to identify the optimal architecture for maximum adhesion or anti-fouling properties. Moreover, by simulating interactions between the polymer and potential foulants, researchers can assess the polymer's efficacy as an anti-fouling agent before conducting time-consuming and costly experiments. This approach not only accelerates the research process but also allows for a more targeted investigation of promising candidates.

Further research should also include the following:

- **Investigating the response of random copolymers to BSA (Bovine Serum Albumin):** The random copolymers listed in Table 5.2 were not tested against BSA due to time constraints. Conducting this analysis could provide valuable insights into how different ratios of MAETAC (Methacryloyloxyethyl Trimethyl Ammonium Chloride) to DMAEMA (Dimethylaminoethyl Methacrylate) affect interactions with BSA. This information could be critical for designing coatings with improved protein resistance, which is essential in applications such as biomedical devices and water filtration systems.

- **Assessing the long-term performance and durability of polymer coatings:** To ensure that the developed polymer coatings are viable for real-world applications, it is crucial to evaluate their long-term performance under various conditions. Future studies should include accelerated ageing tests that simulate extended exposure to environmental factors such as temperature fluctuations, and humidity. Mechanical wear testing is also important to assess the coatings' ability to withstand physical stress and abrasion over time. These tests will provide a comprehensive understanding of the coatings' longevity and robustness, guiding further optimisation efforts.

- **Developing standardised testing protocols for anti-fouling performance:**
  The effectiveness of anti-fouling coatings can vary significantly depending on the application environment. To accurately assess their practical utility, it is essential to develop standardised testing protocols that mimic real-life scenarios. For instance, testing in household toilets, which involve frequent exposure to water, cleaning agents, and biological waste, would provide a realistic measure of the coatings' performance in domestic settings. Similarly, testing in marine environments, where coatings must resist biofouling from organisms such as barnacles and algae, would be crucial for applications in the shipping and offshore industries. By establishing these standardised protocols, researchers can ensure that their findings are applicable to the intended use cases, facilitating the transition from laboratory research to commercial products.

- **Enhancing Realism and Reliability in Experimental Setup for FLuSHT:**
  To enhance the relevance and accuracy of the FLuSHT system, future work should focus on replicating real-world toilet conditions by incorporating variable geometry and simulating the swirling action of water during flushes. Expanding environmental testing to include controlled temperature, humidity, and water pH will provide deeper insights into coating performance. Testing a broader range of materials, such as stainless steel and composites, and evaluating coating durability over repeated flush cycles will increase the applicability of findings. Refining the formulation of synthetic faeces and automating both their preparation and the experimental setup will improve consistency and data reliability.

  Further, developing standardised, automated cleaning protocols and exploring advanced coating techniques, like spray or dip coating, will ensure uniform performance. Validation of the FLuSHT system through comparison with real-world toilet flushes and employing statistical methods will strengthen result reliability. Finally, disseminating findings through publications, conferences, and collaborations with industry stakeholders will help translate this research into practical applications. Implementing

these enhancements will significantly improve the system's reliability and impact.

These proposed avenues for future research not only build on current findings but also aim to address the challenges and gaps that remain in the field. By pursuing these directions, the development of polymer additives for ceramic coatings can be further refined, leading to more effective, durable, and versatile solutions for a wide range of applications.

# Appendix One

# Section A

```
# 1. Put all force curves to analyse in one folder
# 2. Set folder name below
# 3. Run 1st cell
# 3. Name each sample in the 'samples' variable below - note each name must be in quotation marks, followed by ': [],'
# 4. Run 2nd cell
# 5. Plot data below, calling the relevant samples using the sample names specified

import glob, os
from nanoforce import AFM
import pandas as pd
import seaborn as sns
import plotly.graph_objects as go
from plotly.subplots import make_subplots
import numpy as np
import matplotlib.pyplot as plt

folder_name = r'E:\AFM\4th Year\Borosilicate\Just a few'
```

```
os.chdir(folder_name)
files = glob.glob("*.000")
print(*files, sep='\n')

# Analysis script - only change sample names!
samples = {
    'P4860 ': [],
}

i = 0
adhesion_df = pd.DataFrame()
modulus_df = pd.DataFrame()

for sample in samples.keys():
    samples[sample] = AFM()
    samples[sample].set_run_name(sample)
    samples[sample].file_name = files[i]
    i += 1

    # samples[sample].nanosurf_import() # If using Nanoscope files
       ↪ replace this with:
    samples[sample].input_files()
    samples[sample].nanoscope_params()
    samples[sample].nanoscope_read()
    samples[sample].baseline()
    samples[sample].contact()
    samples[sample].adjust_tip_position()

    samples[sample].calc_adhesion()
```

```
46      # samples[sample].calc_modulus()
47
48      adhesion_df.insert(loc=0, column=sample, value=samples[sample].
            ↪ adhesion)
49      modulus_df.insert(loc=0, column=sample, value=samples[sample].
            ↪ modulus)
50
51  for i in [13, 81]:
52      approach_force = samples['P8571 01'].approach[:, i]
53      approach_distance = samples['P8571 01'].z_approach[:, i]
54      withdraw_force = samples['P8571 01'].retract[:, i]
55      withdraw_distance = samples['P8571 01'].z_withdraw[:, i]
56
57      np.savetxt('P8571 01 good' + str(i) + '.csv',
58                 np.transpose([approach_force, approach_distance,
59                               withdraw_force, withdraw_distance]))
60
61  # Function to plot all force curves for specified sample
62  samples['P8571 01'].plot_curves()
63
64  # Function to overlay all approach and withdraw curves for specified
        ↪ sample
65  expt = samples['Uncoated with PS PROBE']
66
67  fig = make_subplots(rows=1, cols=2,
68                      subplot_titles=("Approach curves", "Retract
                            ↪ curves"))
69
70  for curve_number in range(0, expt.approach.shape[1]):
```

```
    fig.add_trace(go.Scatter(y=expt.approach[:, curve_number],
                             x=expt.z_approach[:, curve_number],
                             mode='lines', name='Approach curve (raw)
                                ↪ '),
                  row=1, col=1)
    fig.add_trace(go.Scatter(y=expt.retract[:, curve_number],
                             x=expt.z_withdraw[:, curve_number],
                             mode='lines', name='Retract curve (raw)'
                                ↪ ),
                  row=1, col=2)

fig['layout']['xaxis']['title'] = 'Piezo position (nm)'
fig['layout']['xaxis2']['title'] = 'Piezo position (nm)'
fig['layout']['yaxis']['title'] = 'Force (nN)'
fig['layout']['yaxis2']['title'] = 'Force (nN)'

fig.update_layout(height=500, width=1200,
                  showlegend=False, template='plotly_white')
fig.show()
```

Listing A.1: AFM Force Curve Analysis Script

# Appendix Two

# Section 2

```
import pandas as pd
import matplotlib.pyplot as plt
import seaborn as sns

# Define the file path
file_path = r'C:\Users\ANN949\OneDrive - University of Birmingham\
    ↪ Birmingham\DATA\Force Board\To find area under the curve.xlsx'

# Load the data into a pandas DataFrame
df = pd.read_excel(file_path)

# Define the columns to be plotted
columns_to_plot = [
    'Bare_Vertical Force',
    '200993_02_Vertical Force',
    '1456_02_Vertical Force',
    '1457_02_Vertical Force',
    '1458_02_Vertical Force',
    '1459_01_Vertical Force',
```

```
    '1460_02_Vertical Force',
    '1461_03_Vertical Force'
]

# Define custom legend texts
custom_legend_texts = [
    '0:0:0',
    '10:90:0',
    '10:80:10',
    '10:60:30',
    '10:45:45',
    '10:30:60',
    '10:10:80',
    '10:0:90'
]

# Subtract the initial time value from the 'Time' column to shift the data
df['Time'] = df['Time'] - df['Time'].min()

# Define the custom color palette
palette = ["#e22e82", "#ec7e08", "#65ae34", "#13a4d9", "#084e7a", "#9E3194", "#F50214", "#878482"]

# Plotting the data with higher DPI and decreased line width for better appearance
plt.figure(figsize=(7, 4), dpi=100)  # Adjusted DPI for better quality
for i, column in enumerate(columns_to_plot):
```

```
    plt.plot(df['Time'], df[column],
             label=custom_legend_texts[i],
             color=palette[i],
             linewidth=1.5)  # Decreased line width

plt.xlabel('Time (seconds)')
plt.ylabel('Vertical Force (N)')
plt.legend(title='AA:MAETAC:DMAEMA', fontsize=9, title_fontsize=10)
    ↪ # Adjusted legend text sizes
plt.xlim(left=0)  # Ensure x-axis starts at zero
plt.show()
```

Listing B.1: Plotting Vertical Force for Different Polymer Compositions

# References


1. Mekonnen, M. M. & Hoekstra, A. Y. Sustainability: Four billion people facing severe water scarcity. *Science Advances* **2,** 2–7. ISSN: 23752548 (2016).
2. Shannon, M. A. *et al.* Science and technology for water purification in the coming decades. *Nature* **452,** 301–310. ISSN: 14764687 (2008).
3. Parker, A. R. & Lawrence, C. R. Water capture by a desert beetle. *brief communications* **414,** 33–34 (2001).
4. *Water Stress by Country: 2040 - World ReliefWeb* 2015. https://reliefweb.int/map/world/water-stress-country-2040.
5. Wang, J. *et al.* Viscoelastic solid-repellent coatings for extreme water saving and global sanitation. *Nature Sustainability* **2,** 1–9. ISSN: 23989629. http://dx.doi.org/10.1038/s41893-019-0421-0 (2019).
6. *Toilet Care Products Market Growth Analysis Report 2023-2033* https://www.factmr.com/report/164/toilet-care-products-market.
7. *Global Toilet Cleaning Products Market Insights and Forecast to 2028* https://www.360marketupdates.com/global-toilet-cleaning-products-market-20167963#.
8. *About Us* https://innospec.com/about-us/.
9. Gedde, U. W. *Polymer Physics* 1–5 (KLUWER ACADEMIC PUBLISHERS, 1995).
10. Paul, D. Chapter 1 - Background and Perspective. *Polymer Blends,* 1–14 (Jan. 1978).

11. Flory, P. J. *Principles of Polymer Chemistry* (1953).

12. Brandrup, J. *et al. POLYMER HANDBOOK* 675–715. ISBN: 0471166286 (1999).

13. Flory, P. J. Thermodynamics of high polymer solutions. *The Journal of Chemical Physics* **9,** 660–661. ISSN: 00219606 (1941).

14. Netz, R. R., Potsdam, D. & Andelman, D. Polyelectrolytes in Solution and at Surfaces. *In Encyclopedia of Electrochemistry* **I,** 1–63 (2002).

15. Mahajan, A. & Pharm, B. Advancements in polymers used in hair care: a review. *International Journal of Research in Cosmetic Science* **6,** 6–16. ISSN: 2277–7172 (2016).

16. Hernández-Rivas, M. *et al.* Deposition of Synthetic and Bio-Based Polycations onto Negatively Charged Solid Surfaces: Effect of the Polymer Cationicity, Ionic Strength, and the Addition of an Anionic Surfactant. *Colloids and Interfaces* **4,** 33 (2020).

17. Wang, Z., Scheres, L., Xia, H. & Zuilhof, H. Developments and Challenges in Self-Healing Antifouling Materials. *Advanced Functional Materials* **30,** 1–25. ISSN: 16163028 (2020).

18. Yethiraj, A. Liquid state theory of polyelectrolyte solutions. *Journal of Physical Chemistry B* **113,** 1539–1551. ISSN: 15206106 (2009).

19. Hubbe, M. A., Rojas, O. J. & Lucia, L. A. Green modification of surface characteristics of cellulosic materials at the molecular or nano scale: A review. *BioResources* **10,** 6095–6206. ISSN: 19302126 (2015).

20. Hubbe, M. A. *Contributions of Polyelectrolyte Complexes and Ionic Bonding to Performance of Barrier Films for Packaging: A Review* 2021.

21. Lochhead, R. Y. The role of polymers in cosmetics: Recent trends. *ACS Symposium Series* **961,** 3–56. ISSN: 00976156. https://pubs.acs.org/doi/abs/10.1021/bk-2007-0961.ch001 (2007).

22. Lochhead, R. Y. *Cosmetic Science and Technology: Theoretical Principles and Applications - Google Books* 2009. https://books.google.co.uk/books?hl=en&lr=&id=HGp_CwAAQBAJ&oi=fnd&pg=PA171&dq=Polyquaternium-10:+Mechanism+of+Action+and+Applications+in+Hair+Care+Products%22+-+Journal+of+Cosmetic+Science,+Vol.+60,+No.+3,+2009,+pp.+327-334&ots=DY_XEZvoDL&sig=rmKKrzo43lRJ.

23. Ariffin, A., Razali, M. A. & Ahmad, Z. PolyDADMAC and polyacrylamide as a hybrid flocculation system in the treatment of pulp and paper mills waste water. *Chemical Engineering Journal* **179,** 107–111. ISSN: 1385-8947 (Jan. 2012).

24. Ribeiro, H. M., Morais, J. A. & Eccleston, G. M. Structure and rheology of semisolid o/w creams containing cetyl alcohol/non-ionic surfactant mixed emulsifier and different polymers. *International Journal of Cosmetic Science* **26,** 47–59. ISSN: 1468-2494 (Apr. 2004).

25. Tedeschi, C. *et al.* Engineering of Layer-by-Layer Coated Capsules with the Prospect of Materials for Efficient and Directed Electron Transfer. *Journal of the American Chemical Society* **126,** 3218–3227. ISSN: 00027863. https://pubs.acs.org/doi/full/10.1021/ja037128b (Mar. 2004).

26. Sukhorukov, G. B. *et al.* Layer-by-layer self assembly of polyelectrolytes on colloidal particles. *Colloids and Surfaces A: Physicochemical and Engineering Aspects* **137,** 253–266. ISSN: 0927-7757 (June 1998).

27. Dobrynin, A. V., Deshkovski, A. & Rubinstein, M. Adsorption of polyelectrolytes at oppositely charged surfaces. *Macromolecules* **34,** 3421–3436. ISSN: 00249297. https://pubs.acs.org/doi/full/10.1021/ma0013713 (May 2001).

28. Grosberg, A. Y., Nguyen, T. T. & Shklovskii, B. I. Colloquium: The physics of charge inversion in chemical and biological systems. *Reviews of Modern Physics* **74,** 329–345. ISSN: 00346861 (2002).

29. Kim, S. *et al.* Complexation and coacervation of like-charged polyelectrolytes inspired by mussels. *Proceedings of the National Academy of Sciences of the United States of America* **113,** E847–E853. ISSN: 10916490 (2016).

30. Hara, M. *Polyelectrolytes: Science and Technology - Google Books* 90–99. https://books.google.co.uk/books?hl=en&lr=&id=Zw7I0WRD9JIC&oi=fnd&pg=PA1&dq=Polyelectrolyte+in+solution+basics+Coulomb%27s+law&ots=-YCl31HpJ4&sig=ps8r2DW6BPpTDVE5z5Nso30QCpA&redir_esc=y#v=onepage&q&f=false (1992).

31. Stuart, M. C., de Vries, R. & Lyklema, H. Polyelectrolytes. *Fundamentals of Interface and Colloid Science* **5,** 1–84. ISSN: 18745679 (2005).

32. Tadmor, R., Hernández-Zapata, E., Chen, N., Pincus, P. & Israelachvili, J. N. Debye length and double-layer forces in polyelectrolyte solutions. *Macromolecules* **35,** 2380–2388. ISSN: 00249297 (2002).

33. Chapman, D. L. A contribution to the theory of electrocapillarity. *Philosophical Magazine Series,* 37–41 (2010).

34. Fuoss, R. M., Katchalsky, A. & Lifson, S. THE POTENTIAL OF AN INFINITE ROD-LIKE MOLECULE AND THE DISTRIBUTION OF THE COUNTER IONS. *The Journal of Chemical Physics* **37,** 579–589 (1951).

35. Alfrey, T. J., Berg, P. W. & Morawetz, H. The Counterion Distribution in Solutions of Rod-Shaped Polyelectrolytes. *Journal of polymer science* **VII,** 543–547 (1951).

36. Manning, G. S. Limiting Laws and Counterion Condensation in Polyelectrolyte Solutions I . Colligative Properties. *The Journal of Chemical Physics* **924,** 1–7 (1969).

37. Manning, S. Counterion Binding in Polyelectrolyte Theory. *Accounts of Chemical Research* **12,** 443–449 (1979).

38. Dobrynin, A. V. & Rubinstein, M. Theory of polyelectrolytes in solutions and at surfaces. *Progress in Polymer Science* **30,** 1049–1118. ISSN: 00796700 (2005).

39. Holm, C. J. e. a. Polyelectrolyte Theory. *Advanced Polymer Science* **166,** 67–111 (2004).

40. Metaxas, A. E., Panwar, V., Olson, R. L. & Dutcher, C. S. Ionic strength and polyelectrolyte molecular weight effects on floc formation and growth in Taylor–Couette flows. *Soft Matter* **17,** 1246–1257. ISSN: 1744-6848. https://pubs.rsc.org/en/content/articlehtml/2021/sm/d0sm01517b%20https://pubs.rsc.org/en/content/articlelanding/2021/sm/d0sm01517b (Feb. 2021).

41. Meneses-Juárez, E., Márquez-Beltrán, C. & González-Melchor, M. Influence of pH on the formation of a polyelectrolyte complex by dissipative particle dynamics simulation: From an extended to a compact shape. *Physical review. E* **100,** 1–11. ISSN: 2470-0053. https://pubmed.ncbi.nlm.nih.gov/31499774/ (July 2019).

42. Tan, H. L., McMurdo, M. J., Pan, G. & Van Patten, P. G. Temperature Dependence of Polyelectrolyte Multilayer Assembly. *Langmuir* **19,** 9311–9314. ISSN: 07437463. https://pubs.acs.org/doi/full/10.1021/la035094f (Oct. 2003).

43. Muthukumar, M. 50th Anniversary Perspective: A Perspective on Polyelectrolyte Solutions. *Macromolecules* **50,** 9528–9560. ISSN: 15205835. /pmc/articles/PMC5746850/%20/pmc/articles/PMC5746850/?report=abstract%20https://www.ncbi.nlm.nih.gov/pmc/articles/PMC5746850/ (Dec. 2017).

44. Akyol, E., Kirboga, S. & Oner, M. *Polyelectrolytes: Science and Application* (eds P. M., V., Bayraktar, O. & Picó, G. A.) 87–112. ISBN: 978-3-319-01679-5. https://link.springer.com/10.1007/978-3-319-01680-1 (Springer International Publishing, Cham, 2014).

45. Lewis, R. & Richards, R. *Polymers at Surfaces and Interfaces* 210–211 (2010).

46. Lichter, J. A., Van Vlietpa, K. J. & Rubner, M. F. Design of antibacterial surfaces and interfaces: Polyelectrolyte multilayers as a multifunctional platform. *Macromolecules* **42,** 8573–8586. ISSN: 00249297 (2009).

47. Yoo, D., Shiratori, S. S. & Rubner, M. F. Controlling bilayer composition and surface wettability of sequentially adsorbed multilayers of weak polyelectrolytes. *Macromolecules* **31,** 4309–4318. ISSN: 00249297 (1998).

48. Sukhishvili, S. A. & Granick, S. Layered, erasable polymer multilayers formed by hydrogen-bonded sequential self-assembly. *Macromolecules* **35,** 301–310. ISSN: 00249297 (2002).

49. Han, U., Seo, Y. & Hong, J. Effect of pH on the structure and drug release profiles of layer-by-layer assembled films containing polyelectrolyte, micelles, and graphene oxide. *Scientific Reports* **6,** 1–10. ISSN: 20452322. http://dx.doi.org/10.1038/srep24158 (2016).

50. Biesheuvel, P. M., Mauser, T., Sukhorukov, G. B. & Möhwald, H. Micromechanical theory for pH-dependent polyelectrolyte multilayer capsule swelling. *Macromolecules* **39,** 8480–8486. ISSN: 00249297 (2006).

51. Kim, B. S. & Vinogradova, O. I. pH-controlled swelling of polyelectrolyte multilayer microcapsules. *Journal of Physical Chemistry B* **108,** 8161–8165. ISSN: 15206106 (2004).

52. Mendelsohn, J. D., Yang, S. Y., Hiller, J. A., Hochbaum, A. I. & Rubner, M. F. Rational design of cytophilic and cytophobic polyelectrolyte multilayer thin films. *Biomacromolecules* **4,** 96–106. ISSN: 15257797 (2003).

53. Büscher, K., Graf, K., Ahrens, H. & Helm, C. A. Influence of adsorption conditions on the structure of polyelectrolyte multilayers. *Langmuir* **18,** 3585–3591. ISSN: 07437463 (2002).

54. Salomäki, M., Vinokurov, I. A. & Kankare, J. Effect of temperature on the buildup of polyelectrolyte multilayers. *Langmuir* **21,** 11232–11240. ISSN: 07437463 (2005).

55. Michna, A., Adamczyk, Z., Kubiak, K. & Jamrozy, K. Formation of PDADMAC monolayers evaluated in situ by QCM and streaming potential measurements. *Journal of Colloid and Interface Science* **428,** 170–177. ISSN: 10957103 (2014).

56. Dobraszczyk, B. J. The rheological basis of dough stickiness. *Journal of Texture Studies* **28,** 139–162. ISSN: 00224901 (1997).

57. Wang, J., Xu, H., Battocchi, D. & Bierwagen, G. The determination of critical pigment volume concentration (CPVC) in organic coatings with fluorescence microscopy. *Progress in Organic Coatings* **77,** 2147–2154. ISSN: 03009440 (Dec. 2014).

58. Gent, A. & Hamed, G. *Fundamentals of Adhesion* **1,** 39–73 (1990).

59. Cunningham, M. F. *et al.* Future green chemistry and sustainability needs in polymeric coatings. *Green Chemistry* **21,** 4919–4926. ISSN: 14639270. http://dx.doi.org/10.1039/c9gc02462j (2019).

60. Lowe, S., O'Brien-Simpson, N. M. & Connal, L. A. Antibiofouling polymer interfaces: Poly(ethylene glycol) and other promising candidates. *Polymer Chemistry* **6,** 198–212. ISSN: 17599962. http://dx.doi.org/10.1039/c4py01356e (2015).

61. Li, C., Li, M., Qi, W., Su, R. & Yu, J. Effect of Hydrophobicity and Charge Separation on the Antifouling Properties of Surface-Tethered Zwitterionic Peptides. *Langmuir* **37,** 8455–8462. ISSN: 15205827 (2021).

62. Huellemeier, H. A., Eren, N. M., Ortega-Anaya, J., Jimenez-Flores, R. & Heldman, D. R. Application of quartz crystal microbalance with dissipation (QCM-D) to study low-temperature adsorption and fouling of milk fractions on stainless steel. *Chemical Engineering Science* **247,** 117004. ISSN: 0009-2509 (Jan. 2022).

63. Seigel, R. R. *et al.* On-Line Detection of Nonspecific Protein Adsorption at Artificial Surfaces. *Analytical Chemistry* **69,** 3321–3328. ISSN: 00032700 (1997).

64. Kenausis, G. L. *et al.* Poly(L-lysine)-g-poly(ethylene glycol) layers on metal oxide surfaces: Attachment mechanism and effects of polymer architecture on resistance to protein adsorption. *Journal of Physical Chemistry B* **104,** 3298–3309. ISSN: 15206106 (2000).

65. Madaan, N. *et al.* Thiol-ene-thiol photofunctionalization of thiolated monolayers with polybutadiene and functional thiols, including thiolated DNA. *Journal of Physical Chemistry C* **115,** 22931–22938. ISSN: 19327447 (2011).

66. Boschkova, K. & Stålgren, J. J. Cationic and nonionic surfactant adsorption on thiol surfaces with controlled wettability. *Langmuir* **18,** 6802–6806. ISSN: 07437463 (2002).

67. Tugulu, S. & Klok, H. A. Stability and nonfouling properties of poly(poly(ethylene glycol) methacrylate) Brushes under cell culture conditions. *Biomacromolecules* **9,** 906–912. ISSN: 15257797 (2008).

68. Fan, X., Lin, L. & Messersmith, P. B. Cell fouling resistance of polymer brushes grafted from Ti substrates by surface-initiated polymerization: Effect of ethylene glycol side chain length. *Biomacromolecules* **7,** 2443–2448. ISSN: 15257797 (2006).

69. L. G. GRIFFITH. Polymeric Biomaterials. *Biomedical Engineering Fundamentals* **48,** 263–277 (2000).

70. Malmsten, M. Formation of Adsorbed Protein Layers. *Journal of Colloid and Interface Science* **207,** 186–199. ISSN: 00219797 (1998).

71. Uno, K. *et al.* Particle adsorption in evaporating droplets of polymer latex dispersions on hydrophilic and hydrophobic surfaces. *Colloid Polymer Science* **276,** 810–815 (1998).

72. Arai, T. & Norde, W. The behavior of some model proteins at solid-liquid interfaces 2. Sequential and competitive adsorption. *Colloids and Surfaces* **51,** 17–28. ISSN: 01666622 (1990).

73. Prime, K. L. & Whitesides, G. M. Adsorption of Proteins onto Surfaces Containing End-Attached Oligo(ethylene oxide): A Model System Using Self-Assembled Monolayers. *Journal of the American Chemical Society* **115,** 10714–10721. ISSN: 15205126 (1993).

74. Jeon, S., Lee, J., J.D, A. & De Gennes, P. Protein Surface Interactions in the Presence of Polyethylene Oxide. *Journal of Colloid and Interface Science* **142,** 149–158 (1991).

75. Yang, Z., Zhang, S., Tarabara, V. V. & Bruening, M. L. Aqueous Swelling of Zwitterionic Poly(sulfobetaine methacrylate) Brushes in the Presence of Ionic Surfactants. *Macromolecules* **51,** 1161–1171. ISSN: 15205835 (2018).

76. Kurowska, M. *et al.* A Simultaneously Antimicrobial, Protein-Repellent, and Cell-Compatible Polyzwitterion Network. *Biomacromolecules* **18,** 1373–1386. ISSN: 15264602 (2017).

77. Ngo, B. K. D. & Grunlan, M. A. Protein Resistant Polymeric Biomaterials. *ACS Macro Letters* **6,** 992–1000. ISSN: 21611653 (2017).

78. Kalasin, S., Letteri, R. A., Emrick, T. & Santore, M. M. Adsorbed Polyzwitterion Copolymer Layers Designed for Protein Repellency and Interfacial Retention. *Langmuir* **33,** 13708–13717. ISSN: 15205827 (2017).

79. Von Der Lühe, M., Weidner, A., Dutz, S. & Schacher, F. H. Reversible Electrostatic Adsorption of Polyelectrolytes and Bovine Serum Albumin onto Polyzwitterion-Coated Magnetic Multicore Nanoparticles: Implications for Sensing and Drug Delivery. *ACS Applied Nano Materials* **1,** 232–244. ISSN: 25740970 (2018).

80. Dai, F. & Liu, W. Enhanced gene transfection and serum stability of polyplexes by PDMAEMA-polysulfobetaine diblock copolymers. *Biomaterials* **32,** 628–638. ISSN: 0142-9612 (Jan. 2011).

81. Bretscher, M. S. & Raff, M. C. Mammalian plasma membranes. *Nature* **258,** 43–49. ISSN: 00280836 (1975).

82. Zhang, Z., Chen, S., Chang, Y. & Jiang, S. Surface grafted sulfobetaine polymers via atom transfer radical polymerization as superlow fouling coatings. *Journal of Physical Chemistry B* **110,** 10799–10804. ISSN: 15206106 (2006).

83. Tegoulia, V. A., Rao, W., Kalambur, A. T., Rabolt, J. F. & Cooper, S. L. Surface properties, fibrinogen adsorption, and cellular interactions of a novel phosphorylcholine-containing self-assembled monolayer on gold. *Langmuir* **17,** 4396–4404. ISSN: 07437463 (2001).

84. Fabianowski, W. *et al.* Spontaneous Assembly of Phosphatidylcholine Monolayers via Chemisorption onto Gold. *Langmuir* **5,** 35–41. ISSN: 15205827 (1989).

85. Kitano, H. *et al.* Structure of Water in the Vicinity of Phospholipid Analogue Copolymers as Studied by Vibrational Spectroscopy. *Langmuir* **19,** 10260–10266. ISSN: 07437463 (2003).

86. Diem, T., Czajka, B., Weber, B. & Regen, S. L. Spontaneous Assembly of Phospholipid Monolayers via Synthesis and X-ray Crystal Structure of a Soluble Pentametallic Organoyttrium Alkoxide Oxide Complex , of Chemistry. *American Chemical Society,* 6094–6095 (1986).

87. Feng, W. *et al.* Characterization of protein resistant, grafted methacrylate polymer layers bearing oligo(ethylene glycol) and phosphorylcholine side chains by neutron reflectometry. *Biointerphases* **2,** 34–43. ISSN: 1934-8630 (2007).

88. Ishihara, K. *et al.* Why do phospholipid polymers reduce protein adsorption? *Journal of Biomedical Materials Research* **39,** 323–330. ISSN: 00219304 (1998).

89. Jiang, S. & Cao, Z. Ultralow-fouling, functionalizable, and hydrolyzable zwitterionic materials and their derivatives for biological applications. *Advanced Materials* **22,** 920–932. ISSN: 09359648 (2010).

90. Zhang, Z. *et al.* Nonfouling behavior of polycarboxybetaine-grafted surfaces: Structural and environmental effects. *Biomacromolecules* **9,** 2686–2692. ISSN: 15257797 (2008).

91. Zhang, Z. *et al.* Blood compatibility of surfaces with superlow protein adsorption. *Biomaterials* **29,** 4285–4291. ISSN: 0142-9612 (Nov. 2008).

92. Wang, W. *et al.* Zwitterionic-polymer-functionalized poly(vinyl alcohol-co-ethylene) nanofiber membrane for resistance to the adsorption of bacteria and protein. *Journal of Applied Polymer Science* **133,** 1–7. ISSN: 10974628 (2016).

93. Yang, W., Sundaram, H. S., Ella, J. R., He, N. & Jiang, S. Low-fouling electrospun PLLA films modified with zwitterionic poly(sulfobetaine methacrylate)-catechol conjugates. *Acta Biomaterialia* **40,** 92–99. ISSN: 1742-7061 (Aug. 2016).

94. Vaisocherová, H. *et al.* Ultralow fouling and functionalizable surface chemistry based on a zwitterionic polymer enabling sensitive and specific protein detection in undiluted blood plasma. *Analytical Chemistry* **80,** 7894–7901. ISSN: 00032700 (2008).

95. Zhang, Z., Chao, T., Chen, S. & Jiang, S. Superlow fouling sulfobetaine and carboxybetaine polymers on glass slides. *Langmuir* **22,** 10072–10077. ISSN: 07437463 (2006).

96. Ladd, J., Zhang, Z., Chen, S., Hower, J. C. & Jiang, S. Zwitterionic polymers exhibiting high resistance to nonspecific protein adsorption from human serum and plasma. *Biomacromolecules* **9,** 1357–1361. ISSN: 15257797 (2008).

97. Chang, Y. *et al.* A highly stable nonbiofouling surface with well-packed grafted zwitterionic polysulfobetaine for plasma protein repulsion. *Langmuir* **24,** 5453–5458. ISSN: 07437463 (2008).

98. Liu, G. & Zhang, G. *Basic Principles of QCM-D* 1–8. ISBN: 9783642397905 (2013).

99. Reviakine, I., Johannsmann, D. & Richter, R. P. Hearing what you cannot see and visualizing what you hear: Interpreting quartz crystal microbalance data from solvated

interfaces. *Analytical Chemistry* **83,** 8838–8848. ISSN: 00032700. https://pubs.acs.org/doi/full/10.1021/ac201778h (Dec. 2011).

100. Scientific, B. *QSense. The Working Principles of QCM and QCM-D Technology* 2023.

101. Scientific, B. *Biolin Scientific. QCM-D: What Is QCM-D?* https://www.biolinscientific.com/measurements/qcm-d#what-is-qcm-d.

102. Rodahl, M. & Kasemo, B. Frequency and dissipation-factor responses to localized liquid deposits on a QCM electrode. *Sensors and Actuators, B: Chemical* **37,** 111–116. ISSN: 09254005 (1996).

103. Scientific, B. *Why multiple harmonics are important in QCM measurements* https://www.biolinscientific.com/blog/why-are-overtones-important-in-qcm.

104. Raudino, M. *et al.* Probing the Cleaning of Polymeric Coatings by Nanostructured Fluids: A QCM-D Study. *Langmuir* **33,** 5675–5684. ISSN: 15205827 (2017).

105. Voinova, M. V., Rodahl, M., Jonson, M. & Kasemo, B. Viscoelastic Acoustic Response of Layered Polymer Films at Fluid-Solid Interfaces: Continuum Mechanics Approach. *Physica Scripta* **59,** 391–396. ISSN: 0031-8949 (1999).

106. Liu, Y. & Shen, L. From Langmuir kinetics to first- and second-order rate equations for adsorption. *Langmuir* **24,** 11625–11630. ISSN: 07437463 (2008).

107. Eaton, P. & West, P. *Atomic Force Microscopy* 9–101. https://books.google.co.uk/books?hl=en&lr=&id=VB0UDAAAQBAJ&oi=fnd&pg=PR5&dq=who+invented+atomic+force+microscopy&ots=xdCsQYyx1J&sig=018zdrqFJ7Sqz4AhaXviCAEcczI&redir_esc=y#v=onepage&q&f=false (2010).

108. Binnig, G. & Quate, C. F. Atomic Force Microscope. *Physical Review Letters* **56,** 51–57 (1986).

109. Tortonese, M. Cantilevers and Tips for Atomic Force Microscopy. *Engineering In Medicine And Biology* **1,** 28–29 (1997).

110. Butt, H. J., Cappella, B. & Kappl, M. Force measurements with the atomic force microscope: Technique, interpretation and applications. *Surface Science Reports* **59,** 1–152. ISSN: 01675729 (2005).

111. Bowen, R. & Hilal, N. *Atomic Force Microscopy in Process Engineering: An Introduction to AFM* 3–12. https://books.google.co.uk/books?hl=en&lr=&id=XKByFSz316sC&oi=fnd&pg=PP1&dq=atomic+force+microscopy+in+process+engineering&ots=bR4KjorZ5N&sig=ps7dRx70i41NCpiKq5sxsOjKbXI#v=onepage&q=atomic%20force%20microscopy%20in%20process%20engineering&f=false (2009).

112. *Park Systems. Force Distance Spectroscopy* https://www.parksystems.com/index.php/park-spm-modes/95-force-measurement/244-force-distance-spectroscopy.

113. Anton, P. *Characterization of Surface Mechanical Properties of Polymer Coatings using AFM Force Distance Curves* 2023.

114. Benítez, R., Bolós, V. J. & Toca-Herrera, J. L. afmToolkit: An R package for automated AFM force-distance curves analysis. *Contributed Research Article* **9,** 291–308. ISSN: 20734859 (2017).

115. Goodman, F. O. & Garcia, N. Roles of the attractive and repulsive forces in atomic-force micrscopy. *Physical Review B* **43,** 4728–4731 (1991).

116. Magonov, S. N. & Reneker, D. H. Characterization of polymer surfaces with atomic force microscopy. *Annual Review of Materials Science* **27,** 175–222. ISSN: 00846600 (1997).

117. Sedin, D. L. & Rowlen, K. L. Influence of tip size on AFM roughness measurements. *applied surface science* **182,** 40–48 (2001).

118. Cappella, B. & Dietler, G. Force distance curves by atomic force micrscopy. *Surface Science Reports* **34,** 1–104 (1999).

119. Stetefeld, J., McKenna, S. A. & Patel, T. R. Dynamic light scattering: a practical guide and applications in biomedical sciences. *Biophysical Reviews* **8,** 409–427. ISSN: 18672469. http://dx.doi.org/10.1007/s12551-016-0218-6 (2016).

120. Malvern Instruments Ltd. *Zetasizer Nano User Manuall: Size theory* tech. rep. (2013), 1–11.

121. Rodriguez-Loya, J., Lerma, M. & Gardea-Torresdey, J. L. Dynamic Light Scattering and Its Application to Control Nanoparticle Aggregation in Colloidal Systems: A Review. *Micromachines* **15,** 1–21. ISSN: 2072666X (2024).

122. Babaie, B., Najafi, M. & Ataeefard, M. Designing an optimised formulation for in situ emulsion polymerization: printing ink production by response surface methodology. *Pigment and Resin Technology* **1,** 1–15. ISSN: 03699420 (2024).

123. Filippov, S. K. *et al.* Dynamic light scattering and transmission electron microscopy in drug delivery : a roadmap for correct characterization of nanoparticles and interpretation of results. *Materials Horizon* **10,** 5354–5370 (2023).

124. Ball, S. *Dynamic light scattering: Colloidal Gold: The gold standard for drug delivery?* 2015. https://drug-dev.com/dynamic-light-scattering-colloidal-gold-the-gold-standard-for-drug-delivery/.

125. Bhattacharjee, S. DLS and zeta potential - What they are and what they are not? *Journal of Controlled Release* **235,** 337–351. ISSN: 18734995. http://dx.doi.org/10.1016/j.jconrel.2016.06.017 (2016).

126. Uskoković, V. Dynamic Light Scattering Based Microelectrophoresis: Main Prospects and Limitations. *Journal of Dispersion Science and Technology* **33,** 1762–1786. ISSN: 01932691 (2012).

127. Malvern & Instruments, M. *Dynamic Light Scattering : An Introduction in 30 Minutes* 2011. http://scholar.google.com/scholar?hl=en&btnG=Search&q=intitle:Dynamic+Light+Scattering+:+An+Introduction+in+30+Minutes#3.

128. Malvern Ltd. Zeta potential: An Introduction in 30 minutes. *Zetasizer Nano Serles Technical Note. MRK654-01* **2,** 1–6. http://scholar.google.com/scholar?hl=en&btnG=Search&q=intitle:Zeta+Potential+An+Introduction+in+30+Minutes#0 (2011).

129. Malvern Panalytical. *Zeta potential: An Introduction in 30 minutes* 2011.

130. Malvern Panalytical. *Size theory* 2023.

131. *Zeta Potential in Colloid Science: Principles and Applications - Robert J. Hunter - Google Books* https://books.google.co.uk/books?hl=en&lr=&id=9I3-BAAAQBAJ&oi=fnd&pg=PP1&dq=what+is+zeta+potential&ots=EYQZP8Pr-r&sig=ZPsihXXwmqGkt4er-M3KWL_ZwWs&redir_esc=y#v=onepage&q=what%20is%20zeta%20potential&f=false.

132. Navascues, G. Liquid surfaces: Theory of surface tension. *Reports on Progress in Physics* **42,** 1131–1186. ISSN: 00344885 (1979).

133. Eral, H. B., 'T Mannetje, D. J. & Oh, J. M. Contact angle hysteresis: A review of fundamentals and applications. *Colloid and Polymer Science* **291,** 247–260. ISSN: 0303402X (2013).

134. Sophocleous, M. Understanding and explaining surface tension and capillarity. *Hydrogeology Journal* **18,** 811–821. ISSN: 14312174 (2010).

135. Mittal, K. L. in *Advances in Contact Angle, Wettability and Adhesion: Volume 1* 1–412 (wiley, Jan. 2013). ISBN: 9781118795620. https://onlinelibrary.wiley.com/doi/book/10.1002/9781118795620.

136. Kwok, D. Y. & Neumann, A. W. Contact angle measurement and contact angle interpretation. *Advances in Colloid and Interface Science* **81,** 167–249. ISSN: 0001-8686 (Sept. 1999).

137. Industrial Dynamics Sweden AB. *ForceBoard ™ User's Manual* 2022. www.ForceBoard.com!.

138. Gao, F., Zhang, G., Zhang, Q., Zhan, X. & Chen, F. Improved Antifouling Properties of Poly(Ether Sulfone) Membrane by Incorporating the Amphiphilic Comb Copolymer with Mixed Poly(Ethylene Glycol) and Poly(Dimethylsiloxane) Brushes. *Industrial and Engineering Chemistry Research* **54,** 8789–8800. ISSN: 15205045 (2015).

139. Gao, J. *et al.* Probing Interfacial Behavior and Antifouling Activity of Adsorbed Copolymers at Solid Liquid Interfaces. *Langmuir* **39,** 4557–4570. ISSN: 15205827 (2023).

140. Nurioglu, A. G., Esteves, A. C. C. & De With, G. Non-toxic, non-biocide-release antifouling coatings based on molecular structure design for marine applications. *Journal of Materials Chemistry B* **3,** 6547–6570. ISSN: 2050750X (2015).

141. Vuoriluoto, M. *et al.* Effect of Molecular Architecture of PDMAEMA-POEGMA Random and Block Copolymers on Their Adsorption on Regenerated and Anionic Nanocelluloses and Evidence of Interfacial Water Expulsion. *Journal of Physical Chemistry B* **119,** 15275–15286. ISSN: 15205207 (2015).

142. Wu, Y. *et al.* Construction of Self-Assembled Polyelectrolyte/Cationic Microgel Multilayers and Their Interaction with Anionic Dyes Using Quartz Crystal Microbalance and Atomic Force Microscopy. *ACS Omega* **6,** 5764–5774. ISSN: 24701343 (2021).

143. Zhang, Z. J. *et al.* Blob Size Controls Diffusion of Free Polymer in a Chemically Identical Brush in Semidilute Solution. *Macromolecules* **51,** 6312–6317. ISSN: 15205835 (2018).

144. Zhang, Z., Tomlinson, M. R., Golestanian, R. & Geoghegan, M. The interfacial behaviour of single poly(N,N-dimethylacrylamide) chains as a function of pH. *Nanotechnology* **19.** ISSN: 09574484 (2008).

145. Farris, S. *et al.* Wetting of Biopolymer Coatings : Contact Angle Kinetics and Image Analysis Investigation. *American Chemical Society* **27,** 7563–7574 (2011).

146. Pérez-Fuentes, L., Drummond, C., Faraudo, J. & Bastos-González, D. Adsorption of milk proteins ($\beta$-casein and $\beta$-lactoglobulin) and BSA onto hydrophobic surfaces. *Materials* **10,** 1–25. ISSN: 19961944 (2017).

147. Kokufuta, E. & Takahashi, K. Adsorption of Poly(diallyldimethylammonium chloride) on Colloid Silica from Water and Salt Solution. *Macromolecules* **19,** 351–354. ISSN: 15205835 (1986).

148. Banerjee, I., Pangule, R. C. & Kane, R. S. Antifouling Coatings : Recent Developments in the Design of Surfaces That Prevent Fouling by Proteins , Bacteria , and Marine Organisms. *Advanced Materials* **23,** 690–718 (2011).

149. Müller, M. T., Yan, X., Lee, S., Perry, S. S. & Spencer, N. D. Lubrication properties of a brushlike copolymer as a function of the amount of solvent absorbed within the brush. *Macromolecules* **38,** 5706–5713. ISSN: 00249297 (2005).

150. Claesson, P. M., Poptoshev, E., Blomberg, E. & Dedinaite, A. *Polyelectrolyte-mediated surface interactions* June 2005.

151. Jones, R. A. L. & Richards, R. W. *Polymers at Surfaces and Interfaces* (Cambridge University Press, Apr. 1999).

152. Gombotz, W. R., Guanghui, W., Horbett, T. A. & Hoffman, A. S. Protein adsorption to poly ( ethy1ene oxide ) surfaces. *Journal of Biomedical Materials Research* **25,** 1547–1562 (1991).

153. Bergstrom, K. *et al.* Reduction of fibrinogen adsorption on PEG-coated polystyrene surfaces. *Journal of Biomedical Materials Research* **26,** 779–790 (1992).

154. Garg, A., Heflin, J. R., Gibson, H. W. & Davis, R. M. Study of film structure and adsorption kinetics of polyelectrolyte multilayer films: Effect of pH and polymer concentration. *Langmuir* **24,** 10887–10894. ISSN: 07437463 (2008).

155. Víšová, I. *et al.* Surface Preconditioning Influences the Antifouling Capabilities of Zwitterionic and Nonionic Polymer Brushes. *Langmuir* **36,** 8485–8493. ISSN: 0743-7463 (2020).

156. Dobraszczyk, B. J. The rheological basis of dough stickiness. *Journal of Texture Studies* **28,** 139–162. ISSN: 00224901 (1997).

157. Popa, I., Cahill, B. P., Maroni, P., Papastavrou, G. & Borkovec, M. Thin adsorbed films of a strong cationic polyelectrolyte on silica substrates. *Journal of Colloid and Interface Science* **309,** 28–35. ISSN: 00219797 (May 2007).

158. Popa, I., Cahill, B. P., Maroni, P., Papastavrou, G. & Borkovec, M. Thin adsorbed films of a strong cationic polyelectrolyte on silica substrates. *Journal of Colloid and Interface Science* **309,** 28–35. ISSN: 00219797 (2007).

159. Su, B. *et al.* Abrasion-Resistant Super-Slippery Flush Toilets Fabricated by a Selective Laser Sintering 3D Printing Technology. *SSRN Electronic Journal* **2300703,** 1–9. ISSN: 15272648 (2022).

160. Dobrynin, A. V., Deshkovski, A. & Rubinstein, M. Adsorption of polyelectrolytes at oppositely charged surfaces. *Macromolecules* **34,** 3421–3436. ISSN: 00249297. https://pubs.acs.org/doi/full/10.1021/ma0013713 (May 2001).

161. Kaur, K. *et al.* Application of a quartz crystal microbalance to measure the mass concentration of combustion particle suspensions. *Journal of Aerosol Science* **137,** 105445. www.elsevier.com/locate/jaerosci (2019).

162. Huellemeier, H. A. *et al.* Assessing the Scalability of the High-Pressure High-Temperature Quartz Crystal Microbalance with Dissipation (HPHT QCM-D) for Milk Fouling Studies. *ACS Food Science and Technology* **3,** 1216–1228. ISSN: 26921944. https://pubs.acs.org/doi/full/10.1021/acsfoodscitech.3c00131 (July 2023).

163. García, R. & Paulo, A. S. Attractive and repulsive tip-sample interaction regimes in tapping-mode atomic force microscopy. *Physical Review B - Condensed Matter and Materials Physics* **60,** 4961–4967. ISSN: 1550235X (1999).

164. Adibnia, V. *et al. Bioinspired polymers for lubrication and wear resistance* 101298. ISBN: 0000000000. https://doi.org/10.1016/j.progpolymsci.2020.101298 (Elsevier B.V., 2020).

165. Adibnia, V. *et al.* Bioinspired polymers for lubrication and wear resistance. *Progress in Polymer Science* **110,** 101298. ISSN: 0079-6700 (Nov. 2020).

166. Kawelah, M. *et al.* Dynamic Adsorption of Functionalized Zwitterionic Copolymers on Carbonate Surfaces under Extreme Reservoir Conditions. *Energy and Fuels* **34,** 14526–14536 (2020).

167. Avila-Sierra, A. *et al.* Effects of structural and chemical properties of surface coatings on the adsorption characteristics of proteins. *Surface and Coatings Technology* **452,** 129054. ISSN: 02578972. https://doi.org/10.1016/j.surfcoat.2022.129054 (2023).

168. Lin, Y. T. *et al.* Elucidating Interfacial Chain Conformation of Superhydrophilic Polymer Brushes by Vibrational Sum Frequency Generation Spectroscopy. *Langmuir* **38,** 14704–14711. ISSN: 15205827 (2022).

169. Butt, H. J., Cappella, B. & Kappl, M. Force measurements with the atomic force microscope: Technique, interpretation and applications. *Surface Science Reports* **59,** 1–152. ISSN: 0167-5729 (Oct. 2005).

170. Michna, A., Adamczyk, Z., Kubiak, K. & Jamrozy, K. Formation of PDADMAC monolayers evaluated in situ by QCM and streaming potential measurements. *Journal of Colloid and Interface Science* **428,** 170–177. ISSN: 10957103 (2014).

171. Lapitsky, Y. & Kaler, E. W. Formation of surfactant and polyelectrolyte gel particles in aqueous solutions. *Colloids and Surfaces* **250,** 179–187 (2004).

172. Technology, M. P. *Iso-electric Point (IEP) and Point of Zero Charge (PZC)* 2015.

173. Sakai, K. *et al.* pH-Responsive Diblock Copolymer Micelles at the Silica / Aqueous Solution Interface : Adsorption Kinetics and Equilibrium Studies. *Physical Chemistry* **110,** 14744–14753 (2006).

174. Stoll, S. & Chodanowski. Polyelectrolyte Adsorption on an Oppositely Charged Spherical Particle. Chain Rigidity Effects. *Soft Matter* **35,** 9556–9562. ISSN: 1744683X (2002).

175. Thünemann, A. F., Müller, M., Dautzenberg, H., Joanny, J. F. & Löwen, H. Polyelectrolyte Complexes. *Advances in Polymer Science* **166,** 113–171. ISSN: 00653195 (2004).

176. Zanini, S., Müller, M., Riccardi, C. & Orlandi, M. Polyethylene glycol grafting on polypropylene membranes for anti-fouling properties. *Plasma Chemistry and Plasma Processing* **27,** 446–457. ISSN: 02724324. https://link.springer.com/article/10.1007/s11090-007-9094-y (Aug. 2007).

177. Halperin, A. Polymer brushes that resist adsorption of model proteins: Design parameters. *Langmuir* **15,** 2525–2533. ISSN: 07437463 (1999).

178. Schonhoff, M. Self-assembled polyelectrolyte multilayers. *Colloids and Interface Science* **8,** 86–95 (2003).

179. Nakahata, R. & Yusa, S. I. Solution Properties of Amphoteric Random Copolymers Bearing Pendant Sulfonate and Quaternary Ammonium Groups with Controlled Structures. *Langmuir* **35,** 1690–1698. ISSN: 15205827 (2019).

180. Kitano, H., Nagaoka, K., Tada, S., Gemmei-Ide, M. & Tanaka, M. Structure of water incorporated in amphoteric polymer thin films as revealed by FT-IR spectroscopy. *Macromolecular Bioscience* **8,** 77–85. ISSN: 16165187 (2008).

181. Altay, B. N. *et al.* Surface Free Energy Estimation : A New Methodology for Solid Surfaces. *Advanced Materials Interfaces* **1901570,** 1–11 (2020).